Cosmology with galaxy clusters

Vincent R. Eke

Cosmology with Galaxy Clusters

Vincent R. Eke

A thesis submitted to the University of Durham
in accordance with the regulations for
admittance to the Degree of Doctor of Philosophy.

The copyright of this thesis rests with the author. No quotation from it
should be published without his prior written consent and
information derived from it should be acknowledged.

Department of Physics
University of Durham
September 1996

Cosmology with Galaxy Clusters

Vincent R. Eke

Abstract

A number of different ways of using galaxy clusters to provide information concerning fundamental cosmological parameters are considered.

Using the observed local cluster X-ray temperature function in conjunction with the Press-Schechter formalism, the normalisation of a CDM power spectrum is found to be $\sigma_8 = (0.52 \pm 0.04)\Omega_0^{-0.46+0.10\Omega_0}$ if $\Lambda_0 = 0$ or $\sigma_8 = (0.52 \pm 0.04)\Omega_0^{-0.52+0.13\Omega_0}$ if $\Lambda_0 = 1 - \Omega_0$. This result is employed to provide detailed predictions for the abundance of clusters at high redshift, and the differences between predictions for various cosmologies are emphasised. New tests using available high-redshift cluster data are presented. For the adopted power spectrum normalisation, it is found that an $\Omega_0 = 0.3$, $\Lambda_0 = 0$ cosmology vastly overpredicts the number of clusters that were actually found with $0.4 < z < 0.6$ in the Extended Medium Sensitivity Survey. The rapid variation in the expected abundance with both σ_8 and the assumed scatter in the $L_x - T_x$ relation limits the significance of this result, but this model is still ruled out at the $\sim 95\%$ confidence level. Order statistics are utilised to calculate the probability of finding extremely massive clusters at high redshifts. With presently available observations, no interesting upper limit can yet be placed on Ω_0.

Systematic variations in the cluster-cluster correlation length calculated using numerical simulations and resulting from the definition of clusters, the chosen σ_8, the mean intercluster separation and whether or not redshift space distortions are included, are found to exceed the statistical errors on the measurements. Although the uncertainty in ξ_{cc} derived from an ensemble of 10 Standard CDM simulations is not sufficient at large separations to remove the discrepancy between this model and results from the APM Cluster Survey, this does suggest that the level at which such a scenario has previously been rejected using ξ_{cc} should be significantly reduced.

Details and a few tests of a procedure for improving mass and spatial resolution in cosmological simulations are presented. After showing that a coarse-sampling technique can be used to represent the large-scale forces sufficiently accurately, the method is then used to perform ten simulations of clusters forming in an $\Omega_0 = 0.3$, $\Lambda_0 = 0.7$ CDM cosmology. To incorporate non-radiative gas, an SPH code adapted to work on a *GRAPE* supercomputer is used. The resulting clusters are found to have virial radii in good agreement with the predictions of the spherical collapse model, dark matter density profiles well described by the 'NFW' formula and isothermal central gas components, with temperatures dropping by a factor of ~ 2 near the virial radius. The evolution of these properties is studied as well as that of the bulk quantities describing the clusters, with particular reference to the β parameters relating cluster gas temperatures with virial mass or velocity dispersion. Slightly greater evolution in the luminosity is seen than in previous $\Omega_0 = 1$ simulations, suggesting that the improved resolution is important. The β parameter relevant to the normalisation of the mass fluctuation spectrum is found to be 0.98 ± 0.07.

Preface

The work described in this thesis was undertaken between 1993 and 1996 whilst the author was a research student under the supervision of Prof. C. S. Frenk in the Department of Physics at the University of Durham. This work has not been submitted for any other degree at the University of Durham or at any other University.

The work in Chapters 2 and 3 was undertaken in collaboration with Dr S. Cole and Prof C. S. Frenk. Dr P. Coles also provided valuable input concerning order statistics. Chapter 4 resulted from a project with Dr S. Cole, Prof C. S. Frenk and Dr J. F. Navarro. Chapters 5 and 6 benefitted considerably from discussions with Dr A. R. Jenkins, Prof C. S. Frenk, Dr J. F. Navarro and Dr S. Cole. However, the majority of the material presented here is the author's own work.

A number of the results presented here have appeared in the following papers :

Eke V. R., Cole S., Frenk C. S., Navarro J. F., 1996, MNRAS, 281, 703
Eke V. R., Cole S., Frenk C. S., 1996, MNRAS, 282, 263

Acknowledgments

I'd like to thank all of the astronomy group at Durham for providing a friendly and stimulating environment in which to learn. My supervisor, Carlos Frenk, deserves particular thanks for his boundless enthusiasm and ideas. I'm very grateful for all the wise words and guidance offered by Shaun Cole. Adrian Jenkins must also be thanked for explaining to me why whales don't suffer from the 'bends', amongst other things! The help of Julio Navarro, who often applied his intuition to solve my problems, was also invaluable. Collectively, this 'rapid reaction force', particularly Carlos, also merit my appreciation for their much-needed comments on my first attempt at writing a thesis.

It is my pleasure to thank Luis Teodoro for talking so much during the past 3 years. I must also extend gratitude to not just arat, but The Rat, for supporting such appallingly bad American sports teams that even my favourites from Seattle could beat them with pleasing regularity. Thanks to Doug Burke and Paul Young for their donkey-friendly explanations of how to persuade computers to do useful things. Alan Lotts in Durham and Douglas Heggie in Edinburgh both deserve credit for computer resuscitation and amusing email messages.

Finally, I'd like to thank my parents for their support and interest. At least you'll be able to trust the = signs in Appendix B!

"If the world was an orange, it would be like, much too small."

Neil, The Young Ones.

Contents

Chapter 1

Introduction

Modern cosmology is based upon Einstein's theory of General Relativity and the observations that on very large scales the galaxy distribution appears to be smooth and that galaxies are receding from one another with velocities that increase in proportion to their distance (Hubble 1927; Hubble & Humason 1931). During the middle of this century, there was considerable debate concerning the relative merits of the Steady State (Bondi & Gold 1948; Hoyle 1948) and Big Bang models. Whilst this argument is still continuing at a low level (e.g. Wright 1995; Hoyle, Burbidge & Narlikar 1995), 'mainstream' cosmology has interpreted the very uniform microwave background radiation, discovered by Penzias & Wilson (1965), as a remnant of the hot early phase of a universe of the kind predicted by the Big Bang cosmological scenario. A lack of alternative viable models has led to the present situation where the Big Bang is almost universally accepted. Any awkward observations lead investigators to tinker with the available parameters within a framework where the universe is expanding from an initially very hot, dense primordial soup and objects grow through the gravitational amplification of small density fluctuations created in the early universe.

The nature of these fluctuations depends on the material content of the universe, a topic on which a good deal remains to be learnt. However, models dominated by cold dark matter (CDM), slow-moving particles essentially interacting only via gravity, have achieved many successes in describing the observed structures in the universe (see Frenk 1991 for example). In such a scenario, small perturbations collapse first and larger objects result from the association of many smaller clumps. This hierarchical clustering is in contrast to that expected to occur in a universe dominated by Hot Dark Matter (HDM). These particles are fast-moving and at early times their free-streaming smooths out the small-scale perturbations. Consequently, supercluster-sized bodies collapse first and smaller structures form as a result of the fragmentation of these larger bodies. One possibile candidate for HDM is a massive neutrino. This has the advantage over the elementary particle CDM candidates that it is at least known to exist. However, to date, no significantly non-zero mass has been measured for any of the three neutrino species, although the upper limits on the neutrino masses do not rule out the possibility that neutrinos could possess

sufficient mass to affect the dynamics of the universe.

After gravity has caused large structures to collapse, small-scale non-gravitational forces contribute significantly to their subsequent evolution. Given the complications which arise as a result of this (us for example!), it appears sensible to study large objects in order to try and learn about the underlying properties of the universe. With experiments to measure fluctuations in the microwave background radiation not yet capable of discriminating between different cosmological models, huge galaxy clusters provide an excellent probe of the large-scale structure.

This thesis aims to address some of the issues which can be tackled using clusters of galaxies. The extent to which present understanding and observations constrain the fundamental cosmological parameters will be considered. As each of the chapters contains an introduction aiming to stress the importance of that particular application of galaxy clusters, the purpose of the remainder of this overall introduction will be to give a brief outline of the 'framework' which was referred to above. Comprehensive reviews of the subject are available from many sources (e.g. Kolb & Turner 1990; Peebles 1980, 1993; Padmanabhan 1993; Narlikar 1993), so attention will be focussed on defining the parameters that will be used extensively throughout the subsequent chapters.

1.1 Basic cosmology

A major assumption underlying standard cosmology is the cosmological principle. This states that the universe is homogeneous and isotropic on large scales, implying that there is no preferred position or direction in the universe. In the four-dimensional spacetime of the universe, freely falling bodies are said to follow geodesics. These paths are defined as extremal intervals between events. The metric describing this interval needs to take into account both the radial distortion, or curvature, of spacetime produced by massive bodies and the consequences of the cosmological principle. This is uniquely achieved by the Friedmann-Robertson-Walker metric:

$$\mathrm{d}s^2 = \mathrm{d}t^2 - \frac{R^2(t)}{c^2}\{\mathrm{d}\chi^2 + [S(\chi)]^2(\mathrm{d}\theta^2 + \sin^2\theta\ \mathrm{d}\phi^2)\}, \tag{1.1}$$

where

$$S(\chi) = \begin{cases} \sin\chi & \text{if } k = +1\ ; \\ \chi & \text{if } k = 0\ ; \\ \sinh\chi & \text{if } k = -1\ . \end{cases} \tag{1.2}$$

$\mathrm{d}s^2$ defines the interval and the terms on the right hand side give the time and three space components. $R(t)$ is a scale factor with dimensions of length, c is the speed of light and χ is a radial coordinate. $k = -1, 0, +1$ refer to the cases of negative, zero or positive curvature, and the influence of this curvature on the metric comes through $S(\chi)$.

Another pillar on which modern cosmology rests is the need for the laws of physics

as we understand them to be independent of both position and epoch. Familiar features in the spectra of distant objects suggest that this is a reasonable assumption to make. If the scale factor of the universe is a function of time then a photon emitted at a time t_e with wavelength λ_e will have a wavelength $\lambda_0 = \lambda_e R(t_0)/R(t_e)$ when observed at the present day t_0. Given that the universe is seen to be expanding, i.e. Hubble's (time-varying!) constant defined by

$$H = \frac{\dot{R}}{R} \tag{1.3}$$

is positive, the observed wavelength of a photon will increase with time. This 'redshift' z, is defined through

$$1 + z = \frac{\lambda_0}{\lambda_e} = \frac{R(t_0)}{R(t_e)}. \tag{1.4}$$

A dimensionless scale factor for the universe can then be defined by

$$a = \frac{1}{1+z}\,. \tag{1.5}$$

Using these definitions and the fact that photons follow geodesics with $\mathrm{d}s^2 = 0$, the following useful expression gives the radial coordinate of a photon emitted at a redshift of z:

$$\chi = \frac{c}{R_0}\int_0^z \frac{\mathrm{d}z'}{H(z')}. \tag{1.6}$$

The differential change in comoving volume with redshift can also be found, using the metric, to be

$$\frac{\mathrm{d}V}{\mathrm{d}z} = 4\pi\frac{c}{H}(R_0 S(\chi))^2. \tag{1.7}$$

Before equations (1.6) and (1.7) can be exploited, knowledge about the evolution of the Hubble parameter is required. To deal with this properly needs General Relativity. However, the forms of the two cosmological field equations can be largely understood in terms of Newtonian physics. One complication from relativity is that both radiation and matter act as source terms for gravity, and this is included through the equation of state

$$\epsilon = \frac{3p}{\rho c^2}\begin{cases} = 1 & \text{radiation dominated ;} \\ \approx 0 & \text{matter dominated,} \end{cases} \tag{1.8}$$

where p and ρ represent pressure and density (energy density/c^2 for radiation) respectively. The matter density varies like R^{-3} and the radiation 'energy-density' decreases with R^{-4}, so the universe is becoming increasingly matter dominated. An epoch of equality, before which the universe was radiation dominated, existed prior to recombination. However, this represents only a very small fraction of the age of the universe so the parameter ϵ is usually set to zero for most cosmological applications. The first of the cosmological field equations describes the deceleration of the universal expansion.

$$\frac{\ddot{R}}{R} + \frac{4\pi G\rho(1+\epsilon)}{3} - \frac{\lambda}{3} = 0. \tag{1.9}$$

λ is the 'cosmological constant' which, if positive, acts like a repulsive vacuum energy density. This opposes the gravitational attraction represented by the second term. The other field equation comes from energy considerations, with the contributions corresponding to kinetic, gravitational potential, vacuum and curvature energies respectively:

$$\left(\frac{\dot{R}}{R}\right)^2 - \frac{8\pi G\rho}{3} - \frac{\lambda}{3} = -\frac{kc^2}{R^2}. \tag{1.10}$$

A less frightening form of this second field equation is

$$\Omega_\rho + \Omega_\Lambda + \Omega_R = 1, \tag{1.11}$$

where the mass density term is defined as the ratio between the mean density and a critical density

$$\Omega_\rho = \Omega = \frac{\rho}{\rho_c} = \frac{8\pi G\rho}{3H^2}, \tag{1.12}$$

and the vacuum energy and curvature contributions are given by

$$\Omega_\Lambda = \Lambda = \frac{\lambda}{3H^2} \tag{1.13}$$

and

$$\Omega_R = -k\left(\frac{c}{RH}\right)^2. \tag{1.14}$$

As before, k can take one of three values. $k = -1$ refers to an open model, $k = +1$ for a closed model, and $k = 0$ is the flat case. The Einstein-de Sitter cosmology (Einstein & de Sitter 1932) assumes that $\Lambda = 0$, $k = 0$ (therefore $\Omega = 1$) and $\epsilon = 0$ and is the simplest solution of the field equations that is compatible with the observation that the universe is expanding. Much of the current research activity is focussed on the affects of varying Ω, Λ and k.

To calculate a useful general expression for Hubble's parameter, under the assumption that $\epsilon = 0$, the curvature term needs to be eliminated from equation (1.10). This can be achieved by evaluating the expression at $z = 0$, denoting these parameters with a subscript zero, and resubstituting for kc^2. Using the additional information that $\rho/\rho_0 = (1+z)^3$, one finds that

$$\left(\frac{H}{H_0}\right)^2 = (1+z)^2(1+\Omega_0 z) - \Lambda_0 z(2+z). \tag{1.15}$$

Plugging this back into equation (1.7), the differential comoving volume as a function of redshift can be calculated for a variety of cosmologies. For the non-flat cosmologies one also requires an expression for R_0/c which can be found by evaluating equation (1.10) at $z = 0$. The results of the whole calculation are shown in Fig. 1.1. It can be seen that the low-density models contain more volume than the Einstein-de Sitter case. This result is often used to try and discriminate between competing models, and it is relevant for Chapters 2 and 3 where the evolution of the population of galaxy clusters is considered.

Following this whistle-stop tour of how the universe as a whole behaves, it is now pertinent to spend a short time considering the growth of structure within this expanding spacetime.

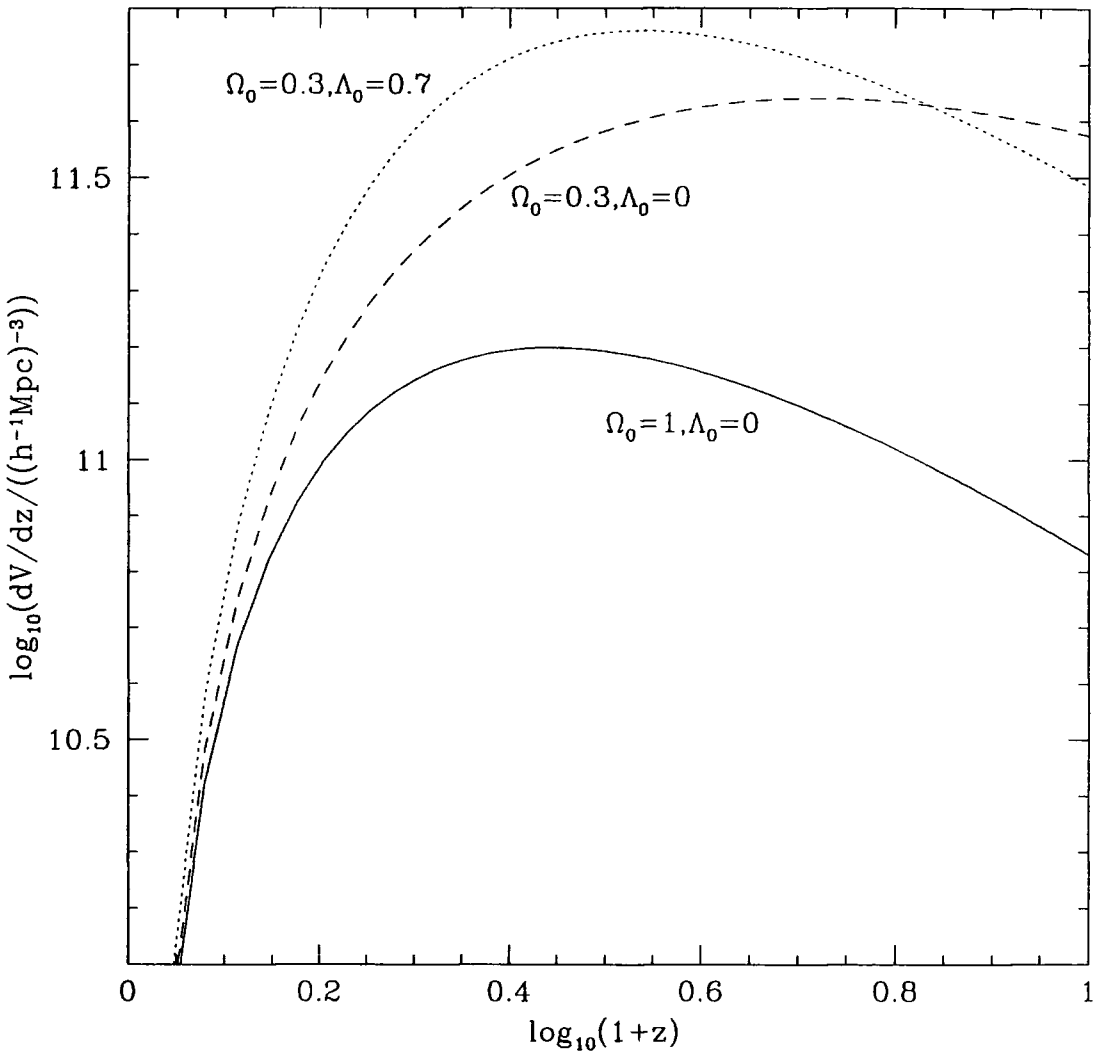

Figure 1.1: The differential comoving volume as a function of redshift for three different cosmological models. A solid curve represents the result for the Einstein-de Sitter model, whereas the dotted line shows another flat universe dominated at the present day by a cosmological constant term. The dashed curve traces the differential volume in an open $\Omega_0 = 0.3$ model.

1.2 Linear theory growth of perturbations

As was stated previously, on large scales the mass distribution as traced by galaxies, appears to be smooth. What clumpiness does exist on smaller scales results from gravitational attraction causing regions that were initially slightly overdense to collapse inwards. Conversely, material flows out of underdensities, forming large 'voids' that are only sparsely populated with galaxies. This amplification of the primordial perturbations is described by the gravitational instability theory. The very small temperature fluctuations in the microwave background radiation ($\Delta T/T \sim 10^{-5}$) detected by the *COBE* satellite represent these perturbations smoothed over very large scales at the redshift of recombination ($z \sim 1400$). An extensive treatment of their linear theory growth is provided by Peebles (1980) amongst others, so a mere outline will be provided here, with particular reference to the differences between the various competing cosmological models.

The starting points for calculations concerning the growth of structure in a gravitating pressureless fluid are the following three equations:
1) Mass conservation

$$\frac{\partial \rho}{\partial t} + \nabla \cdot (\rho \mathbf{u}) = 0, \tag{1.16}$$

2) The Euler equation of motion

$$\frac{\partial \mathbf{u}}{\partial t} + (\mathbf{u} \cdot \nabla)\mathbf{u} = -\nabla \Phi, \tag{1.17}$$

and
3) Poisson's equation

$$\nabla^2 \Phi = 4\pi G \rho. \tag{1.18}$$

Φ and $\mathbf{u}$ represent the gravitational potential and the velocity field respectively. These equations are more easily solved when they are transformed into comoving coordinates. Keeping only terms that are linear in the overdensity δ, leads to the following second order partial differential equation for the time variation of the perturbation size:

$$\frac{\partial^2 \delta}{\partial t^2} + 2\frac{\dot{a}}{a}\frac{\partial \delta}{\partial t} = 4\pi G \bar{\rho} \delta \tag{1.19}$$

where $\bar{\rho}$ is the mean background matter density. The cosmology dependence of the evolution of the dimensionless scale factor a is contained in equation (1.15). Including this allows the linear theory overdensity to be calculated as a function of time, or equivalently scale factor. The usual nomenclature is to use a linear theory growth factor $D(a)$ to relate the linear theory overdensity at $z = 0$ to some previous epoch through

$$\delta(a) = D(a)\delta_0. \tag{1.20}$$

For the Einstein-de Sitter cosmology, $a \propto t^{2/3}$ and the two solutions to equation (1.19) are readily found to be $\delta \propto t^{2/3}$ and $\delta \propto t^{-1}$. The first of these is called the growing mode because the perturbation becomes amplified, whereas the second solution is a decaying mode. Therefore it is the first of these solutions which

is relevant and the linear theory growth factor is given by $D(a) = a$ in this case. For other cosmologies, the solution becomes more complicated (see Peebles 1980). Fig. 1.2 shows the 'velocity factor', so called because it governs the magnitude of linear theory peculiar velocities, as a function of expansion factor. (The dashed lines depict a much-used approximation.) This illustrates the rate of change of $D(a)$ rather than the growth factor itself. It can be seen that the 'growth rate' remains constant in the Einstein-de Sitter case, but for $\Omega_0 = 0.3$ $\Lambda_0 = 0$ and $\Omega_0 = 0.3$ $\Lambda_0 = 0.7$ models this growth rate has decreased by a factor of two by redshift zero. At early times, when $\Omega \approx 1$ for all of these three cosmologies, they behave in a similar fashion. For the non-zero Λ_0 model, the turn off in the accretion rate occurs later than for the open model, but it happens more quickly because of the repulsive effect of the Λ_0 term. This keeps the universe expanding rapidly and prevents anything further from collapsing. The lack of evolution predicted to happen in the recent past in the low-density models relative to the $\Omega_0 = 1$ case provides most of the discriminatory power to the tests described in Chapters 2 and 3. It is also apparent in the simulations detailed in Chapter 6.

1.3 References

Bondi H., Gold T., 1948, MNRAS, 108, 252
Einstein A., de Sitter W., 1932, Proc Nat Acad Sci, 18, 213
Frenk C. S., 1991, Physica Scripta, T36, 70
Hoyle F., 1948, MNRAS, 108, 372
Hoyle F., Burbidge G., Narlikar J. V., 1995, MNRAS, 277, L1
Hubble E., 1927, Proc Nat Acad Sci, 15, 168
Hubble E., Humason M. L., 1931, ApJ, 74, 43
Kolb E. W., Turner M. S., 1990, The Early Universe, Addison Wesley
Narlikar J. V., 1993, Introduction to cosmology, 2nd ed., CUP
Padmanabhan T., 1993, Structure formation in the universe, CUP
Peebles P. J. E., 1980, The Large Scale Structure of the Universe. Princeton Univ. Press, Princeton, NJ
Peebles P. J. E., 1993, Principles of physical cosmology, Princeton Univ. Press, Princeton, NJ
Penzias A. A., Wilson R. W., 1965, ApJ, 142, 419
Wright E. L., 1995, MNRAS, 276, 1421

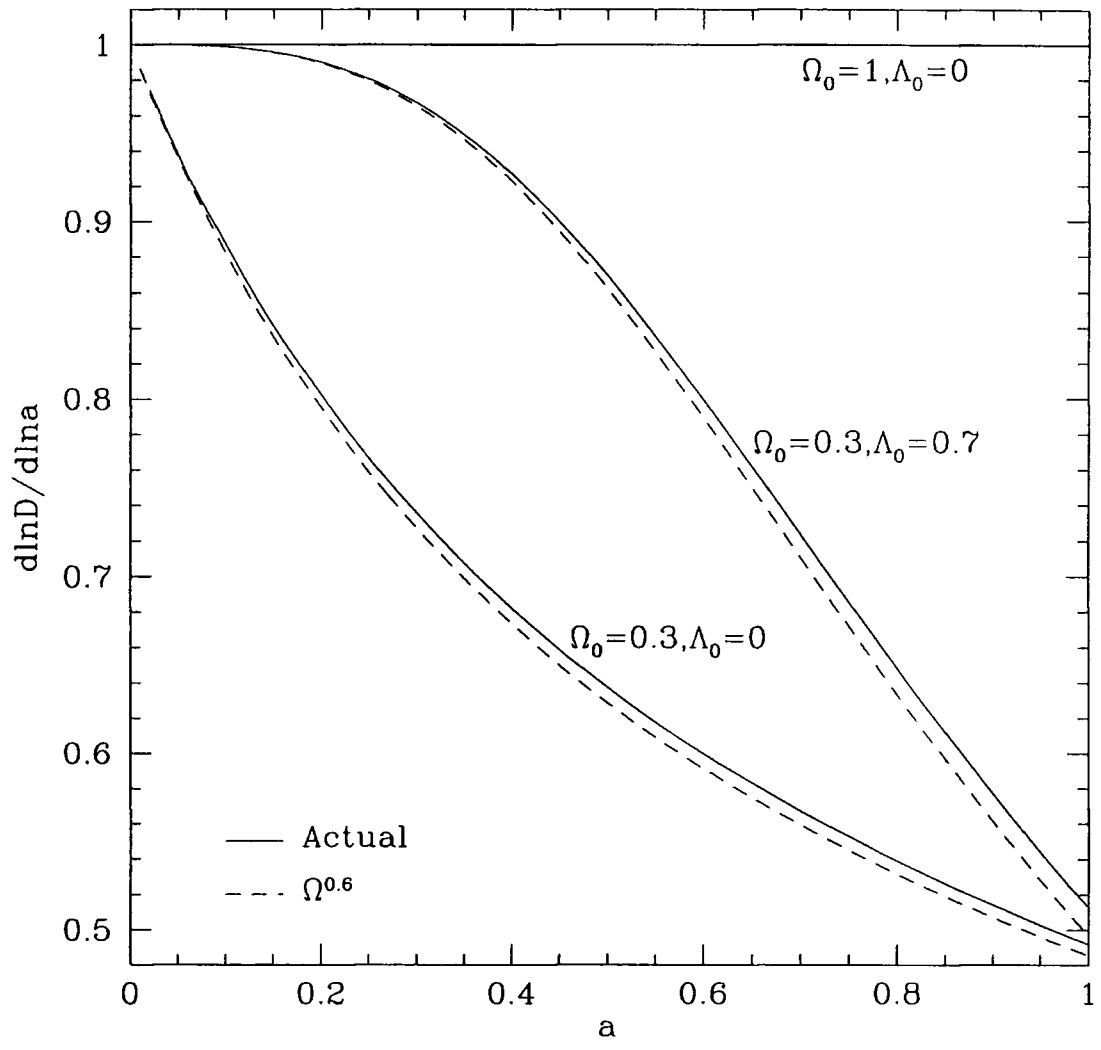

Figure 1.2: Logarithmic change in the linear theory growth factor with expansion factor. This illustrates how the rate of growth of perturbations differs in these three cosmologies. Fluctuations all grow at a similar rate at early times, but the open $\Omega_0 = 0.3$, $\Lambda_0 = 0$ model soon exhibits a significantly lower growth rate. When the Λ_0 term becomes dominant in the low-density flat model, the mass accretion rate falls away rapidly and the structure growth 'freezes out'.

Chapter 2

Cluster abundances and evolution

2.1 Introduction

Galaxy clusters are exceptionally useful tools for estimating fundamental cosmological parameters. Their utility stems largely from their relative dynamical youth. In hierarchical clustering theories, clusters form by the gravitational amplification of primordial density fluctuations, usually assumed to have an initially Gaussian distribution of amplitudes. Rich clusters correspond to the rarest collapsed objects in this distribution and their abundance varies very rapidly with properties such as mass or potential well depth.

The mass within the virial radius of a rich cluster ($\sim 5 \times 10^{14} h^{-1} \mathrm{M}_{\odot}$) is very close to the mass enclosed within a sphere of radius $8\,h^{-1}$Mpc in the unperturbed universe (Evrard 1989, White, Efstathiou & Frenk 1993). Because of this, the present-day abundance of rich clusters directly reflects the amplitude of density fluctuations on a scale of $\sim 8\,h^{-1}$Mpc and can be used to measure this amplitude with a minimum of assumptions. In general, this measure depends only weakly on the amplitude of fluctuations on other scales. It does, however, depend on the value of the cosmological density parameter, Ω_0. Thus, the observed local cluster abundance fixes the value of σ_8, the rms density fluctuation in spheres of radius $8\,h^{-1}$Mpc, as a function of Ω_0.

The temporal *evolution* of the cluster abundance is determined by the rate at which density perturbations grow. This, in turn, depends primarily on the value of Ω and, to a lesser extent, the value of the cosmological constant, Λ[1], and the shape of the power spectrum of density fluctuations. In a low-density universe, fluctuations cease to grow after a redshift $z \sim \Omega_0^{-1} - 1$ (e.g. Peebles 1980), resulting in a cluster population that evolves very slowly at low redshift. In an $\Omega_0 = 1$ universe, on the other hand, density fluctuations continue to grow even at the present epoch

[1] Λ is expressed in units of $3H_0^2$, where $H_0 = 100h$ km s^{-1}Mpc^{-1} is the present value of the Hubble constant.

and so the cluster population is still evolving rapidly. Measurement of the cluster abundance at moderate redshifts provides a powerful method for estimating Ω_0.

In order to apply these tests, it is necessary to predict and measure the abundance of clusters as a function of some property such as mass, X-ray luminosity or the equilibrium temperature of the X-ray emitting intracluster gas. Theoretical predictions and observational measurements are subject to different uncertainties. The cluster mass within the virial radius is the simplest quantity to predict theoretically, but one of the hardest to measure reliably. Traditional virial analyses are prone to contamination by projection effects (Frenk et al. 1990; Van Haarlem, Frenk & White 1996; Mazure et al. 1995) and X-ray data do not generally extend to the virial radius. A novel and highly promising technique to measure cluster masses employs the shape distortions of background galaxies produced by weak gravitational lensing in the cluster potential (Kaiser & Squires 1993; Fahlman et al. 1994; Wilson, Cole & Frenk 1996; Seitz & Schneider 1995 and references therein.) The limited field of view of the current generation of CCD cameras, however, restricts such measurements to the inner parts of clusters.

The simplest quantity to measure empirically is the cluster X-ray luminosity. However, since the bremsstrahlung emissivity per unit volume is proportional to the square of the gas density, the total power radiated is very sensitively dependent upon the distribution of gas in the cluster core. This is difficult to model, particularly at high redshift (Evrard 1990; Navarro, Frenk & White 1995 and references therein). Nevertheless, X-ray luminosity provides a convenient means to select complete samples of galaxy clusters. In contrast, the temperature of the intracluster gas can be predicted quite reliably using modern hydrodynamic simulations. These show that, as a cluster collapses, the gas is shock heated to the virial temperature and rapidly settles into hydrostatic equilibrium with an approximate isothermal structure (Evrard 1990; Cen & Ostriker 1994; Bryan et al. 1994; Navarro et al. 1995). Average (luminosity-weighted) X-ray temperatures have now been measured for fairly large samples of clusters, with the *Einstein Observatory* (Henry & Arnaud 1991), and *EXOSAT* (Edge et al. 1990), and the radial variation of temperature is now beginning to be probed with *ASCA* (Markevitch et al. 1996). Early results show that the gas is indeed approximately isothermal. Finally, another observable that is also insensitive to the detailed distribution of the gas within the cluster is the $\Delta T/T$ decrement in the cosmic microwave background radiation produced by the Sunyaev-Zel'dovich (S–Z) effect (Sunyaev & Zel'dovich 1972). The line-of-sight decrement from the cluster depends only on the product of the column density of gas and the temperature and is independent of the cluster redshift. Sunyaev-Zel'dovich decrements have now been reliably measured for several clusters (e.g. Grainge et al. 1993; Wilbanks et al. 1994; Birkinshaw & Hughes 1994).

In this chapter, those cluster properties that are best determined theoretically and observationally are utilised to describe cluster evolution for different values of the cosmological parameters. First, the distribution of X-ray temperatures at the *present day* is used to estimate σ_8. Then, the cosmology-dependent *evolution* of the cluster population is examined, and predictions are presented for the mass function, the

temperature function and the distribution of S-Z decrements at $z \simeq 0.3 - 0.5$. This range of redshifts is a rich area of observational work. Ongoing programmes include mass measurements from weak gravitational lensing using *HST* and large-format CCDs (Ellis, private communication; Kaiser, private communication); estimates of the cluster temperature function (Henry, private communication); and S–Z source counts and redshift distributions from ground-based radio telescopes and, in future, from the *COBRAS/SAMBA* satellite mission.

Related calculations have been carried out by Evrard (1989), Frenk et al. (1990), Bond & Myers (1993), Lilje (1992), Oukbir & Blanchard (1992), Bahcall & Cen (1993), Hanami (1993), White et al. (1993), Bartlett & Silk (1993, 1994), Jing & Fang (1994) Barbosa et al. (1995), Hattori & Matsuzawa (1995) and Viana & Liddle (1996), amongst others. This work differs from these earlier studies in various respects. A wider range of cosmological models are considered here than in most previous analyses, particularly models with low values of Ω_0, with and without a cosmological constant. Secondly, some of the largest N-body simulations ever carried out are used in order to verify the accuracy of the analytical calculations. Finally, special emphasis is placed on making detailed predictions in a manner that can be compared with observational data with a minimum of assumptions.

This chapter is structured as follows. Section 2.2 reviews the Press-Schechter model for the abundance of clusters, extended to open and flat cosmological models ($\Omega_0 < 1$ with $\Lambda_0 = 0$ or $\Lambda_0 = 1 - \Omega_0$). The predictions of this model are compared with a set of 192^3 particle N-body simulations in Section 2.3. In Section 2.4 the analytical models are normalised using the cumulative cluster temperature function estimated from the data compiled by Henry & Arnaud (1991). The evolution of the cluster mass and temperature functions, the S-Z source counts and the dependence of these quantities on Ω_0 and Λ_0 are predicted in Sections 2.5.1 – 2.5.3. Finally, the importance and implications of these results are discusssed in Section 2.6.

2.2 Model

An analytical expression for the comoving number density of dark matter haloes of mass M in the interval $\mathrm{d}M$, originally derived by Press & Schechter (1974) (see also Bond et al. 1991), is

$$\frac{\mathrm{d}n}{\mathrm{d}M} = \left(\frac{2}{\pi}\right)^{\frac{1}{2}} \frac{\bar{\rho}}{M^2} \frac{\delta_{\mathrm{c}}(z)}{\sigma} \left|\frac{\mathrm{d}\ln\sigma}{\mathrm{d}\ln M}\right| \exp\left[-\frac{\delta_{\mathrm{c}}(z)^2}{2\sigma^2}\right], \tag{2.1}$$

where $\bar{\rho}$ is the present mean density of the universe, and $\sigma(M)$ the present, linear theory rms density fluctuation in spheres containing a mean mass M. The evolution with redshift is controlled by the redshift-dependent density threshold $\delta_{\mathrm{c}}(z)$. For the case of $\Omega_0 = 1$, the conventional choice of this threshold is $\delta_{\mathrm{c}}(z) = 1.686(1+z)$. This is the value, extrapolated to the present using linear theory, of the overdensity of a uniform spherical overdense region at the point at which the exact non-linear model predicts that it should collapse to a singularity. This threshold, along with

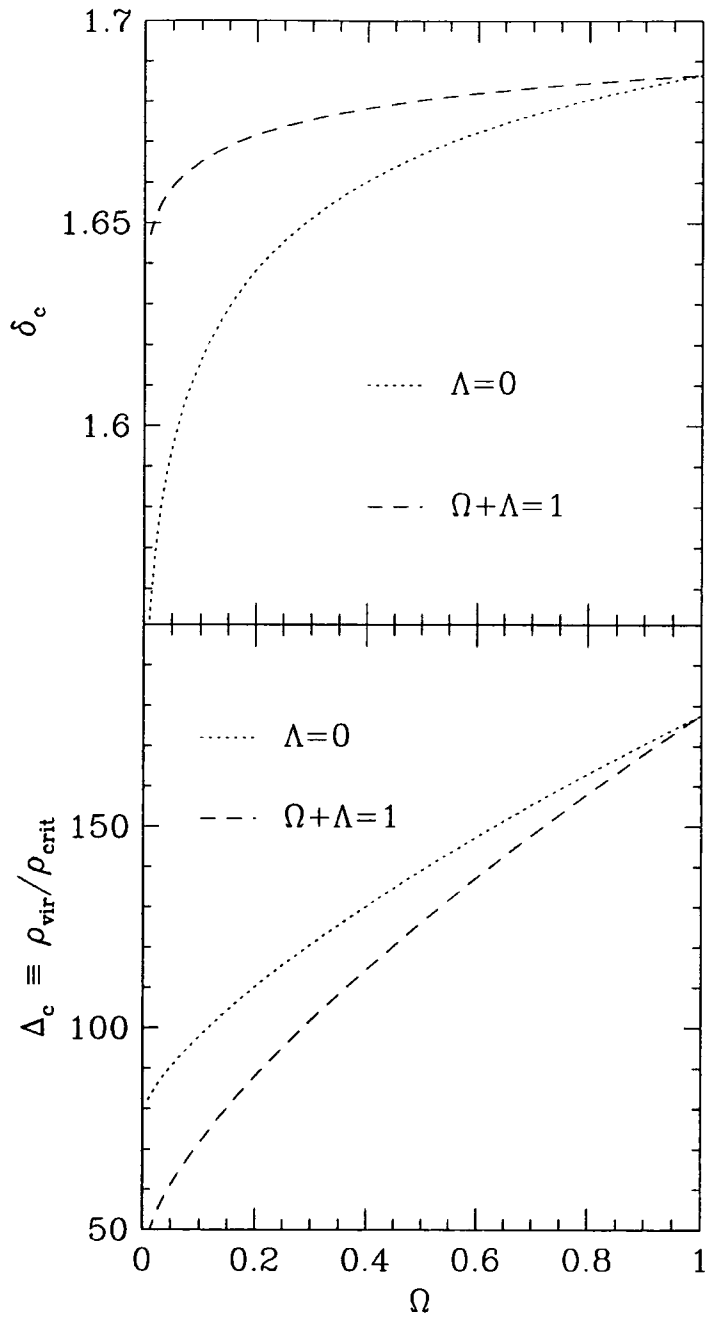

Figure 2.1: *Upper panel*: critical threshold for collapse, δ_c, as a function of Ω, in the spherical collapse model. Results are plotted for open models with $\Lambda = 0$ (dotted line) and flat models with $\Omega + \Lambda = 1$ (dashed line). *Lower panel*: the virial density of collapsed objects in units of the critical density. The dotted and dashed lines are as in the upper panel.

the choice of top-hat filtering to define $\sigma(M)$, gives a mass function that agrees remarkably well with the results of N-body simulations (e.g. Efstathiou et al. 1985; Lacey & Cole 1994). For $\Omega \neq 1$ one can use the spherical collapse model to derive a general expression for the density threshold. Expressing the threshold as $\delta_c(z) = \delta_c(0)/D(z, \Omega_0, \Lambda_0)$ where $D(z, \Omega_0, \Lambda_0)$ is the linear growth factor normalised to unity at $z = 0$ (Peebles 1980), it can be seen that $\delta_c(0)$ has only a weak dependence on Ω for both open models with $\Lambda = 0$ and flat models with $\Omega + \Lambda = 1$ (see Fig. 2.1). The details of the $\Lambda = 0$ calculation can be found in Lacey & Cole (1993; see also Maoz 1990), and the $\Omega + \Lambda = 1$ result is derived here in Appendix A (see also Lilje 1992; White et al. 1993; Kochaneck 1995).

In order to convert the mass function obtained from (2.1) to a temperature function it is assumed that the gas is isothermal. In this case,

$$kT_{\rm gas} = \frac{7.75}{\beta}\left(\frac{6.8}{5X+3}\right)\left(\frac{M}{10^{15}h^{-1}{\rm M}_\odot}\right)^{\frac{2}{3}}(1+z)\left(\frac{\Omega_0}{\Omega(z)}\right)^{\frac{1}{3}}\left(\frac{\Delta_c}{178}\right)^{\frac{1}{3}}\ {\rm keV}, \qquad (2.2)$$

where Δ_c is the ratio of the mean halo density to the critical density at that redshift, β is the ratio of specific galaxy kinetic energy to specific gas thermal energy and X is the hydrogen mass fraction which we take to be $X = 0.76$. Recent work by Navarro et al. (1995) shows that equation (2.2) is accurately obeyed in N-body/hydrodynamic simulations of the formation of clusters in universes with $\Omega_0 = 1$. Their simulations predict an X-ray luminosity-weighted $\beta = 1.07 \pm 0.05$ for individual clusters, in fair agreement with observational determinations (e.g. Forman & Jones 1990). In Chapter 6 the relevant quantity has been measured for the $\Omega_0 = 0.3, \Lambda_0 = 0.7$ cosmology to be 0.98 ± 0.07. The value $\beta = 1.0 \pm 0.1$ is adopted here, but the results may be modified for different choices simply by rescaling all predicted temperatures by β^{-1}.

The density contrast Δ_c is computed from the spherical collapse model assuming that the cluster virialises at the redshift at which we view it. Its dependence on Ω (and therefore on redshift) is given in the lower panel of Fig. 2.1. The assumption that clusters form at the redshift at which we view them is a good approximation in the $\Omega_0 = 1$ model since in this case halos are continuously accreting material. The value $\Delta_c = 178$, appropriate to $\Omega = 1$, has recently been shown to separate well the interior of the virialised halo from the surrounding infalling material (Cole & Lacey 1996). In low-Ω models the accretion rate on to a halo declines after $z \approx \Omega_0^{-1} - 1$ and so little evolution in the density and temperature of the bulk of the gas takes place at low redshift. The density in the simple spherical collapse model, $\rho^0_{\rm crit}(1+z)^3(\Omega_0/\Omega(z))\Delta_c$ (where $\rho^0_{\rm crit}$ is the critical density at the present day), does not accurately reproduce this behaviour. Nevertheless, for the range of redshifts and Ω_0s considered here, the simple model is a good approximation.

The Sunyaev-Zel'dovich (Sunyaev & Zel'dovich 1972) effect is produced by the inverse Compton scattering of cosmic microwave background (CMB) photons off high-energy electrons in the intracluster gas. This process distorts the blackbody spectrum by shifting microwave photons to higher energies. At long wavelengths (longward of $\lambda = 1.37$ mm for $T_{\rm CMB} = 2.726$ K), the cluster produces a negative

fluctuation in the surface brightness of the CMB, while at shorter wavelengths it produces a positive fluctuation. In the long-wavelength regime the microwave background decrement from the cluster is given by

$$\frac{\Delta T}{T} = -2y, \tag{2.3}$$

where y is the integral of the electron pressure along a line-of-sight through the cluster,

$$y = \int n_{\rm e} \sigma_{\rm T} \left(\frac{kT}{m_{\rm e} c^2} \right) {\rm d}l. \tag{2.4}$$

Here $n_{\rm e}$ is the number density of electrons, m_e the electron mass, and $\sigma_{\rm T}$ the Thompson cross-section. Defining an effective angular cross-section, Y, by integrating y over the projected area of the cluster and dividing by the square of the angular diameter distance, $r_{\rm d}$, gives

$$Y = r_{\rm d}^{-2} \int y \, {\rm d}A. \tag{2.5}$$

This quantity has a simple physical interpretation. In the long-wavelength regime $2Y$ is simply the effective angular area of the microwave background obscured by the cluster. An unresolved observation of a cluster with a radio telescope of effective beam area $A_{\rm beam}$ would, in the long-wavelength regime, measure a signal $\Delta T/T = -2Y/A_{\rm beam}$. If the cluster is resolved, then the signal depends on the density profile of the cluster. Assuming a surface density proportional to R^{-1}, as in an isothermal sphere, then $\Delta T/T = -2Y/(A_{\rm clus}\, A_{\rm beam})^{1/2}$, where $A_{\rm clus}$ is the angular cross-section of the virialised cluster. Using the virial radius to define the edge of the cluster, it can be shown that

$$A_{\rm clus} = 436\, \beta \left(\frac{5X+3}{6.8} \right) \left(\frac{kT_{\rm gas}}{\rm keV} \right) (1+z)^{-3} \left(\frac{\Omega(z)}{\Omega_0} \right) \left(\frac{\Delta_{\rm c}}{178} \right)^{-1} \left(\frac{r_{\rm d}}{100\, h^{-1}{\rm Mpc}} \right)^{-2} {\rm arcmin}^2. \tag{2.6}$$

The effective angular area, Y, is also easily related to the CMB flux absorbed (or re-emitted) by the cluster at other frequencies. With a dimensionless frequency defined by $x = h_{\rm p}\nu/kT_{\rm CMB} = \lambda_0/\lambda$, where $h_{\rm p}$ is Planck's constant and $\lambda_0 = 5.28$ mm for $T_{\rm CMB} = 2.726$ K (Mather et al. 1994), the emitted flux is

$$S_\nu(x) = S_\nu^{\rm CMB}(x)\, Q(x)\, Y \tag{2.7}$$

$$= 2.29 \times 10^4 \frac{x^3}{{\rm e}^x - 1} Q(x) \left(\frac{Y}{\rm arcmin^2} \right) {\rm mJy}, \tag{2.8}$$

where

$$Q(x) = \frac{x{\rm e}^x}{{\rm e}^x - 1} \left[\frac{x}{\tanh(x/2)} - 4 \right] \tag{2.9}$$

and 1 mJy$\equiv 10^{-29}$ J s^{-1} m^{-2} Hz^{-1}. In the long-wavelength limit, $x \to 0$, $Q(x) \to -2$ and this reduces to the result stated earlier, $\Delta T/T = S_\nu/S_\nu^{\rm CMB} = -2Y$. At $x \approx 3.83$ ($\lambda = 1.37$ mm) $Q(x) = 0$ and at higher frequencies the cluster appears as a source of emission.

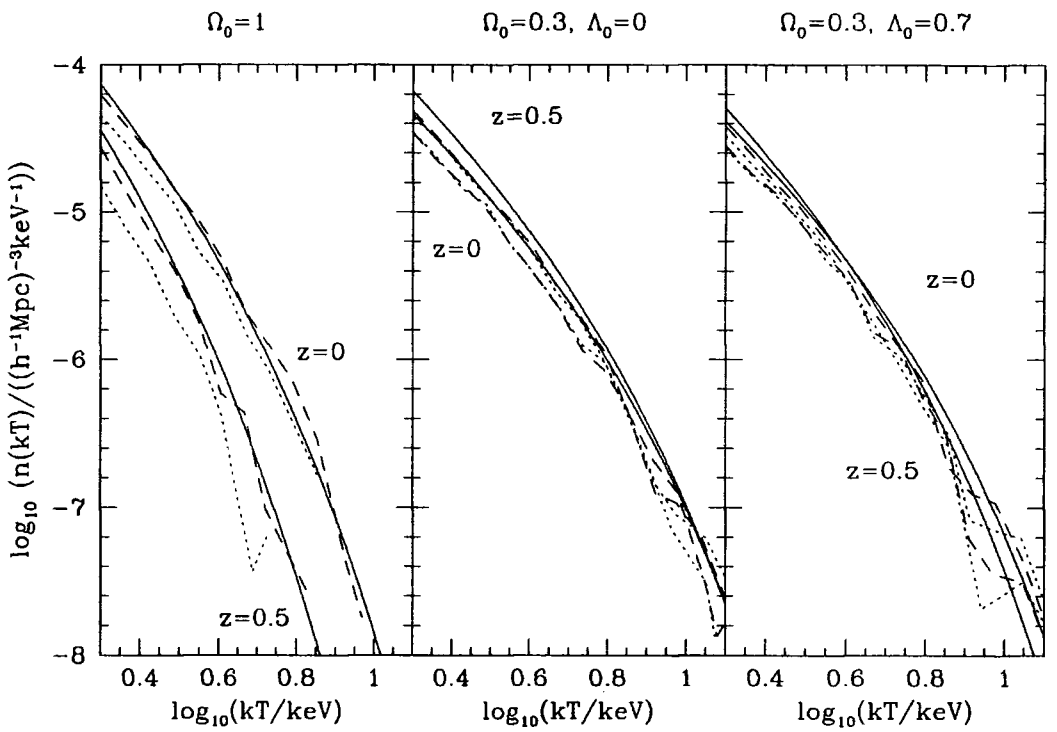

Figure 2.2: Comparison of the temperature functions predicted by the Press-Schechter distribution and the results of N-body simulations. For each of the three cosmological models (with parameters given at the top of each panel), temperature functions are plotted for $z = 0$ and $z = 0.5$. The Press-Schechter predictions, which are normalised according to the spherical collapse model, are shown by solid lines. The simulation results are plotted with dashed lines for clusters identified with a friends-of-friends algorithm and with dotted lines for clusters found with the spherical overdensity algorithm. Over the full range of abundances and redshifts shown the agreement between theory and simulations is very good.

The effective cross-section, Y, defined by equations (2.4) and (2.5), is proportional to the total mass and average temperature of the intracluster gas. Specifically, for an isothermal intracluster gas,

$$\begin{aligned} Y &= \frac{\sigma_{\rm T}}{2m_{\rm e}m_{\rm p}c^2} f_{\rm ICM}\,(1+X)\,M\,kT_{\rm gas}\,r_{\rm d}^{-2} \\ &= 1.70\times10^{-2}h\left(\frac{f_{\rm ICM}}{0.1}\right)\left(\frac{1+X}{1.76}\right)\left(\frac{M}{10^{15}h^{-1}{\rm M}_\odot}\right) \\ &\quad \left(\frac{kT_{\rm gas}}{\rm keV}\right)\left(\frac{r_{\rm d}}{100\,h^{-1}{\rm Mpc}}\right)^{-2}\ {\rm arcmin}^2, \end{aligned} \tag{2.10}$$

where $f_{\rm ICM}$ is the fraction of the cluster mass represented by the hot intracluster gas. Values of $\beta = 1$, $X = 0.76$ and $f_{\rm ICM} = 0.1$ are adopted here but the results can readily be rescaled to other choices. Note that here it is appropriate to use the mass-weighted temperature for which Navarro et al. (1995) find $\beta = 1.2$ for their $\Omega_0 = 1$ simulations. In Chapter 6 a mean value of $\beta = 1.27 \pm 0.06$ is found for clusters forming in an $\Omega_0 = 0.3$, $\Lambda_0 = 0.7$ model.

2.3 Comparison with N-body Simulations

In order to assess the accuracy of the Press-Schechter mass distribution in the regime of interest – the mass scale of rich galaxy clusters – the model predictions are compared with the abundance of dark matter clumps found in a new set of large cosmological N-body simulations (Cole, Frenk & Weinberg, in preparation). The simulations were performed with the AP^{3}M code of Couchman (1991) using $192^3 \approx 7\times10^6$ particles in a periodic box of size $l_{\rm box} = 345.6\,h^{-1}$Mpc. The particle mass was $M_{\rm p} = 1.64\times10^{12}\Omega_0 h^{-1}{\rm M}_\odot$ and the force resolution $\epsilon = 180{\rm h}^{-1}$kpc, where ϵ is the equivalent Plummer potential softening parameter. Two sequences of simulations were carried out with different values of Ω_0, a sequence of open models with $\Lambda_0 = 0$ and a sequence of flat models with $\Omega_0 + \Lambda_0 = 1$. Both were normalised to have $\sigma_8 = 0.55\,\Omega_0^{-0.6}$ so as to reproduce, approximately, the observed abundance of galaxy clusters (White et al. 1993). The number of timesteps required to evolve the simulations accurately from the linear regime to the present epoch was approximately $100/\Omega_0$. The initial linear power spectrum was the same in all simulations, a CDM spectrum with scale parameter $\Gamma = \Omega_0 h = 0.25$. This value of Γ is suggested by observations of large-scale galaxy clustering (e.g. Maddox et al. 1990). Here we will consider only three representative models, one with $\Omega_0 = 1$, another with $\Omega_0 = 0.3$ and $\Lambda_0 = 0$, and a third one with $\Omega_0 = 0.3$ and $\Lambda_0 = 0.7$.

Groups of particles were identified in the simulations using two different algorithms. The first was the standard friends-of-friends algorithm (Davis et al. 1985) with linking length $b_{\rm l}$ times the mean interparticle separation; the second was the spherical overdensity algorithm (Lacey & Cole 1994) with density contrast κ_ρ. Values of $b_{\rm l}$ and κ_ρ were chosen so that, on average, groups have the overdensity characteristic of virialised objects predicted by the spherical collapse model. The friends-of-friends linking length was taken to be $b_{\rm l} = 0.2$ in the $\Omega_0 = 1$ simulation and

scaled as $b_l \propto (\Delta_c/\Omega)^{-1/3}$ for the other cases. In both the simulations and the Press-Schechter model, mass was converted to temperature using relation (2.2).

Fig. 2.2 compares cluster abundances as a function of kT at $z = 0$ and $z = 0.5$ in the N-body simulations and in the Press-Schechter model. Overall, the analytical predictions are in excellent agreement with the N-body results and reproduce the near-exponential fall-off of the temperature functions very accurately. The threshold density, δ_c, has *not* been treated as a free parameter, but has instead been fixed at the value prescribed by the spherical collapse model. For the $\Omega_0 = 1$ case at $z = 0$ this value is essentially perfect and produces a temperature function midway between those obtained using the friends-of-friends and spherical overdensity algorithms. For $z = 0.5$, the spherical overdensity algorithm finds somewhat fewer high-temperature clusters than either the friends-of-friends algorithm or the Press-Schechter model. This may partially reflect the relatively low resolution of the N-body simulations as the most massive groups contain only about 100 particles in the $\Omega_0 = 1$ simulation at $z = 0.5$. In the two $\Omega_0 = 0.3$ cases, the Press-Schechter model matches the very slow evolution of the halo abundances in the simulations extremely well. If one were to adjust δ_c upwards by approximately 4%, then the N-body results would be reproduced almost perfectly over the temperature range plotted in Fig. 2.2. This uncertainty is taken into account in our analysis of the error in σ_8 in Section 2.4 (see also Table 2.1). Note that, for the more common, lower temperature clusters not shown in this figure, the Press-Schechter distribution predicts a significantly higher abundance than found in the simulations. However, for the range of masses of interest, the agreement with the numerical results is sufficiently good that we can confidently use the Press-Schechter model for detailed calculations.

2.4 Normalisation of the models

2.4.1 Determination of σ_8 from the cluster X-ray temperature function

The predicted and observed distributions of cluster X-ray temperatures in the local universe are now compared in order to obtain an estimate of σ_8, the rms mass fluctuation in spheres of radius $8\,h^{-1}$Mpc. The observational data comprise the complete flux-limited sample of 25 clusters compiled by Henry & Arnaud (1991). This estimate is then compared with earlier determinations of σ_8 from both X-ray and optical data (Henry & Arnaud 1991; White et al. 1993; Viana & Liddle 1996) and the reasons why these earlier determinations gave slightly different values of σ_8 are discussed.

The stepped curve in Fig. 2.3 shows the following simple estimate of the cumulative cluster temperature function derived from the Henry & Arnaud data:

$$N(>kT) = \sum_{kT_i > kT} 1/V_{\mathrm{max},i}, \qquad (2.11)$$

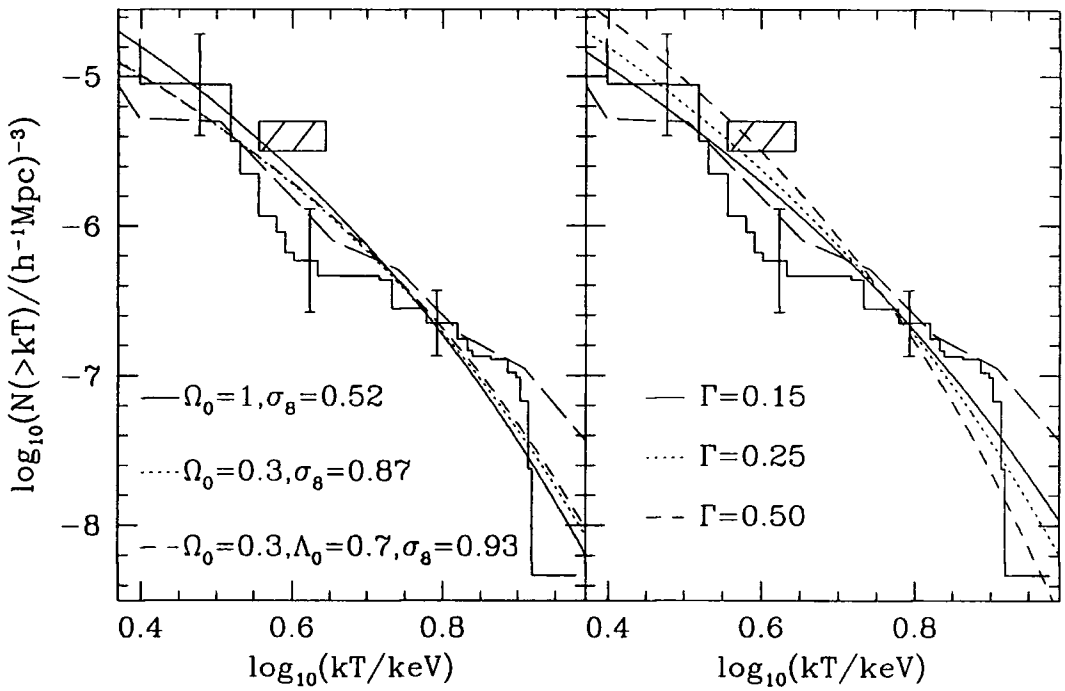

Figure 2.3: Predicted and observed X-ray temperature functions. The left-hand panel shows Press-Schechter predictions for $\Gamma = 0.25$ and $\Omega_0 = 1$ (smooth solid line), $\Omega_0 = 0.3$, $\Lambda_0 = 0$ (dotted line) and $\Omega_0 = 0.3$, $\Lambda_0 = 0.7$ (dashed line). The models are normalised by fitting to the observed data as described in the text. The observed temperature function, shown as a solid line with steps, was derived from the data compiled by Henry & Arnaud (1991). The error bars at the three temperatures where the models were fitted were obtained from a bootstrap analysis. The best-fitting values of σ_8 are given in the figure. The long-dashed line shows the cumulative temperature function obtained by Edge et al. (1990). The hatched box represents the range of normalisations derived by White et al. (1993) from a similar theoretical analysis of combined X-ray and optical data. The right-hand panel gives model predictions for $\Omega_0 = 1$, $\sigma_8 = 0.52$ and three values of Γ: 0.15 (solid line), 0.25 (dotted line), and 0.50 (dashed line). The observational data and the hatched box are the same as in the left-hand panel.

Table 2.1: A list of the uncertainties contributing to the error in the value of σ_8 estimated by fitting a Press-Schechter distribution to the redshift-zero cluster temperature function.

Source of error	Contribution to error in σ_8 (for $\Omega_0 = 1$)
Systematic error due to uncertain cluster temperatures	-0.007
25% incompleteness in the catalogue	$+0.01$
Statistical error in the fit to $N(> kT)$	± 0.02
4% uncertainty in the threshold δ_c	± 0.02
10% uncertainty in β	± 0.026
Sum in quadrature	± 0.04

where $V_{\mathrm{max},i}$ is the maximum volume in which the cluster could be detected given the flux limit and geometric boundaries of the survey. The results are presented in cumulative form in order to avoid binning the data. Since the cluster abundance falls very rapidly with increasing temperature, the differential temperature function averaged over each bin can be significantly larger than the underlying unbinned distribution. Henry & Arnaud (1991) estimated the differential temperature function by weighting the number of clusters in each temperature bin with the *average* value of $V_{\mathrm{max},i}$ in that bin. This estimator is only equivalent to (2.11) if $V_{\mathrm{max},i}$ is the same for all of the clusters in each bin. However, since the bins have non-zero width and the L_X–T_X relation has considerable scatter, there is also considerable scatter in the individual $V_{\mathrm{max},i}$ values in each temperature bin. For the Henry & Arnaud dataset this is a large effect and would have led them to underestimate the cluster abundance by approximately a factor of 4. However (Henry, private communication), in computing each $V_{\mathrm{max},i}$, a spurious factor of 4.2 entered their calculation and this largely compensated for the bias in the estimator. Thus the published Henry & Arnaud (1991) temperature function is in reasonably good agreement with the estimate made here. It is also in reasonable agreement with the cumulative temperature function of Edge et al. (1990), reproduced as the long-dashed line in Fig 2.3.

σ_8 was determined by fitting the model predictions to the estimate of the temperature function. A boostrap procedure was used to calculate the statistical errors in the temperature function. At three selected temperatures, T_i, the temperature function was computed (using equation 2.11) for a large number of samples of 25 clusters constructed by selecting randomly, with replacement, from the original list of 25 clusters in Henry & Arnaud's compilation. To take into account the uncertainties in the individual cluster temperature measurements, the temperatures of the individual bootstrap clusters were chosen from Gaussian distributions with means and standard deviations taken from this same list. The error bars in Fig. 2.3 show the resulting 1σ ranges in the bootstrap distribution of $\log_{10} N_{\mathrm{boot}}(> kT)$, at the three temperatures. This distribution was also used to compute the covariance between the estimates at different temperatures. Averaging over the bootstrap samples

gives the covariance matrix,

$$C_{ij} = \langle \epsilon_i \epsilon_j \rangle, \tag{2.12}$$

where $\epsilon_i = \log_{10} N_{\rm boot}(> kT_i) - \log_{10} N_{\rm data}(> kT_i)$. The model temperature functions are then fitted by minimising

$$\chi^2 = \sum_{ij} \delta_i C_{ij}^{-1} \delta_j, \tag{2.13}$$

where $\delta_i = \log_{10} N_{\rm model}(> kT_i) - \log_{10} N_{\rm data}(> kT_i)$. If the data points are uncorrelated then C_{ij} is diagonal and equation (2.13) reduces to the normal definition of χ^2. At the three selected temperatures there are significant correlations between the estimates of $\log_{10} N(> kT)$, but the models which minimise χ^2 are insensitive to whether the correlations are treated as above or simply ignored.

The best-fitting models are shown in Fig. 2.3 for $\Omega_0 = 1$ and $\Omega_0 = 0.3$, with and without a cosmological constant. The models in the left-hand panel all have the same CDM power spectrum with $\Gamma = 0.25$. Because of the very sensitive dependence of cluster abundance on spectrum normalisation, σ_8 can be estimated with high precision even though the errors in the empirical cluster abundance are quite large. The formal error on σ_8 from the fits in Fig. 2.3 is $\pm 4\%$, but this is likely to be an underestimate of the true uncertainty because, with only 25 clusters, the errors in the temperature function are unlikely to be Gaussian and, in addition, systematic errors are likely to be significant.

The right-hand panel of Fig. 2.3 shows the effect of allowing Γ to vary for the case of $\Omega_0 = 1$. Values of $\Gamma < 0.25$ produce more large-scale power and more very hot clusters. This produces a temperature function with a shallower slope, which is in better agreement with the observations. (The best-fitting model has $\Gamma = 0.13$ and $\sigma_8 = 0.52$, but this is not a reliable way of constraining Γ because the high- and low-temperature points are anticorrelated, and this creates a large uncertainty in the slope of the temperature function.) Fortunately, the best-fitting values of σ_8 are quite insensitive to the adopted value of Γ, because as Γ varies it is the slope of the temperature function that varies with the pivot point remaining in the middle of the range of rich cluster temperatures. This simply reflects the fact noted above that the average mass within a sphere of radius $8\,h^{-1}$Mpc in an unperturbed universe with $\Omega_0 \approx 1$ is very close to the mass of a rich galaxy cluster.

In addition to the formal statistical error on σ_8 mentioned above, other sources of error include uncertainties in the model parameters $\delta_{\rm c}$ and β and possible systematic effects arising both from incompleteness in the flux-limited cluster catalogue and errors in the temperature measurements. Table 2.1 contains a list of the uncertainties that have been considered, evaluated for the $\Omega_0 = 1$ cosmology. The error in $\delta_{\rm c}$ is estimated from Fig. 2.2 to be $\lesssim 4\%$, and the uncertainty in β is taken to be 10% (Section 2.2; Navarro et al. 1995; Chapter 6). Adopting $\beta = 1.1$ would increase the value of σ_8 by $\sim 5\%$. Lahav et al. (1989) estimate the sample of X-ray clusters to be 90% complete; a conservative value of 75% would only increase σ_8 by ~ 0.01 (in the $\Omega_0 = 1$ case). The final error that is considered is the systematic overestimation of σ_8 arising from errors in the temperature measurements which change the shape

of the steeply declining temperature function. The magnitude of the resulting offset in σ_8 has been estimated both by smoothing the model temperature function with a Gaussian before fitting a new σ_8 to the resulting curve, and from the difference between the best-fitting σ_8 and the average of the values from the bootstrap catalogues. Assuming Gaussian errors in the measured temperatures with rms of 10%, we find that both these methods increase our estimated value of σ_8 by only 0.007 for the case where $\Omega_0 = 1$. Combining all of these uncertainties in quadrature we estimate the overall uncertainty in σ_8 to be approximately 8%, twice as large as the formal statistical error in the fits of Fig. 2.3.

In summary, the observed temperature function is well fitted by the CDM models which have been considered here if

$$\sigma_8 = (0.52 \pm 0.04)\Omega_0^{-0.46+0.10\Omega_0} \quad \text{for} \quad \Lambda_0 = 0 \tag{2.14}$$

and

$$\sigma_8 = (0.52 \pm 0.04)\Omega_0^{-0.52+0.13\Omega_0} \quad \text{for} \quad \Omega_0 + \Lambda_0 = 1. \tag{2.15}$$

2.4.2 Comparison with previous results

The values of σ_8 inferred above from the X-ray data are systematically lower than those obtained by White et al. (1993) who found $\sigma_8 = 0.57\Omega_0^{-0.56}$. The modelling of the cluster abundances is almost identical and the difference in the resulting values of σ_8 arises almost entirely from the different observational data that are fitted. White et al. estimated the mass of clusters with abundance $4 \times 10^{-6} h^3$ Mpc^{-3} in two different ways. The first and larger estimate was based on the median velocity dispersion of rich Abell clusters. The second was based on the cumulative temperature functions of Henry & Arnaud (1991) and Edge et al. (1990). The range spanned by these two estimates, expressed as a temperature rather than a mass using equation (2.2), is indicated by the hatched box in Fig. 2.3. The lower estimate of the X-ray temperature is slightly higher than the analysis presented here of the Henry & Arnaud data implies. This difference results from the fact that the White et al. estimate was inferred indirectly from the differential temperature function presented by Henry & Arnaud, not directly from the cumulative temperature function.

Henry & Arnaud (1991) found $\sigma_8 = 0.59 \pm 0.02$ for $\Omega_0 = 1$ and a power-law fluctuation spectrum. Whilst employing essentially the same data as have been used here, they adopted $\beta = 1.2$ in equation (2.2), rather than $\beta = 1$ assumed above. Thus, for the same value of σ_8, their model temperature functions are shifted to lower temperatures by ~ 0.08 in $\log_{10}(kT)$, and this largely accounts for the difference in the inferred values of σ_8. Viana & Liddle (1996) obtained $\sigma_8 = 0.6$ for $\Omega_0 = 1$, with a dependence on Ω_0 close to that found here, by fitting only to the abundance of clusters at 7 keV. It may be seen from Fig. 2.3 that fitting the cumulative temperature function just at this temperature yields a higher value of σ_8 than the one obtained from fitting all the X-ray data. Given the small number of clusters with temperatures as great as 7 keV, fitting over a wider temperature range seems more appropriate.

In summary, the modelling of the cluster temperature function presented here is consistent with those of Henry & Arnaud (1991), White et al. (1993) and Viana & Liddle (1996). The range in the values of σ_8 deduced by these authors arises from the different data points they chose to fit and, in the case of Henry & Arnaud (1991), from the value of β they used to relate virial to gas temperature. Assuming $\beta = 1$, it can be concluded that the X-ray data are best fitted by the values of σ_8 given by equations (2.14) and (2.15). Since the abundance of Abell clusters of richness class ≥ 1 is $8 \times 10^{-6} h^3$ Mpc^{-3}, these results imply that the median 1D virial velocity dispersion of these clusters should be approximately 680 km s^{-1}. This is smaller than the median values of around 800 km s^{-1}, found in the compilations of Zabludoff, Huchra & Geller (1990) and Girardi et al. (1993). These differences may be understood if, as argued by Frenk et al. (1990) and others, the higher velocity dispersion estimates are artificially boosted by contamination from infalling groups around the cluster. Alternatively, these larger velocity dispersions (and a higher value of σ_8) would be consistent with the X-ray data if the intracluster gas were significantly cooler than the virial temperature, but this would require $\beta \gtrsim 1.4$. However, such large values of β are not supported either by the data or by recent hydrodynamic simulations of cluster formation (Navarro et al. 1995; Evrard, Metzler & Navarro 1996; Chapter 6).

2.5 Cluster evolution

Having fixed the normalisation of the models by requiring that they should match the local abundance of rich clusters, their evolutionary properties are now considered. Specifically, the variations with redshift of the mass function, the X-ray temperature function and the distribution of S-Z decrements are calculated. For each model, the evolution of the cluster mass function (equation 2.1) is governed by the linear growth factor, $D(z, \Omega_0, \Lambda_0)$. The evolution of the X-ray temperature and S-Z effect depends, in addition, on the evolution of the virial density $\Delta_c \Omega_0 / \Omega(z)$, which determines the relation (2.2) between mass and temperature.

2.5.1 Evolution of the cluster mass function

The growth of fluctuations continues at a rapid rate at recent times if $\Omega_0 = 1$ and very little if $\Omega_0 = 0.3$. As a result, the rich cluster mass function evolves dramatically between $z = 0.5$ and $z = 0$ if $\Omega_0 = 1$, but much less so if Ω_0 is low, whether or not the cosmological constant is zero. This evolution is illustrated in Fig. 2.4. For $\Omega_0 = 1$, the comoving number density of clusters of virial mass $M = 3.5 \times 10^{14} h^{-1} \mathrm{M}_\odot$, typical of Abell clusters of richness class $R \geq 1$, declines by a factor of 25 between $z = 0$ and $z = 0.33$ and, by $z = 0.5$, it is tiny. By contrast, for $\Omega_0 = 0.3$, $\Lambda_0 = 0.7$, the abundance of clusters of this mass has only dropped by a factor of ~ 5 below the present-day abundance even at $z = 0.5$; if $\Lambda_0 = 0$ the decline is even slower.

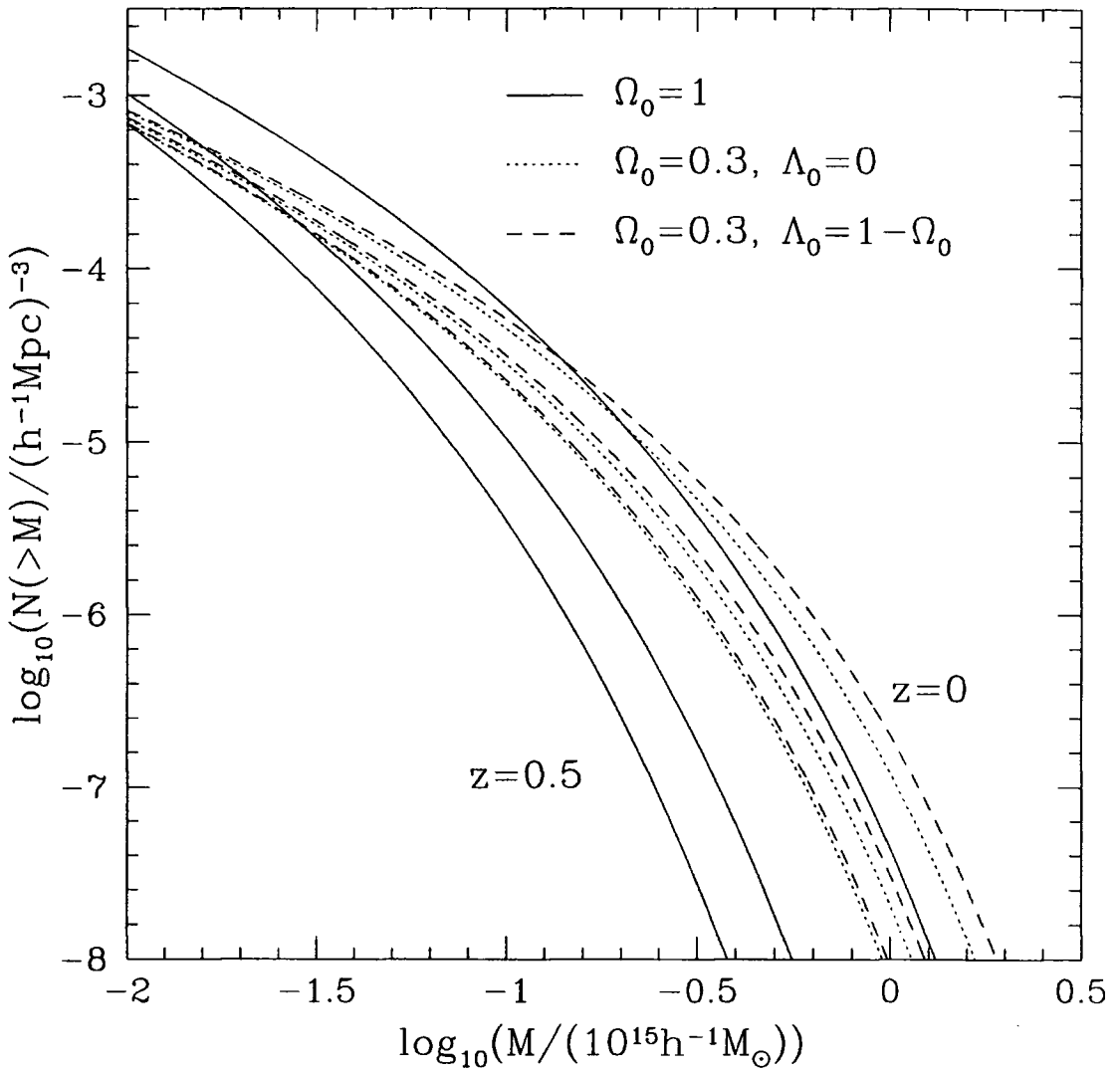

Figure 2.4: Predicted evolution of the cluster mass function. The comoving number density of clusters per $(h^{-1}\mathrm{Mpc})^3$ with masses larger than M is shown as a function of M. Solid lines correspond to $\Omega = 1$; dotted lines to an open model with $\Omega_0 = 0.3$; and the dashed lines to a flat model with $\Omega_0 = 0.3$ and $\Lambda_0 = 0.7$. Predictions for $z = 0$, $z = 0.33$ and $z = 0.5$ are plotted. There is relatively little evolution in the $\Omega_0 < 1$ cosmologies but, in an $\Omega_0 = 1$ model, the abundance of clusters declines precipitously with redshift.

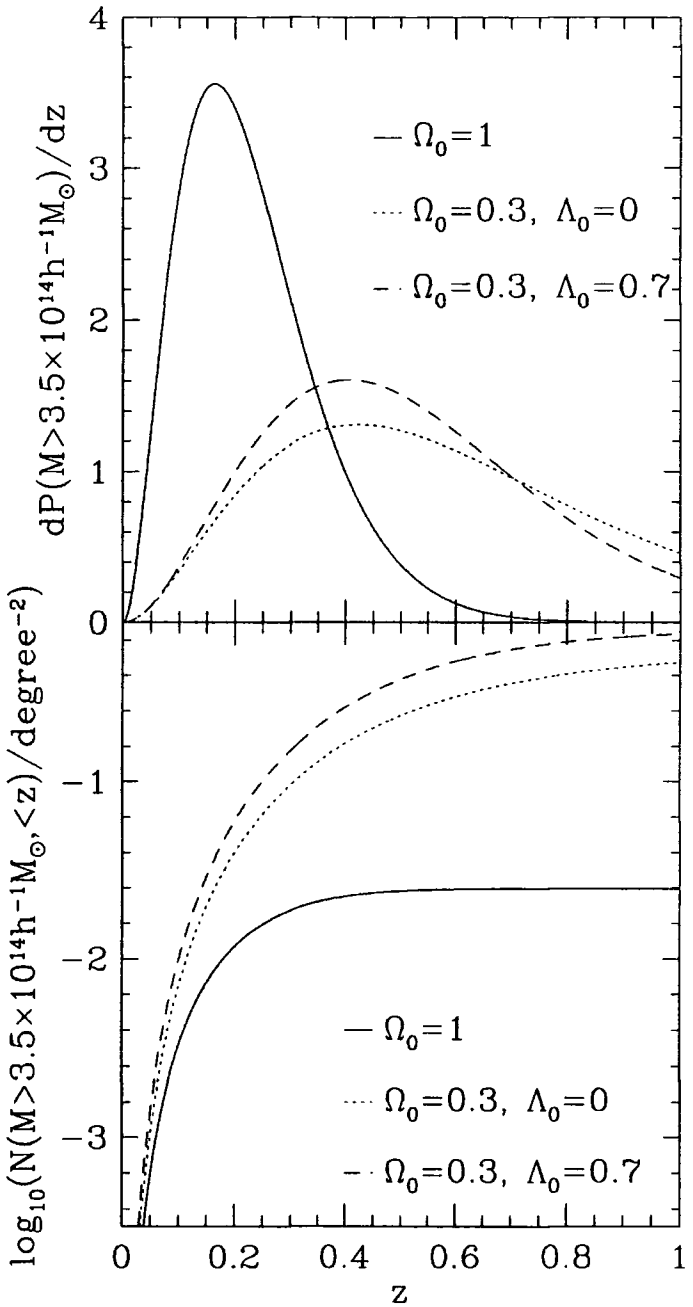

Figure 2.5: *Upper panel:* Redshift distribution of massive clusters ($M > 3.5 \times 10^{14} h^{-1} \mathrm{M}_\odot$) in different cosmological models. The ordinate gives the probability distribution of clusters per unit redshift interval. *Lower panel:* Number counts of clusters with mass $M > 3.5 \times 10^{14} h^{-1} \mathrm{M}_\odot$ out to a given redshift. The ordinate gives the count per unit area on the sky. In both panels solid lines correspond to $\Omega_0 = 1$, dotted lines to $\Omega_0 = 0.3$ and dashed lines to $\Omega_0 = 0.3, \Lambda_0 = 0.7$. The models are normalised by the value of σ_8 for which the predicted temperature function at $z = 0$ best fits the data. The low-Ω_0 cosmologies produce significantly more clusters at high redshifts than the $\Omega_0 = 1$ model.

The strong Ω_0-dependence of the rate at which the mass function evolves is reflected in the expected redshift distributions of massive clusters ($M > 3.5 \times 10^{14} h^{-1} \mathrm{M}_\odot$), illustrated in the top panel of Fig. 2.5. For $\Omega_0 = 1$ the distribution peaks sharply at very low redshift, whereas for low Ω_0 a broader peak exists and is displaced to higher redshift. The effect of Λ_0 is to move the peak back to a somewhat lower redshift, reflecting the slightly later epoch at which structure ceases to grow in non-zero Λ_0 cosmologies.

Integrating over the redshift distributions yields the number count of clusters per unit area on the sky. The change in the volume element corresponding to a fixed redshift interval enhances the differences between the high- and low-Ω models. At redshift $z = 0.33$, the volumes per unit redshift are in the ratios $1 : 1.23 : 1.7$ for $\Omega_0 = 1$, $\Omega_0 = 0.3$, $\Lambda_0 = 0$ and $\Omega_0 = 0.3$, $\Lambda_0 = 0.7$ respectively. At $z = 0.5$ the corresponding ratios increase to $1 : 1.35 : 2.02$. Thus, for $\Omega_0 = 1$, one should expect to find only 0.02 clusters per square degree with mass greater than $3.5 \times 10^{14} h^{-1} \mathrm{M}_\odot$ out to $z = 0.5$ and virtually none at higher redshifts. By contrast, for $\Omega_0 = 0.3$, we expect to find more than 10 times as many clusters above this mass with $z < 0.5$. Note that predictions for low-Ω models are relatively insensitive to the value of Λ_0, with only about 50% more clusters predicted to exist in the non-zero Λ_0 model. This factor results largely from the difference in the volume elements.

The cluster mass that enters into equation (2.1) and Figs 2.4 and 2.5 is the virial mass, i.e. the mass contained within a sphere of mean overdensity Δ_c. In practice, gravitational lensing measurements give the mean projected surface density, $\bar{\Sigma}(r)$, within a radius, r, which is typically less than $1\, h^{-1}\mathrm{Mpc}$. To relate these two masses requires a model of the cluster mass distribution. Recent high-resolution N-body simulations show that, over most of the cluster, the dark matter density profile is well approximated by an isothermal profile (Navarro et al. 1995; Cole & Lacey 1996). Although in principle it would be straightforward to use the analytical fit to the N-body profile given by Navarro et al. (1995), for these purposes the isothermal profile approximation is quite adequate. In this case, mean surface density is related to virial mass by (see Appendix D)

$$M_{\mathrm{vir}} = \frac{4}{H}\left(\frac{G r^3 \bar{\Sigma}(r)^3}{\Delta_c}\right)^{1/2}, \tag{2.16}$$

where r is any radius inside the virial radius, H is Hubble's constant at the redshift of the cluster and the overdensity Δ_c is given in Fig. 2.1 as a function of Ω. This formula may be used to relate the surface mass density estimated from weak gravitational lensing analyses to the virial mass. Note, however, this has implicitly assumed that any foreground or background mass makes a negligible contribution to the lensing signal.

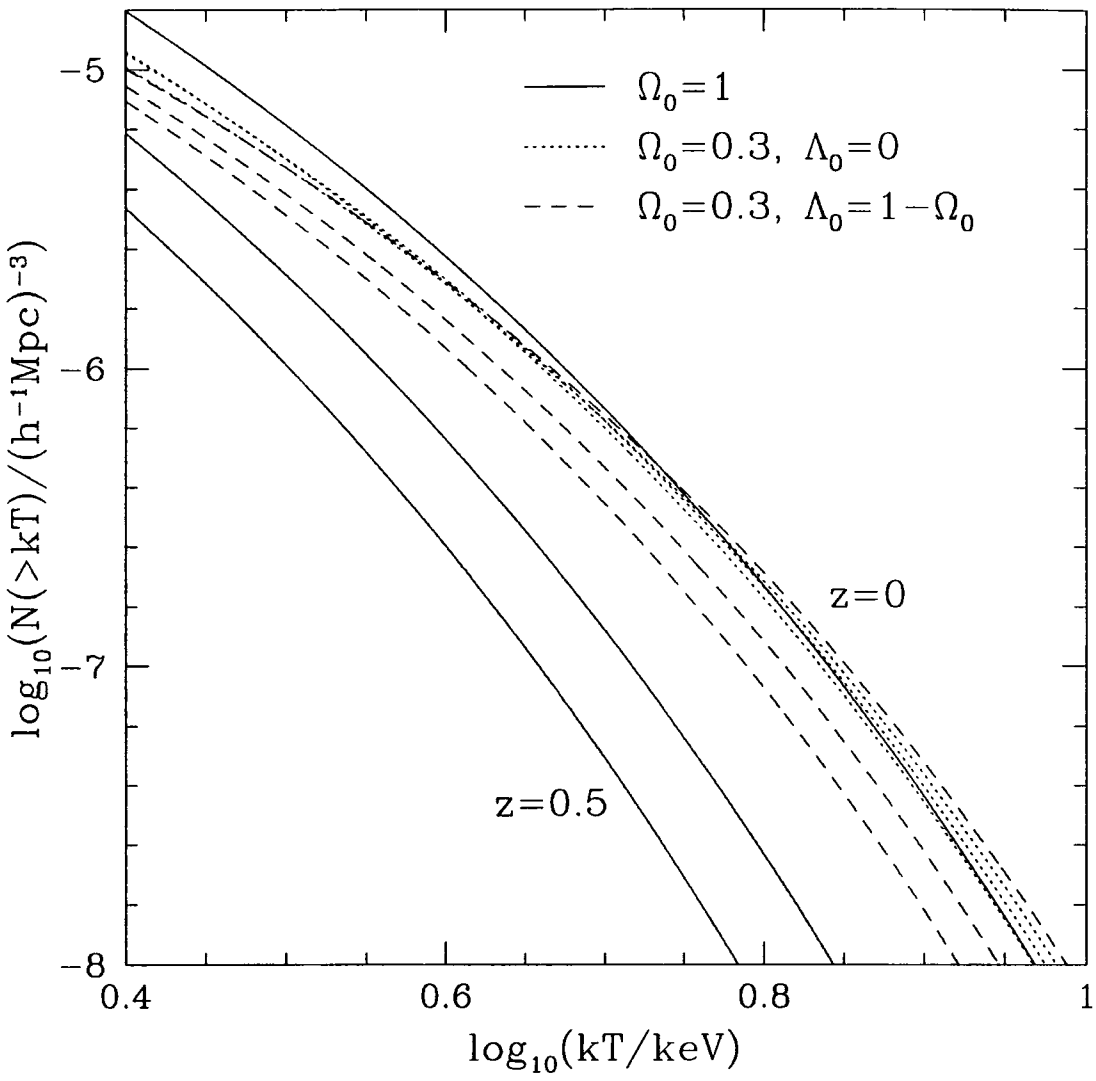

Figure 2.6: Predicted evolution of the cluster X-ray temperature function. The comoving number density of clusters per $(h^{-1}\mathrm{Mpc})^3$ hotter than kT is shown as a function of kT. Solid lines correspond to $\Omega = 1$; dotted lines to an open model with $\Omega_0 = 0.3$; and the dashed lines to a flat model with $\Omega_0 = 0.3$ and $\Lambda_0 = 0.7$. Predictions for $z = 0$, $z = 0.33$ and $z = 0.5$ are plotted. There is little evolution in the $\Omega_0 < 1$ cosmologies but, in an $\Omega_0 = 1$ model, the abundance of clusters declines precipitously with redshift.

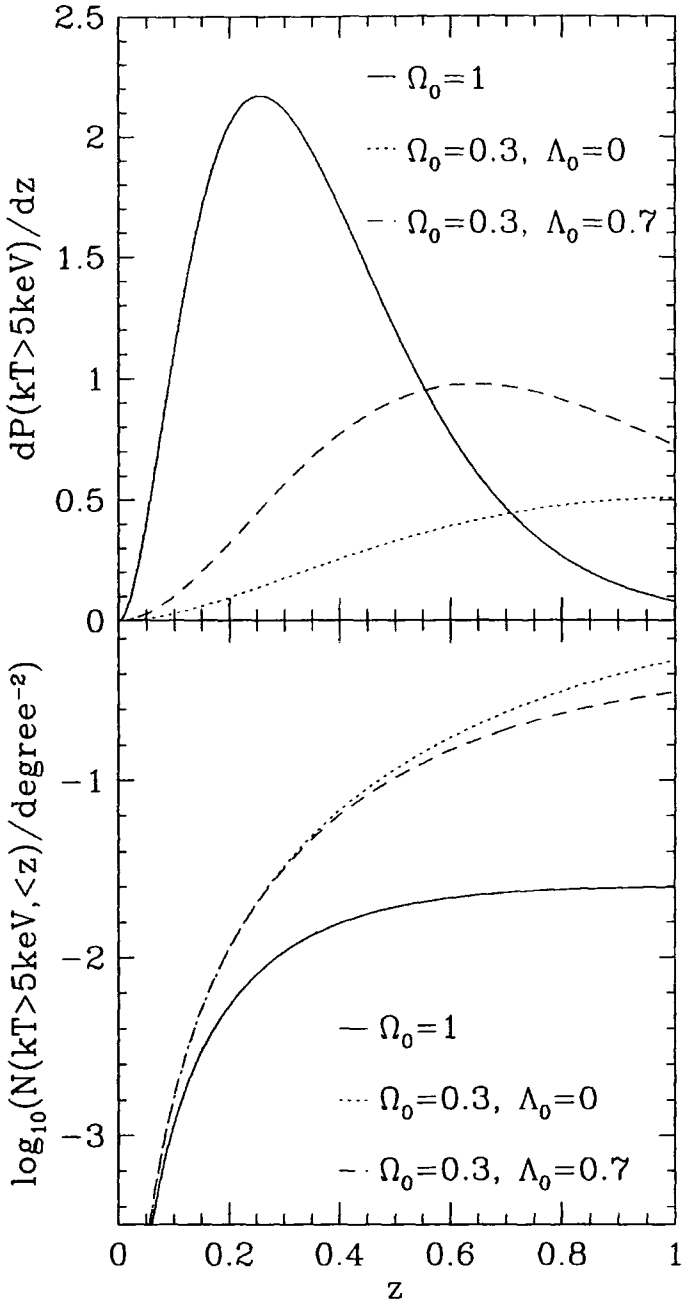

Figure 2.7: *Upper panel:* Redshift distribution of hot clusters ($kT > 5$ keV) in different cosmological models. The ordinate gives the probability distribution of clusters per unit redshift interval. *Lower panel:* Number counts of clusters hotter than $kT > 5$ keV out to a given redshift. The ordinate gives the count per unit area on the sky. In both panels solid lines correspond to $\Omega_0 = 1$, dotted lines to $\Omega_0 = 0.3$ and dashed lines to $\Omega_0 = 0.3, \Lambda_0 = 0.7$. The models are normalised by the value of σ_8 for which the predicted temperature function at $z = 0$ best fits the data. The low-Ω_0 cosmologies produce significantly more clusters at high redshifts than the $\Omega_0 = 1$ model.

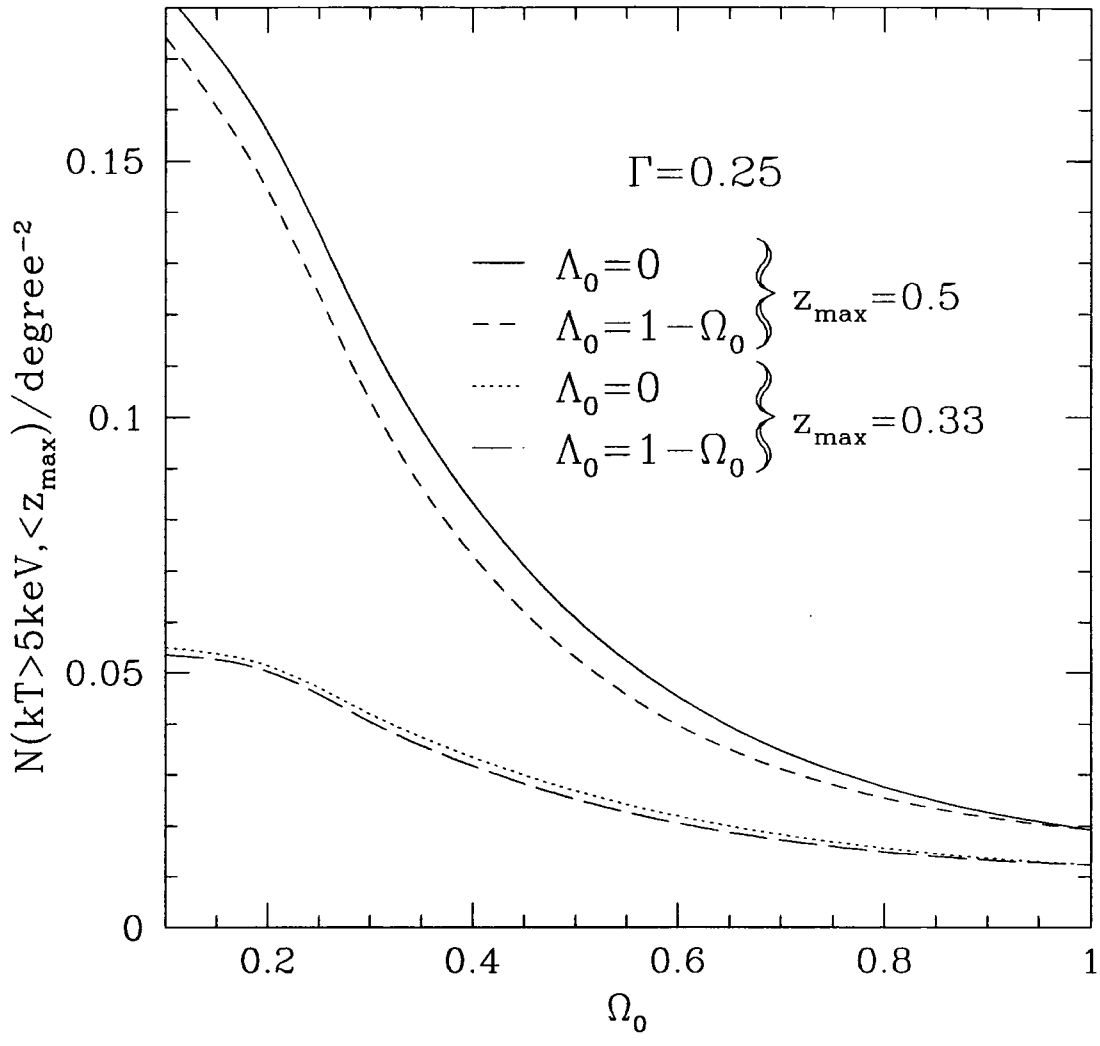

Figure 2.8: Predicted number counts of clusters hotter than 5 keV out to $z = 0.33$ and 0.5, as a function of Ω_0. The solid and dotted lines correspond to open models ($\Lambda_0 = 0$) and the dashed lines to flat models ($\Lambda_0 = 1 - \Omega_0$). The abundances are sensitive to the choice of σ_8, but the ratio of the numbers expected in different cosmologies is less so.

2.5.2 Evolution of the cluster X-ray temperature function

The evolution of the X-ray temperature function depends both on the growth factor, $D(z, \Omega_0, \Lambda_0)$, and on the virial density, $\Delta_c \Omega_0 / \Omega(z)$. Thus, at high z, the abundance of clusters of a given temperature is determined by the balance between the overall decline in the population of virialized clusters and the lower mass associated with each temperature. If $\Omega_0 = 1$, the first factor is dominant and the temperature function declines precipitously (see Fig. 2.6). By contrast, in an open, $\Omega_0 = 0.3$, universe, the two effects nearly cancel out and the temperature function remains virtually unchanged at least out to $z = 0.5$. A flat, $\Omega_0 = 0.3$, universe is intermediate and, in this case, the temperature function declines slowly with redshift.

The redshift distribution of clusters hotter than 5 keV is shown in Fig. 2.7. As was the case for the mass function, the $\Omega_0 = 1$ model produces large clusters predominantly at low redshifts. The $\Omega_0 = 0.3$ models, on the other hand, give rise to extended redshift distributions. Again, the lower redshift at which structure 'freezes-out' when a Λ_0 term is included produces somewhat stronger evolution in this case compared with an open cosmology. When integrating over redshift, the effect of different evolutionary rates is enhanced by the larger volume in low-density universes. As a result, the number counts per unit area of sky, displayed in the lower panel of Fig. 2.7, depend strongly on the value of Ω_0. For the parameters chosen here, the counts in the two $\Omega_0 = 0.3$ models are very similar and the total number of clusters hotter than 5 keV at redshifts less than 0.5 is about 6 times higher in these models than in the $\Omega_0 = 1$ case. The expected number counts for different values of Ω_0 are shown in Fig. 2.8, for both open and flat models.

It should be emphasized that the results shown in Figs 2.6 – 2.8 are very sensitive to the normalisation of the fluctuation amplitude. The adopted values of σ_8 were fixed by requiring that each model should agree well with the present-day X-ray temperature function. With this particular choice, the inclusion of a Λ_0 term turns out to make very little difference to the predicted abundance of hot clusters out to a redshift of 0.5. However, the number counts out to this redshift do discriminate well between different values of Ω_0.

2.5.3 Evolution of the Sunyaev-Zel'dovich function

As discussed in Section 2.2, the S-Z effect is characterised by the Y-function given in equations (2.5) and (2.10). (Here, $X = 0.76$, $f_{\rm ICM} = 0.1$ and $\beta = 1$ are used, but the results are readily scaled to other values using $Y \propto (1+X) f_{\rm ICM} \beta^{-1}$.) The evolution of the Y-function is similar to that of the temperature function, but, since $Y \propto M^{5/3}$ whilst $T \propto M^{2/3}$, the detailed behaviour is slightly different. More importantly, the appearance of the diameter distance in equation (2.5) causes Y to drop off with redshift more rapidly than kT.

Fig. 2.9 confirms the rapid decline in the Y-function with redshift, resulting from

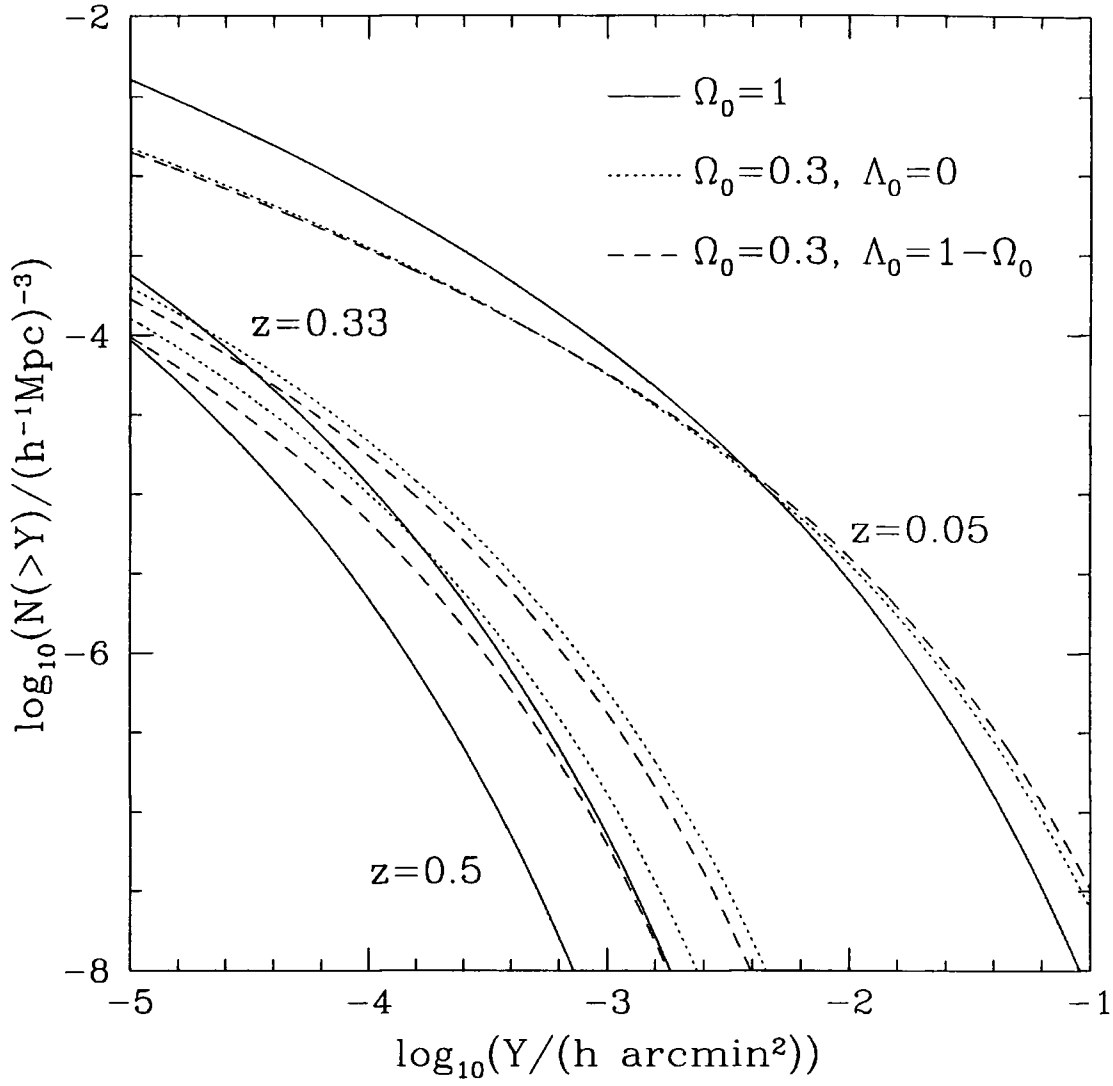

Figure 2.9: Predicted evolution of the cumulative cluster S-Z Y-function. The ordinate gives the comoving number density of clusters per $(h^{-1}\mathrm{Mpc})^3$. The solid lines are for $\Omega_0 = 1$; the dotted lines for $\Omega_0 = 0.3$ and the dashed lines for $\Omega_0 = 0.3$ and $\Lambda_0 = 0.7$. Predictions for $z = 0.05$, $z = 0.33$ and $z = 0.5$ are plotted. The Y-function evolves significantly in the three cosmologies, but the evolution is strongest for $\Omega_0 = 1$.

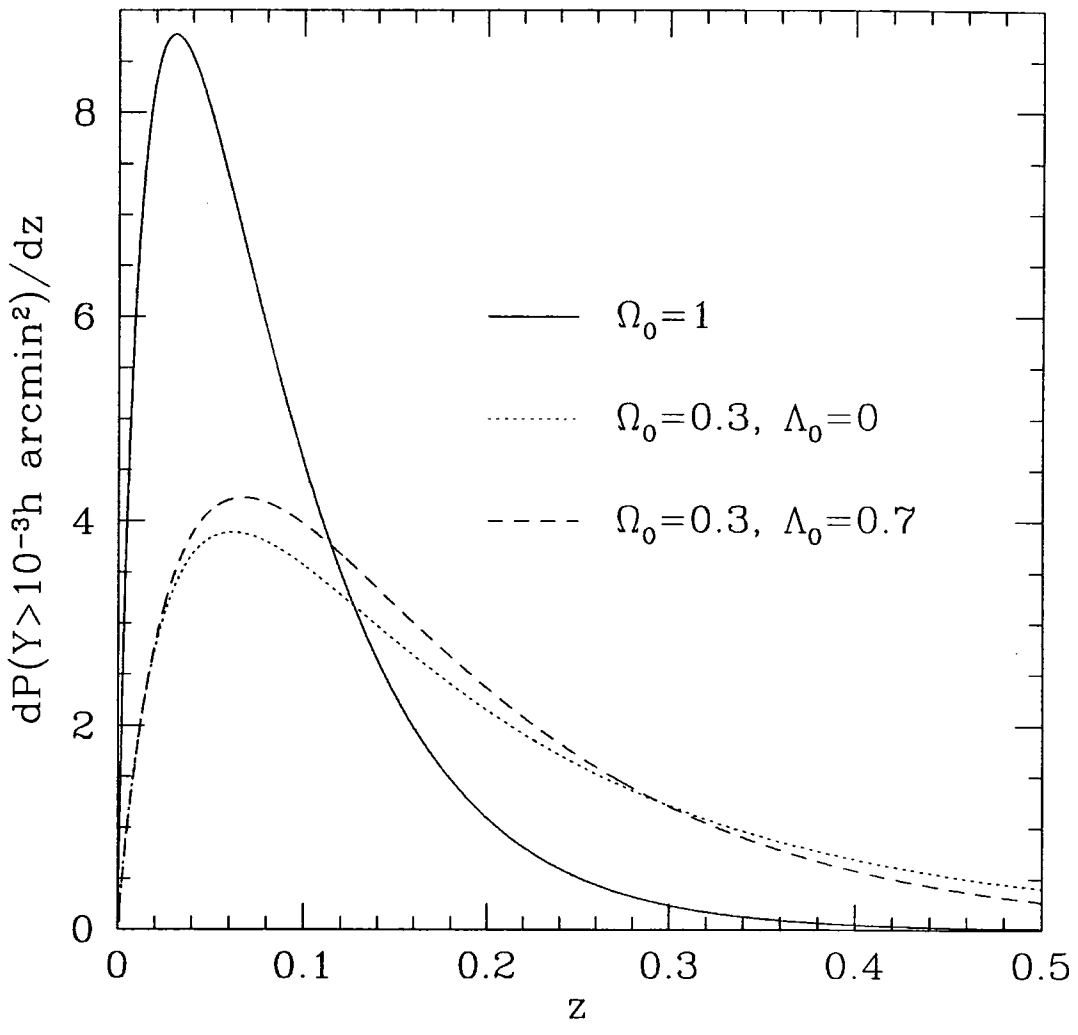

Figure 2.10: Redshift distribution of S-Z bright clusters ($Y > 10^{-3}h$ arcmin^2) in different cosmological models. The ordinate gives the probability distribution of clusters per unit redshift interval. The solid line corresponds to $\Omega_0 = 1$, the dotted line to $\Omega_0 = 0.3$ and the dashed line to $\Omega_0 = 0.3$ and $\Lambda_0 = 0.7$.

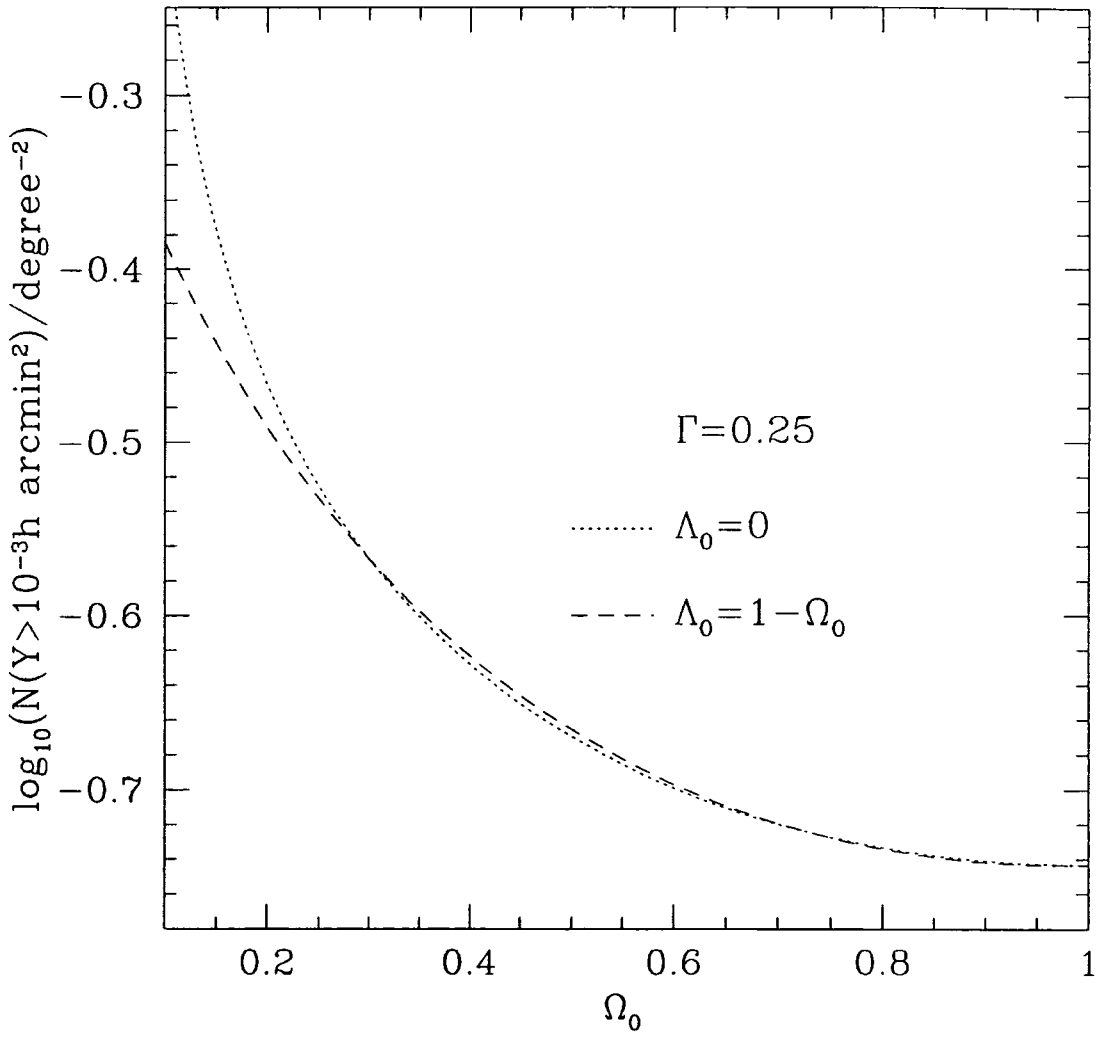

Figure 2.11: Predicted number counts of S-Z clusters with $Y > 10^{-3}h$ arcmin^2 as a function of Ω_0. The dotted line corresponds to open models ($\Lambda_0 = 0$) and the dashed line to flat models ($\Lambda_0 = 1 - \Omega_0$). The fractional difference between the models is smaller than in the corresponding plot for the temperature function because the counts are dominated by objects at low redshift where the models have been normalised to match the observed temperature function.

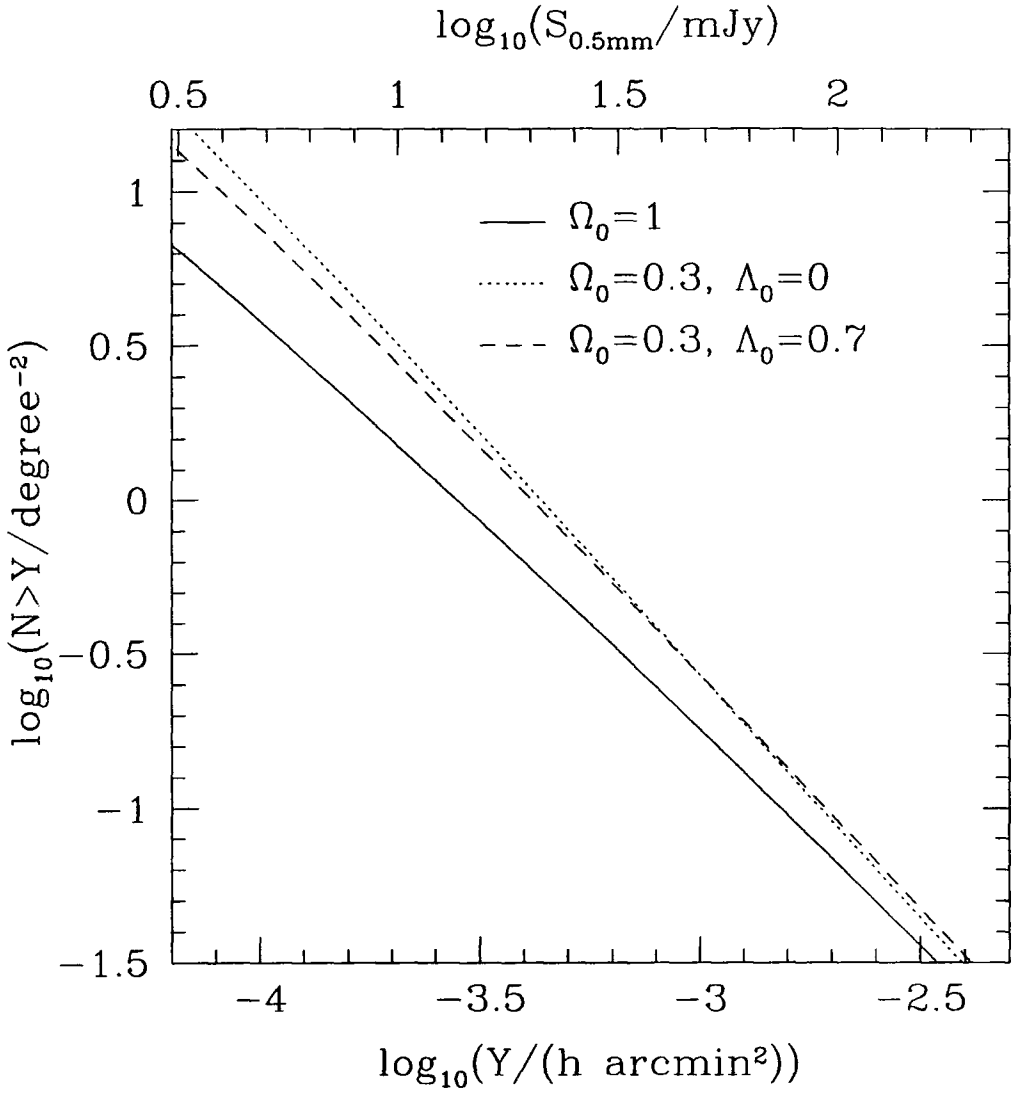

Figure 2.12: Sunyaev-Zel'dovich source counts as a function of Y for three different cosmologies. Solid lines correspond to $\Omega_0 = 1$, dotted lines to $\Omega_0 = 0.3$, and dashed lines to $\Omega_0 = 0.3, \Lambda_0 = 0.7$. The corresponding 0.5 mm fluxes in mJy are shown on the top axis. About 50% more clusters with $Y > 10^{-3}h$ arcmin^2 are expected in the $\Omega_0 = 0.3$ models than in the $\Omega_0 = 1$ case.

the r_d^{-2} term, in all the cosmological models (which, as before, are normalised using the local cluster X-ray temperature function). Evolution is in the same sense as evolution in the cluster mass and X-ray temperature functions. Also, for $z > 0$, the differences between the Y-functions of the various models are of similar magnitudes. To understand why this is so it is necessary to consider the two factors mentioned above. In the $\Omega_0 = 1$ model, in which the fluctuation growth factor is still changing rapidly at low redshifts, $M^{5/3}$ decreases faster with redshift than either M, which is relevant to the mass function, or $M^{2/3}$, which is relevant to the temperature function. Thus, for $\Omega_0 = 1$, the Y-function evolves more rapidly than the mass or temperature functions. This is partly offset, in the low-Ω_0 models, by their larger angular diameter distance out to a particular redshift.

As a result of the strong evolution apparent in Fig. 2.9, the redshift distribution of 'S-Z bright' clusters is highly peaked at low redshift in all our models. This distribution is plotted in Fig. 2.10 for clusters with $Y > 10^{-3}h$ arcmin^2. The corresponding number counts as a function of Ω_0 are shown in Fig. 2.11. These counts are dominated by local clusters and, since all the models are normalised to the local temperature function, the counts are similar in all cases. Nevertheless, $\sim 50\%$ more $Y > 10^{-3}h$ arcmin^2 clusters are expected if $\Omega_0 = 0.3$ than if $\Omega_0 = 1$. The splitting between the various cosmologies increases if the Y threshold is reduced, as illustrated in Fig. 2.12. As the threshold is lowered, the counts probe higher redshifts where the predictions are increasingly sensitive to Ω_0. Thus, if the threshold is taken to be $10^{-4}h$ arcmin^2, over twice as many clusters are expected per unit area if $\Omega_0 = 0.3$ than if $\Omega_0 = 1$. As with the counts as a function of mass or X-ray temperature, the counts as a function of Y are quite insensitive to Λ_0. The redshift distribution of a sample of Y-selected clusters gives a more promising method of constraining Ω_0. For clusters with $Y > 10^{-3}h$ arcmin^2 the median redshift (see Fig. 2.10) in the two $\Omega_0 = 0.3$ models is approximately $\bar{z} = 0.147$, which is a little over twice that of the $\Omega_0 = 1$ model. Thus optical follow-up on a relatively small sample of Y-selected clusters could easily distinguish between these two models.

2.6 Discussion and Conclusions

The Press-Schechter formalism has been used to investigate the evolution of the population of rich galaxy clusters. This work extends and complements earlier work using this formalism by Evrard (1989), Henry & Arnaud (1991), Lilje (1992), Oukbir & Blanchard (1992), Hanami (1993), White et al. (1993), Barbosa et al. (1995), Hattori & Matsuzawa (1995), and Viana & Liddle (1996), amongst others. It was shown that the Press-Schechter formula predicts the correct abundance of rich clusters at $z = 0$ and $z = 0.5$ by comparing with the results of large cosmological N-body simulations. The agreement is excellent, at least for the models considered here: CDM cosmologies with spectral shape parameter $\Gamma = 0.25$ and with (a) $\Omega_0 = 1$, (b) $\Omega_0 = 0.3$, $\Lambda_0 = 0$ and (c) $\Omega_0 = 0.3$, $\Lambda_0 = 0.7$.

The problem of normalising the amplitude of mass fluctuations on cluster scales

by reference to the present day abundance of rich clusters has been reconsidered. From the rederivation of the X-ray temperature distribution of clusters, using Henry & Arnaud's (1991) data, the following values for the rms density fluctuation in spheres of radius $8\,h^{-1}$Mpc, σ_8, were found:

$$\sigma_8 = (0.52 \pm 0.04)\Omega_0^{-0.46+0.10\Omega_0} \quad \text{for} \quad \Lambda_0 = 0 \tag{2.17}$$

and

$$\sigma_8 = (0.52 \pm 0.04)\Omega_0^{-0.52+0.13\Omega_0} \quad \text{for} \quad \Omega_0 + \Lambda_0 = 1. \tag{2.18}$$

For $\Omega_0 = 1$, this estimate is independent of the shape of the power spectrum and, for other values of Ω_0, there is only a very weak dependence. Note that σ_8 is only slightly larger if the Λ term is non-zero. For $\Omega_0 > 0.2$, the difference between the flat and open models is always less than 10%. Note also that, since the rms fluctuation in the bright galaxy distribution is 0.96 (Maddox, Efstathiou & Sutherland 1996) in spheres of radius $8\,h^{-1}$Mpc, these estimates of σ_8 imply that the biasing parameter defined as $b = 0.96/\sigma_8$ is greater than unity for open models with $\Omega_0 > 0.24$ and for flat models with $\Omega_0 > 0.28$. Models with Ω_0 smaller than this require antibiasing, that is they require bright galaxies to be less clustered than the mass. The estimates of σ_8 differ slightly from those obtained by previous authors and, in Section 2.4.2, the reasons for these differences were discussed in detail.

The quoted uncertainties in equations (2.17) and (2.18) represent the estimated overall errors in the model fits to the observed X-ray temperature function. The main source of uncertainty in our analysis is our modelling of the X-ray emitting intracluster medium as a homogeneous, isothermal gas in hydrostatic equilibrium (cf equation 2.2). There is some tentative evidence from *ASCA* data that the temperature in some clusters may be declining at large radii (Markevitch et al. 1996). On the other hand, hydrodynamic simulations show that the isothermal assumption is a good approximation in the region where most of the X-rays are emitted, at least in the case where cooling flows are ignored (Evrard 1990; Tsai, Katz & Bertschinger 1994; Navarro et al. 1995). The ratio of the specific galaxy kinetic energy to the specific gas thermal energy, was chosen to be $\beta = 1$, consistent with the results of simulations. If bulk motions or magnetic stresses contributed to the support of the gas, then a larger value of β would be appropriate. In this case, the results may be recast by scaling all temperatures inversely with β and this would lead to higher estimates of σ_8. Finally, the estimated gas temperatures and the inferred values of σ_8 may also be underestimated if small-scale inhomogeneities in the gas distribution affect the measured X-ray spectrum.

The values of σ_8 required to match the local abundance of clusters may be compared with measurements of the fluctuation amplitude on larger scales, particularly with those inferred from the microwave background anisotropies in the *COBE* 4-year data. By assuming a specific shape for the fluctuation spectrum, the *COBE* results may be extrapolated to $8\,h^{-1}$Mpc and, in principle, comparison with equa-

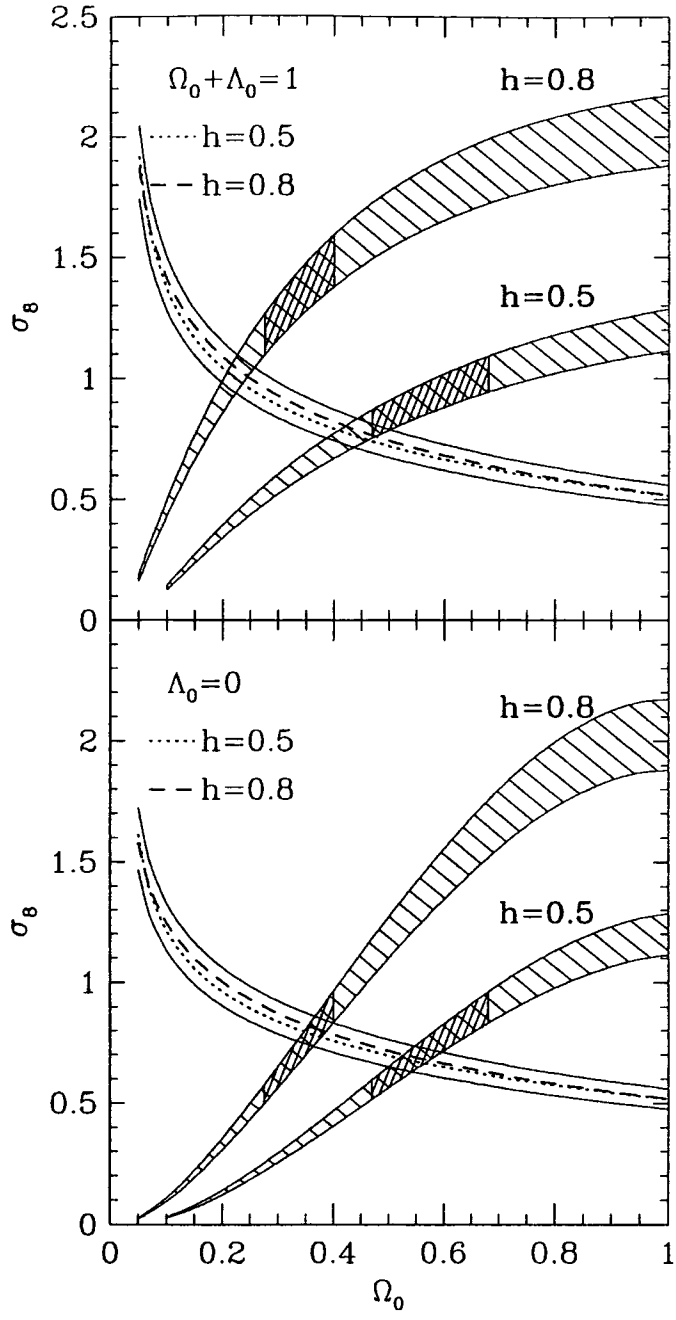

Figure 2.13: Comparison of σ_8 estimated from the *COBE* 4-year data and from the abundance of rich galaxy clusters. The top panel corresponds to flat models and the bottom panel to open models. The upper hatched region shows the *COBE* estimates for $h = 0.8$ and the lower hatched region the estimates for $h = 0.5$ as parametrised by Liddle et al. (1996a, 1996b) with 7.5% errors in both cases. The cross-hatching defines regions with $0.2 \leq \Gamma \leq 0.3$, where $\Gamma = \Omega_0 h \exp(-\Omega_b - \Omega_b/\Omega_0)$, and $\Omega_b = 0.013/h^2$ is the ratio of the mean baryon density to the critical density. The dashed and dotted lines show our estimates from the cluster abundance for $h = 0.8$ and $h = 0.5$ respectively, obtained through the procedure of Section 2.4 with Γ defined as above. The solid lines represent $\pm 8\%$ from the mean of these two curves.

tions (2.17) and (2.18) provides a test of the assumed spectral shape. This test, however, cannot yet be made completely rigorous because the available anisotropy data do not distinguish between contributions from scalar modes which determine the amplitude of the mass fluctuations, and contributions from tensor modes which produce gravitational waves. Furthermore, the asymptotic slope of the mass power spectrum, n, is poorly constrained by the anisotropy data and this introduces further uncertainty in the analysis of the *COBE* results (but not in the cluster abundance argument). As an illustration, Fig. 2.13 compares the estimates of σ_8 presented here with the *COBE* values for the simplest possible case in which n takes the standard value of unity and tensor contributions are neglected. The hatched regions in the figure show *COBE* estimates for $h = 0.8$ and $h = 0.5$, taken from Liddle et al. (1996a) in the open case, and from Liddle et al. (1996b) in the flat case. The dashed and dotted lines give estimates of σ_8 for the same two values of h, derived from the procedure described in Section 2.4, setting $\Gamma = \Omega_0 h \exp(-\Omega_b - \Omega_b/\Omega_0)$ (Sugiyama 1995) and adopting the big bang nucleosynthesis value of $\Omega_b = 0.013/h^2$ (Copi, Schramm & Turner 1995). The cross-hatched areas mark the regions where Γ takes on values in the range $0.2 \leq \Gamma \leq 0.3$, consistent with measurements of the large-scale galaxy distribution (Maddox et al. 1996).

For the open models, there is a fairly wide range in Ω_0 where all three constraints in Fig. 2.13 are compatible, but, for the flat models, consistency between the *COBE* and cluster abundance constraints requires $\Gamma \lesssim 0.15$. Large values of h pick out low values of Ω_0. For $h > 0.5$, $\Omega_0 \gtrsim 0.60$ is ruled out by this test whether or not $\Lambda_0 = 0$. Relaxing the large-scale structure constraint on Γ, $h = 0.8$ requires Ω_0 to be less than 0.26, in the flat case, and less than 0.40 in the open case. For $\Omega_0 = 1$, the *COBE* and cluster abundance results are consistent only if $h = 0.30$ (which gives an acceptable value of Γ). Thus, as noted before by Efstathiou, Bond & White (1992) and White et al. (1993), the abundance of clusters in the standard CDM model ($h = 0.5$) is incompatible with the *COBE* fluctuations unless gravitational waves make a significant contribution to the measured microwave background anisotropies or there is a strong tilt in the primordial spectrum ($n \lesssim 0.8$; Bond 1995).

While the present-day abundance of clusters may be used to determine the value of σ_8 with only a weak dependence on the power spectrum of fluctuations, the evolution of the cluster abundance may be used to set constraints on Ω_0 itself. These depend sensitively on the value of σ_8 and, to a lesser extent, on the shape of the fluctuation spectrum. Here, attention has been restricted, for the most part, to models with spectral shape parameter, $\Gamma = 0.25$, consistent with observations of the large-scale distribution of galaxies (Efstathiou et al. 1992). Since the Ω_0 dependence of the evolutionary rate is so strong, the main effect of changing Γ is through its influence on the model normalization, σ_8. However, as Fig. 2.13 shows, this is a weak effect. Thus, in practice, this test of Ω_0 is insensitive to small departures from the assumed value of Γ. Furthermore, for interesting values of Ω_0, the diagnostics that have been considered here depend only very weakly on Λ_0. Thus, statistical studies of clusters at intermediate redshifts offer an excellent prospect for determining Ω_0 without the complications arising from the uncertain shape of the galaxy power spectrum and the poorly understood relation between the distributions of galaxies

and mass.

Different observables may be used to characterize the evolution of the cluster population. Here, three properties for which observational data are likely to be obtained in the near future have been considered: the distribution of cluster masses, X-ray temperatures and S-Z decrements. The first may be derived from weak gravitational lensing studies; the second from existing and forthcoming X-ray surveys; and the last from ground-based observations and space missions such as *COBRAS/SAMBA*. Although the masses are perhaps the most difficult to measure, they provide a particularly robust test since, apart from the Press-Schechter Ansatz, the only model assumption is the form of the density distribution of dark matter haloes. In rough agreement with N-body simulations, this has been taken to be a singular isothermal sphere. In all cases, the expected distributions at $z = 0.33$ and $z = 0.5$ and the predicted number counts of the largest clusters, both in space and in projection on the sky, as a function of redshift have been presented.

In agreement with previous analyses, it is found that, even at redshifts as low as 0.33, the comoving abundance of clusters with high mass or high X-ray temperature is radically different in universes with $\Omega_0 = 1$ and $\Omega_0 = 0.3$. For example, at this redshift 15 times as many clusters with $M > 3.5 \times 10^{14} h^{-1} \mathrm{M}_\odot$ and 5 times as many clusters with $kT > 5$ keV are predicted to exist if $\Omega_0 = 0.3$ than if $\Omega_0 = 1$. The corresponding factors at $z = 0.5$ are ~ 65 and 10. When integrating these cluster number densities with respect to redshift the effects of the different volume elements are included. Thus, the expected numbers of clusters per square degree on the sky out to redshift 0.5 differ by factors of ~ 6 and 10 for $M > 3.5 \times 10^{14} h^{-1} \mathrm{M}_\odot$ and $kT > 5$ keV respectively in these two cosmologies.

Whereas the mass and temperature functions only evolve dramatically if $\Omega_0 = 1$, the distribution of S-Z decrements (as measured by the Y-function of equation 2.10) declines rapidly with redshift in all cosmologies. This is mainly because, for the range of redshifts considered here, an object far away subtends a smaller angle on the sky than the same object placed nearby. Even so, at $z = 0.33$, the comoving number density of clusters with $Y = 10^{-3} h$ arcmin^2 is 10 times higher if $\Omega_0 = 0.3$ than if $\Omega_0 = 1$. However, the overall abundances at this redshift are all very low because of the rapid decrease in the angular size of the clusters with redshift. The projected counts are dominated by low-redshift clusters and, as a result, the expected excess of clusters with $Y > 10^{-3} h$ arcmin^2 is only $\sim 50\%$ if $\Omega_0 = 0.3$. This excess becomes larger as the Y threshold is lowered and higher redshift clusters are included.

To obtain an estimate of Ω_0 using any of the tests proposed in this chapter requires complete samples of intermediate-redshift clusters selected according to the statistic under consideration. Samples of S-Z clusters are likely to be Y-limited in any case. For the other diagnostics, selecting by X-ray luminosity is probably an efficient method. Since X-ray luminosity correlates reasonably well with X-ray temperature (at least locally), and apparently also with lensing mass (Smail et al. 1996), the sample completeness with respect to the relevant statistic may be determined a posteriori from these data. Incomplete datasets, on the other hand, may be used

to set *upper limits* on Ω_0 because the abundance of clusters at intermediate redshift declines monotonically with increasing Ω_0.

There are already several X-ray bright clusters known at high redshift. For example, Luppino & Gioia (1995) report the detection of six such clusters with $z = 0.5$ in the EMSS survey (Henry et al. 1992). Measurements of their X-ray temperatures would be extremely valuable. They might confirm the indication from velocity dispersion measurements that these clusters are hot, suggesting that Ω_0 is low, or they might show that these velocity dispersions are overestimated as a result of contamination by projection effects. The lowest velocity dispersion reported for these clusters corresponds to a temperature of 6.6 keV. As an illustration, assuming that the effective area surveyed to find these six clusters was 200 square degrees, then one would expect to find < 0.09 clusters above this temperature if $\Omega_0 = 1$; ~ 9 if $\Omega_0 = 0.3$ and $\Lambda_0 = 0.7$; and $\sim$ 45 if $\Omega_0 = 0.3$ and $\Lambda_0 = 0$. However, if the coolest of these clusters actually has a temperature of only 3 keV, then ~ 50 examples are predicted by the model with $\Omega_0 = 1$.

In summary, a statistical sample of X-ray clusters at intermediate redshifts with measured temperatures or S-Z decrements could place a strong constraint on the density parameter Ω_0.

2.7 References

Bahcall N. A., Cen R., 1993, ApJ, 407, L49
Barbosa D., Bartlett J. G., Blanchard A., Oukbir J., 1996, A&A, submitted (astro-ph 9511084)
Bartlett J. G., Silk J., 1993, ApJ, 407, L45
Bartlett J. G., Silk J., 1994, ApJ, 423, 12
Birkinshaw M., Hughes J. P., 1994, ApJ, 420, 33
Bond J. R., 1995, in The Evolution of the Universe, Dahlem Workshop Report ES19, in press (astro-ph 9512142)
Bond J. R., Myers S. T., 1993, in The Evolution of Galaxies and Their Environment. NASA Ames Research Center, p.52
Bond J. R., Cole S., Efstathiou G., Kaiser N., 1991, ApJ, 379, 440
Bryan G. L., Cen R., Norman M. L., Ostriker J. P., Stone J. M., 1994, ApJ, 428, 405
Cen R. Y., Ostriker J. P., 1994, ApJ, 429, 4
Cole S., Lacey C., 1996, MNRAS, 281, 716
Copi C. J., Schramm D. N., Turner M. S., 1995, Science, 267, 192
Couchman H. M. P., 1991, ApJ, 368, L23
Davis M., Efstathiou G., Frenk C. S., White S. D. M., 1985, ApJ, 292, 371
Edge A. C., 1988, PhD Thesis, University of Leicester
Edge A. C., Stewart G. C., Fabian A. C., Arnaud K. A., 1990, MNRAS, 245, 559
Efstathiou G., Bond J. R., White S. D. M., 1992, MNRAS, 258, 1P
Efstathiou G., Davis M., Frenk C. S., White S. D. M., 1985, ApJS, 57, 241

Evrard A. E., 1989, ApJ, 341, L71
Evrard A. E., 1990, ApJ, 363, 349
Evrard A. E., Metzler C. A., Navarro J. F., 1996, ApJ, submitted (astro-ph 9510058)
Fahlman G., Kaiser N., Squires G., Woods D., 1994, ApJ, 437, 56
Forman W. F., Jones C. J., 1990, eds Oegerle, W. R., Fitchett, M. J., Danly, L., Clusters of Galaxies, Cambridge Univ. Press, Cambridge, p.257
Frenk C. S., White S. D. M., Efstathiou G., Davis M., 1990, ApJ, 351, 10
Girardi M., Biviano A., Giuricin G., Mardirosian F., Mezzetti M., 1993, ApJ, 404, 38
Grainge K., Jones M., Pooley G., Saunders R., Edge A., 1993, MNRAS, 265, L57
van Haarlem M. P., Frenk C. S., White S. D. M., 1996, MNRAS, submitted
Hanami H., 1993, ApJ, 415, 42
Hattori M., Matsuzawa H., 1995, A&A, 300, 637
Henry J. P., Arnaud K. A., 1991, ApJ, 372, 410
Henry J. P., Gioia I. M., Maccacaro T., Morris S. L., Stocke J. T., Wolter A., 1992, ApJ, 386, 408
Jing Y. P., Fang L. Z., 1994, ApJ, 432, 438
Kaiser N., Squires G., 1993, ApJ, 404, 441
Kochaneck C. S., 1995, ApJ, 453, 545
Lacey C., Cole S., 1993, MNRAS, 262, 627
Lacey C., Cole S., 1994, MNRAS, 271, 676
Lahav O., Edge A. C., Fabian A. C., Putney A., 1989, MNRAS, 238, 881
Lahav O., Lilje P. B., Primack J. R., Rees M. J., 1991, MNRAS, 251, 128
Liddle A. R., Lyth D. H., Roberts D., Viana P. T. P., 1996a, MNRAS, 278, 644
Liddle A. R., Lyth D. H., Viana P. T. P., White M., 1996b, MNRAS, 282, 281
Lilje P. B., 1992, ApJ, 386, L33
Luppino G. A., Gioia I. M., 1995, ApJ.Lett, 445, L77
Maddox S. J., Efstathiou G., Sutherland W. J., Loveday J., 1990, MNRAS, 242, 43P
Maddox S. J., Efstathiou G., Sutherland W. J., 1996, MNRAS, submitted
Maoz E., 1990, ApJ, 359, 257
Markevitch M., Mushotzky R., Inoue H., Yamashita K., Furuzawa A., Tawara Y., 1996, ApJ, 456, 437
Mather J. C., et al. , 1994, ApJ, 420, 439
Mazure A., et al. , 1996, A&A, 310, 31
Navarro J. F., Frenk C. S., White S. D. M., 1995, MNRAS, 275, 720
Oukbir J., Blanchard A., 1992, A&A, 262, L21
Peebles P. J. E., 1980, The Large Scale Structure of the Universe. Princeton Univ. Press, Princeton, NJ
Peebles P. J. E., 1984, ApJ, 284, 439
Press W. H., Schechter P., 1974, ApJ, 187, 425
Seitz C., Schneider P., 1995, A&A, 297, 287
Smail I., Ellis R. S., Dressler A., Couch W. J., Oemler A., Butcher H., Sharples R. M., 1996, ApJ, submitted
Sugiyama N., 1995, ApJS, 100, 281
Sunyaev R. A., Zel'dovich Ya. B., 1972, Comm. Astrophys. Space Phys. 4, 173
Tsai J. C., Katz N., Bertschinger E., 1994, ApJ, 423, 553

Viana P. T. P., Liddle A. R., 1996, MNRAS, 281, 323
White S. D. M., Efstathiou G., Frenk C. S., 1993, MNRAS, 262, 1023
Wilbanks T. M., Ade P. A. R., Fischer M. L., Holzapfel W. L., Lange A. E., 1994, ApJ, 427, L75
Wilson G., Cole S., Frenk C. S., 1996, MNRAS, 280, 199
Zabludoff A. I., Huchra J. P., Geller M. J., 1990, ApJS, 74, 1

Chapter 3

Constraints on Ω_0 from cluster evolution

3.1 Introduction

As shown in the previous chapter, the evolution of the population of galaxy cluster dark matter haloes, both predicted by the Press–Schechter equation (2.1) and measured in numerical simulations, discriminates strongly amongst CDM universes with different mean matter densities. In this chapter, the theoretical predictions are compared with the presently available observations of very massive clusters at high redshifts in order to constrain the value of Ω_0.

Given that they are the largest virialised structures in the universe, it might seem surprising that the identification of galaxy clusters is a non-trivial task. The pioneering work of Abell (1958) served both to stimulate this field of study and to illustrate some of the difficulties. In it, clusters were defined as overdensities in the projected two-dimensional galaxy distribution. The size of each cluster was described by its *richness*, defined as the number of galaxies within two magnitudes of the third brightest galaxy, after subtracting a mean background, within a projected circle centred on the peak overdensity. This 'counting circle' defines a cone of volume in which all galaxies contribute to the total. To calculate the opening angle for each cone, the absolute magnitude of the tenth brightest galaxy within the cone was assumed to be a standard candle and an angle corresponding to a cluster radius of $1.5\,h^{-1}$Mpc was chosen. This iterative procedure was used to produce a list of cluster candidates. As has been noted by many authors (e.g. Lucey 1983; Frenk et al. 1990; van Haarlem, Frenk & White 1996) including Abell himself, this definition of clusters can lead to the inclusion of spurious clusters which merely appear because physically distinct objects along a line-of-sight have been associated with each other. More recent catalogues of optically-selected clusters have used machine-generated galaxy catalogues and automated cluster-finding algorithms with smaller counting circles in an attempt to avoid such misidentifications (e.g. Lumsden et al. 1992; Dalton

et al. 1992). However, these catalogues still quantify the sizes of clusters using richness, a variable that is not readily related to the dark matter haloes described by Press–Schechter theory.

An alternative method for identifying galaxy clusters is to search for extended X-ray sources, because hot intracluster gas emits bremsstrahlung radiation profusely at these wavelengths. Early X-ray surveys were made by instruments having large beam-widths and simple proportional counters. Consequently the ability to discriminate between clusters and other X-ray sources, active galactic nuclei (AGN) for example, was limited. Nevertheless, a number of Abell clusters were detected (e.g. Kellogg & Murray (1974) using *UHURU* data (Giacconi et al. 1974) and *HEAO-1 A-2* (Piccinotti et al. 1982)). Later satellite X-ray observatories were equipped with position sensitive proportional counters, and this imaging capability significantly reduced the problem of cluster identification. The *Einstein* X-ray observatory was one such mission. From the Extended Medium Sensitivity Survey (EMSS, Gioia et al. 1990) that it returned, Henry et al. (1992) produced a flux-limited sample of clusters with the furthest at a redshift of 0.58. Given an X-ray flux-selected catalogue of clusters, the two X-ray properties used to describe the sizes of the clusters are luminosity and temperature. As it takes more photons to measure a temperature than it does to find a broad-band luminosity, the study of how the cluster temperature function evolves has had to wait for satellites with detectors that are more sensitive and have better spectral resolution such as *ASCA* (e.g. Markevitch et al. 1996). Evolution of the luminosity function, on the other hand, has probably been detected; the space density of very luminous clusters seems smaller at high redshifts than nearby (Edge et al. 1990; Henry et al. 1992; Bower et al. 1994). In the next section, this evidence will be used in conjunction with Press-Schechter theory to attempt to constrain Ω_0.

Other methods that can be utilised to measure cluster sizes include gravitational lensing and the S–Z (Sunyaev & Zel'dovich 1972) effect. Lensing techniques provide an estimate of the projected mass surface density by measuring the shear distortion of faint background galaxies. This requires good angular resolution and long integration times and, as a consequence, only pointed observations of already identified clusters have been carried out (for example see Smail & Dickinson 1995). The S–Z effect, namely the distortion of the microwave background radiation by inverse Compton scattering off hot electrons associated with intracluster gas, provides an observable which is proportional to the product of cluster mass and temperature. Long integration times are also required so, to date, only a few clusters have been detected (e.g. Grainge et al. 1993), although future space missions such as *MAP* (Bennett et al. 1995) and *COBRAS/SAMBA* (Tauber, Pace & Volonte 1994) may provide surveys of more representative patches of sky.

In Section 3.2 the extent to which X-ray luminous clusters evolve is investigated with a view to discriminating between different cosmologies. Methods to set an upper limit on Ω_0 using pointed observations of large clusters at high redshift are considered in Section 3.3. Section 3.4 contains the conclusions from these exercises.

3.2 Constraining Ω_0 using the number of very X-ray luminous high-redshift clusters

Edge et al. (1990), Henry et al. (1992) and Bower et al. (1994) have all claimed that the space density of high-luminosity X-ray clusters was lower in the past. More recently Nichol et al. (1996) have produced a qualitatively similar result, although at a lower significance. This evolution is in the opposite sense to the one predicted by Kaiser (1986) using simple scaling relations. Various models have been proposed in order to explain the observed evolution, such as mergers of subclusters (Edge et al. 1990) or constant entropy cores in clusters (Evrard & Henry 1991). It seems fair to say that the detailed thermal history of the intracluster gas is not yet sufficiently well understood to discriminate between these different scenarios. Unfortunately, given that the bremsstrahlung emissivity depends on the square of the local gas density, the cluster X-ray luminosity may be expected to depend on the detailed history of the gas. Nevertheless it is still informative to calculate how many $0.4 < z < 0.6$ clusters the Press-Schechter theory, normalised by the local temperature function, predicts that the *EMSS* should have found in different cosmologies. The main purpose of focussing on high redshifts is to maximise the difference between the cosmological models.

3.2.1 The cluster sample

The flux-limited *EMSS* is described by Gioia et al. (1990) and the cluster sample is given in Henry et al. (1992) and updated in Gioia & Luppino (1994). For completeness, the pertinent features of the catalogue are repeated here. The 2.4×2.4 arcmin^2 detect cell flux derived from the measured count rate must be at least 1.33×10^{-24}J m^{-2} s^{-1} in the $0.3 - 3.5$ keV waveband. The flux is determined after removing the contribution from any known point sources, allowing for galactic hydrogen extinction and assumes a 6 keV thermal spectrum. These restrictions left 733 of the original 835 *EMSS* sources. Henry et al. identified all but twelve of these, yielding 93 clusters, 5 of which had redshifts in the range $0.4 < z < 0.6$, the interval that will be considered here. Gioia & Luppino later found that one of these five was in fact two distinct clusters and one of the unidentified sources was also a cluster in this redshift interval. This gives a total of seven clusters in the subsample. Since the extent of the cluster emission generally exceeds the size of the detect cell, an additional factor is required to convert the detect cell flux into a total cluster flux. This factor is a function of both cluster radius and redshift. However, fig. 1 of Henry et al. shows that for $0.4 < z < 0.6$ the ratio of total cluster flux to detect cell flux can be reasonably described by a constant in the range $[1.5, 2.0]$. A final complication is that the area of sky surveyed varied with sensitivity, i.e. only a small fraction of the total survey area was observed at the maximum sensitivity. Using the data from table 3 in Henry et al., the following expression has been found to give the area of sky surveyed, A, to within 10% at all detect cell fluxes:

$$A(f_{\rm det}) = A_{\rm tot}(1 - 3.05\,\exp(-0.41 f_{\rm det}) + 2.30\,\exp(-0.77 f_{\rm det})), \qquad (3.1)$$

where $f_{\rm det}$ is the detect cell flux in units of 10^{-24}J m^{-2} s^{-1} and $A_{\rm tot}$ is the total area available, 735 square degrees.

3.2.2 Predicting the expected number of clusters in the *EMSS* with $0.4 < z < 0.6$

In order to compare the number of clusters selected above with a prediction based upon the Press-Schechter formalism it is necessary to convert virial mass to a luminosity in the relevant waveband. The method that has been adopted to perform this transformation involves using equation (2.2) to map mass to temperature and then converting to luminosity using the $L_{\rm x} - T_{\rm x}$ relation derived from low-redshift cluster data. This procedure implicitly assumes that clusters with a particular mass all have exactly the same temperature, and that the expression relating temperature to luminosity is independent of redshift. Preliminary data from the *ASCA* satellite (Tsuru et al. 1996) suggest that this second assumption provides a reasonable approximation for a sample of 17 clusters with $0.14 < z < 0.55$. The data are also consistent with an increase in the mean $2 - 10$ keV luminosity at a given temperature at higher redshift, but by not more than about 50%. The redshift zero $L_{\rm x} - T_{\rm x}$ relation, shown in Fig. 3.1, was constructed using the 25 clusters listed by Henry & Arnaud (1991). Luminosities were converted from the quoted bolometric values to the required $0.3 - 3.5$keV ones assuming an optically thin 5keV plasma and the *mekal* model (see Mewe, Gronenschild & van den Oord, G.H.J. 1985) provided in the *XSPEC* software. As can be seen from the figure, there is considerable scatter about the best-fitting power law, given by

$$\log_{10} L_{41} = 3.54 \log_{10}(kT) - 2.53, \tag{3.2}$$

where L_{41} is the $0.3 - 3.5$keV luminosity measured in $10^{41} h^{-2}$ J m^{-2} s^{-1} and kT is in units of keV. This fit results from a simple χ^2 minimisation assuming that the luminosity errors are negligible compared with the uncertainties in the temperatures. Both the fitted slope and intercept have formal 1σ uncertainties of $\sim 4\%$, but a straight line does not provide a very good fit to the data. The scatter (assumed to be Gaussian) in $\log_{10} L_{41}$, which the outliers with small error bars suggest is intrinsic to the cluster population rather than just experimental, was parametrised by

$$\sigma_{\log_{10} L_{41}} = 0.69 - 0.47 \log_{10}(kT) \tag{3.3}$$

and is shown by the dashed lines in the figure. This was calculated by measuring the dispersions of the coldest and hottest ten clusters about the mean relation and using these two points to define the line.

With these tools in place, the operation to estimate how many $0.4 < z < 0.6$ clusters are expected in the *EMSS* is readily explained. A list of cluster temperatures and redshifts consistent with Press-Schechter theory (which also predicts the number of clusters in the list) is produced for an area of 735 square degrees i.e. the whole survey area. Each temperature is then turned into a luminosity using

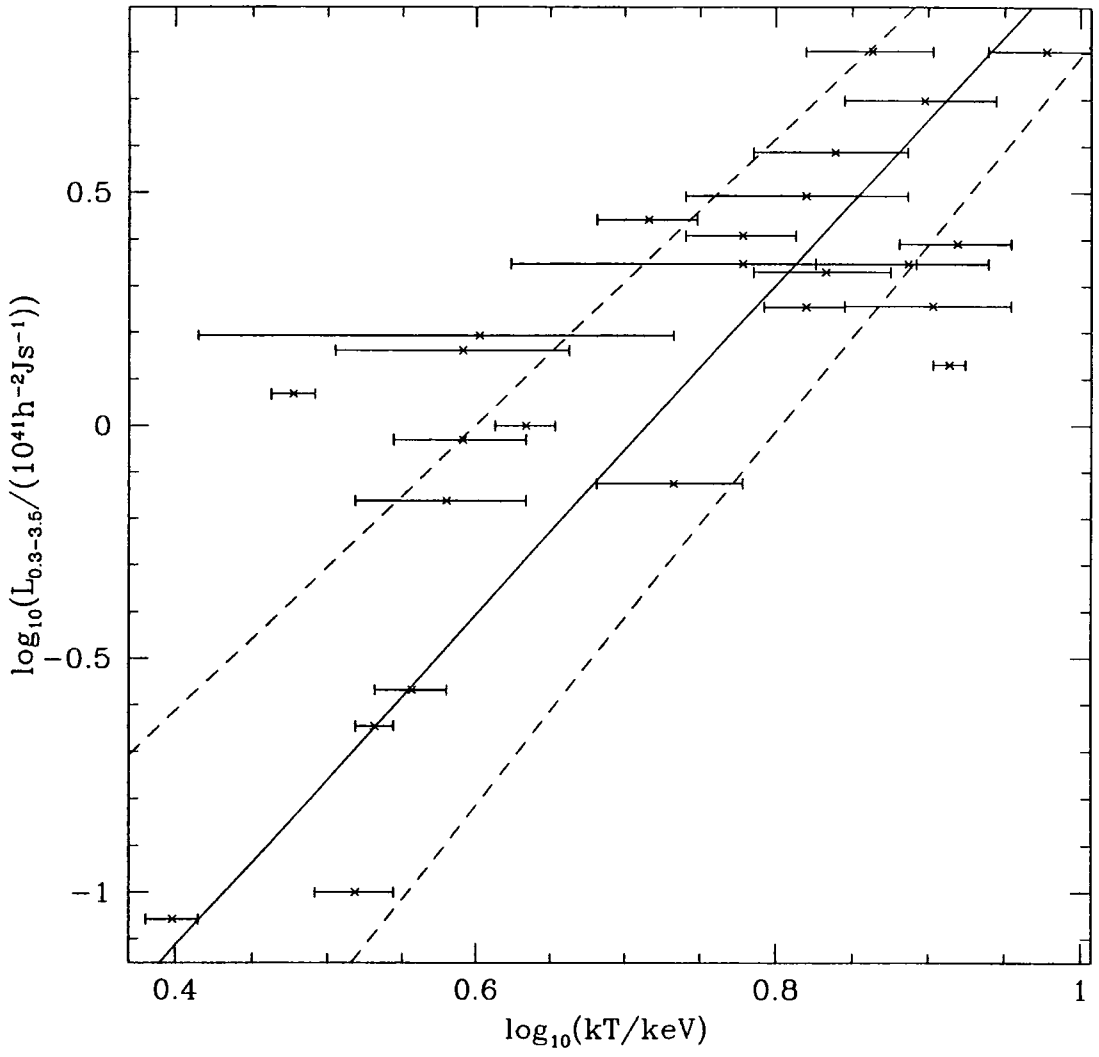

Figure 3.1: The cluster luminosity–temperature relation found from the 25 clusters listed by Henry & Arnaud (1991). The best-fitting power law is shown with a solid line and the dotted lines on either side represent the 1σ scatter given by equation (3.3).

equation (3.2) including, by randomly choosing from a Gaussian distribution with standard deviation σ, the scatter given by equation (3.3). The combination of luminosity, redshift and cosmology imply a flux through the luminosity-distance relation. If, for the chosen ratio of total to detect cell fluxes, $f_{\rm clus}/f_{\rm det}$, this corresponds to a flux exceeding the detect cell limit, then the cluster is counted with a probability $A(f_{\rm det})/A_{\rm tot}$ to take into account the flux-dependent sky coverage. Twenty realisations of each cosmology were produced in order to reduce the statistical noise in the predicted number of clusters.

3.2.3 Results

The expected number of clusters as a function of $f_{\rm clus}/f_{\rm det}$ is shown for three different cosmologies in Fig. 3.2. The cross illustrates the *EMSS* measurement, with the horizontal error representing the uncertainty in the conversion from cluster flux to detect cell flux as described in the previous subsection and the vertical error bar showing $\pm\sqrt{7}$. The three lines illustrate results for, from bottom to top, $\Omega_0 = 1$, $\Omega_0 = 0.3$ with $\Lambda_0 = 0.7$ and $\Omega_0 = 0.3, \Lambda_0 = 0$. Whilst all models overpredict the observed number of clusters, the high-density cosmology is significantly closer than the low-Ω_0 models. These overpredict the number of clusters by factors of ~ 8 and 10 for the $\Lambda_0 = 0.7$ and $\Lambda_0 = 0$ models respectively. This result would appear to provide a conflict between the low density models and the *EMSS* measurement, despite the uncertainty in the conversion from $f_{\rm clus}$ to $f_{\rm det}$ giving rise to a factor of two change in the predicted number of clusters. However, the assumptions and uncertainties need investigation before the significance of this result can be more strongly quantified. Changing the best-fitting parameters of the redshift-zero $L_{\rm x} - T_{\rm x}$ relation by 4% produces a negligible change in the predicted number of clusters. The tentative evidence concerning the evolution of this relation would, if anything, suggest that even more bright objects should be seen at high redshifts thus strengthening the rejection of all the models.

Fig. 3.3 illustrates the affect of varying σ_8 and the amplitude of the $L_{\rm x} - T_{\rm x}$ scatter. Horizontal lines give the *EMSS* observation and a value at $3\sqrt{7}$ above this. The other solid lines show the $\Omega_0 = 0.3$, $\Lambda_0 = 0$ model predictions assuming $L_{\rm x} - T_{\rm x}$ dispersions given by equation (3.3) and 80% of this amplitude. These lines are interpolations between the calculated points represented with crosses. For both cases a ratio of $f_{\rm clus}/f_{\rm det} = 2$, i.e. on the conservative side, has been adopted. A dotted curve is provided to show the probability that σ_8 is less than a particular value for the best-fitting Gaussian $\sigma_8 = 0.873 \pm 0.067$ found in Chapter 2.

It can be seen for the full $L_{\rm x} - T_{\rm x}$ scatter that, while the best-fitting σ_8 produces ten times too many clusters, a value of $\sigma_8 \approx 0.70$ gives a number consistent with the *EMSS* measurement. The probability of σ_8 being at least as small as this, if the error really has a Gaussian distribution, is $\sim 1\%$. With the lower scatter in the $L_{\rm x} - T_{\rm x}$ relation, the largest tolerable value of σ_8 becomes about 0.77 and this implies that the model is ruled out only about 90% of the time. The reason for the dramatic decrease in clusters when the scatter is reduced by a relatively small amount is that

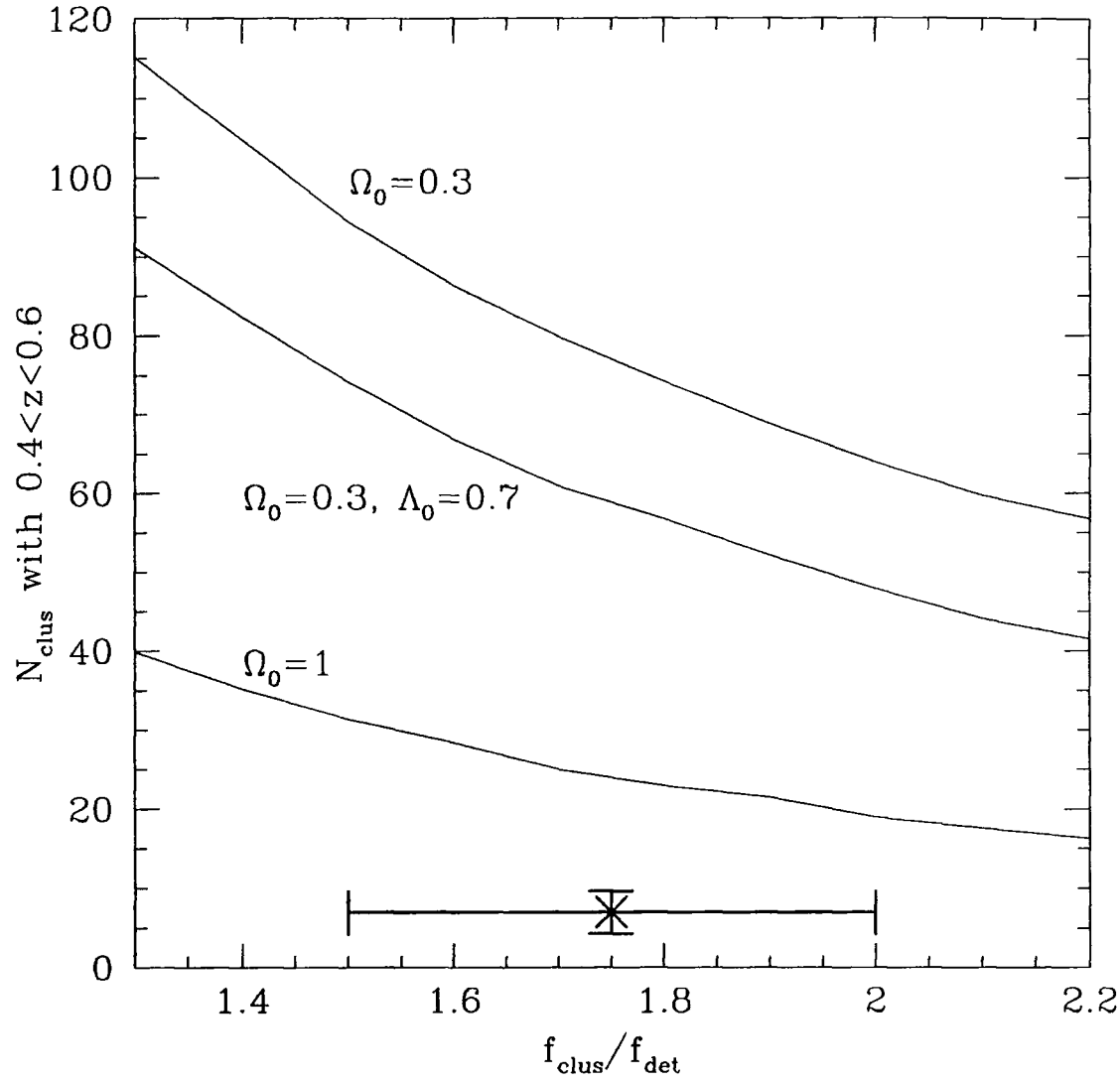

Figure 3.2: The predicted and observed numbers of clusters with redshifts $0.4 < z < 0.6$ in the *EMSS* catalogue as a function of the ratio of the total cluster flux to the detect cell flux (assumed to be the same for all clusters). Each of the three lines corresponds to a different cosmology: $\Omega_0 = 1$ - bottom; $\Omega_0 = 0.3, \Lambda_0 = 0.7$ - middle; $\Omega_0 = 0.3, \Lambda_0 = 0$ - top. The cross represents the seven observed clusters with an estimate of the uncertainty in f_{clus}/f_{det} obtained from fig. 1 of Henry et al. (1992). For the amplitude of the vertical error bar, the square root of the observed number of clusters is used.

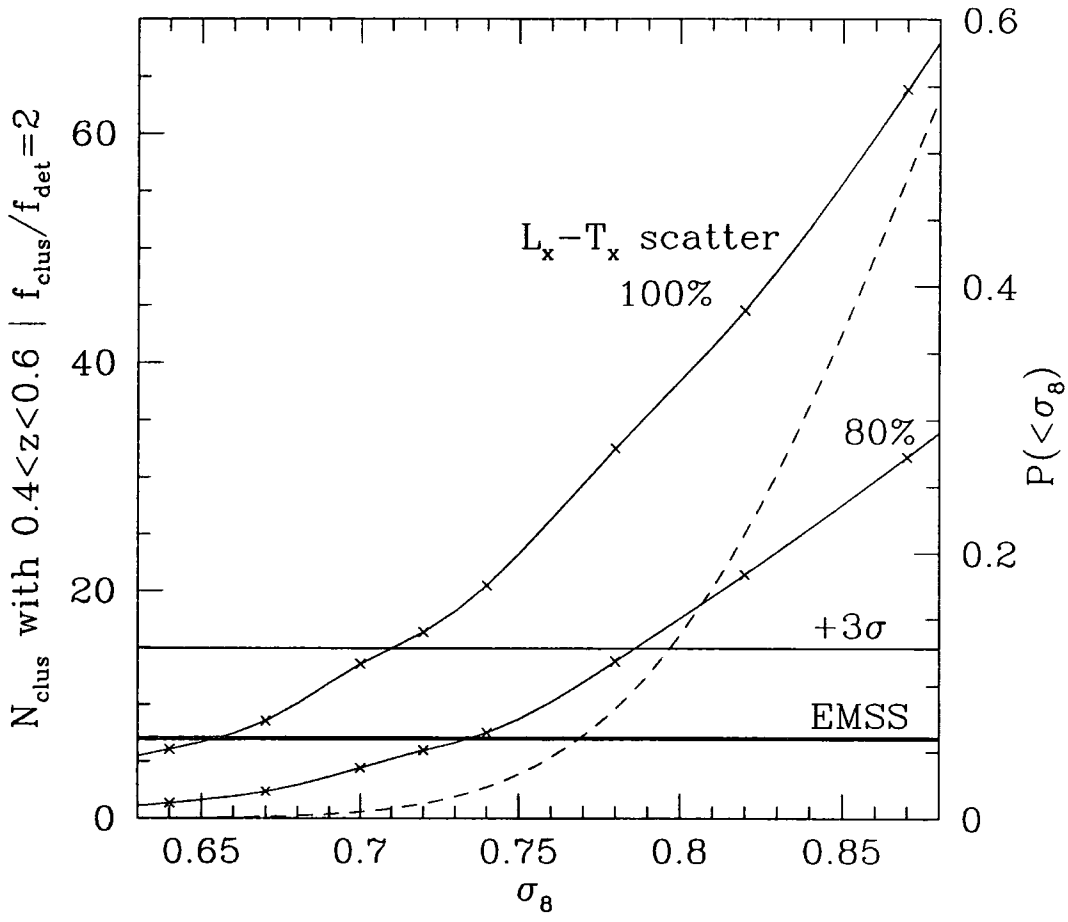

Figure 3.3: Dependence on σ_8 of the estimated number of clusters with $0.4 < z < 0.6$ in the *EMSS* for the $\Omega_0 = 0.3$ and $\Lambda_0 = 0$ model. The bold horizontal line shows the *EMSS* result of 7 clusters and the other horizontal line is drawn at 3σ (assuming Poisson counting statistics) above this. Solid lines represent the model predictions when the $L_x - T_x$ scatter given in equation (3.3) is used and when it is only 80% of the fitted value. The dashed line (which refers to the scale on the right-hand axis) shows the integral of a Gaussian with mean 0.873 and standard deviation 0.067 from $-\infty$ to σ_8. This represents the probability that σ_8 is less than a particular value.

the objects which contribute to the total number of observed clusters in this high redshift range are largely composed of those which have luminosities that are a few σ above the mean expected value given their temperatures. Decreasing the size of the scatter in the luminosity-temperature relation slightly will drastically reduce the number of objects in the high-luminosity tail of the distribution. If $f_{\rm clus}/f_{\rm det} = 1.7$ is assumed instead of 2 then the maximum σ_8 producing less than ~ 15 clusters is decreased by approximately 0.02 in both cases.

3.2.4 Conclusions

If the shape of the error distribution in the best-fitting σ_8 was quantified better and the scatter about the relation converting from temperature to luminosity was known more accurately, then the above procedure might be able to produce a very significant constraint on Ω_0. This would still be the case if the scatter in the $L_{\rm x} - T_{\rm x}$ equation was large, as long as it was well defined. As it is, whilst the assumptions adopted here have favoured the $\Omega_0 = 1$ model with its rapid decline in the number density of large clusters with increasing redshift, the statistical significance of the rejection of an open $\Omega_0 = 0.3$ cosmology is only about 95%. At the very least, a method has been proposed which uses the observed luminosity function evolution to constrain Ω_0.

3.3 Constraining Ω_0 using pointed observations of very massive high-redshift clusters

It is often the case that the discovery of a large and distant galaxy cluster will be accompanied by a claim concerning how such an object provides a powerful test of competing cosmological scenarios. In this section, the Press-Schechter formalism underlying Chapter 2 will be employed to quantify the probabilities of finding particular rare objects at high redshifts. It should be noted that the methods described in this section rely upon the Press-Schechter formalism being a good description of the abundance of very hot clusters at high redshifts for an $\Omega_0 = 1$ universe. Given that the volume simulated in order to compare numerical results with the Press-Schechter expression in Chapter 2 was only large enough to contain a few ~ 5 keV clusters at $z = 0.5$, this assumption should be viewed as an extrapolation and treated with the corresponding caution. Of course, with simulations of larger volumes the need to extrapolate could be removed.

3.3.1 A procedure to calculate the probability of finding a single rare cluster

Donahue (1996) reports the existence of a 10.4 ± 1.2 keV cluster at redshift 0.54. The temperature estimate comes from recent *ASCA* data. If in the $\Omega_0 = 1$ model all clusters at least as hot as this formed only at redshifts lower than 0.5, then this observation would rule out this model. Using the Press-Schechter theory, the expected number of clusters having $kT > 10.4$ keV and $z > 0.54$ can be predicted and an upper limit placed on Ω_0. As this cluster has been specifically targeted for observation, it is difficult to define the area of sky over which the Press-Schechter prediction should be made. For a conservative estimate, it has been assumed that this cluster has been found as a result of a whole-sky survey. This sets an upper limit to the expected number of clusters. Throughout this section, it will be assumed that the entire 4π steradians have been searched in order to find the rare clusters.

The two crucially important measurements when asking how many clusters Press-Schechter theory predicts should be observed above a given temperature and redshift for a particular cosmology are the temperature and the normalisation of the mass fluctuation spectrum, σ_8. Whilst the redshift is normally determined accurately, the temperature is not usually known to much better than $\sim 10\%$ accuracy. As the abundance of clusters is such a sensitive function of temperature, this measurement error needs to be taken into account. Fig. 3.4 shows the result of a simple marginalisation procedure where the probability of finding at least one cluster above $kT_{\rm det}$ is weighted by the probability that the actual temperature of the cluster is $kT_{\rm clus}$. The probability distribution of $kT_{\rm det}$ has been taken to be a symmetric Gaussian (mean 10.4 keV, standard deviation 1.2 keV) and is shown by the dashed line in the upper panel. A solid line shows the abundance of $z > 0.54$ clusters as a function of $kT_{\rm clus}$ in an $\Omega_0 = 1$ cosmology. Taking this quantity to be the mean number of clusters in the whole sky, a, above $kT_{\rm clus}$ and with $z > 0.54$ and using Poissonian statistics, the probability of finding at least one such object can be written as

$$P(>0) = 1 - P(0) = 1 - \exp(-a). \tag{3.4}$$

The full line in the lower panel of Fig. 3.4 illustrates this probability. A dashed line is used to represent the following integral

$$P(>0, kT) = \int_0^{kT} P(>0 \mid > x) \frac{1}{\sqrt{2\pi}1.2} \exp\left(-\frac{1}{2}\left(\frac{x-10.4}{1.2}\right)^2\right) \mathrm{d}x, \tag{3.5}$$

where x is in keV. The total probability of finding at least one cluster in the whole sky having $kT > 10.4 \pm 1.2$ keV and $z > 0.54$, given by the limit of $P(>0, kT)$ as $kT \rightarrow \infty$, is ~ 0.04. This is sufficiently small to be on the verge of being interesting. However, the dependence of abundance on σ_8 has not yet been folded in to the calculation and the very reason that the cluster temperature function is a useful tool for measuring σ_8 is that a small change in the normalisation gives a large variation in the predicted cluster abundance. Fig. 3.5 shows probability contours, again for $\Omega_0 = 1$, with the dotted lines being the product of the Gaussian temperature distribution with the Gaussian distribution $\sigma_8 = 0.52 \pm 0.04$. The solid

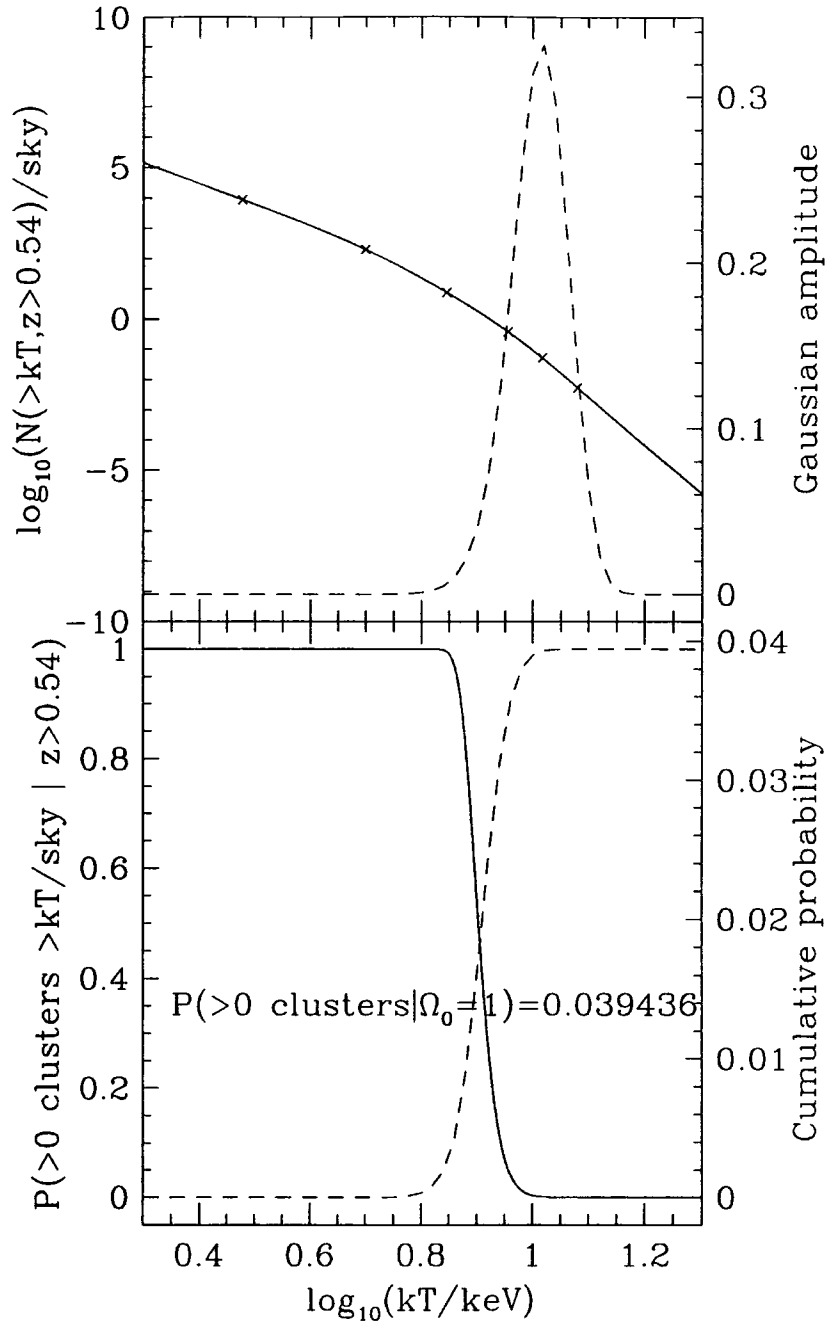

Figure 3.4: The *upper panel* shows the cumulative abundance of clusters hotter than a particular temperature and at redshift higher than 0.54 for the $\Omega_0 = 1$ cosmology. A spline has been used to interpolate (and extrapolate) between the calculated points which are shown with crosses. The dashed line represents a Gaussian probability distribution with a mean temperature of 10.4keV and $\sigma = 1.2$keV. In the *lower panel*, the full line represents the probability of finding at least one cluster hotter than $kT_{\rm clus}$ and with redshift larger than 0.54 in the whole sky. The integral with respect to temperature of the product of this full line and the Gaussian in the upper panel is shown by the dashed line.

contours correspond to the product of this two-dimensional probability density with the probability of finding at least 1 cluster in the whole sky above a particular kT given the value of σ_8. (Contour levels are given in the figure caption.) Integrating under the surface defined by the full lines gives the final marginalised probability of 0.22 for finding at least one $kT > 10.4 \pm 1.2$ keV cluster above $z = 0.54$ given that $\Omega_0 = 1$ and $\sigma_8 = 0.52 \pm 0.04$. This value is sufficiently large that it provides essentially no useful rejection of this cosmology. The maximum probability contour levels occur at $\sigma_8 \approx 0.56$ and an additional concern about the validity of this method must be that it is not clear what shape the error in the best-fitting value of σ_8 should take.

3.3.2 Using order statistics

Basing a conclusion on the observation of a single cluster is not an ideal situation. However, when a test relies on finding extreme objects in order to rule out a model which does not produce them, then it is inevitable that such a problem will arise. In this subsection, some rather more reliable statistics, still relating to rare clusters, are explored. This will involve using order statistics in conjunction with Press-Schechter theory in order to give the redshift distribution of hot clusters.

From the Press-Schechter expression, it is possible to calculate the redshift distribution of all clusters hotter than a particular value given a cosmology and normalisation amplitude. The probability that, from the population of clusters hotter than a particular temperature, a cluster is situated at a redshift less than z will be denoted by $P(< z)$. Using this notation the probability that the furthest cluster (at z_1) has a redshift at least greater than z can be written

$$P(z_1 \geq z) = 1 - P(z_1 < z) = 1 - (P(< z))^{N_{\rm clus}}, \tag{3.6}$$

where $N_{\rm clus}$ is the total number of clusters above the chosen temperature limit in the whole universe, given by Press-Schechter. Clearly, for a particular redshift distribution, larger $N_{\rm clus}$ will probe further into the tail of the distribution and z_1 will be expected to be larger. This effect is shown in Fig. 3.6 where $N_{\rm clus}$ is increased by a factor of 100 and the median z_1 then increases from about 0.3 to 1 for all clusters hotter than 9 keV (for example) in an $\Omega_0 = 1$ universe with $\sigma_8 = 0.60$.

This procedure can be extended to give the redshift distributions of the kth furthest clusters as follows. As in equation (3.6), the probability that the kth futhest cluster has a redshift greater than or equal to a particular value is given by

$$P(z_k \geq z) = 1 - P(z_k < z). \tag{3.7}$$

Now the probability that z_k is less than z needs to take into account the various combinations of clusters which could allow this to be the case. This probability can then be written, using the combination function C, as

$$P(z_k < z|N_{\rm clus}) = \sum_{j=0}^{k} {}^{N_{\rm clus}}C_j \; P(< z)^{N_{\rm clus}-j}(1 - P(< z))^j \tag{3.8}$$

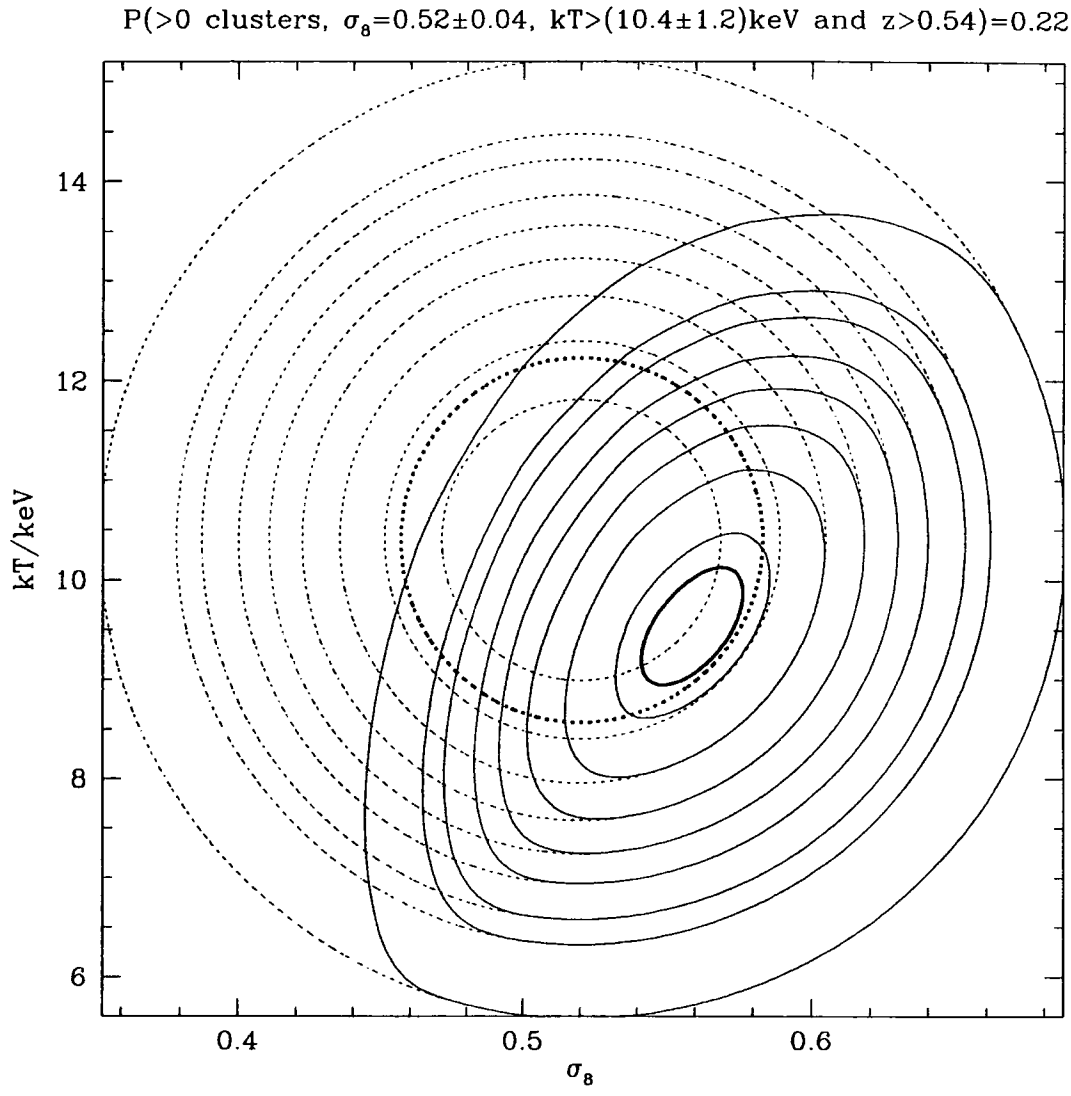

Figure 3.5: The dotted lines join points of equal probability and the solid lines give the product of the two Gaussians producing the dotted contours and the probability of finding at least one cluster in the whole sky with $z > 0.54$ given a temperature $> kT$ and σ_8. The contour levels are 0.001, 0.01, 0.02, 0.05, 0.1, 0.2, 0.4, 0.8, 1.0 (bold) and 1.6. The integral under the surface defined by the solid contours equals the overall probability of finding the cluster.

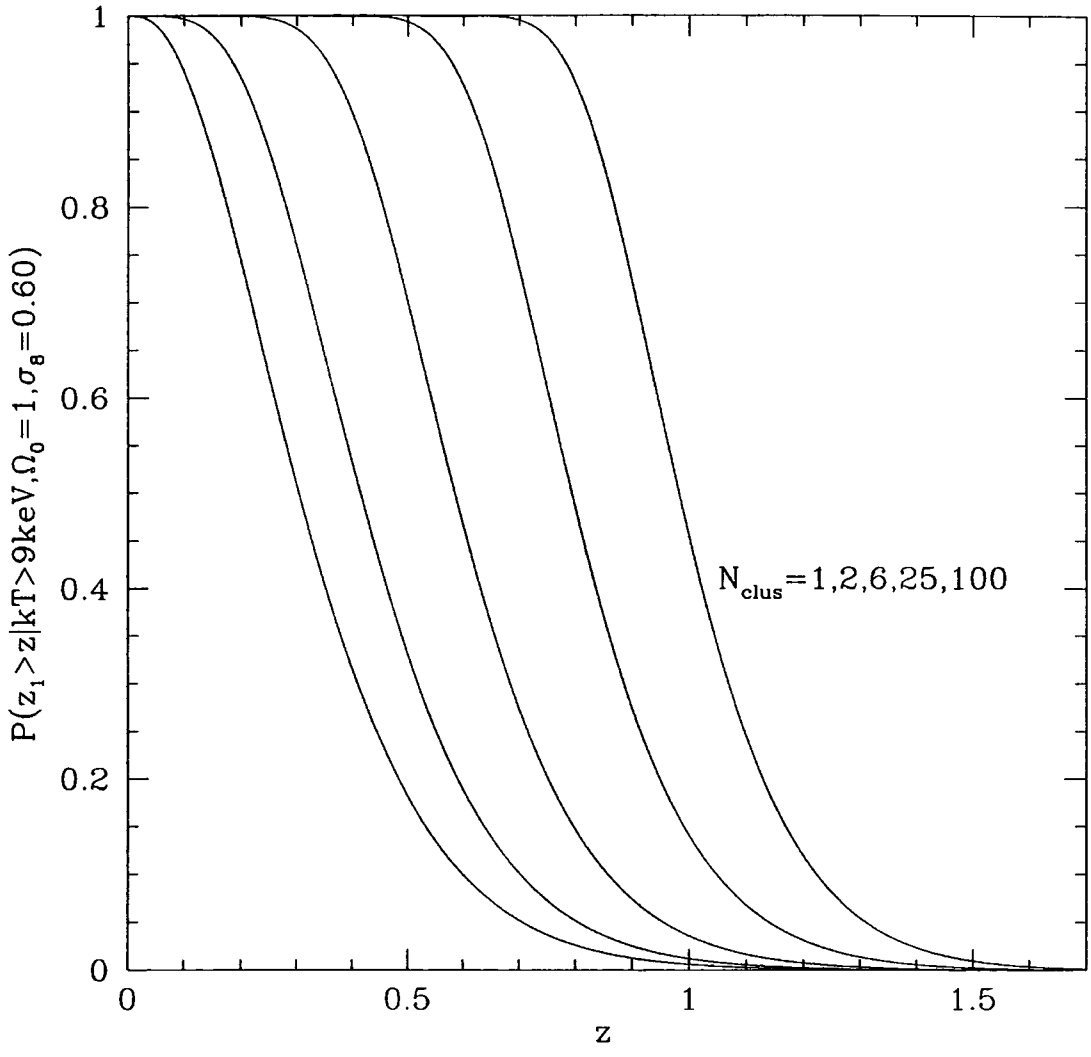

Figure 3.6: The dependence of the maximum redshift z_1 on the number of clusters used to sample the redshift distribution of clusters hotter than 9 keV in an $\Omega_0 = 1$, $\sigma_8 = 0.60$ universe. Larger values of $N_{\rm clus}$ produce larger values of z_1.

and this, combined with equation (3.7) gives $P(z_k \geq k)$. (It should be noted that the Poissonian approximation used in the previous subsection is equivalent to this binomial expression.) Fig. 3.7 illustrates how the different cosmologies, and the value of σ_8 affect the redshift distribution of the third furthest cluster which is hotter than 9 keV. These clusters are sufficiently common in the $\Omega_0 = 0.3$ models with and without a Λ_0 term (shown with dashed and dotted lines respectively) that the redshifts at which these clusters exist stretch well out of the range of present observational techniques. However, for the high density model, any $kT >$ 9 keV clusters at redshifts greater than ~ 0.5 should start to provide a constraint. The two full lines correspond to $\sigma_8 = 0.52$ and 0.60 with the higher normalisation approximately doubling the redshifts at which the third furthest cluster is predicted to exist. Given this rapid variation with normalisation, a marginalisation procedure similar to those adopted in the previous subsection is required. Fig. 3.8 shows the Gaussian uncertainty in σ_8 and a dashed line depicts the probability that the third furthest $kT > 9$ keV cluster is at a redshift greater than one, as a function of the normalisation. Integrating the product of these two curves gives rise to an overall probability of 0.005 for the third furthest cluster being at a redshift of at least 1.

This procedure can now be extended to include errors on temperature measurements and this involves a two-dimensional marginalisation at each separate redshift. The results of such an operation are shown in Fig. 3.9. Both the probability of finding the furthest and third furthest clusters hotter than $kT > 10 \pm 1$ keV at redshifts greater than z are illustrated. At present, only the cluster $MS0451 - 03$ with redshift 0.54 and temperature 10.4 ± 1.2 keV (Donahue 1996) satisfies the temperature constraint. Fig 3.9 shows that the probability that the furthest $kT > 10 \pm 1$ keV cluster is at $z > 0.54$ is about 25% (cf the result from the previous subsection). If an additional two similarly distant and hot clusters were found, then this probability would drop beneath 10% improving the constraint on the $\Omega_0 = 1$ model. As the observations stand, insufficient rare clusters have been found in order to reject the $\Omega_0 = 1$ model to any great significance.

3.3.3 Conclusions

Two different techniques for setting an upper limit on Ω_0 have been described. One difficulty in the methods employed is the lack of knowledge of the fraction of sky observed. Adopting the conservative approach that all 4π steradians have been surveyed to find the 'rare' objects inevitably weakens the tests. An additional worry is that the numerical simulations described in Chapter 2 do not contain enough volume to test whether or not Press-Schechter theory provides an adequate description of the abundance of $kT > 8$ keV clusters at redshifts greater than about 0.5 in an $\Omega_0 = 1$ cosmology.

In summary, presently available data coupled with the uncertainties in σ_8 and in the adequacy of the Press-Schechter expression for describing very massive clusters at high redshifts are incapable of ruling out the $\Omega_0 = 1$ cosmology.

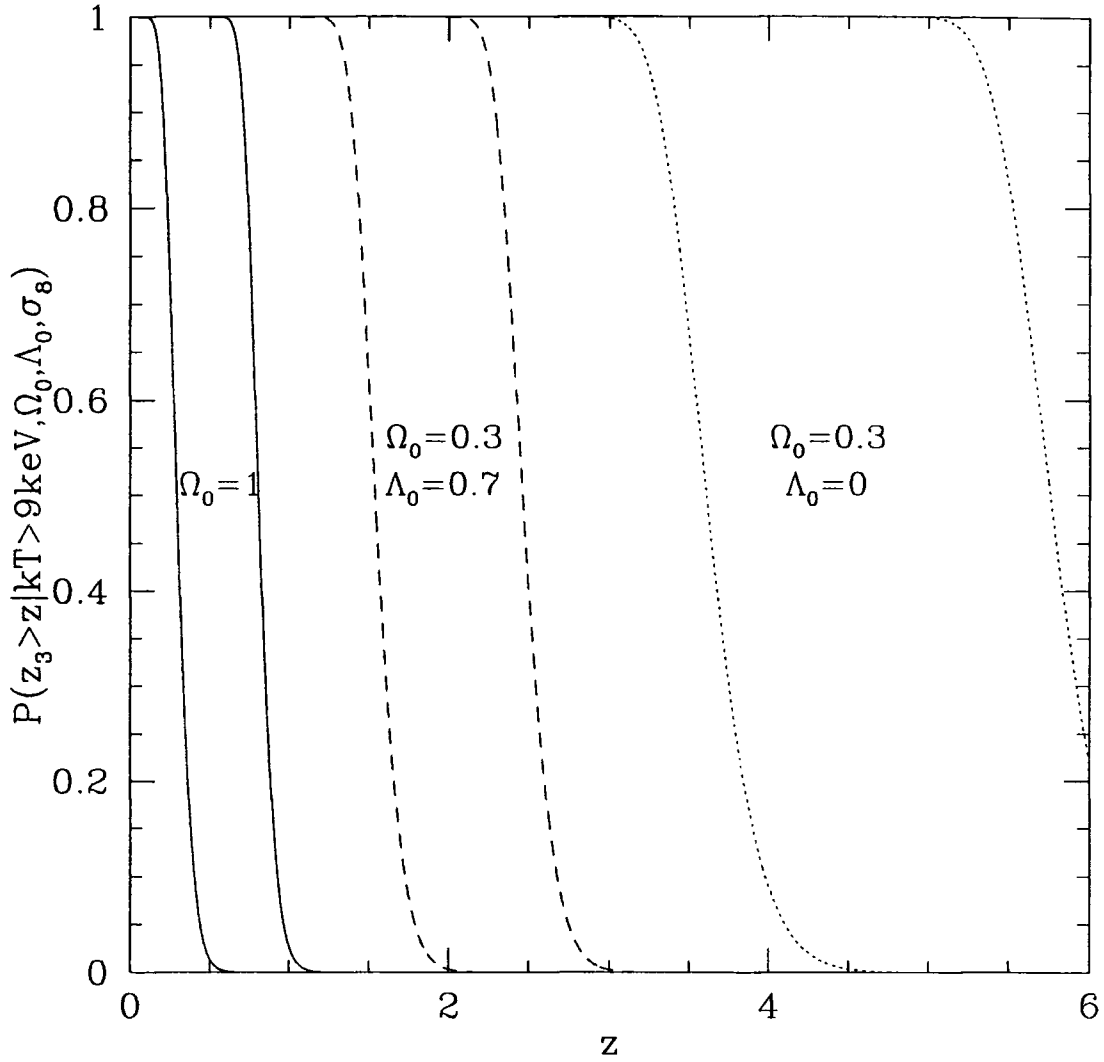

Figure 3.7: The distribution of the third furthest cluster redshift for all clusters hotter than 9 keV as a function of cosmology and σ_8. Solid, dashed and dotted lines correspond to $\Omega_0 = 1$, $\Omega_0 = 0.3$ with $\Lambda_0 = 0.7$ and $\Omega_0 = 0.3$ with $\Lambda_0 = 0$ respectively. For each model the two curves correspond to the best-fitting σ_8 value (to the left) and the one which has a $+2\sigma$ value of σ_8 (to the right).

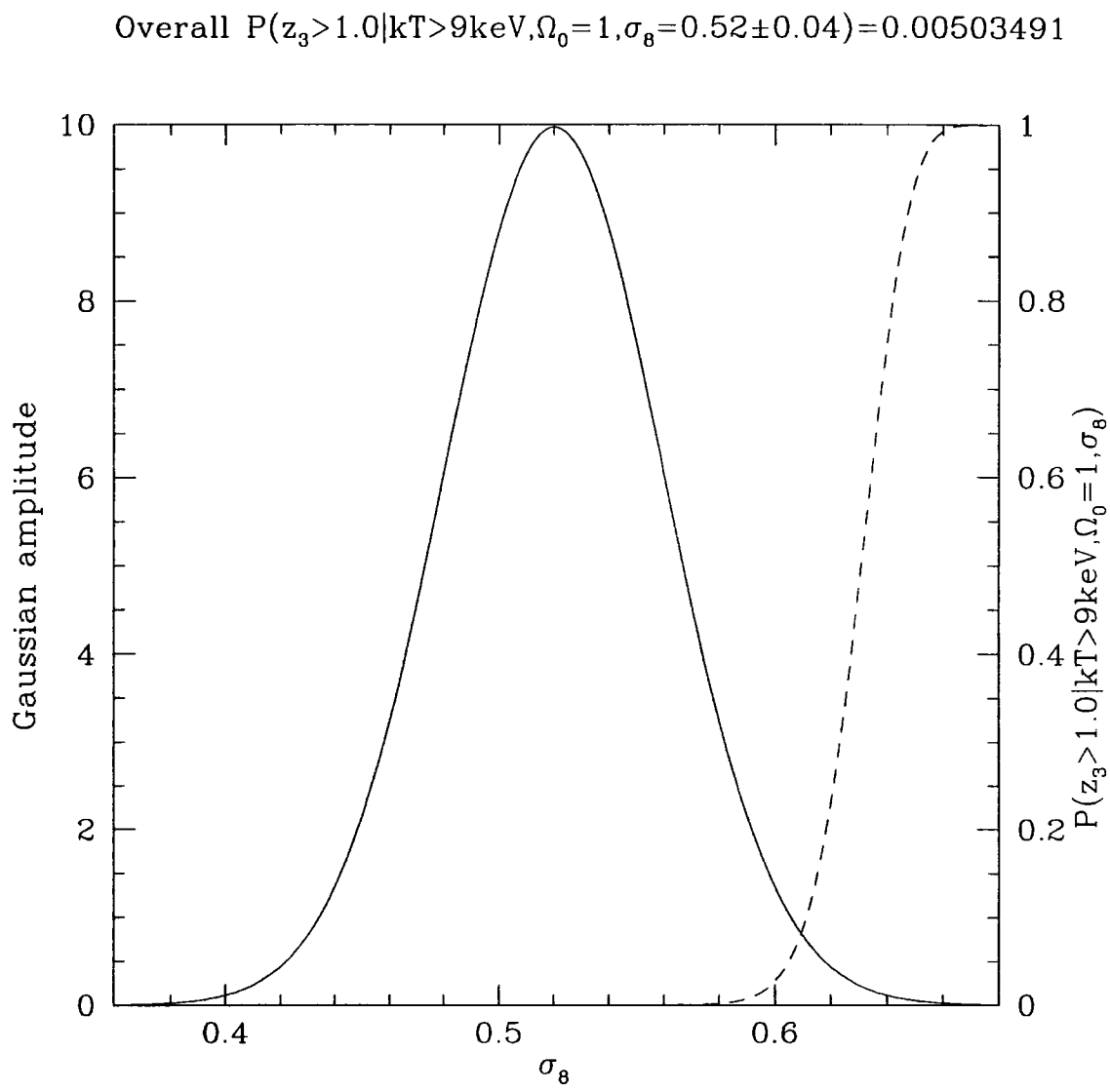

Figure 3.8: The probability that the third furthest cluster having $kT > 9$ keV in an $\Omega_0 = 1$ universe has a redshift greater than 1. The dashed line represents the probability that $z_3 > 1$ as a function of σ_8. A Gaussian (normalised to have unit area beneath the curve) illustrating the uncertainty in σ_8 is shown with a solid line. The integral over σ_8 of the product of the two curves gives the overall probability of 0.005.

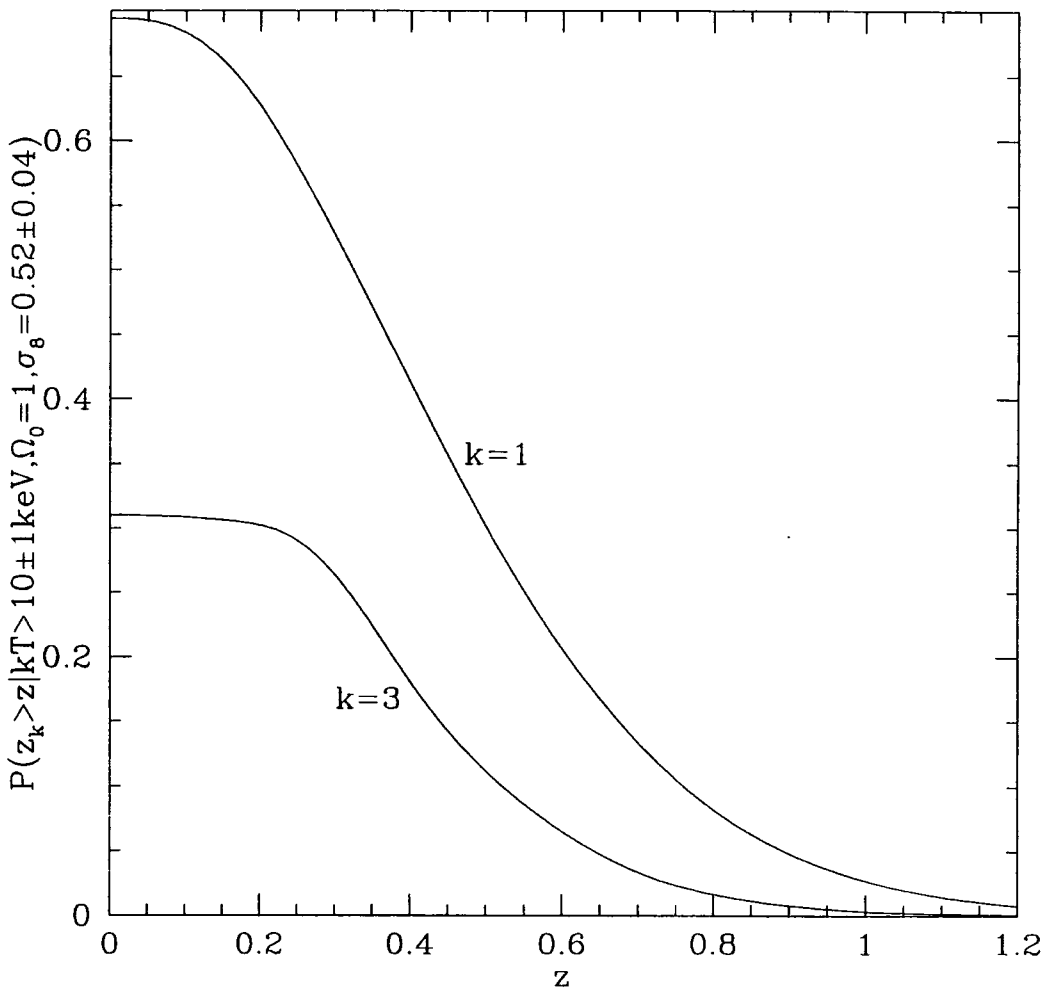

Figure 3.9: The cumulative distributions of z_1 and z_3 in an $\Omega_0 = 1$ universe, marginalised over both kT and σ_8. Neither of the two curves pass through the point $(0, 1)$ because it is not inevitable that any $kT > 10 \pm 1$ keV clusters will exist in an $\Omega_0 = 1$ universe with $\sigma_8 = 0.52 \pm 0.04$.

3.4 Conclusions of this Chapter

In Section 3.2 a procedure for constraining the value of Ω_0 using the luminous clusters at high redshifts in the *EMSS* was introduced. Despite the uncertainties in the $L_x - T_x$ relation, more particularly the shape of the scatter, and in the best-fitting value of σ_8 calculated in the previous Chapter, the test exploited the differences between the various cosmologies and was able to rule out the $\Omega_0 = 0.3$, $\Lambda_0 = 0$ model to a significance of about 95%. The main reasons that a stronger rejection was not obtained were the uncertainty in the normalisation of the mass fluctuation spectrum, σ_8, and the uncertainty in the shape and magnitude of the cluster $L_x - T_x$ scatter.

Having expended energy trying to rule out low-density cosmologies in Section 3.2 it was only fair that an equally vigorous attack should be launched upon the $\Omega_0 = 1$ model in Section 3.3. Some methods using order statistics and marginalisation procedures were described which might conceivably set a useful upper limit on Ω_0. However, with the presently available data it was not possible to rule out $\Omega_0 = 1$ with any significant probability.

Additional data which will have a bearing on the subject of the evolution of clusters and how this restricts the possible values of Ω_0 should come from at least the following three routes. A temperature function should soon be available for the high-redshift *EMSS* sources (Henry, private communication) using data from the *ASCA* satellite. Improvements in the techniques for measuring cluster masses from weak gravitational lensing should lead to more information about the mass function at high redshifts. Thirdly, future space-based microwave observatories such as COBRAS/SAMBA should provide well-defined samples of S-Z clusters. The redshift distribution of these objects can then be found, leading to a limit on Ω_0.

3.5 References

Abell G. O., 1958, ApJS, 3, 211
Bennett C. L., et al. , 1995, BAAS, 187, 7109
Bower R. G., Böhringer H., Briel U. G., Ellis R. S., Castander F. J., Couch W. J., 1994, MNRAS, 268, 345
Dalton G. B., Efstathiou G., Maddox S. J., Sutherland W. J., 1992, ApJ, 390, L1
Donahue M., 1996, ApJ, 468, 79
Edge A. C., Stewart G. C., Fabian A. C., Arnaud K. A., 1990, MNRAS, 245, 559
Evrard A. E., Henry J. P., 1991, ApJ, 383, 95
Frenk C. S., White S. D. M., Efstathiou G., Davis M., 1990, ApJ, 351, 10
Giacconi R., Murray S., Gursky H., Kellogg E., Schreier E., Matilsky T., Koch D., Tananbaum H., 1974, ApJS, 27, 37
Gioia I. M., Henry J. P., Maccacaro T., Morris S. L., Stocke J. T., Wolter A., 1990, ApJ, 356, L35

Gioia I. M., Luppino G. A., 1994, ApJS, 94, 583
Grainge K., Jones M., Pooley G., Saunders R., Edge A., 1993, MNRAS, 265, L57
van Haarlem M. P., Frenk C. S., White S. D. M., 1996, MNRAS, submitted
Henry J. P., Arnaud K. A., 1991, ApJ, 372, 410
Henry J. P., Gioia I. M., Maccacaro T., Morris S. L., Stocke J. T., Wolter A., 1992, ApJ, 386, 408
Kaiser N., 1986, MNRAS, 222, 323
Kellogg E., Murray S., 1974, ApJ, 193, L57
Lucey J. R., 1983, MNRAS, 204, 33
Lumsden S. L., Nichol R. C., Collins C. A., Guzzo L., 1992, MNRAS, 258, 1
Markevitch M., Mushotzky R., Inoue H., Yamashita K., Furuzawa A., Tawara Y., 1996, ApJ, 456, 437
Mewe R., Gronenschild E. H. B. M., van den Oord G. H. J., 1985, A&AS, 62, 197
Nichol R. C., Holden B. P., Romer A. K., Ulmer M. P., Burke D. J., Collins C. A., 1996, pre-print.
Piccinotti G., Mushotzky R. F., Boldt E. A., Holt S. S., Marshall F. E., Serlemitsos P. J., Shafer R. A., 1982, ApJ, 253, 485
Smail I., Dickinson M., 1995, ApJ, 455, L99
Sunyaev R. A., Zel'dovich Ya. B., 1972, Comm. Astrophys. Space Phys. 4, 173
Tauber J., Pace O., Volonte S., 1994, ESAJ, 18, 239
Tsuru T., Koyama K., Hughes J. P., Arimoto N., Kii T., Hattori M., 1996, eds Watanabe T., Yamashita K., The 11th international colloquium on UV and X-ray spectroscopy of Astrophysical and Laboratory Plasmas, in press

Chapter 4

Cluster correlation functions in N-body simulations

4.1 Introduction

The clustering strength of rich galaxy clusters has long been used as a constraint on models of large-scale structure. The two-point correlation function, ξ_{cc}, was first estimated for a sample of about 100 rich Abell clusters (Abell 1958; Abell, Corwin & Olowin 1989) by Bahcall & Soneira (1983) and by Klypin & Kopylov (1983) who noted that clusters have a larger clustering amplitude than galaxies. This difference has a natural explanation in theories in which large-scale structure grows by gravitational amplification of small fluctuations in an initially Gaussian density field. In such theories, collapsed objects form near peaks of the initial density field and a clustering pattern which depends on the height of the peak is imprinted at the epoch of formation (Kaiser 1984; Barnes et al. 1985).

Although the statistics of rare peaks provide an appealing explanation for the different clustering strength of galaxies and clusters, it soon became apparent that the early estimates of ξ_{cc} were inconsistent with the predictions of the cold dark matter model, the paradigm of gravitational clustering theories (Davis et al. 1985). Using N-body simulations of this model, White et al. (1987) calculated a cluster clustering length, $r_0 \simeq 11\,h^{-1}$Mpc (r_0 is defined as the separation at which $\xi_{cc} = 1$), whereas Bahcall & Soneira (1983) had obtained $r_0 \sim 25\,h^{-1}$Mpc for Abell clusters of richness class $R \geq 1$. Bahcall & Soneira's estimate helped to motivate an alternative explanation for the formation of structure, based on fluctuations seeded by cosmic strings (Turok 1983; Turok & Brandenberger 1986).

Sutherland (1988) pointed out that the apparent clustering amplitude of rich clusters would be artificially enhanced if intrinsically poor clusters that happened to lie near the line-of-sight to a rich cluster – and thus appear rich in projection – were included in a rich cluster sample. A signature of this effect is an anisotropy in the correlation function which appears stronger along the line-of-sight than in the

perpendicular direction. Soltan (1988) and Sutherland & Efstathiou (1991) showed that such anisotropies were clearly present in Bahcall & Soneira's sample and they, as well as Dekel et al. (1989), argued that correcting for this effect would lower the clustering length of rich Abell clusters to $\sim 14\,h^{-1}$Mpc. Nevertheless, Postman, Huchra & Geller (1992), using a sample of 351 Abell clusters of richness class $R \geq 0$, supported Bahcall & Soneira's original estimate.

Further progress had to await the construction of new cluster catalogues. These finally began to arrive in the early 1990s. Dalton et al. (1992) and Lumsden et al. (1992) constructed the first automated cluster catalogues using the positions and magnitudes of galaxies in photographic plates scanned with the APM and Cosmos machines respectively; Lahav et al. (1989), Romer et al. (1994) and Nichol, Briel & Henry (1994) constructed cluster catalogues using a combination of X-ray and optical data. The ensuing redshift surveys led to new determinations of $\xi_{\rm cc}$. The Oxford group estimated $r_0 = 12.9 \pm 1.4\,h^{-1}$Mpc (Dalton et al. 1992) from a sample of about 200 APM clusters, and $r_0 = 14.3 \pm 1.2\,h^{-1}$Mpc from an extended sample of 364 APM clusters (Dalton et al. 1994); Romer et al. obtained $r_0 = 13.7 \pm 2.3\,h^{-1}$Mpc from an X-ray flux-limited sample of 128 clusters.

Unfortunately the new cluster samples have not fully resolved the debate surrounding $\xi_{\rm cc}$. Bahcall & Soneira (1983) argued that the measured values of r_0 depend very strongly on cluster richness. Bahcall & West (1992) interpreted the discrepancies between different samples as a reflection of their different mean cluster richness, rather than as a result of contamination in Abell's catalogue (see also Peacock & West 1992). N-body simulations by Bahcall & Cen (1992) seem to support this view, whereas simulations by Croft & Efstathiou (1994) suggest that the dependence of r_0 on cluster richness is weak. Furthermore, the Oxford group have claimed that the low values of r_0 that they obtain for APM cluster catalogues, although much smaller than Bahcall & Soneira's (1983) value, are still inconsistent with the standard CDM cosmology and favour either CDM models with a low mean density and a non-zero cosmological constant or mixed dark matter models (Dalton et al. 1992, 1994; Croft & Efstathiou 1994). They base this conclusion on Croft & Efstathiou's (1994) set of large N-body simulations which, they argue, enable theoretical predictions for $\xi_{\rm cc}$ to be made with better than 10 per cent accuracy over a wide range of scales.

The work of Bahcall & Cen (1992), Croft & Efstathiou (1994) and Watanabe, Matsubara & Suto (1994) has highlighted how, as the observational data on $\xi_{\rm cc}$ improve, the need for precise theoretical predictions becomes increasingly important. Making theoretical predictions that are relevant to the interpretation of the data, however, is not straightforward, even for well-specified models such as CDM and its variants. In these models the evolution of the *mass* density field on the relevant scales can indeed be predicted quite accurately, particularly through large N-body simulations. Alternatively, on large scales, the Zel'dovich approximation can be used to follow the evolution of the density field (e.g. Borgani et al. 1995). The primary difficulty with these methods lies in the uncertain identification of clusters in the models with the real clusters found in galaxy surveys. Bahcall & Cen, Croft & Efstathiou and Watanabe et al. , like White et al. (1987), identified 'galaxy clusters'

in their simulations with large mass concentrations in the three-dimensional mass distribution. This is, of course, a very different procedure from that applied to real data where clusters are identified from the *projected* galaxy distribution using relatively complex algorithms. Possible biases in statistics such as ξ_{cc} which might be introduced by this procedure remain largely unexplored.

The restricted question of how the clustering strength of model clusters identified using the full three-dimensional mass distribution in N-body simulations depends on the details of the cluster-finding algorithm and on the way in which the cluster catalogues are constructed is addressed in this chapter. For definitiveness, only one specific cosmological model is considered, namely the standard CDM model.

In the following section the simulations and methods for constructing cluster catalogues are described. In Section 4.3 estimates of the correlation function for these catalogues are presented. In Section 4.4 the results are compared with those obtained in previous related studies. The findings are discussed and some conclusions are drawn in Section 4.5.

4.2 Techniques

4.2.1 Numerical simulations

The analysis is based on an ensemble of 10 CDM simulations performed with the adaptive AP^{3}M code of Couchman (1991, 1995). Each simulation represents a comoving periodic box of length $l_{\rm box} = 256\,h^{-1}$Mpc containing 128^3 particles, each of mass $\sim 2.2 \times 10^{12} h^{-1}{\rm M}_\odot$. The force softening (for an equivalent Plummer potential) was chosen to be $\sim 65 h^{-1}$kpc and remained fixed in comoving coordinates.

Initial conditions were laid down by perturbing particles from a uniform grid using the Zel'dovich approximation (Zel'dovich 1970; Efstathiou et al. 1985), and assuming the Bardeen et al. (1986) CDM transfer function for the case of zero baryons and $H_0 = 50$ km s^{-1}Mpc^{-1}. The expansion factor a was defined such that $\sigma_8 = a$, where σ_8 is the linear rms amplitude of mass fluctuations in spheres of radius $8\,h^{-1}$Mpc. Each simulation was evolved from $a = 0.05$ to $a = 0.63$ using a timestep $\Delta a = 0.002$ and each took approximately two days of CPU on a Decstation 5000/240. The timestep and initial redshift were chosen after running a series of trial simulations in which these parameters were varied. Although the cluster correlation function turned out to be insensitive to these variations, it was found that adopting either a later starting time or a larger timestep made a significant change to the abundance of clusters as a function of both mass and temperature, while adopting earlier starting times and smaller timesteps left them essentially unchanged.

In the following analysis the present day is identified with the epoch at which $\sigma_8 = 0.5$ or 0.63. These values were chosen to span the range of normalisations that are consistent with the mass and abundance of rich clusters of galaxies (White,

Efstathiou & Frenk 1993) and are lower than would be required for consistency with the *COBE* microwave background anisotropy measurements in the absence of a tensor mode contribution to the anisotropy (Smoot et al. 1992; Wright et al. 1994). The simulations have a slightly smaller volume, but better mass and spatial resolution than those of Croft & Efstathiou (1994).

4.2.2 Group-finders

In order to investigate the effect of varying the criteria by which clusters are defined and selected, five different group-finding algorithms are employed to identify clusters of particles in the N-body simulations. In all cases only groups with 8 or more particles, corresponding to a mass $M \geq 3.5 \times 10^{13} h^{-1} \mathrm{M}_{\odot}$, were considered.

The first was the standard friends-of-friends algorithm (Davis et al. 1985) which links together particles closer than some specified separation. A linking length of $b = 0.2$ times the mean interparticle separation was adopted, giving groups with typical mean overdensities of ~ 200. These groups will be referred to as FOF.

The second group-finder was the 'spherical overdensities' algorithm described in more detail in Lacey & Cole (1994). This algorithm estimates the local density at the position of each particle by finding the distance to its tenth nearest neighbour. Particles are ranked by local density and, starting with the particle in the densest environment, they are used as centres about which spheres are inflated until the mean enclosed overdensity falls below a specfied threshold. Overlapping groups are merged and centres recalculated until they lie within $0.2\, h^{-1}\mathrm{Mpc}$ of the centre-of-mass of the grouped particles. An overdensity threshold of 180 was adopted. The resulting groups will be referred to as SO.

For the third algorithm, a variant of the spherical overdensities algorithm was used. Each particle is assigned an 'X-ray luminosity', $L_{\mathrm{x},i} = \rho_i V_i$, where ρ_i and V_i denote estimates of the local density and velocity dispersion obtained from the ten nearest neighbours. The motivation for this choice is that, when summed over a group of particles, the total 'luminosity' will depend on density and temperature in the same way as bremsstrahlung emission, namely $L_{\mathrm{x}} \propto \int \rho^2 T_{\mathrm{x}}^{0.5} \mathrm{d}^3 r$. The mean X-ray luminosity density is calculated by summing all of the individual particle values and dividing by the volume of the simulation box. Then the particles are ranked by X-ray luminosity and spheres inflated until the luminosity contrast in the spherical volume, $\delta L_{\mathrm{x}} / L_{\mathrm{x}} = 10^4$. Although our simulations lack the spatial resolution to define the X-ray emitting regions well, this group-finder does give a higher weighting to the centres of the clusters and therefore has an effect which is qualitatively similar to the one it is intended to represent. Groups identified in this way are referred to as SOX.

The final two group-finders that were used are identical to those adopted by Croft & Efstathiou (1994) and allow a direct comparison to be made with their results. The algorithm first locates potential group centres using the FOF algorithm with

$b = 0.1$ to find tight knots of particles. Spheres of radius either 0.5 or $1.5\,h^{-1}$Mpc are constructed about these centres and, after merging overlapping spheres and recentring, the particles within this radius are considered as a group. These groups are denoted by CE(0.5) and CE(1.5) respectively.

In summary, five different group-finding algorithms have been investigated. The first, FOF, is the standard group-finder used extensively in previous analyses of N-body simulations. This is a simple and elegant algorithm which picks out most of the clusters identified as such by eye, although occasionally it classes two distinct lumps as a single group if they are linked by a tenuous bridge of particles. The second algorithm, SO, avoids this situation by working with the average densities within spheres. This method has the shortcoming that it unnaturally forces the boundaries of groups to be spheres. The third algorithm, SOX, attempts to emulate selecting clusters by X-ray emission. Given the nature and resolution of the simulations it is only approximate, but it does succeed in giving increased weight to groups containing dense cores. The fourth and fifth group-finders, CE(0.5) and CE(1.5), are used for comparison with Croft & Efstathiou (1994) who adopted them as idealized 3D versions of the galaxy counting algorithms employed in the construction of the APM and Abell galaxy cluster catalogues respectively.

4.2.3 Cluster selection

The next step is to construct cluster catalogues from each set of groups identified by the different algorithms. In the real world, the abundance of clusters in a sample is determined by setting a threshold in apparent optical richness or X-ray flux. For each choice of group-finder, the groups identified in all $N_{\rm sim} = 10$ simulations were ranked according to mass (M), velocity dispersion (v), or X-ray luminosity ($L_{\rm x}$). The $N_{\rm clus}$ highest ranked clusters were then selected to produce a cluster catalogue in each simulation for which the mean intercluster separation was given by

$$d_{\rm c} = (N_{\rm sim}/N_{\rm clus})^{1/3} l_{\rm box}. \tag{4.1}$$

The dependence of the resulting cluster correlation function on abundance, which has been parametrised by $d_{\rm c}$, as well as on the other details of the cluster selection process was then investigated.

Cluster X-ray luminosities were defined in one of two ways. For the SOX groups, they were simply the sum of the luminosities assigned to the individual particles in the group. For clusters obtained with other group-finders, first a velocity dispersion was estimated (from the measured mass assuming an isothermal density distribution). This was then converted into an X-ray temperature, $T_{\rm x}$, by assuming that the specific kinetic energy in the dark matter was equal to the specific thermal energy in the gas (Evrard 1990; Navarro, Frenk & White 1995), and an X-ray luminosity was inferred from the empirical $L_{\rm x} - T_{\rm x}$ relation. The last step was accomplished using the mean relation given by David et al. (1993), $L_{\rm x} \propto T_{\rm x}^{3.4}$. (The constant of proportionality is immaterial because only the ranking of the clusters by X-ray luminosity

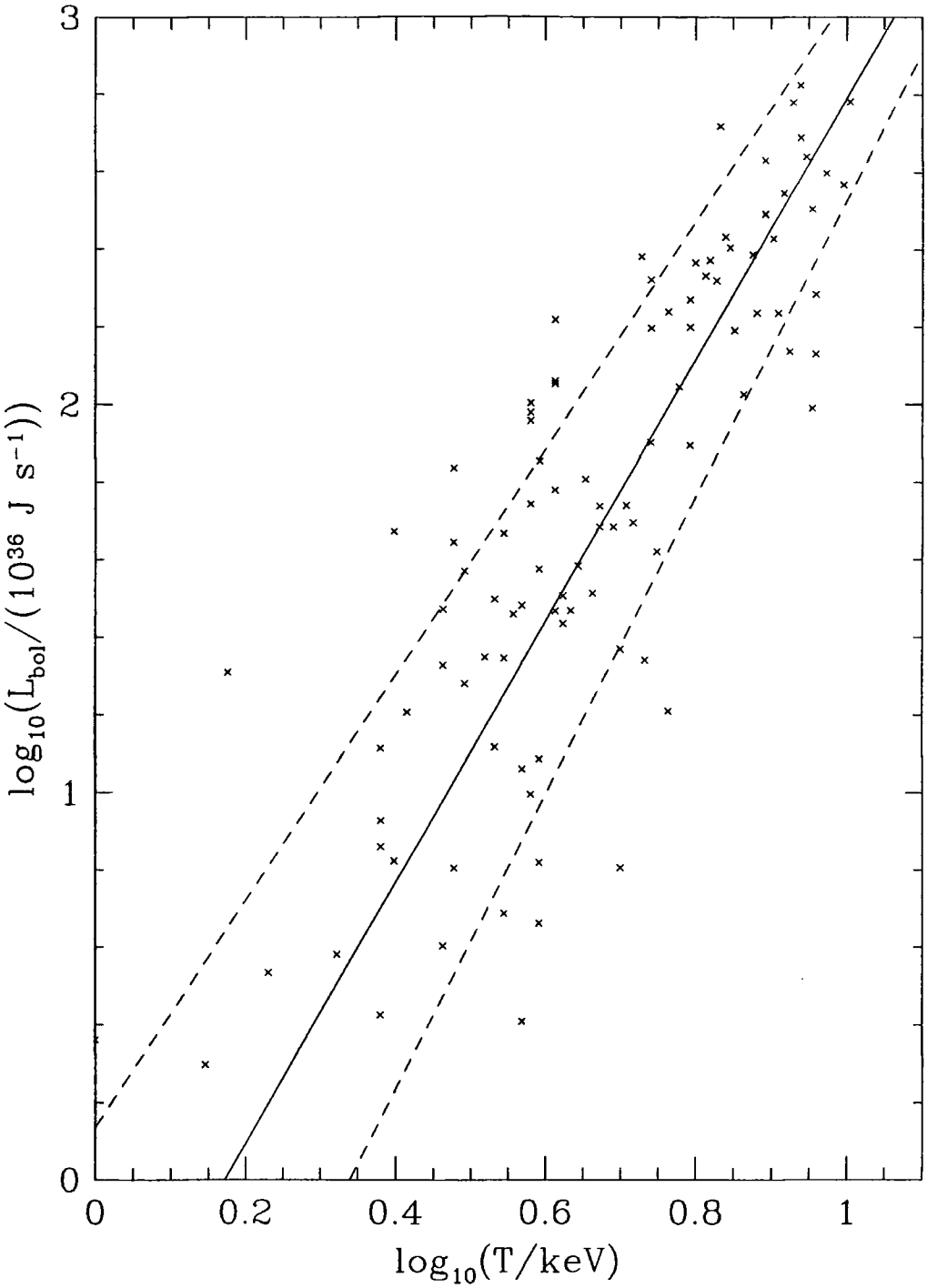

Figure 4.1: The relation between cluster X-ray luminosity and temperature for the David et al. (1993) sample. Crosses show the individual cluster measurements. A solid line represents the best-fitting power law, and dashed lines show the calculated $\pm 1\sigma$ uncertainty.

is important.) In addition, a Gaussian scatter with variance varying linearly with $\log_{10}T_{\rm x}$ was included. This gave $\sigma_{\log_{10}L_{\rm x}} = 0.58$ at $\log_{10}T_{\rm x} = 0.3$, and $\sigma_{\log_{10}L_{\rm x}} = 0.31$ at $\log_{10}T_{\rm x} = 0.9$. Fig. 4.1 shows the best-fitting relation and the $\pm 1\sigma$ lines. This procedure essentially scrambles up a v-selected catalogue by introducing some lower velocity dispersion clusters at the expense of higher velocity dispersion ones.

For each of the group-finders and selection statistics, catalogues with $20 \leq d_{\rm c} \leq 70\,h^{-1}$Mpc were created for both $\sigma_8 = 0.5$ and $\sigma_8 = 0.63$. Figs 4.2 and 4.3 show a slice through one of the simulations. In both cases, clusters were found using FOF, but the clusters in Fig. 4.2 were selected by mass whereas those in Fig. 4.3 were selected by 'X-ray' luminosity. The 'X-ray' sample can be seen to have some very small clusters that have come in at the expense of more extended objects in the mass-selected sample.

In summary, five different group-finders have been used: FOF, SO, SOX and the two employed by Croft & Efstathiou (1994), CE(0.5) and CE(1.5). From the FOF and SO groups, cluster catalogues selected according to mass, velocity dispersion and X-ray luminosity were produced. For the SOX group-finder, clusters were selected either by X-ray luminosity or by velocity dispersion. The cluster catalogues produced from the CE(0.5) and CE(1.5) groups were selected according to mass only, in the same way as the clusters analysed by Croft & Efstathiou (1994). Given a list of groups obtained with a particular group-finder, the statistic used for constructing a catalogue will be indicated in what follows by a subscript. Thus, for example, FOF_M denotes clusters identified with the friends-of-friends group-finder and selected according to mass.

4.2.4 Correlation function estimator

Cluster correlation functions in real space, $\xi_{\rm cc}(r)$, and in redshift space, $\xi_{\rm cc}(s)$, were obtained for each of our cluster catalogues. In the latter case, the simulations were projected along one of the principal axes and the component of each cluster's peculiar velocity along that axis was added to the Hubble velocity. The estimator used was

$$\xi_{\rm cc}(x) = \frac{N_{\rm p}}{n_{\rm c}^2 V {\rm d}V} - 1, \tag{4.2}$$

where x denotes either r or s, $N_{\rm p}$ is the number of cluster pairs with separation in a bin of volume ${\rm d}V$ centred at x, $n_{\rm c}$ is the number density of clusters in the catalogue, and V is the total volume. Estimates from all 10 simulations were averaged and the scatter amongst them used to obtain the error in $\xi_{\rm cc}$.

The correlation functions are not well fitted by a single power law over the entire range of pair separations sampled in our models. Thus, to estimate the correlation length, x_0, a two-parameter χ^2 fit of the form

$$\xi_{\rm cc}(x) = \left(\frac{x_0}{x}\right)^{\gamma} \tag{4.3}$$

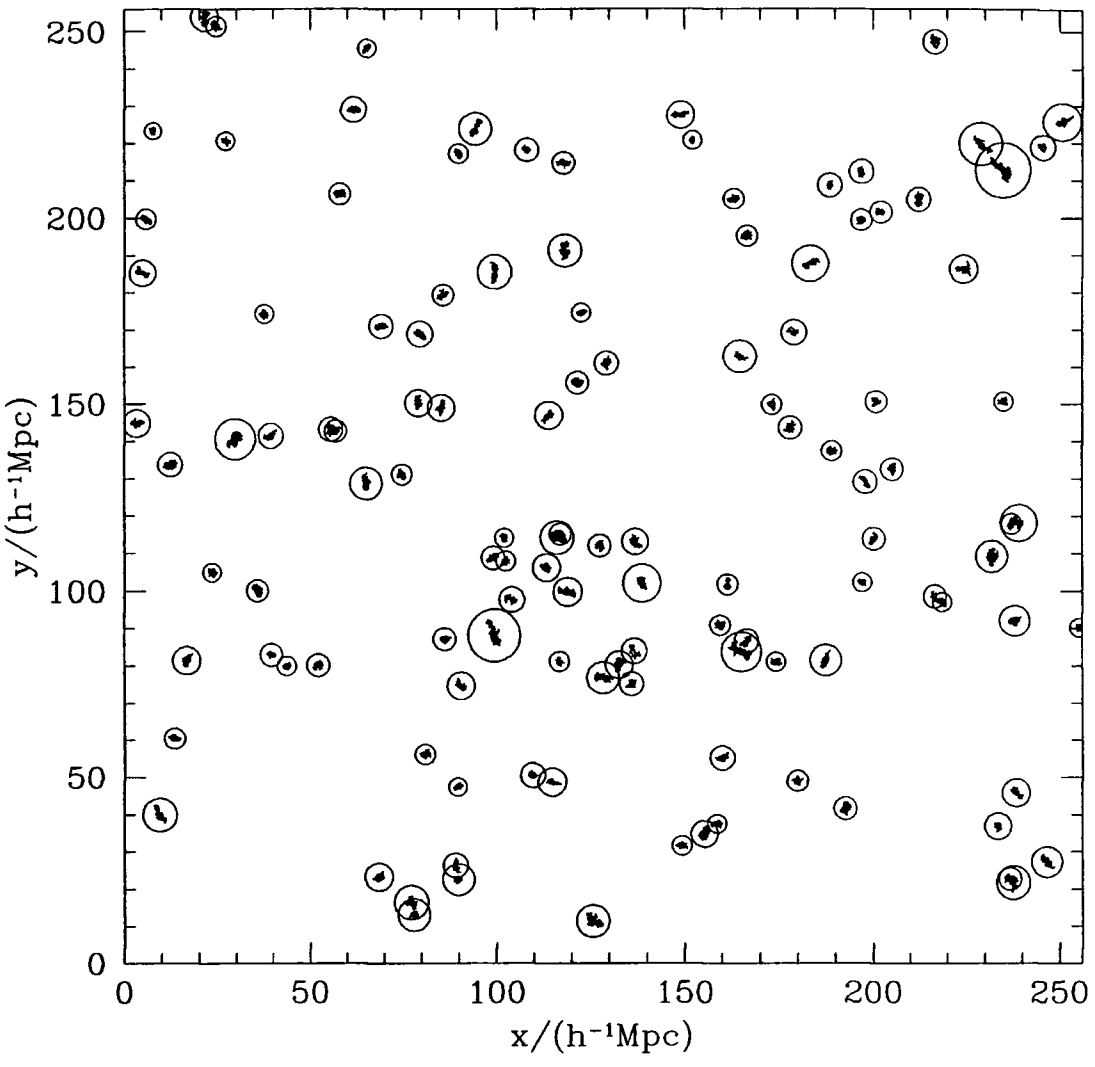

Figure 4.2: A $50\,h^{-1}$Mpc thick slice through one of the ten simulations with $\sigma_8 = 0.63$. The clusters were selected using the friends-of-friends (FOF) group-finder and adopting a lower mass cutoff such that the mean cluster separation $d_c = 30\,h^{-1}$Mpc. Particles belonging to clusters are shown as dots and each cluster is delineated by a circle around its centre with radius equal to 1.5 times the true distance to the most distant cluster particle.

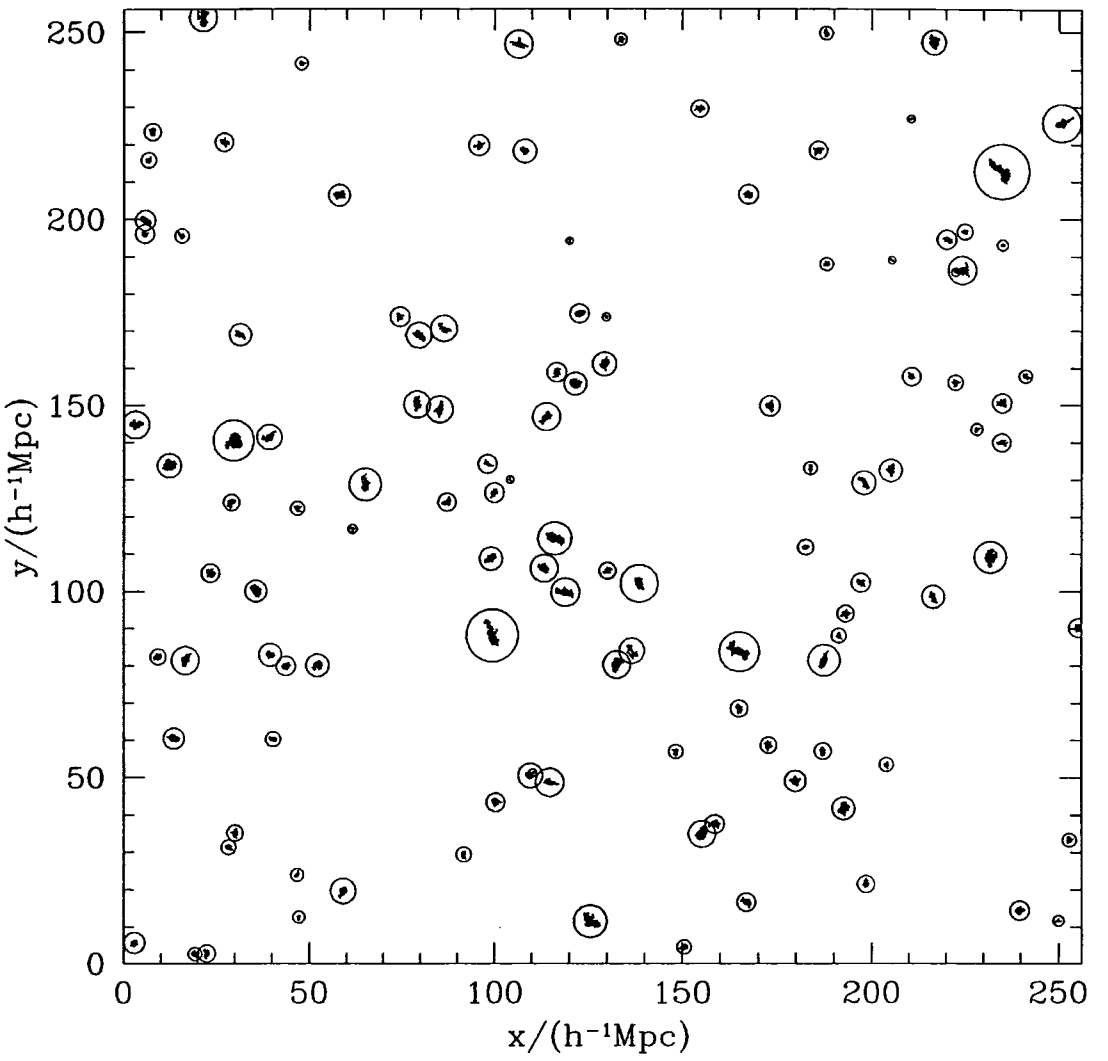

Figure 4.3: As Fig. 4.2, but with X-ray luminosity rather than mass as the selection statistic for the FOF groups.

was used over a limited range in x, near the value where $\xi_{cc} = 1$. By fitting over a narrow range in x, the inferred values of x_0 do not depend strongly on the value of the slope, γ, but the estimates of γ are only applicable in this limited range of pair separations. The actual range in x used depends on the amplitude of ξ_{cc}, but is well approximated by the limits

$$\frac{d_c - 10}{150} + 0.5 < \log_{10}(x) < \frac{d_c - 10}{150} + 1.0, \tag{4.4}$$

where d_c and x are measured in h^{-1}Mpc. This range corresponds to four or five radial bins around $x = x_0$. The variances of the fit parameters were recovered from the diagonal elements of the covariance matrix.

4.3 Results

Tables 4.1 and 4.2 give correlation lengths and power-law slopes for real and redshift space correlation functions, for a selection of the cluster catalogues. (Error bars were obtained as described in Section 4.2.4.) Full correlation functions are plotted in Figs 4.4 and 4.5 for samples constructed using a subset of the selection statistics and spanning a wider range of values of d_c than those shown in the tables. Several trends apparent in the data are now discussed, focussing exclusively on estimates of the correlation length, and ignoring variations in the slope, γ, since it is most often the former that is used to compare models with data. (For reference, the estimates of γ are listed in the tables. It should be recalled that they refer exclusively to the region where $\xi_{cc} \simeq 1$.)

4.3.1 Dependence of the real space correlation function on cluster selection and abundance

Firstly, the effect on ξ_{cc} of varying the procedure for identifying and selecting clusters in real space is considered. For each choice of selection statistic (M, v and L_x), FOF and SO clusters give consistent results in almost all cases. For the groups under consideration here – the most massive in the simulations – the FOF and SO finders essentially pick out the same objects. SOX clusters also tend to have similar values of r_0 to FOF and SO clusters, whether they are selected by v or L_x.

The real space results for CE clusters are in excellent agreement with those obtained by Croft & Efstathiou (1994). Note that, whilst the $\mathrm{CE}(1.5)_M$ clusters give results consistent with those of FOF_M and SO_M, the $\mathrm{CE}(0.5)_M$ clusters give the smallest values of r_0 of any mass-selected clusters. The largest difference between $\mathrm{CE}(0.5)_M$ and SO_M clusters is $3.3\,h^{-1}$Mpc and occurs for $d_c = 50\,h^{-1}$Mpc and $\sigma_8 = 0.5$.

For any given cluster-finding algorithm there are often trends either with the selection statistic or with σ_8. For example, when d_c is large, clusters selected by

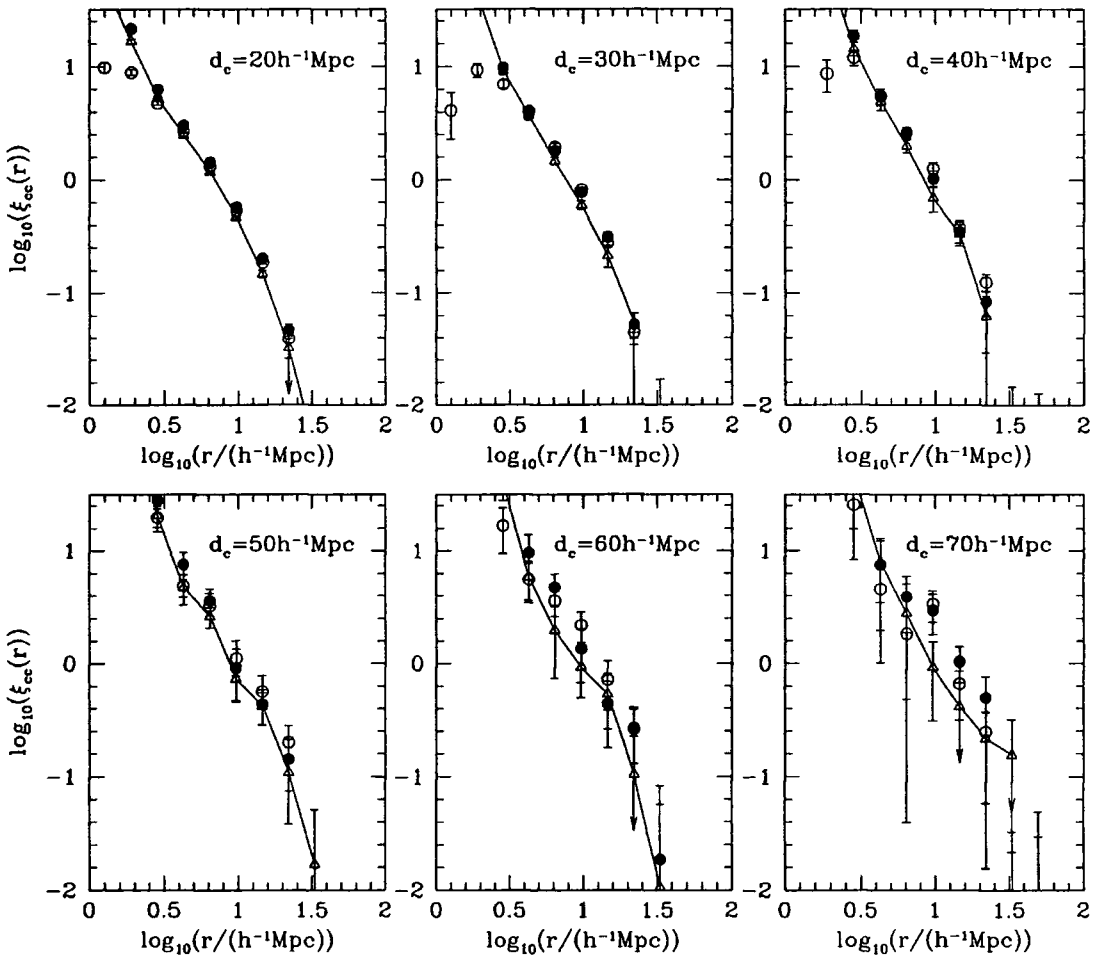

Figure 4.4: Real space correlation functions for SO groups in a CDM model with $\sigma_8 = 0.63$. The different symbols correspond to catalogues selected according to mass (open circles), velocity dispersion (filled circles), and 'X-ray' luminosity (open triangles). The lines in each panel link the triangles and appear also on Fig. 4.5 for ease of comparison.

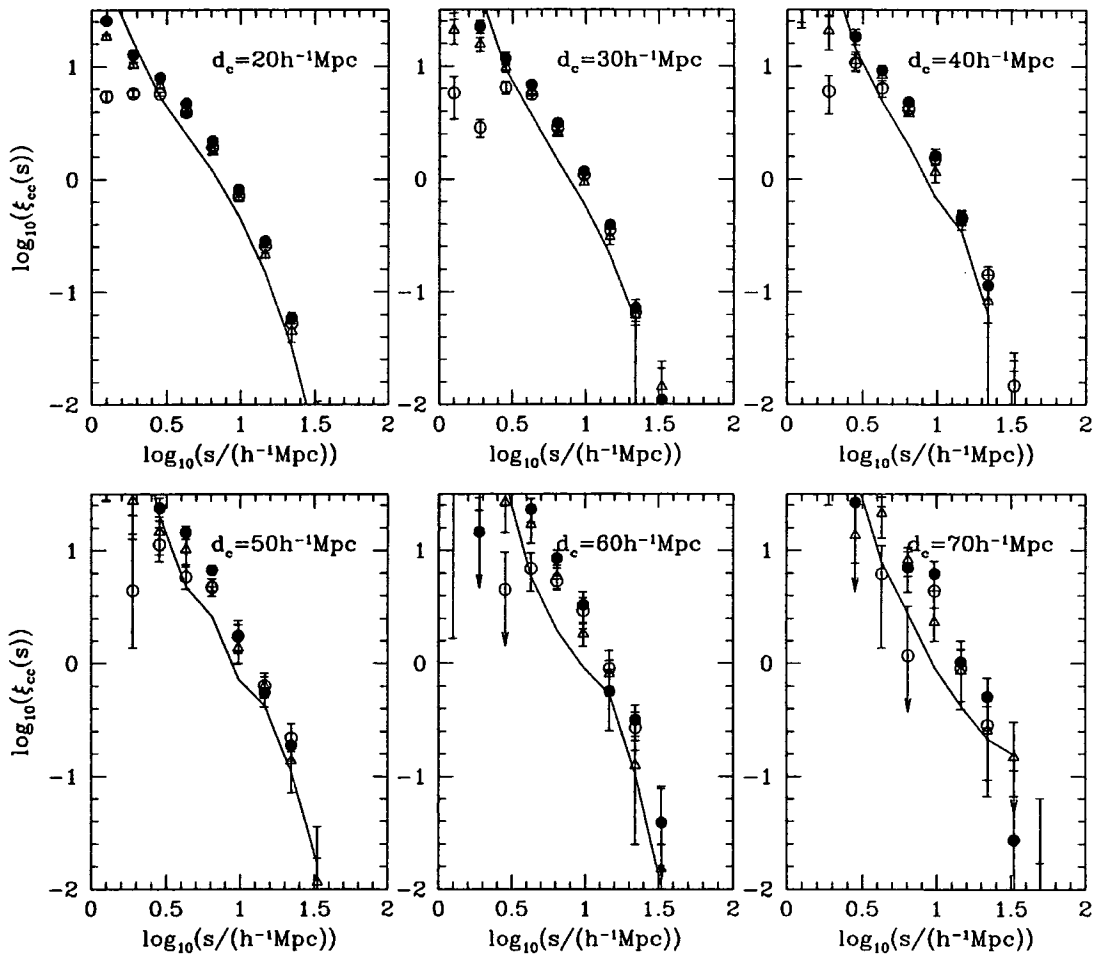

Figure 4.5: Redshift space correlation functions for SO groups in a CDM model with $\sigma_8 = 0.63$. The different symbols correspond to catalogues according to mass (open circles), velocity dispersion (filled circles), and 'X-ray' luminosity (open triangles). The solid lines are the same as those in Fig. 4.4 and are repeated here so that the increase in ξ_{cc} caused by using redshift distances rather than true distances may be seen clearly.

Table 4.1: The real space correlation length, r_0, and the slope of the correlation function, γ, for a variety of group-finders and cluster selection criteria for two different values of mean cluster separation, d_c, and normalization, σ_8. Errors are 1σ and were estimated as described in Section 4.2.4.

Group-Finder	Selection	$d_c = 30\,h^{-1}$Mpc $\sigma_8 = 0.5$	$d_c = 50\,h^{-1}$Mpc $\sigma_8 = 0.5$	$d_c = 30\,h^{-1}$Mpc $\sigma_8 = 0.63$	$d_c = 50\,h^{-1}$Mpc $\sigma_8 = 0.63$
FOF	Mass	$r_0 = 8.50 \pm 0.15$	10.15 ± 0.79	8.79 ± 0.18	12.01 ± 0.58
		$\gamma = 2.15 \pm 0.11$	2.13 ± 0.57	2.18 ± 0.13	2.63 ± 0.37
SO	Mass	$r_0 = 8.56 \pm 0.15$	11.24 ± 0.70	8.73 ± 0.17	10.80 ± 0.84
		$\gamma = 2.18 \pm 0.11$	2.25 ± 0.49	2.22 ± 0.11	2.21 ± 0.61
CE(0.5)	Mass	$r_0 = 8.31 \pm 0.17$	7.97 ± 0.71	8.29 ± 0.17	9.59 ± 0.52
		$\gamma = 2.02 \pm 0.12$	1.89 ± 0.48	2.14 ± 0.12	3.09 ± 0.64
CE(1.5)	Mass	$r_0 = 8.80 \pm 0.13$	10.70 ± 0.64	8.84 ± 0.16	11.22 ± 0.64
		$\gamma = 2.27 \pm 0.09$	2.53 ± 0.51	2.42 ± 0.12	2.96 ± 0.55
FOF	v	$r_0 = 8.64 \pm 0.16$	8.45 ± 0.71	8.75 ± 0.20	10.12 ± 0.69
		$\gamma = 2.21 \pm 0.12$	2.48 ± 0.73	2.19 ± 0.15	2.74 ± 0.66
SO	v	$r_0 = 8.54 \pm 0.14$	9.28 ± 0.50	8.59 ± 0.17	9.89 ± 0.68
		$\gamma = 2.19 \pm 0.11$	2.85 ± 0.66	2.04 ± 0.11	2.67 ± 0.65
SOX	v	$r_0 = 8.26 \pm 0.18$	9.00 ± 0.76	8.32 ± 0.19	10.29 ± 0.66
		$\gamma = 1.95 \pm 0.12$	1.91 ± 0.46	2.17 ± 0.15	2.81 ± 0.66
FOF	L_x	$r_0 = 7.88 \pm 0.19$	9.14 ± 0.73	7.87 ± 0.16	8.83 ± 0.80
		$\gamma = 2.33 \pm 0.17$	2.60 ± 0.98	2.11 ± 0.14	1.99 ± 0.50
SO	L_x	$r_0 = 7.34 \pm 0.19$	6.41 ± 1.12	7.72 ± 0.17	9.46 ± 0.62
		$\gamma = 2.17 \pm 0.15$	2.26 ± 0.85	2.27 ± 0.15	2.72 ± 0.77
SOX	L_x	$r_0 = 7.76 \pm 0.16$	5.28 ± 1.80	8.05 ± 0.18	10.02 ± 0.70
		$\gamma = 2.26 \pm 0.13$	1.53 ± 0.85	2.28 ± 0.13	2.45 ± 0.60

Table 4.2: The redshift space correlation length, s_0, and the slope of the correlation function, γ, for a variety of group-finders and cluster selection criteria for two different values of mean cluster separation, d_c, and normalization, σ_8. Errors are 1σ and were estimated as described in Section 4.2.4.

Group-Finder	Selection	$d_c = 30\,h^{-1}$Mpc $\sigma_8 = 0.5$	$d_c = 50\,h^{-1}$Mpc $\sigma_8 = 0.5$	$d_c = 30\,h^{-1}$Mpc $\sigma_8 = 0.63$	$d_c = 50\,h^{-1}$Mpc $\sigma_8 = 0.63$
FOF	Mass	$s_0 = 9.31 \pm 0.16$	10.76 ± 0.76	9.93 ± 0.16	12.33 ± 0.65
		$\gamma = 2.46 \pm 0.12$	2.02 ± 0.47	2.29 ± 0.09	2.61 ± 0.35
SO	Mass	$s_0 = 9.30 \pm 0.15$	11.82 ± 0.62	9.81 ± 0.16	12.22 ± 0.76
		$\gamma = 2.55 \pm 0.10$	2.59 ± 0.47	2.36 ± 0.08	2.41 ± 0.43
CE(0.5)	Mass	$s_0 = 9.25 \pm 0.16$	10.45 ± 0.53	9.89 ± 0.16	11.26 ± 0.56
		$\gamma = 2.30 \pm 0.10$	2.58 ± 0.44	2.04 ± 0.09	2.64 ± 0.43
CE(1.5)	Mass	$s_0 = 9.38 \pm 0.16$	10.89 ± 0.56	9.89 ± 0.15	11.90 ± 0.64
		$\gamma = 2.52 \pm 0.09$	2.70 ± 0.47	2.41 ± 0.10	2.71 ± 0.40
FOF	v	$s_0 = 9.31 \pm 0.14$	9.28 ± 0.71	10.04 ± 0.17	11.07 ± 0.66
		$\gamma = 2.51 \pm 0.11$	2.79 ± 0.67	2.45 ± 0.10	3.12 ± 0.62
SO	v	$s_0 = 9.59 \pm 0.16$	10.18 ± 0.53	10.29 ± 0.15	12.03 ± 0.58
		$\gamma = 2.53 \pm 0.12$	3.14 ± 0.54	2.36 ± 0.07	3.05 ± 0.34
SOX	v	$s_0 = 9.42 \pm 0.16$	11.61 ± 0.60	10.32 ± 0.15	12.02 ± 0.56
		$\gamma = 2.52 \pm 0.13$	2.74 ± 0.34	2.41 ± 0.08	2.99 ± 0.40
FOF	L_x	$s_0 = 8.67 \pm 0.16$	9.39 ± 0.94	9.19 ± 0.15	11.10 ± 0.56
		$\gamma = 2.60 \pm 0.12$	2.00 ± 0.70	2.46 ± 0.10	2.82 ± 0.59
SO	L_x	$s_0 = 8.53 \pm 0.14$	7.94 ± 0.49	9.44 ± 0.15	11.65 ± 0.62
		$\gamma = 2.32 \pm 0.12$	2.69 ± 0.47	2.45 ± 0.10	2.74 ± 0.33
SOX	L_x	$s_0 = 8.72 \pm 0.14$	9.21 ± 0.59	9.18 ± 0.13	10.98 ± 0.69
		$\gamma = 2.53 \pm 0.13$	2.37 ± 0.55	2.33 ± 0.09	2.64 ± 0.55

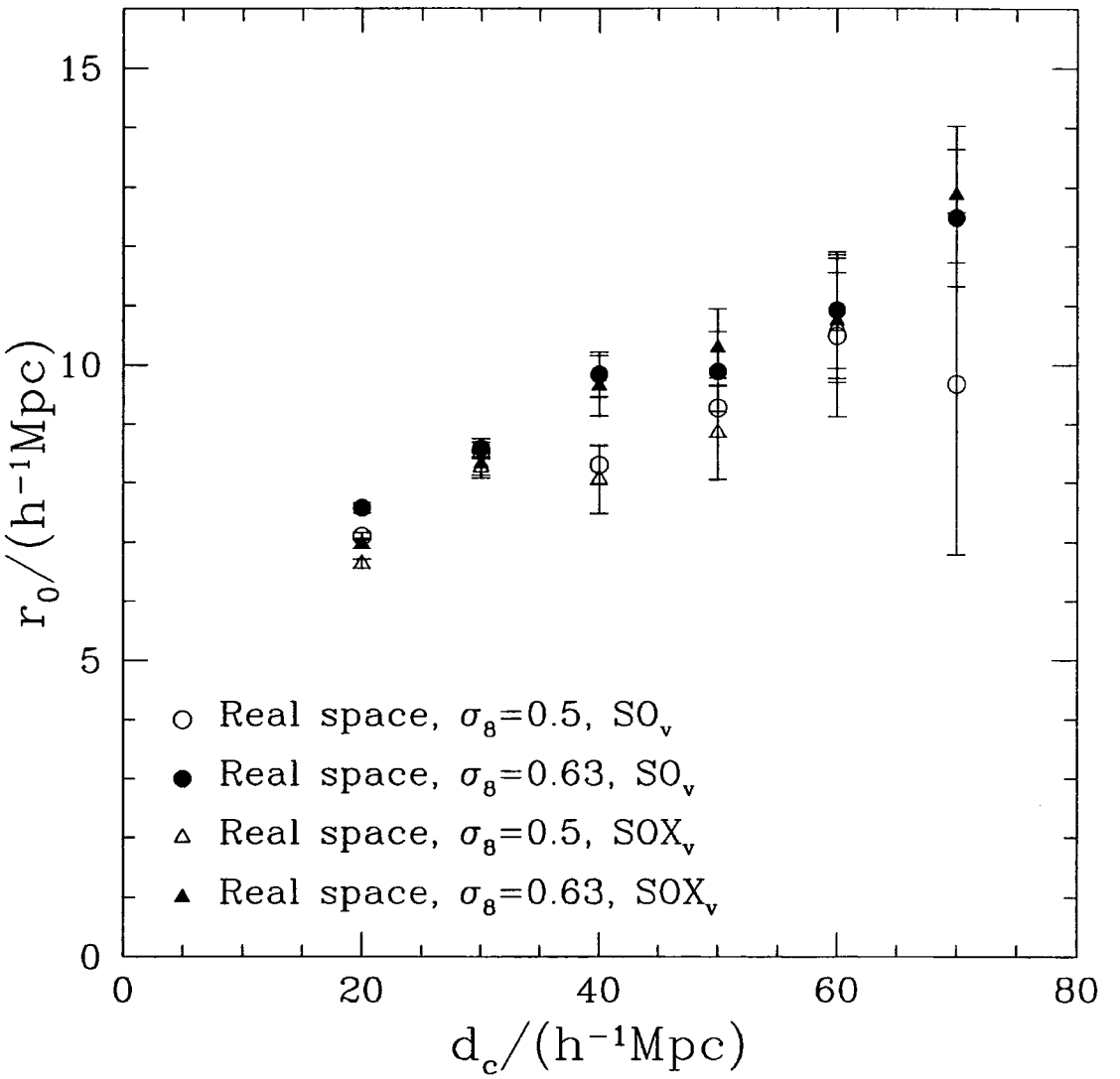

Figure 4.6: Variation of the real space correlation length, r_0, with mean intercluster separation, d_c, for a selection of cluster catalogues. Real space correlation functions were calculated for catalogues selected according to 1D velocity dispersion, v, for SO (circles) and SOX (triangles) clusters. Open symbols are for $\sigma_8 = 0.5$ and filled symbols for 0.63.

mass have larger values of r_0 than clusters selected by v, with a largest difference of 2.8 h^{-1}Mpc between SO_M and FOF_v clusters for $\sigma_8 = 0.5$. Clusters selected by X-ray luminosity tend to be slightly more weakly clustered than clusters selected by mass or velocity dispersion. This is because of the scatter in the $L_x - T_x$ relation and the trend of clustering strength with velocity dispersion. Thus, for fixed d_c and σ_8, the SO_{L_x} and SOX clusters tend to give smaller values of r_0 than the other catalogues. At $d_c = 30\,h^{-1}$Mpc, where the statistical errors are small, the differences between the correlation lengths measured from the various cluster catalogues can exceed 5σ and at $d_c = 50\,h^{-1}$Mpc the minimum and maximum are separated by at least 4σ. The data also show a weak but significant trend for r_0 to increase with increasing σ_8. Typically, with the same cluster definition at $\sigma_8 = 0.5$ and $\sigma_8 = 0.63$, the differences in r_0 are $1\,h^{-1}$Mpc or less.

A clear trend in the real space data is the tendency for the correlation length to increase with increasing mean cluster separation. This trend is stronger for the larger value of σ_8. Some illustrative cases are plotted in Fig. 4.6 (for v-selected clusters). The data are reasonably well fitted by a linear relation, although for $d_c > 40\,h^{-1}$Mpc the uncertainties are too large to rule out a flatter trend as advocated by Croft & Efstathiou (1994). A more detailed comparison with this and other work is made in the next section. For the SO_v clusters, the $r_0 - d_c$ relation can be approximately fitted by a linear relation of the form:

$$r_0 = (0.056 \pm 0.014)d_c + (6.36 \pm 0.69)\ h^{-1}\text{Mpc} \tag{4.5}$$

and

$$r_0 = (0.090 \pm 0.009)d_c + (5.82 \pm 0.44)\ h^{-1}\text{Mpc} \tag{4.6}$$

for $\sigma_8 = 0.5$ and 0.63 respectively.

In summary, the real space correlation length of rich clusters identified in three dimensions is only weakly dependent on the normalization of the power spectrum, but it can vary considerably depending on the procedure used to define a cluster catalogue and on the abundance of the objects under consideration. This variation can be much larger than the statistical uncertainties in the individual determinations. For example, for $\sigma_8 = 0.5$ and $d_c = 30\,h^{-1}$Mpc, the largest variation seen in Table 4.1 is $1.46\,h^{-1}$Mpc, compared with a typical uncertainty of $\sim 0.16\,h^{-1}$Mpc in the individual determinations.

4.3.2 Redshift space effects

When redshift distances rather than true distances are used, the correlation function is distorted in various ways. Structures on small scales are smeared out by peculiar velocities, while structures on large scales are amplified by coherent infall (Kaiser 1987). As a result, the correlation function in redshift space is flatter on small scales, is steeper on intermediate scales and has a larger amplitude on large scales than the real space correlation function. These effects are readily apparent in Fig. 4.7 which

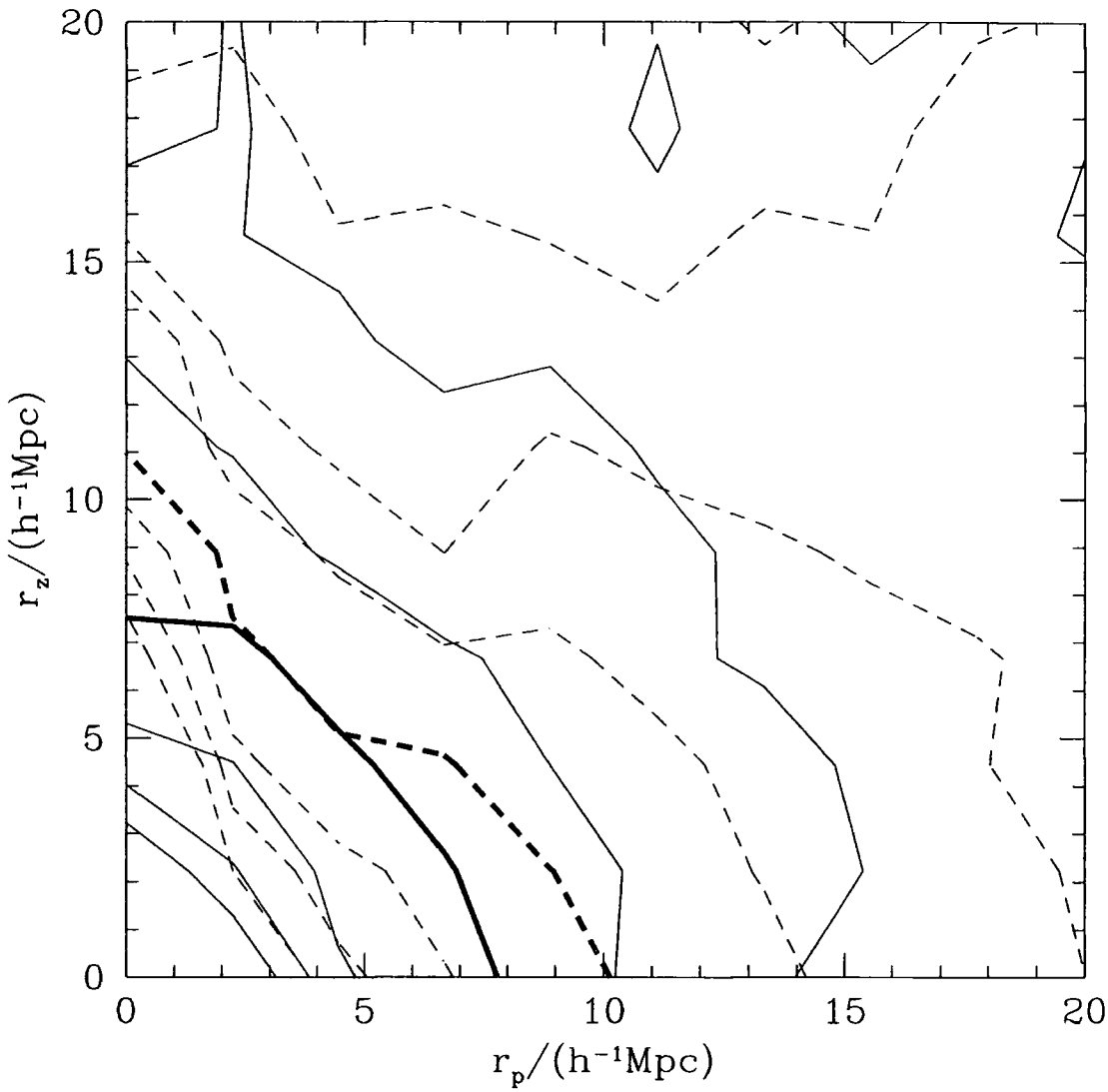

Figure 4.7: Contours of constant ξ_{cc} for a CDM model with $\sigma_8 = 0.63$. Results are shown for SO_v clusters with $d_c = 20\,h^{-1}$Mpc. The levels are at $0, 0.2, 0.5, 1, 2, 3$ and 4. Real space correlations are plotted as full lines and redshift space correlations as dashed lines, with the $\xi_{cc} = 1$ contour in bold.

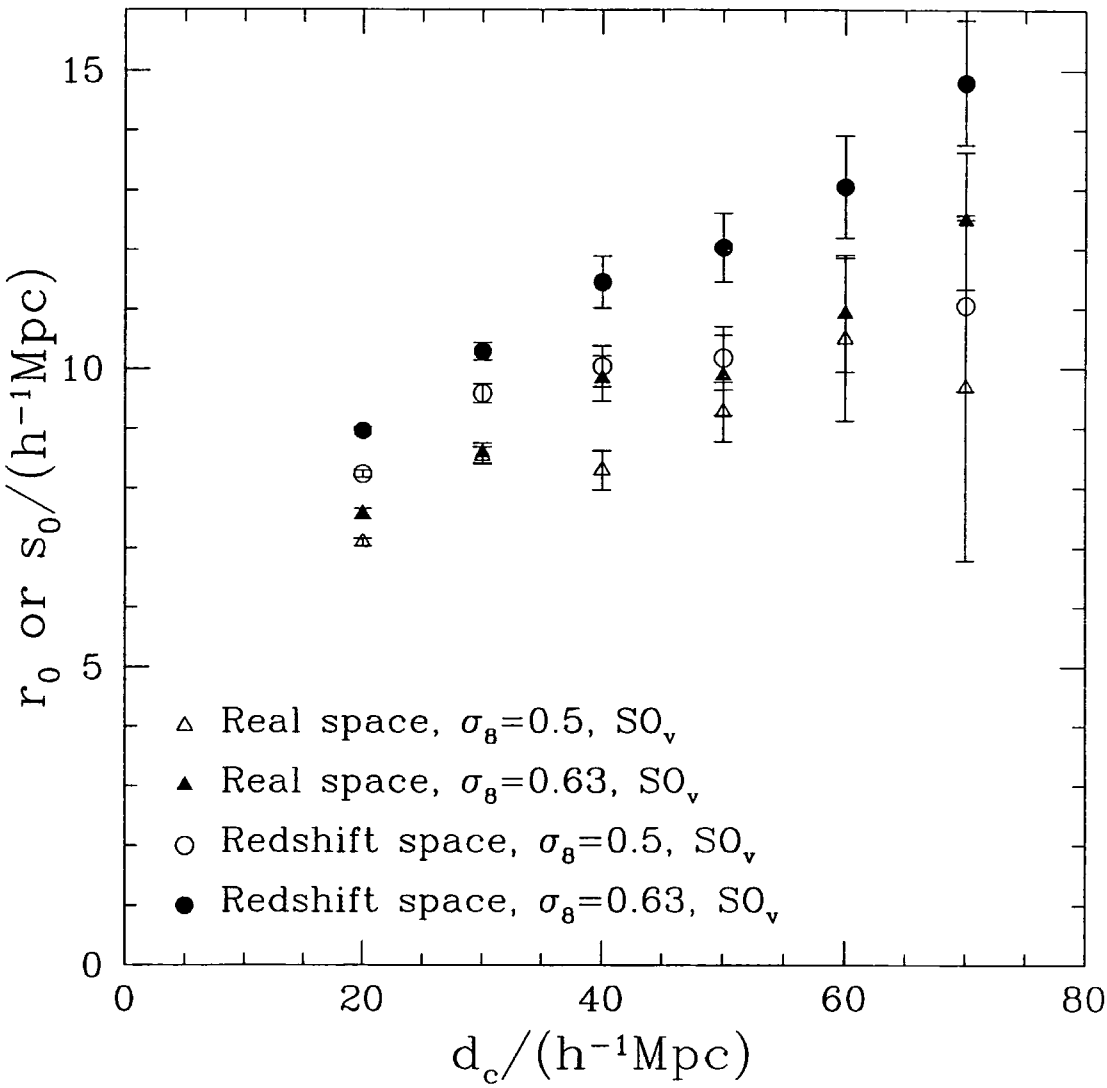

Figure 4.8: Variation of the redshift space correlation length, s_0, with mean inter-cluster separation, d_c, for a selection of cluster catalogues. Data are for SO groups selected according to velocity dispersion. Open symbols show results for $\sigma_8 = 0.5$ and filled symbols for $\sigma_8 = 0.63$. Circles represent our redshift space results and triangles the corresponding real space results from Fig. 4.6 which are included for comparison.

shows contour plots of ξ_{cc} as a function of projected separation on the sky, r_p, and distance along the line-of-sight, r_z. For small values of r_p, the contours of constant ξ_{cc} are elongated along the r_z direction because of smearing, and for large values of r_p they are elongated along the r_p direction as a result of coherent infall.

A selection of the redshift space correlation functions are plotted and compared with their real space counterparts in Fig. 4.5. In all cases, the net effect of redshift space distortions is to increase the amplitude of the correlation function on scales $3 \lesssim s/(h^{-1}\mathrm{Mpc}) \lesssim 30$. As a result, the values of s_0 (the redshift space separation at which $\xi_{cc}(s) = 1$) are significantly larger than the corresponding values of r_0. As expected, the differences are greater for larger values of σ_8 since the induced peculiar velocities grow with the amplitude of the mass fluctuations. These effects are further demonstrated in Tables 4.1 and 4.2. The enhancement of the correlation length in redshift space depends somewhat on the group-finder and selection statistic used. On average, s_0 is larger than r_0 by $1.1\,h^{-1}$Mpc for $\sigma_8 = 0.5$ and by $1.4\,h^{-1}$Mpc for $\sigma_8 = 0.63$. Note, however, that in individual cases the redshift space enhancement can be considerably larger than this.

The increase in the correlation length with increasing intercluster separation is slightly more pronounced in redshift space than in real space. An illustrative case, SO_v clusters, is shown and compared with the corresponding real space data in Fig. 4.8. For $\sigma_8 = 0.63$, s_0 grows approximately linearly with d_c out to the largest values of d_c considered, $d_c = 70\,h^{-1}$Mpc, at which $s_0 \simeq 15\,h^{-1}$Mpc. The relation between s_0 and d_c is approximately given by

$$s_0 = (0.063 \pm 0.020) d_c + (7.31 \pm 0.72)\ h^{-1}\mathrm{Mpc} \tag{4.7}$$

and

$$s_0 = (0.109 \pm 0.007) d_c + (6.87 \pm 0.35)\ h^{-1}\mathrm{Mpc} \tag{4.8}$$

for $\sigma_8 = 0.5$ and 0.63 respectively.

4.4 Comparison with previous simulations

Cluster correlation functions calculated from N-body simulations of the CDM model have been published previously by White et al. (1987), Bahcall & Cen (1992), and Croft & Efstathiou (1994). The first of these studies sampled a relatively small volume so the resulting correlation functions have large uncertainties; they are consistent with the results found here.

Bahcall & Cen (1992) simulated a single cube of side $400\,h^{-1}$Mpc, in the standard CDM model, and calculated cluster correlation functions in real space only (Cen, private communication). They identified groups of particles using a variant of the FOF algorithm and selected clusters according to mass. Thus, for a fair comparison, we consider the catalogue of FOF_M clusters. The comparison is done in Fig. 4.9 where correlation lengths are plotted in real space as a function of mean intercluster

separation. For small values of d_c (corresponding to relatively poor clusters), Bahcall & Cen's results lie only slightly below the FOF_M correlation lengths, and for intermediate values the agreement is very good. For the rarest objects ($d_c \gtrsim 50\,h^{-1}\mathrm{Mpc}$), Bahcall & Cen apparently find that the r_0–d_c relation continues to increase linearly whereas that found here flattens off. Unfortunately, Bahcall & Cen do not quote uncertainties in their estimates but, since the volume they simulated is only about 40 per cent of the volume simulated for this study, their error bars will typically be ~ 1.6 larger and so the disagreement at large values of d_c is only marginally significant.

In Fig. 4.9 the real space results are also compared with those of Croft & Efstathiou (1994). Like Bahcall & Cen, they examined only one cluster selection algorithm (CE in Section 4.2.2) which was deliberately included in the list used here for comparison purposes. Again, the agreement is very good, particularly for $d_c \sim 40\,h^{-1}\mathrm{Mpc}$, where the error bars are small. For larger values of d_c the results are still statistically consistent although Croft & Efstathiou's values lie somewhat lower (Croft & Efstathiou do give error bars but, for clarity, these are omitted in the figure; they are slightly smaller than those for CE(0.5).) As pointed out by Croft & Efstathiou, their results disagree with those of Bahcall & Cen, except for the smallest values of d_c. Croft & Efstathiou suggested that this discrepancy could be due to a statistical fluctuation in Bahcall & Cen's single simulation. The two simulations also differ in their value of σ_8 (0.77 in the case of Bahcall & Cen; 0.59 in the case of Croft & Efstathiou; and an intermediate value in our case). However, as Fig. 4.8 shows, the effect of σ_8 on the real space correlation length is too weak to account for the difference between the results of Bahcall & Cen and those of Croft & Efstathiou. Fig. 4.9 suggests that the discrepancy might be caused by the use of different cluster selection criteria. When similar selection criteria are used, reasonably good agreement is found with both studies.

The previous comparison referred exclusively to correlation lengths in real space. Bahcall & Cen do not give any results in redshift space, but Croft & Efstathiou do and a comparison of their results and those presented here (for the same cluster selection criteria) is made in Fig. 4.10. Here the full correlation functions are plotted for CE(0.5) clusters with $d_c = 30\,h^{-1}\mathrm{Mpc}$, both in real space (open symbols) and in redshift space (filled symbols). The agreement in real space is excellent, confirming the earlier conclusion from Fig. 4.9. In redshift space, on the other hand, there are some discrepancies, particularly at small and intermediate pair separations, where the CE(0.5) correlation function lies systematically above Croft & Efstathiou's. The differences are small but significant given the small quoted errors. For example, at $s = 6.3\,h^{-1}\mathrm{Mpc}$, the value of ξ_{cc} is about 60 per cent higher than Croft & Efstathiou's. These differences are likely to be an underestimate since the simulation utilised here has $\sigma_8 = 0.63$, whereas theirs has $\sigma_8 = 1$ and, as has been shown, in redshift space $\xi_{cc}(s)$ is greater for larger values of σ_8. Apart from this difference in σ_8, the only other difference between the two analyses is the sampling strategy in the computation of $\xi_{cc}(s)$. The estimator in Section 4.2.4 is based on a straightforward computation using all the clusters in the simulations satisfying the selection criteria. whereas Croft & Efstathiou averaged over several realizations of subcatalogues with

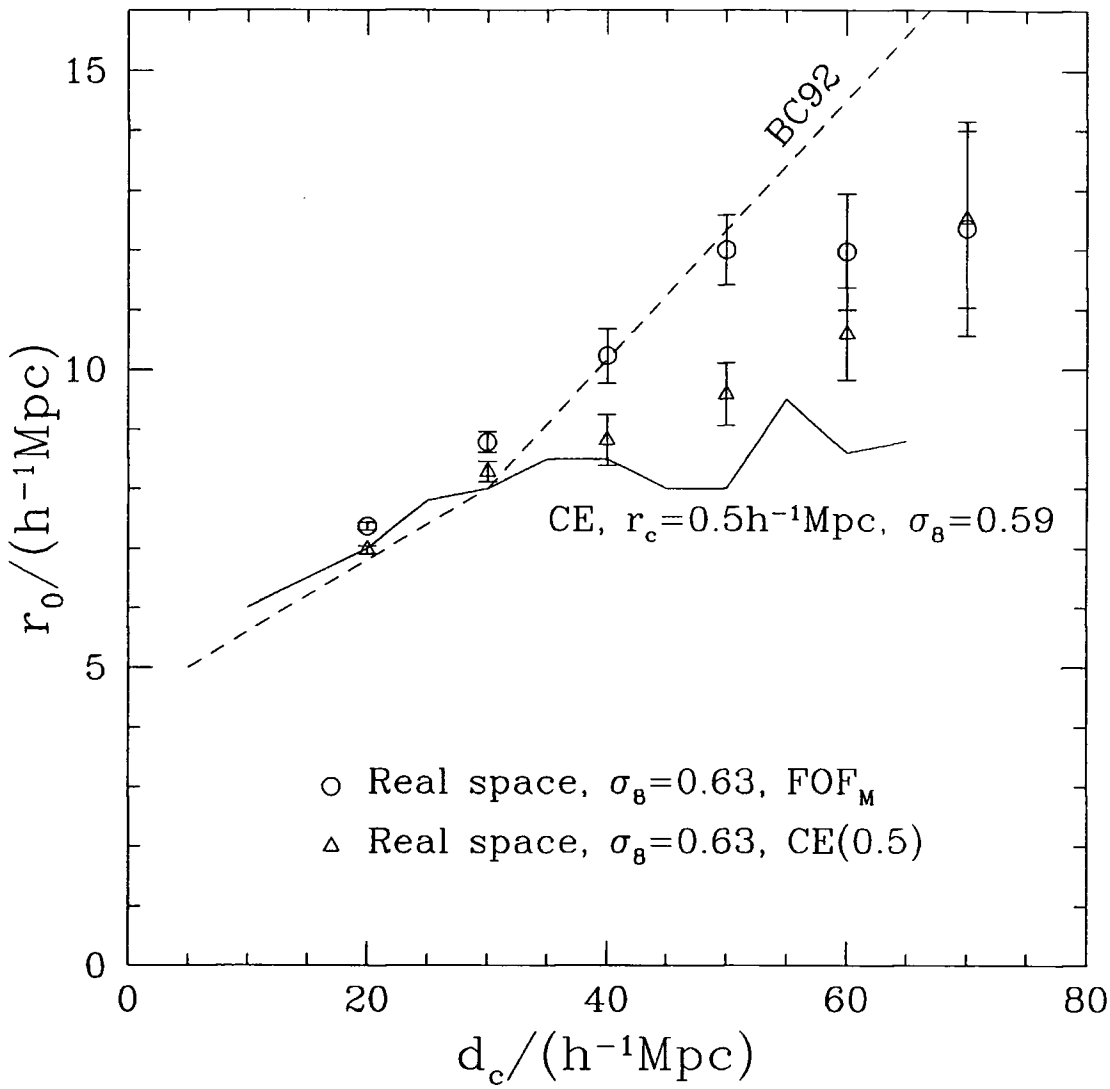

Figure 4.9: Comparison of simulation results from different studies. The plot shows the real space correlation length, r_0, as a function of the mean intercluster separation, d_c. The dashed line gives the results of Bahcall & Cen (1992) which should be compared with the results for FOF_M clusters (circles). The solid line gives results from Croft & Efstathiou (1994) which should be compared with the results for CE(0.5) (triangles). Within the statistical errors, the results agree with the two other studies even though these are inconsistent with one another.

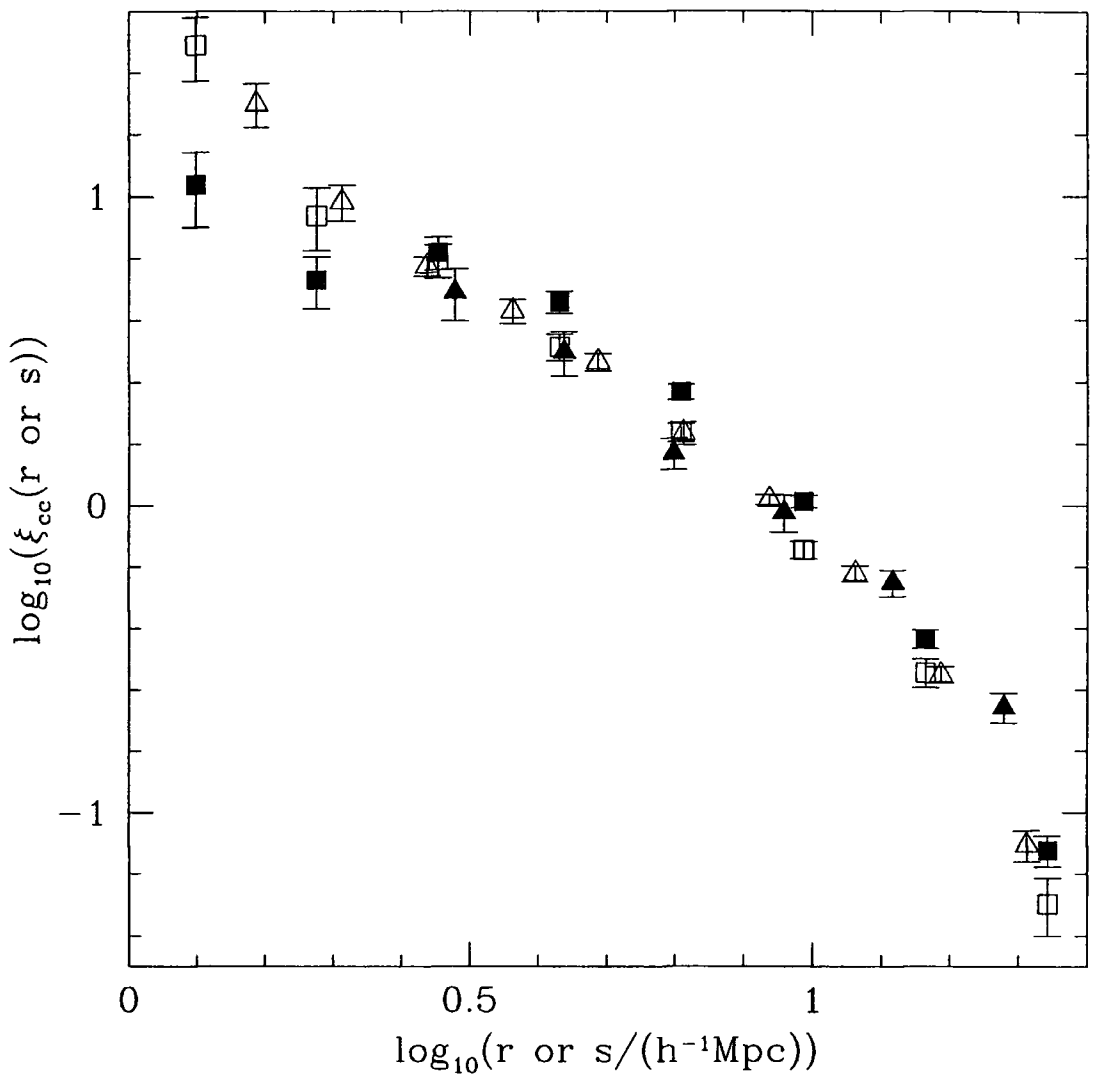

Figure 4.10: Comparison with the results of Croft & Efstathiou (1994). Correlation functions from the present study are shown by squares and those from Croft & Efstathiou by triangles. Open symbols show data in real space and filled symbols in redshift space. All correlation functions are for CE(0.5) groups with $d_c = 30\,h^{-1}$Mpc, but the simulations presented here have $\sigma_8 = 0.63$ whereas those of Croft & Efstathiou have $\sigma_8 = 1.0$.

the same abundance and selection function as the APM cluster catalogue of Dalton et al. (1992). Provided the correct selection function is used this procedure will give an unbiased estimate of the true correlation function in the simulation as a whole – the quantity which has been calculated directly here. Possible explanations for the relatively small discrepancies in Fig. 4.10 are residual systematic differences resulting from different simulation techniques and the choice of σ_8.

In summary, apart from the small differences in redshift space just mentioned, the cluster correlation functions in this study agree well with previous published work, provided the comparison is made *for cluster catalogues identified and selected in similar ways.* The apparent disagreement between the work of Bahcall & Cen (1992) and that of Croft & Efstathiou (1994) appears to have been largely caused by a different choice of group-finding algorithm.

4.5 Discussion and Conclusions

Bahcall & Cen (1992) and Croft & Efstathiou (1994) compared their simulation results with real data and in both cases concluded that the correlation function of clusters is incompatible with the standard CDM model, but is consistent with a low-density CDM model with $\Omega h \simeq 0.2$. At first sight this consensus seems rather surprising since, as Fig. 4.9 shows, the predicted cluster correlation functions in these two studies disagree. The explanation is simply that the comparison in each case was made against different datasets. Croft & Efstathiou compared their models with the APM cluster catalogue of Dalton et al. (1992) whereas Bahcall & Cen compared theirs with this catalogue and with Abell's catalogue as well. As may be seen from fig. 3 of Bahcall & Cen (1992), their cluster correlation function for the low-density model does not agree particularly well with the APM data and, as can be seen from fig. 4 of Croft & Efstathiou (1994), their low-density model strongly disagrees with the Abell cluster data. Thus, the two studies were able to arrive at the same conclusion because they compared different theoretical predictions for the same cosmological models against datasets that exhibit different clustering properties.

It has been shown here that, even in the idealized case where clusters are identified in the three-dimensional mass distribution of a simulation, significantly different outcomes for the cluster correlation function are possible depending on how exactly the clusters are defined and on how the data are analysed. It is unclear which, if any, of the various possible definitions of clusters in the simulations is appropriate for a comparison with the real data. This difficulty is particularly severe in the case of optical catalogues since the identification of clusters in the projected galaxy distribution is very different from the identification of clusters in the three-dimensional mass distribution of a simulation. Biases in ξ_{cc} arising from projection effects have been shown to be present in Abell's catalogue (Sutherland 1988; Sutherland & Efstathiou 1991; Dekel et al. 1989). The lack of large anisotropies in ξ_{cc} for APM clusters suggests that this catalogue is largely unaffected by biases of this kind, but this important feature by itself does not remove the ambiguity regarding the

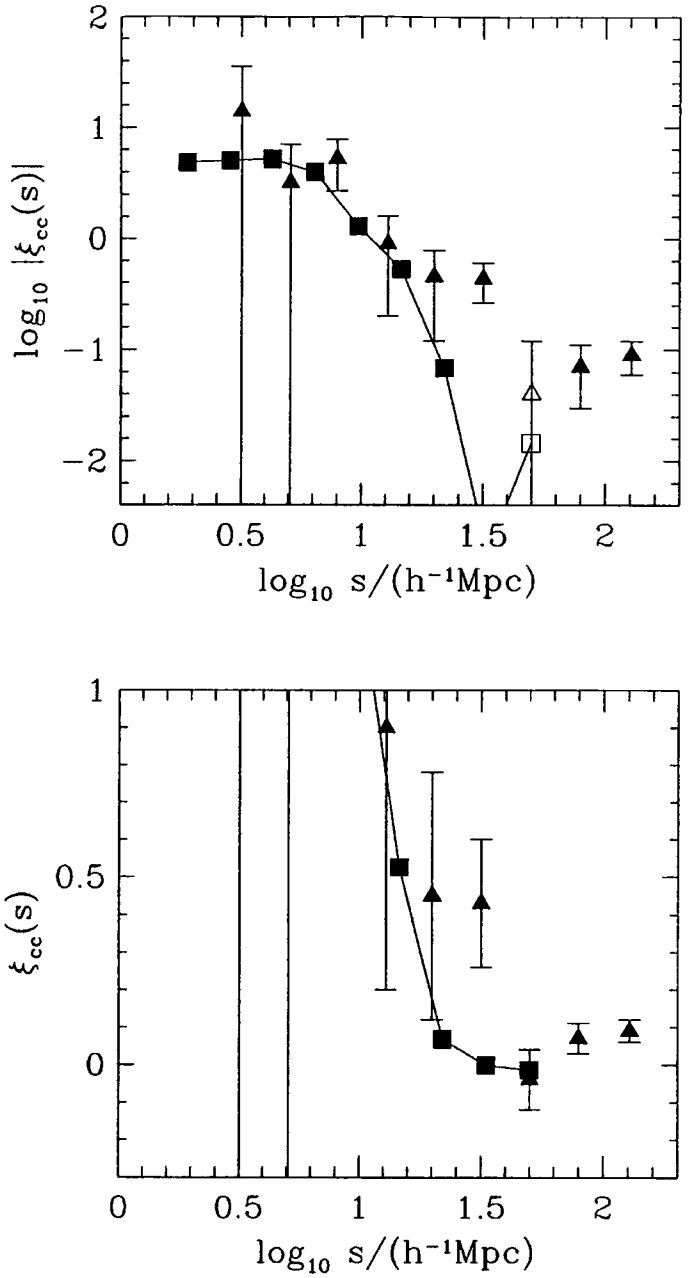

Figure 4.11: Comparison between the CDM cluster correlation function and data for X-ray selected clusters. The squares show redshift space results for SOX_{L_x} clusters with $d_c = 40\,h^{-1}\mathrm{Mpc}$ and $\sigma_8 = 0.63$. The triangles show the correlation function estimated by Romer et al. (1994) for a sample of clusters selected using a combination of *ROSAT* X-ray data and optical data. The upper panel shows $\log_{10}|\xi_{cc}(s)|$, with open symbols corresponding to values of $\xi_{cc}(s) < 0$. The lower panel is a linear-log plot of the region where $\xi_{cc} < 1$ which shows the large-scale behaviour more clearly.

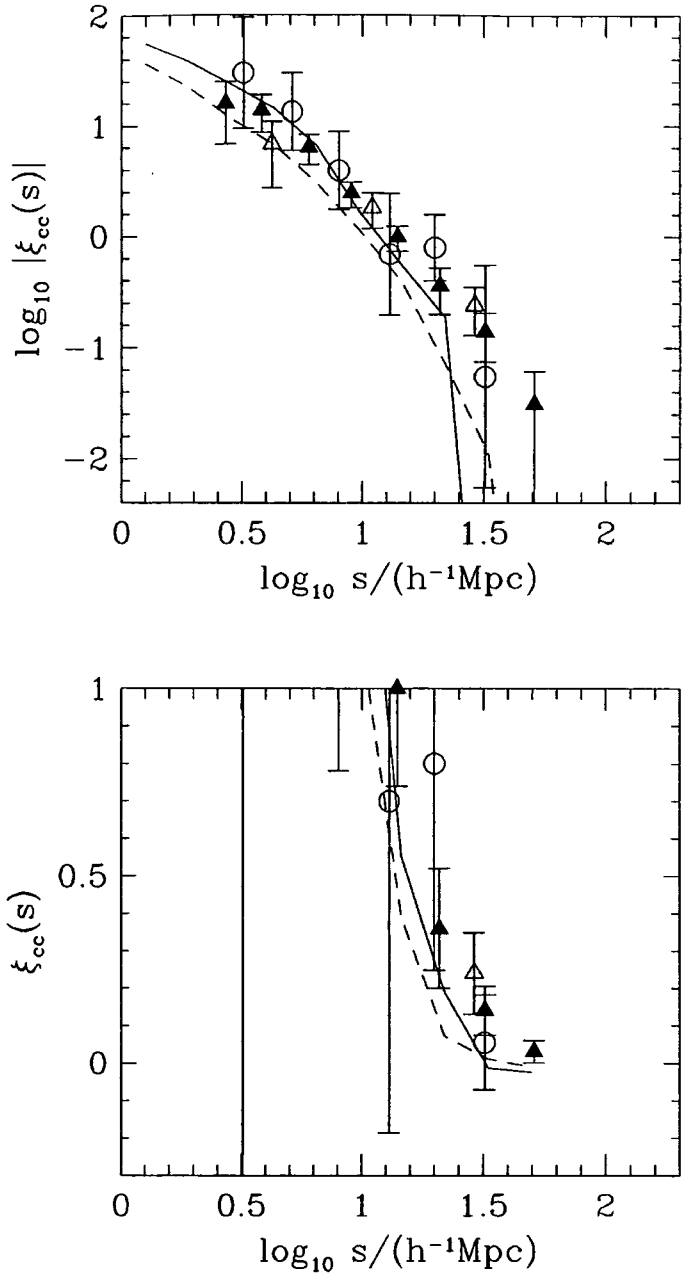

Figure 4.12: Comparison between CDM cluster correlation functions and data for optically selected clusters. The triangles show correlation functions for APM clusters: filled triangles for the $d_c = 31\,h^{-1}$Mpc sample of Dalton et al. (1994), and open triangles for the $d_c = 45\,h^{-1}$Mpc sample of Efstathiou et al. (1992). The open circles show the correlation function estimated by Nichol et al. (1992) for the $d_c \simeq 50\,h^{-1}$Mpc clusters in the Durham-Edinburgh survey. The dashed line shows the model results for SO_v clusters, with $d_c = 30\,h^{-1}$Mpc, and the solid line for SO_v clusters with $d_c = 50\,h^{-1}$Mpc. All model correlation functions were calculated in redshift space.

identification of galaxy clusters in real catalogues with mass clusters in simulations. Identifying cluster populations in both by matching the spatial number density is not a unique procedure since, as has been shown, even at a fixed number density, the cluster correlation function depends, for example, on the statistic used to rank the clusters. In practice, it seems likely that even larger uncertainties will be introduced by the difficulty of determining the richness of clusters in projection and by the associated uncertainties in the estimation of their spatial number density. X-ray selected clusters provide, in principle, cleaner observational samples, but even in this case the comparison with theoretical models is restricted by the lack of reliable predictions.

Figs 4.11 and 4.12 illustrate how some of the uncertainties that have been mentioned can affect the confidence with which a specific model is constrained by measurements of ξ_{cc}. Here, predictions based on the standard cold dark matter model – the model which Bahcall & Cen (1992), Croft & Efstathiou (1994) and Dalton et al. (1994) claim to be strongly excluded by the cluster correlation function data – are compared with various observational determinations of ξ_{cc}. In Fig. 4.11 estimates for SOX 'X-ray selected' clusters are compared with the *ROSAT* data of Romer et al. (1994). This catalogue is not volume-limited and thus contains clusters with a range of intrinsic X-ray luminosities. The simulations, however, indicate that the variation of the correlation length of SOX 'X-ray selected' clusters with cluster X-ray luminosity (or richness) is small compared with the uncertainties in the data. Within these large statistical errors, the agreement is good except, perhaps, on the largest scales where the observed signal is small and could be affected by systematic uncertainties in the mean number density of clusters. The size of the discrepancy on large scales may be better appreciated in the linear-log plot in the lower panel of this figure.

In Fig. 4.12, the estimates for SO_v clusters (in redshift space) are compared with data for 'optical' clusters from the APM (Efstathiou et al. 1992; Dalton et al. 1992, 1994) and Edinburgh-Durham (EDCC) (Nichol et al. 1992) catalogues. The APM sample shown by filled triangles has a mean intercluster separation $d_c \simeq 31\,h^{-1}$Mpc, and should be compared with the dashed line which shows the model predictions for approximately the same mean intercluster separation. The APM sample shown by open triangles has $d_c \simeq 45\,h^{-1}$Mpc and the EDCC sample has $d_c \simeq 50\,h^{-1}$Mpc. These should be compared with the solid line which shows the model results for $d_c = 50\,h^{-1}$Mpc. On intermediate scales only the denser sample (which has the smaller error bars) is inconsistent with the model, but the discrepancy is quite small and certainly much smaller than the discrepancy found by Dalton et al. (1994) for the same model (cf. their fig. 4). The reason for this difference is simply that the group-finder applied to the simulations by Dalton et al. happens to give one of the lowest correlation functions of all the group-finders that have been explored in this chapter. On large scales there is an indication that the data are more clustered than the models and, again, the linear-log plot clearly shows that this discrepancy is small.

To summarize, large N-body simulations allow very precise estimates of the clus-

ter correlation function once a specific prescription for identifying clusters is adopted. For a given cosmological model, the statistical uncertainties in these predictions are small compared with the observational errors for existing cluster samples. Unfortunately, they are also small compared with the systematic variations exhibited by cluster samples constructed from the simulations by making different assumptions. This analysis shows that the exact form and amplitude of the correlation function of clusters identified in the mass distribution of N-body simulations depend on various factors. In rough order of importance these include: (i) the group-finding algorithm and the statistic used to rank clusters in a catalogue (e.g. mass, velocity dispersion, 'X-ray' luminosity, etc.); (ii) the mean density of clusters in the catalogue; (iii) whether clustering is measured in real or in redshift space; and (iv) the assumed value of σ_8. These various factors can produce large variations in the resulting clustering length. For example, in the range most relevant to observational data, $30 \leq d_c \leq 60\,h^{-1}$Mpc, the 'X-ray selected' catalogues in a model with $\sigma_8 = 0.5$ have real space clustering lengths varying between 7 and 10 h^{-1}Mpc, whereas catalogues selected by velocity dispersion in a model with $\sigma_8 = 0.63$ have redshift space correlation lengths varying from 10 to $13\,h^{-1}$Mpc.

Of the four complicating factors listed above, only the first two refer directly to cluster catalogues. The third one should be straightforward to eliminate but it has sometimes been ignored in comparisons of model predictions with data (e.g. Bahcall & Cen 1992). Similarly, the value of σ_8 appropriate to a given cosmological model is usually fixed from other considerations such as the amplitude of fluctuations in the temperature of the cosmic microwave background or the abundance of galaxy clusters (White et al. 1993). There are, however, uncertainties associated with this procedure arising, for example, from possible contamination of the microwave background signal by tensor modes or uncertainties in the masses of clusters.

The resolution of the cluster clustering debate will require further observational and theoretical work. From the observational point of view, progress will come from the analysis of large homogeneous samples of clusters selected entirely from X-ray data or from large redshift surveys such as the forthcoming SDSS and 2df galaxy surveys. From the theoretical point of view, it will be necessary to model in detail the selection procedures employed by observers. Artificial catalogues constructed from cosmological simulations are a valuable aid, but several complications need to be borne in mind. For example, to model the selection of APM clusters, it is necessary to simulate the entire APM galaxy survey and this, in turn, requires modelling the uncertain connection between the distribution of dark matter and the formation sites of galaxies. Modelling cluster catalogues constructed from X-ray data is a simpler problem theoretically since it bypasses the complications associated with galaxy formation. Nevertheless, it requires a better understanding of the mechanisms that determine the total cluster X-ray luminosity than is available at present.

4.6 References

Abell G. O., 1958, ApJS, 3, 211
Abell G. O., Corwin H. C., Olowin R. P., 1989, ApJS, 70, 1
Bahcall N. A., Cen R., 1992, ApJ, 398, L81
Bahcall N. A., Soneira R. M., 1983, ApJ, 270, 20
Bahcall N. A., West M. J., 1992, ApJ, 392, 419
Bardeen J. M., Bond J. R., Kaiser N., Szalay A. S., 1986, ApJ, 304, 15
Barnes J., Dekel A., Efstathiou G., Frenk C. S., 1985, ApJ, 295, 368
Borgani S., Plionis M., Coles P., Moscardini L., 1995, MNRAS, 277, 1191
Couchman H. M. P., 1991, ApJ, 368, L23
Couchman H. M. P., 1995, in Numerical Methods in Astrophysics, Vol. II, Springer-Verlag, New York, in press
Croft R. A. C., Efstathiou G., 1994, MNRAS, 267, 390
Dalton G. B., Efstathiou G., Maddox S. J., Sutherland W. J., 1992, ApJ, 390, L1
Dalton G. B., Croft R. A. C., Efstathiou G., Sutherland W. J., Maddox S. J., Davis M., 1994, MNRAS, 271, L47
David L. P., Slyz A., Jones C., Forman W., Vrtilek S. D., 1993, ApJ, 412, 479
Davis M., Efstathiou G., Frenk C. S., White S. D. M., 1985, ApJ, 292, 371
Dekel A., Blumenthal G. R., Primack J. R., Olivier S., 1989, ApJ, 338, L5
Efstathiou G., Eastwood J., 1981, MNRAS, 194, 503
Efstathiou G., Davis M., Frenk C. S., White S. D. M., 1985, ApJS, 57, 241
Efstathiou G., Dalton G. B., Maddox S. J., Sutherland W. J., 1992, MNRAS, 257, 125
Evrard A. E., 1990, ApJ, 363, 349
Kaiser N., 1984, ApJ, 284, L9
Kaiser N., 1987, MNRAS, 227, 1
Klypin A. A., Kopylov A. I., 1983, Sov. Astron. Lett., 9, 41
Lacey C., Cole S., 1994, MNRAS, 271, 676
Lahav O., Edge A., Fabian A. C., Putney A., 1989, MNRAS, 238, 881
Lumsden S. L., Nichol R. C., Collins C. A., Guzzo L., 1992, MNRAS, 258, 1
Navarro J. F., Frenk C. S., White S. D. M., 1995, MNRAS, 275, 720
Nichol R. C., Collins C. A., Guzzo L., Lumsden S. L., 1992, MNRAS, 255, 21p
Nichol R. C., Briel U. G., Henry J. P., 1994, MNRAS, 267, 771
Peacock J. A., West M. J., 1992, MNRAS, 259, 494
Postman M., Huchra J. P., Geller M. J., 1992, ApJ, 384, 404
Romer A. K., Collins C. A., Cruddace R. G., MacGillivray H., Ebeling H., Böhringer H., 1994, Nature, 372, 75
Smoot G. F., et al., 1992, ApJ, 396, L1
Soltan A., 1988, MNRAS, 231, 309
Sutherland W. J., 1988, MNRAS, 234, 159
Sutherland W. J., Efstathiou G., 1991, MNRAS, 248, 159
Turok N., 1983, Phys. Lett., 123B, 387
Turok N., Brandenberger R., 1986, Phys. Rev., D33, 2175
Watanabe T., Matsubara T., Suto Y., 1994, ApJ, 432, 17
White S. D. M., Frenk C. S., Davis M., Efstathiou G., 1987, ApJ, 313, 505

White S. D. M., Efstathiou G., Frenk C. S., 1993, MNRAS, 262, 1023
Wright E. L., Smoot G. F., Kogut A., Hinshaw G., Tenorio L., Lineweaver C., Bennett C. L., Lubin P. M., 1994, ApJ, 420, 1
Zel'dovich Ya. B., 1970, A&A, 5, 84

Chapter 5

A procedure for improving the spatial resolution of numerical simulations

5.1 A brief overview of simulation techniques

There are three main requirements in all numerical simulations of the growth and evolution of large-scale structure. First of all, a set of initial particle positions and velocities representing the desired mass fluctuation spectrum needs to be generated. Then it is necessary to calculate the forces on the particles. Finally, an integration scheme is needed to use the accelerations and propagate the particles forward in time. Most of the diversity in the methods currently being used for numerical simulations exists in the second category. The force calculation is by far the most time-consuming part of the simulation method. Consequently, the technique employed to perform this operation is of paramount importance in deciding what type of simulations can be attempted.

For the vast majority of simulations of large-scale structure, initial conditions are produced using the Zel'dovich approximation (Zel'dovich 1970). Particles are placed on a regular cubic grid and then displaced in such a way that the required mass fluctuation spectrum is obtained. According to the Zel'dovich approximation, the particle displacements are proportional to their peculiar velocities. Thus, initial conditions must be set up at a time before any significant structure forms. Specific details of the implementations used are given in Efstathiou et al. (1985) and Couchman (1995). Second-order accurate integration routines are ubiquitous among cosmological simulation methods, with either a leapfrog or a Runge-Kutta integrator being typical. A review of this aspect of the field is given in the excellent article by Benz (1990a).

The calculation of forces will be considered in two sections; first the case where all particles interact only via gravity, and then the case where additional gas physics

is incorporated.

The simplest way to calculate the forces on N particles resulting from the gravity of the other ones is by direct summation of the forces from the remaining $N-1$ particles. Unfortunately, with the requirement that N be large, the time spent per step for this procedure, which scales with N^2, becomes impractically long. One of the earliest applications of this technique to the study of rich galaxy clusters was performed by Aarseth in 1963. He took advantage of "the introduction of high-speed computers" to present simulations with values of N in the range $25-100$. Comparing this with the largest modern simulations which have $N \sim 16$ million (Gelb & Bertschinger 1994, Jenkins et al. in preparation), the extent to which the numerical capabilities have advanced can be appreciated. With present-day computers, direct particle-particle (PP) summation methods can only reasonably be used for $N \lesssim 10^5$, so the factor by which N has increased as a result of gains in computational speed is similar to that from improvements in the efficiency of the force-calculating algorithms. A major step forward in simulation techniques was produced by calculating the force using a mesh. This involves gridding the particles to form a density field and then using a Fast-Fourier Transform (FFT) to derive the gravitational potential according to Poisson's equation. By differencing the resulting potentials on the grid points, smooth forces can be found at any position within the simulation. Hockney & Eastwood (1981) give an account of these particle-mesh (PM) calculations, and early examples of their use in cosmology include Klypin & Shandarin (1983), Miller (1983) and White, Frenk & Davis (1983). For large grids including M cells this method scales, like an FFT, with $M\ln(M)$. To maximise the spatial resolution of the force without being inefficient, the number of cells in the mesh is chosen to be similar to the number of particles in the simulation, so this method is much more economical than a simple PP calculation when N is large. The drawback is that the spatial resolution is essentially fixed by the size of an individual mesh cell. When structure becomes significantly clumpy, the internal structures of objects smaller than this mesh size are washed out.

This difficulty can be surmounted by combining the PP and PM methods. The resulting P^3M technique is described by Hockney & Eastwood, and Efstathiou et al. (1985) give a comprehsive description of the application to cosmological simulations. While a mesh is used to calculate the force resulting from material at large distances, the nearby matter is treated in a PP fashion. Efstathiou et al. illustrate how the mesh and short-range forces are matched to produce a smooth overall force. When the mass becomes significantly clustered however, the performance of P^3M degrades rapidly because of the large number of PP calculations required to evolve particles accurately in the overdensities. Couchman (1991) addressed this problem by introducing additional sub-meshes to help in the calculation of the short-range force. These refinements are only placed in regions of sufficiently high density. By using a fine grid to calculate some of the close-range forces, the amount of PP evaluation is reduced and the performance degradation for clumpy distributions is dramatically reduced. Depending on the overdensity in any particular piece of a simulation, extra layers of refinement can be put down to cover the region of difficulty. This flexibility gives rise to the name Adaptive P^3M or AP^3M.

A slightly different procedure for calculating gravity is based on using a tree structure to group particles with their near neighbours. With the tree trunk representing the node containing all particles in the simulation, the individual particles correspond to leaves at the end of a network of branches. When calculating the gravitational force on a particular particle, only nearby particles are treated individually, whereas further ones are lumped together and the contribution from entire 'branches' is used. When deciding whether or not to open a particular node into subnodes, the ratio of the size of the node to the distance to the particle under consideration is the crucial parameter. The inverse tangent of this is the 'opening angle' which needs to exceed a threshold value before a node is sufficiently close to merit being split into subnodes. Different ways of defining the 'branches' have been employed in astronomical situations (for example see Barnes & Hut 1986; Benz et al. 1990).

While treecodes are used for gravity-only simulations, they are particularly well suited to experiments including gas using the Smoothed Particle Hydrodynamics (SPH) method. SPH will be described in more detail in the next section, but the main requirement of the method is a list of nearby gas neighbours which will contribute to the non-gravitational acceleration of a given gas particle. Hernquist & Katz (1989), Steinmetz & Müller (1993) and Navarro & White (1993) describe different implementations of TreeSPH. Using neighbours found when calculating the PP force, one can also combine SPH with P^3M-type methods. Evrard (1988) produced the first P^3MSPH code and, more recently, an AP^3MSPH code (also called Hydra) has been developed (Couchman, Thomas & Pearce 1995). Other methods of including hydrodynamics into large cosmological simulations include the 'sticky' particles used by Carlberg (1988), and the mesh-based techniques advocated by Cen et al. (1990) amongst others. The relative merits of the main different hydrodynamical methods will be considered at the end of the next section.

5.2 The Smoothed Particle Hydrodynamics (SPH) method

The SPH method (see Gingold & Monaghan 1977, Benz 1990b or Monaghan 1992 for a more complete review) assigns thermodynamic properties to individual 'gas' particles in a simulation. Calculating the thermodynamic properties of any particle involves a sum over other particles, with a kernel weighting the contributions depending on the distance to the interpolation centre. More specifically, the estimated value of a particular quantity, $f(\mathbf{x_i})$, at position $\mathbf{x_i}$ is given by

$$\langle f(\mathbf{x_i}) \rangle = \sum_{j=1}^{N} \frac{m_j}{\rho(\mathbf{x_j})} f(\mathbf{x_j}) W(|\mathbf{x_i} - \mathbf{x_j}|, h). \tag{5.1}$$

The kernel, denoted by W, depends upon the individual gas particle smoothing lengths through the smoothing length h. m_j, $\mathbf{x_j}$ and $\rho(\mathbf{x_j})$ represent the mass, three-dimensional position and density of particle j. The sum is carried out over all other

gas particles, although in practice a form is chosen for the kernel that has $W = 0$ for $|\mathbf{x_i} - \mathbf{x_j}| \geq 2h$. In addition, the individual particle smoothing lengths are set depending on $\rho(\mathbf{x_j})^{-1/3}$, in order to keep approximately $N = 35$ nearest neighbours contributing to the sum. The smoothing length is often defined as $h = 0.5(h_i + h_j)$, i.e. the arithmetic mean of the two particle smoothing lengths, although when very large density gradients exist, other methods of choosing the weights given to the kernel by each particle can have some advantages (see Hernquist & Katz 1989). As a result of the diversity of SPH implementations, this brief overview will concentrate on the particular options chosen by Navarro & White (1993), for it was a version of the code they produced (based on the one used by Benz et al. 1990) that was adapted for the *GRAPE* and employed in Chapter 6. Following Monaghan & Lattanzio (1985), the shape used for the kernel is

$$W(r,h) = \frac{1}{\pi h^3} \begin{cases} 1 - \frac{3}{2}v^2 + \frac{3}{4}v^3 & \text{if } 0 \leq v \leq 1; \\ \frac{1}{4}(2-v)^3 & \text{if } 1 \leq v \leq 2; \\ 0 & \text{otherwise} \end{cases} \tag{5.2}$$

where $v = r/h$.

As well as a mass, each gas particle is also assigned an internal energy u_i, and then, using an appropriate equation of state, all thermodynamic variables can be calculated via equation (5.1). For cosmological simulations it is usual to treat the gas like an ideal gas, that is $\gamma = 5/3$ and $p = (\gamma - 1)\rho u$ where p represents the pressure. The acceleration of a gas particle resulting from the pressure gradient can then, to second order accuracy in h, be written as

$$\frac{\mathrm{d}\mathbf{v_i}}{\mathrm{d}t}\left(= -\frac{\nabla p}{\rho}\right) = -\sum_{j=1}^{N} m_j \left(\frac{p_i}{\rho_i^2} + \frac{p_j}{\rho_j^2}\right) \nabla W(|\mathbf{x_i} - \mathbf{x_j}|, h). \tag{5.3}$$

In order to allow kinetic energy to be converted to thermal energy as would happen during a shock between colliding gaseous objects an artificial viscosity term is included. As illustrated by Monaghan & Gingold (1983) using simple shock-tube simulations, the additional acceleration can be satisfactorily described by

$$\frac{\mathrm{d}\mathbf{v_i}}{\mathrm{d}t} = -\sum_{j=1}^{N} m_j \Pi_{ij} \nabla W(|\mathbf{x_i} - \mathbf{x_j}|, h), \tag{5.4}$$

where the artificial viscosity term Π_{ij} is given by

$$\Pi_{ij} = \begin{cases} \frac{-\alpha c_{ij}\mu_{ij} + \beta\mu_{ij}^2}{\rho_{ij}} & \text{if } (\mathbf{v_i} - \mathbf{v_j}) \cdot (\mathbf{x_i} - \mathbf{x_j}) \leq 0; \\ 0 & \text{otherwise.} \end{cases} \tag{5.5}$$

c_{ij} and ρ_{ij} represent the arithmetic mean of the sound speeds and the densities respectively of the two particles. The estimate of the velocity divergence is given by

$$\mu_{ij} = \frac{h(\mathbf{v_i} - \mathbf{v_j}) \cdot (\mathbf{x_i} - \mathbf{x_j})}{|\mathbf{x_i} - \mathbf{x_j}|^2 + \epsilon h^2}. \tag{5.6}$$

ϵh^2 is just a small term to avoid divergences.

In addition to the acceleration resulting from gas physics, one also needs to solve equations for the evolution of the internal energy and smoothing length of each particle. These are given by

$$\frac{\mathrm{d}u_i}{\mathrm{d}t} = \sum_{j=1}^{N} \left(\frac{p_i}{\rho_i^2} + \frac{\Pi_{ij}}{2} \right) (\mathbf{v_i} - \mathbf{v_j}) \cdot \nabla W(|\mathbf{x_i} - \mathbf{x_j}|, h) - \frac{\Lambda(u_i, \rho_i)}{\rho_i}. \tag{5.7}$$

and

$$\frac{\mathrm{d}h_i}{\mathrm{d}t} = -\frac{1}{3}\frac{h_i}{\rho_i}\frac{\mathrm{d}\rho_i}{\mathrm{d}t} = \frac{1}{3} h_i \nabla \cdot \mathbf{v_i} \tag{5.8}$$

respectively. The Λ term in equation (5.7) represents cooling (or if negative, heating) processes. As the only experiments attempted here are adiabatic (i.e. $\Lambda = 0$), it will not be considered any further. Equation (5.8) uses the fact that the particle density scales approximately like $\rho_i \propto h_i^{-3}$, and allows the smoothing lengths to be updated to include the desired number of neighbours, taken to be $25 \leq N \leq 45$. If the calculated h_i do not produce satisfactory Ns, then they are repeatedly changed until they do.

This SPH method produces spatially varying resolution; an overdense region with more particles and smaller h_i values will be better modelled than an underdense region with very few particles and large smoothing lengths. In addition, individual time-steps for different particles are readily included, thus making the procedure increasingly efficient by avoiding spending too much time accurately integrating the orbits of particles in underdense regions. Navarro & White (1993) use a second-order Runge-Kutta integrator with a hierarchy of particle time-steps related by factors of 2. For any given particle, the required time-step is chosen such that the size of the higher order error term is less than some specified tolerance.

Combining a tree structure to calculate gravitational forces with SPH, which can readily use near gas neighbours found from the tree, provides a very flexible method for studying two-component systems. The manner in which the forces are calculated also makes it reasonably easy to slot in additional physical processes such as radiative cooling, star formation, feedback from supernovae, photoionization and magnetic fields (see Evrard 1988; Katz & Gunn 1991; Monaghan 1992; Umemura 1993; Navarro & White 1993; Metzler & Evrard 1994; Steinmetz & Müller 1994; Katz, Weinberg & Hernquist 1996 for example). Compared with the Eulerian techniques which give the thermodynamic properties to each fixed mesh cell (Cen et al. 1990 amongst others), the major advantage enjoyed by SPH codes is the larger dynamic range provided by the Lagrangian nature of the method. For example, a medium-sized SPH cluster simulation can provide information about the gas thermodynamic properties on scales down to $\sim 20 - 30\mathrm{h}^{-1}\mathrm{kpc}$, which is about an order of magnitude better than current mesh-based codes can manage. This statement is based on the resolution provided by a 500^3 grid in a simulation cube of side $50\,h^{-1}\mathrm{Mpc}$. In order to sample a representative patch of universe this is about the minimum volume expected to contain a rich cluster and 500^3 cells is about the limit of what is feasible with present supercomputers (Gramann et al. 1995). Results from Cen's (1992) work show that the actual spatial resolution length is actually about $2 - 3$ times the individual cell size. While the Eulerian method is superior to

SPH on large scales and in voids, the ability to resolve small scales in cluster simulations is very important, crucially so if the centrally concentrated cluster X-ray luminosity is to be studied (Navarro et al. 1995).

One shortcoming of the Lagrangian approach is the relative difficulty in following the propagation of error terms and this has led to a certain degree of caution being expressed in the end results of such simulations (e.g. Anninos & Norman 1996). As the name suggests, SPH is most accurate when applied to smooth fluid distributions, so the ad hoc treatment of shocks is not as good as with a mesh technique where shock fronts are significantly sharper. Testing SPH methods against analytical solutions to, preferably relevant, problems such as Bertschinger's (1985) self-similar shocked accretion model is therefore of vital importance in establishing the credibility of such approaches.

5.3 Using the *GRAPE*

5.3.1 What is a *GRAPE* ?

With the fundamental requirements of force-calculation for cosmological simulations set out, the benefits brought by the *GRAPE* hardware should become very apparent. This special-purpose machine is designed specifically to calculate very rapidly PP forces on a large number of particles. It has an additional feature whereby it returns a list of neighbours within a distance h_i of each particle i. Given that the majority of the computational time in the TreeSPH simulations is spent calculating gravity and searching through the tree to find neighbours for the SPH force calculations, the *GRAPE* clearly represents an opportunity to increase the scientific scope of such numerical simulations.

A few different generations of *GRAPE* hardware have been developed and produced in Japan. The *GRAPE* which will be referred to here is the $3Af$ model currently installed in Edinburgh. For technical details concerning the operation of the machine, the reader is referred to Sugimoto et al. (1990) and Okumura et al. (1993). An excellent article describing an adaptation of SPH to the *GRAPE* has been produced by Steinmetz (1996). Nevertheless, some of the changes required to convert TreeSPH to *GRAPE*-SPH will now be reiterated.

5.3.2 Adapting TreeSPH for the *GRAPE*

The *GRAPE* consists of a 'board' onto which the positions and masses of up to 131072 particles can be loaded. Gravitational forces and potentials resulting from the particles on the board can be calculated on up to 8 particles simultaneously

assuming a standard Plummer force law:

$$\frac{\mathrm{d}\mathbf{v_i}}{\mathrm{d}t} = -\sum_{j=1}^{N} \frac{m_j(\mathbf{x_i} - \mathbf{x_j})}{(|\mathbf{x_i} - \mathbf{x_j}|^2 + \epsilon^2)^{1.5}}, \tag{5.9}$$

where ϵ is the gravitational softening. The 8 particles are loaded onto the 8 integrator 'chips'. A correction for the self-potential on particle i should be made by adding m_i/ϵ to the value returned by the *GRAPE* .

If required, then the board particles are searched to find neighbours within $\sqrt{4h_i^2 + \epsilon^2}$ of the individual chip particles. With a variable smoothing length, this procedure does not guarantee the condition of mutual neighbours, leading to asymmetric forces and non-conservation of momentum. To reduce this problem, the search radius is increased by $\sqrt{1.5}$. Another difficulty with the neighbour finding is that the total number of neighbours (not double-counting those board particles that are neighbours of more than one chip particle) is limited to 1023. If cooling is not included then this is unlikely to be a problem, but an extra complication such as loading fewer chips at a time or arranging the particles on the chips all to be in a similar location is required to deal with this. Loading the board separately with dark matter and gas particles assists by preventing dark matter clogging up the neighbour list when it is not going to contribute to the SPH force calculation. See the paper by Steinmetz (1996) for other routes around this problem.

The ranges in length and mass can be given in terms of the minimum length and mass units *minx* and *minm* as $minx[-2^{18}, 2^{18}]$ and $minm[1, 64\epsilon/minx]$. For the simulations described in this thesis only the second of these conditions is important. The method chosen to overcome the difficulty is to load the board a number of times with particles of similar masses at any one time. Forces are calculated using masses scaled to fit into the available range, and after computation they are rescaled to have the correct amplitude.

A peculiarity of the current *GRAPE* in Edinburgh is the tendency to return completely incorrect neighbour lists very occasionally (Jenkins and Heggie, private communications). By checking the first neighbour for the particle on the first chip this event can be detected and the neighbours recalculated. When looping back automatically, allowance should be made for the $\sim 4\%$ error in the measured neighbour distances.

While the *GRAPE* hardware is slightly temperamental when many different users try to run jobs concurrently, the benefits in speed are well worth the very slight adaptations required to TreeSPH codes. The hardware parallelisation coupled with the Fortran or C subroutines provided to return the required quantities make the *GRAPE* a very attractive option. More computational power at the 'front-end' workstation will be required in future to prevent the hydrodynamical calculations carried out on the host from limiting the speed gained by the rapidly evolving *GRAPE* technology.

5.4 The multi-mass approach

With the *GRAPE*-SPH method for carrying out a simulation now in place, the remaining job is to create a sensible set of initial conditions. The procedure which will be outlined below is similar to that utilised by Navarro et al. (1995). It involves taking the final output from a dark matter only AP^{3}M simulation, tracing back the particles which end up in an object of interest to be resimulated at higher resolution, and placing a cube around them in the initial conditions. Many more particles, both dark matter and gas this time, are then placed into this 'high-resolution' cube. In addition to the density perturbations previously present in this region, some more waves coming from smaller scales which are now below the Nyquist frequency of the new particle grid can also be included. This enables a wider range of scales from the desired power spectrum to be represented. Outside the high-resolution region, particles with masses increasing in proportion to their distance from the cube centre are placed down to model the tidal field. More detail of the individual steps is now given, with particular reference to the procedure used in Chapter 6 to resimulate cluster-sized objects.

5.4.1 Selecting a high-resolution region to resimulate

The 'spherical overdensities' algorithm used in Chapters 2 and 4 and described in more detail by Lacey & Cole (1994), was employed to find the largest virialised objects in an AP^{3}M simulation. By measuring the infall pattern of radial velocities, estimates of both the virial and turnaround radii were made. The extracted region was chosen to be a sphere centred on the centre of mass of the virialised clump of particles. Typically the radius of this sphere was between the virial and turnaround values. See section 5.5 for a justification of this choice.

Once a region of interest is defined in the final frame, the positions of the particles within this boundary are then traced back to the initial conditions and the minimum cube (with sides parallel to those of the original large simulation box) is placed around them. This region will be referred to as the high-resolution cube. For the cluster simulations described in Chapter 6 the ratio of high-resolution cube to original simulation box lengths was approximately 40/180, implying that no more than $\sim 1\%$ of the original volume contained mass that collapsed into the final cluster.

5.4.2 Adding extra small-scale power

Once the high-resolution cube has been defined, the next task is to populate it with particles. This could be done by interpolating the displacements used for the original run to allow for the extra particles which will be placed in the high-resolution cube. However, this would not take advantage of the higher Nyquist frequency produced by the improved resolution. Additional power can be included to exploit the extra

resolution at small scales. It is then necessary to decide up to what scale the new fluctuations should be added. If none of the original phases of the long-wavelength modes are retained then it is highly unlikely that the carefully extracted cluster region will contain anything of interest! However, if the crossover length between 'old' and 'new' waves is too small then the inability of the coarse grid to represent small-wavelength perturbations will become a problem. In practice the original long-wavelength modes are retained down to a scale lower than the size of the high-resolution region and larger than the Nyquist wavelength of the original particle grid.

An example of the effect that adding small-wavelength power has on the power spectrum of mass fluctuations $P(k)$ is now considered. From an original $180\,h^{-1}$Mpc-sized cube containing 64^3 particles a high-resolution cube with length $36\,h^{-1}$Mpc was populated with 40^3 particles. This decreases the mean interparticle separation in the region of interest by a factor of ~ 3, thus providing additional resolution. The power spectrum is a measure of the mean square fluctuation in the overdensity field, averaged over the volume. For the curves in Fig. 5.1, it has been calculated by binning the mass into a cubic grid using the triangular-shaped cloud assignment scheme (Efstathiou et al. 1985) then Fourier transforming this field to provide $P(k) \propto |\delta_k|^2$. The δ_ks represent the amplitudes of the different Fourier components in the overdensity field, and $k = 2\pi/\lambda$ is the chosen conversion from reciprocal space k values to real lengths λ.

In more detail, Fig. 5.1 shows with a bold line the CDM $\Gamma = \Omega_0 h = 0.21$ power spectrum, obtained using the fit to the transfer function provided by Bardeen et al. (1986). This curve has been shifted vertically upwards to avoid confusion with the other lines. The long-dashed curve gives the power spectrum of the entire $180\,h^{-1}$Mpc long simulation, calculated using 64^3 cells. Short-dashed, dotted and dot-dashed lines represent the power spectra calculated in the high-resolution cube when long waves, short waves or both long and short waves were present respectively. These were calculated using a Fourier transform of a 32^3 grid of densities. A crossover length, between scales which were called long waves and those designated as short waves, of $\sim 9.5\,h^{-1}$Mpc was used. This corresponds to $\log_{10}(k) \approx -0.2$. At this scale the relative contributions from the long and short wave inclusions swap over. For larger k, the long-wave only power spectrum is affected by the convolution of the particle distribution with the triangular-shaped cloud function. Comparison of the dot-dashed curve with the long-dashed one at $\log_{10}(k) \gtrsim -0.2$ illustrates how the addition of the short waves has enabled the high-resolution region to maintain a spectral slope similar to the CDM $\Gamma = 0.21$ slope for an extra factor of ~ 3 in k. The lack of large-wavelength power (low-k) measured in the spectrum of the high-resolution region is a result of the small cube size in which the power spectrum was calculated. Fluctuations at these larger scales are included in the surrounding coarse-sampled region which will now be considered.

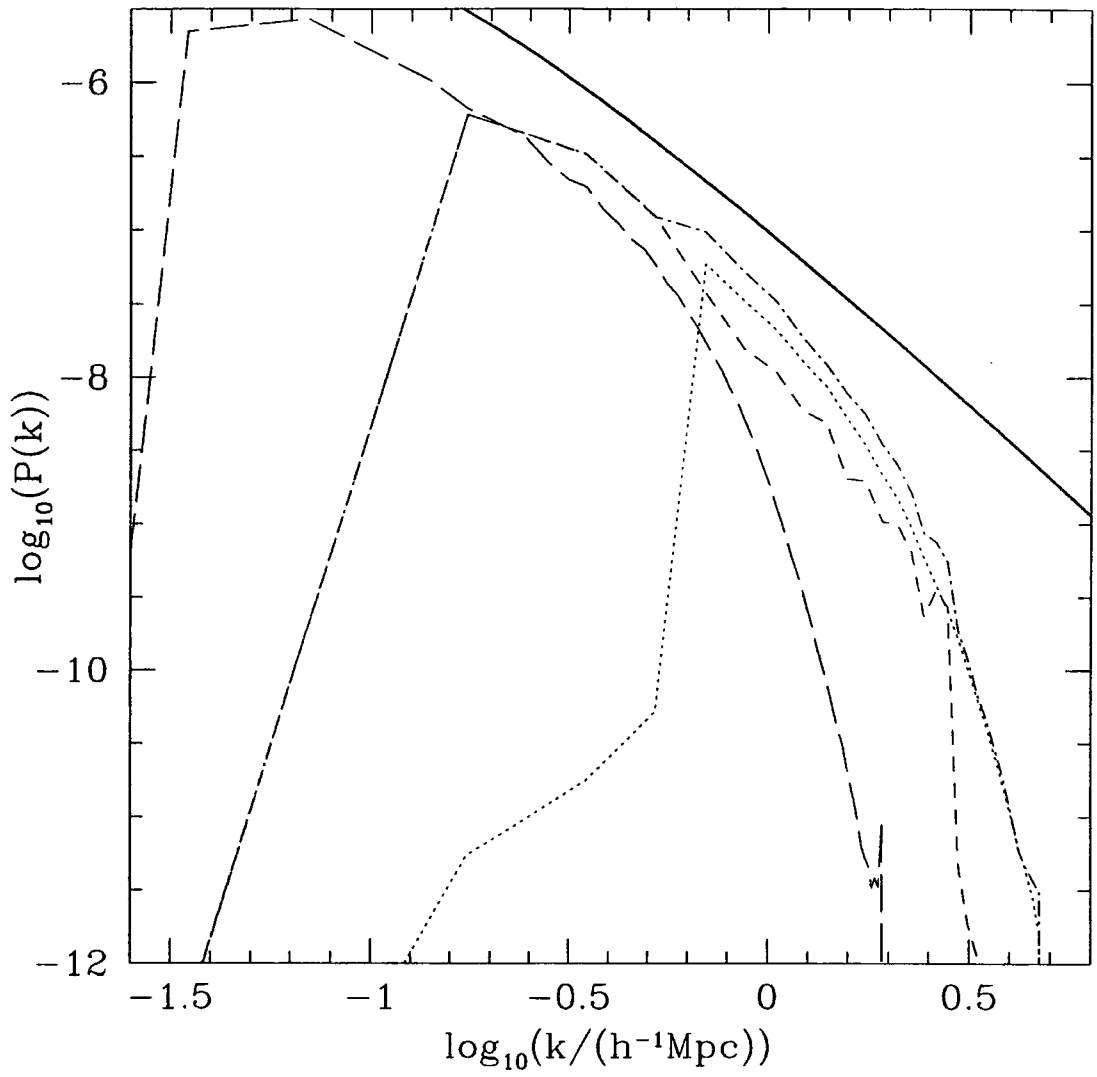

Figure 5.1: Power spectra illustrating the effect of adding extra short-wavelength modes as described in the text. The bold line represents a $\Gamma = 0.21$ CDM spectrum and the long-dashed line follows the fluctuations in the original $180\,h^{-1}$Mpc simulation cube. The 'long-wave' only, 'short-wave' only, and combined long and short wave power spectra measured in the $36\,h^{-1}$Mpc cube are traced with a dashed, a dotted and a dot-dashed line respectively. An arbitrary normalisation is used for the CDM curve and k is defined as 2π divided by the corresponding real-space length.

5.4.3 Coarse sampling the tidal field

With the high-resolution cube in place, the gravitational influence of the surrounding material must be supplied to the extent that the final quantities of interest are unaffected by increasing the number of 'low-resolution' particles. This is accomplished by binning all of the remaining particles outside the high-resolution cube in the original initial conditions into cubic cells in cubic shells. In each shell there are the same number of cells. If the number of cells along the side of a shell is denoted by n then each shell includes $n^3 - (n-2)^3$ cells. The ratio of cell length in shell $i+1$ to shell i, where i increases away from the high-resolution cube, is given by $l_{i+1}/l_i = n/(n-2)$. Defining the distance from the ith shell to the centre of the high-resolution region by $d_i \approx (n/2)l_i$, it can be seen that each low-resolution particle is like a node in a treecode with opening angle $\theta = l_i/d_i \approx 2/n$. This angle will be larger when calculating the force from nearby low-resolution particles on particles near the edge of the high-resolution region, so it is not exactly analogous to a full tree. Nevertheless, an order of magnitude decrease in particles outside the region of interest can be achieved so the method is very much worth pursuing. As well as n, a second parameter is needed to define the coarse sampled region fully, namely the extent of the coarse sampled zone. The cubic shells are bounded by a spherical edge $x_{\rm edge}$ times the original large simulation box length away from the centre of the high-resolution cube. If $x_{\rm edge}$ is so large that the coarse sampled region requires periodic replicas of the original simulation, then cells of constant mass (i.e. n increasing radially outwards) produced by simply binning the simulation into small cubes are added.

Fig. 5.2 illustrates the projected initial, $z_i = 25$, positions in physical coordinates of the 'low-resolution' particles for a high-resolution cube of $36/(1+z_i)\,h^{-1}$Mpc taken from an original cube with length $180/(1+z_i)\,h^{-1}$Mpc. In section 5.5, some tests are presented in order to find acceptable values of n and $x_{\rm edge}$. A more general discussion of some of the pertinent issues for techniques such as these can be found in Jernigan & Porter (1989).

5.4.4 Adding Λ to *GRAPE*-SPH

One final addition to the code described by Navarro & White (1993) is the inclusion of a repulsive force to mimic the effect of the non-zero cosmological constant. Representing the resulting acceleration away from the centre of mass of the simulation by

$$\frac{\mathrm{d}\mathbf{v}}{\mathrm{d}t} = \omega^2 \mathbf{x}, \tag{5.10}$$

where ω is a positive constant to be determined, the ratio of velocity to displacement is given by ω, independent of time. Referring to equation (1.15) and considering the distant future evolution of a non-zero Λ universe one finds

$$\lim_{z\to -1} H = \lim_{z\to -1} H_0[(1+z)^2(1+\Omega_0 z) - \Lambda_0 z(2+z)]^{1/2} = H_0\sqrt{\Lambda_0}. \tag{5.11}$$

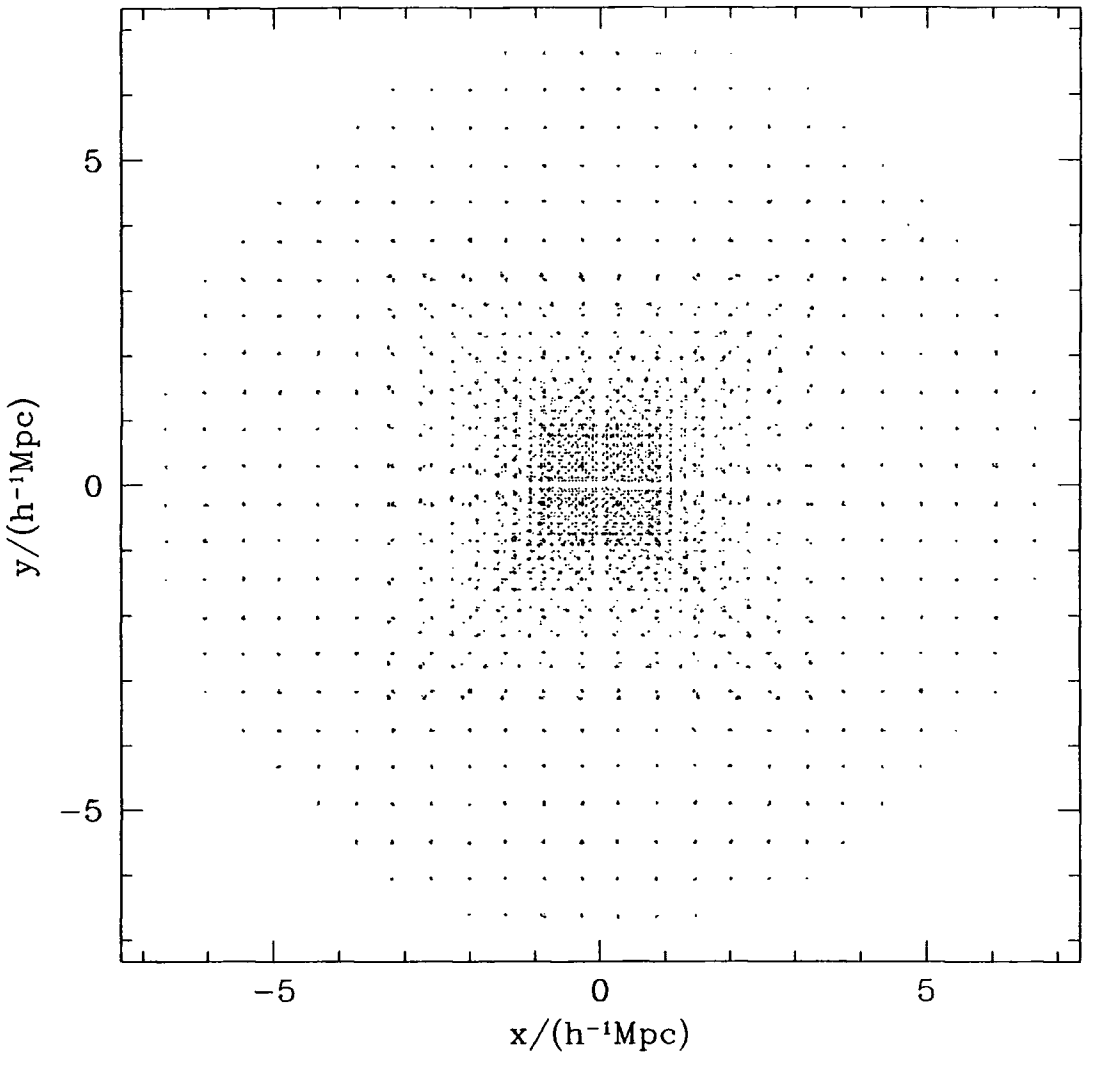

Figure 5.2: Dot plot showing the projected initial low-resolution particle positions in physical coordinates at $z = 25$ for a cluster resimulation. The particle masses increase with distance from the origin.

Hubble's constant is simply the ratio between velocity and displacement and thus the constant in equation (5.10) is found to satisfy

$$\omega^2 = H_0^2 \Lambda_0. \tag{5.12}$$

5.5 Tests of the resimulation procedure

In order to test the method for extracting a cluster, coarse sampling the outer regions of the original simulation and re-running using the *GRAPE*, a series of experiments were carried out. These involved varying n, $x_{\rm edge}$ and the size of the extracted region $r_{\rm extr}$ to see how the resulting cluster was affected. As this procedure only alters the gravitational force from that calculated in the AP^{3}M simulation, only dark matter particles were used. To allow a better comparison with the original cluster, exactly the same displacements and masses were used for the 'high-resolution' region of the resimulation as were in the AP^{3}M run.

The original cube was a $180\,h^{-1}$Mpc long realisation of the $\Omega_0 = 0.3$, $\Lambda_0 = 0.7$ cosmology using 64^3 particles (Frenk, private communication). A value of $\sigma_8 = 1.05$ was adopted and an equivalent Plummer gravitational softening of $\sim 140\mathrm{h}^{-1}$kpc fixed in comoving coordinates was employed. The material within a sphere of radius $r_{\rm extr}$ of the centre of the largest cluster (which had a virial radius of $2.71\,h^{-1}$Mpc and a turnaround radius of $\sim 8\,h^{-1}$Mpc) was extracted and traced back to define the high-resolution cube at $z = 25$. All remaining mass was coarsely sampled, using the n and $x_{\rm edge}$ values listed in Table 5.1, as previously described. For resimulations test3-test10, a physical softening of $100\mathrm{h}^{-1}$kpc was used, whereas softenings of $350\mathrm{h}^{-1}$kpc and $200\mathrm{h}^{-1}$kpc fixed in comoving coordinates were utilised for test1 and test2 respectively. The number of particles within the final virial radius, and the one-dimensional velocity dispersion of these particles is also given in Table 5.1 for each test cluster. In addition to the bulk cluster properties, radial velocity and density profiles and a mass correlation function were calculated. The procedure used for calculating the correlation function of the mass involved considering only the particles within a sphere of radius $6\,h^{-1}$Mpc of the cluster centre. This region typically included $N_d = 1000 - 2000$ points. The $N_d(N_d - 1)$ separations of these particles were binned to give the numbers of pairs $DD(r)$ as a function of distance r. $N_r = 3000$ random particles were placed in a sphere of the same size and used to calculate the total expected number of pairs $RR(r)$ at each separation. The correlation function was then estimated using

$$\xi_{\rho\rho} = \frac{DD(r)}{RR(r)} \left(\frac{N_r}{N_d}\right)^2 - 1. \tag{5.13}$$

It should be emphasised that at any particular separation r, the correlation function will depend on the radius of the sphere in which it is being calculated. This is because the sphere is chosen to be small enough that only particles of the same mass contribute to the counts and, as a result, the requirement that the integral of $\xi_{\rho\rho}$ throughout the sphere equals zero causes a suppression of $\xi_{\rho\rho}$ when a smaller

Table 5.1: Details of the test runs. The parameters n and $x_{\rm edge}$ refer to the coarse-sampled region and $r_{\rm extr}$ is the radius of the sphere extracted from the final conditions and traced back to form the high-resolution region. N and σ_v are the number of (equal mass) particles ending in the cluster virial radius and the velocity dispersion of these particles. The AP^{3}M simulation, test1 and test2 used comoving softenings of $\sim 140\mathrm{h}^{-1}$kpc, $350\mathrm{h}^{-1}$kpc and $200\mathrm{h}^{-1}$kpc respectively, whereas the remaining tests were run with a physical softening of $100\mathrm{h}^{-1}$kpc.

Run Name	n	$x_{\rm edge}$	$r_{\rm extr}/(\,h^{-1}\mathrm{Mpc})$	N	$\sigma_v/(\mathrm{kms}^{-1})$
AP^{3}M run	-	-	-	1171	1225
test1	8	1.0	8	1135	1207
test2	8	1.0	8	1164	1217
test3	8	1.0	8	1096	1244
test4	6	1.0	8	1109	1247
test5	12	1.0	8	1112	1271
test6	8	0.5	8	1102	1241
test7	8	1.5	8	1095	1232
test8	8	1.5	6	1109	1229
test9	8	1.5	10	1083	1265

total volume is used for the calculation. However, with a sphere of $6\,h^{-1}$Mpc chosen for all cases, a comparison between the different results is valid.

5.5.1 Results

From Table 5.1, the following results are apparent. The minimum resimulated cluster mass is about 8% less than the maximum value, but this decreases to $\sim 3\%$ if only the simulations with physical softenings are considered. All of the velocity dispersion measurements lie within 5% of the largest one. It seems likely that the lower masses from the runs with gravitational softenings fixed in physical coordinates result from the choice of softening length. At the starting redshift of 25, 100 comoving h^{-1}kpc corresponds to a scale only slightly less than the mean interparticle separation. This would artificially suppress the growth of structure and give rise to lower final masses for these simulations. On the other hand, the first three rows in the table (corresponding to the high-mass clusters run with comoving softenings) appear to have slightly low velocity dispersions. This might plausibly result from the larger softening of the potential at low redshifts.

Varying the parameters n, $x_{\rm edge}$ and $r_{\rm extr}$ appears to have relatively little effect on the results, with the only systematic trend being a decrease in N with increasing $r_{\rm extr}$ (tests 8, 3 and 9). However, this trend is not apparent in the velocity dispersions from the same tests. Had the value of $r_{\rm extr}$ been chosen to be $3\,h^{-1}$Mpc, the high-

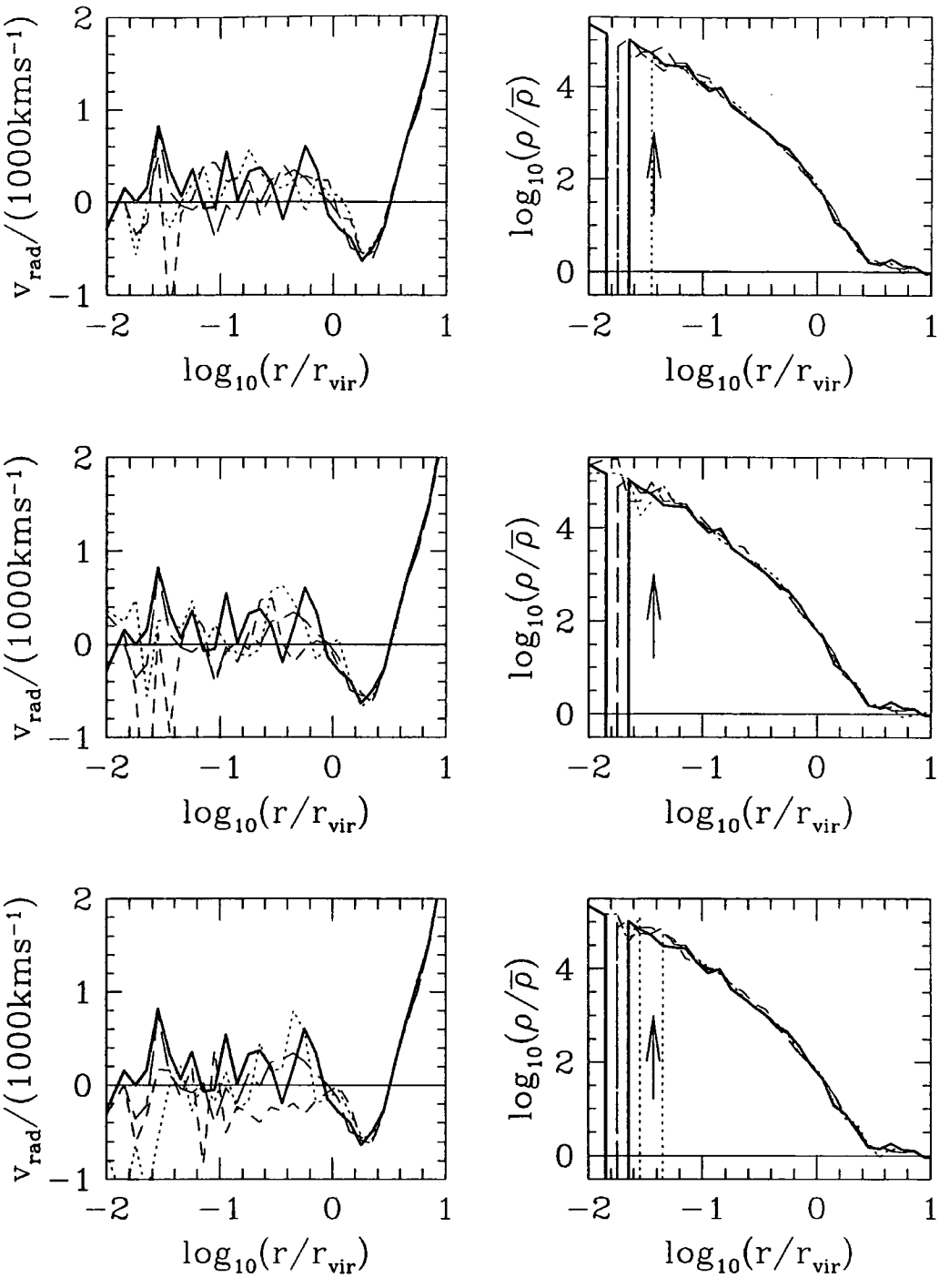

Figure 5.3: Infall patterns and radial density profiles for the final cluster produced by the different test runs. In each panel, the original AP^3M cluster is represented by a bold solid line and the long-dashed line shows the cluster formed in test3. In the top row, test1 and test2 results are given by dotted and short-dashed lines respectively. The middle and bottom rows use dotted curves to illustrate test4 and test8 and short-dashed lines to trace the results from test5 and test9 respectively. An arrow showing $100h^{-1}$kpc is placed in the density profile panels.

resolution cube at $z = 25$ would have been the same as that for test5, thus making this variation appear even less significant.

Fig. 5.3 shows the variation in the cluster infall patterns and density profiles for some of the simulations. The top row illustrates the effect caused by changing the softening, whereas the middle and bottom rows show the variation with n and $r_{\rm edge}$ respectively. For the infall patterns, within the virial radius the motions are quite different, but this does not appear to produce differing density profiles. There is a small scatter in the virial radii, with the AP^{3}M cluster having a lower value than the resimulated cases, but no systematic variation is seen amongst these test cases. Outside the radius where there is a maximum infall velocity, the behaviour of all the different simulations becomes indistinguishable. The density profiles of the simulations with the physical softening of $100\mathrm{h}^{-1}$kpc are very slightly steeper in the centre.

In Fig. 5.4 the most widely varying mass correlation functions from all of the simulations are shown. With the clusters from the original run and test3 again represented by a bold solid line and a long-dashed line, the short-dashed and dotted lines give the results for test5 and test4. Even for these relatively varied cases the range in correlation lengths is only about 20%.

Bearing in mind that the virial radius of this cluster in the original simulation was $2.71\,h^{-1}$Mpc, it seems that the whole resimulation procedure will not affect the final cluster properties to more than a few percent if the extracted region:

1) is at least approximately twice the virial radius (this is conservative in order to allow for the addition of small waves changing the fluctuations slightly),
2) is resimulated using $n \gtrsim 8$ and
3) is resimulated with $x_{\rm edge} = 1.0$.

For the cluster resimulations presented in Chapter 6, $n = 12$ and $x_{\rm edge} = 1.0$ are used. In all but three clusters, the extracted region exceeds $2r_{\rm vir}$. The other cases, which are awkward because of their proximity to one another have $r_{\rm extr} > 1.85r_{\rm vir}$. With a large number of particles in the high-resolution region the majority of the computing time is spent in this zone, so a cautious choice of n and $x_{\rm edge}$ does not significantly affect the speed of the calculation.

The results of including the additional small-scale power and resimulating the most massive cluster are shown in Fig. 5.5. Both the density and infall velocity profiles are illustrated for the AP^{3}M simulation (solid lines) and the high-resolution experiment (dashed lines - run cl01a from Chapter 6). While the two runs produce similar clusters in many respects, the central density of the resimulated cluster is significantly higher than the original run. This results from the greater number of particles allowing a smaller gravitational softening, thus improving the spatial resolution. Some contribution also comes from the additional power included in the initial conditions.

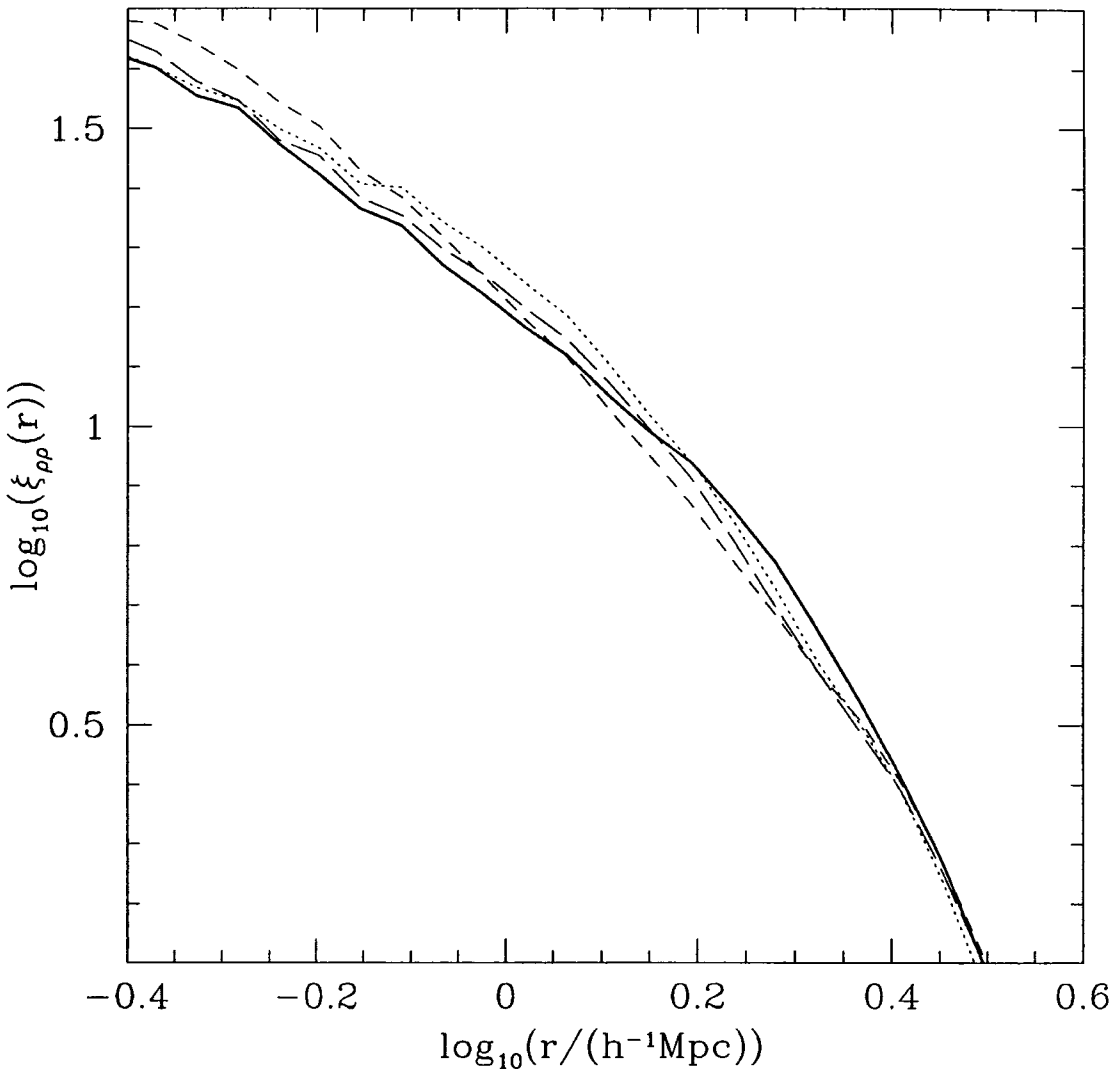

Figure 5.4: The mass correlation functions measured in a sphere of radius $6\,h^{-1}$Mpc centred on the cluster. As in Fig. 5.3, a bold solid line and a long-dashed line are used to show the original cluster and that formed in test3. The dotted and short-dashed lines correspond to test4 and test5.

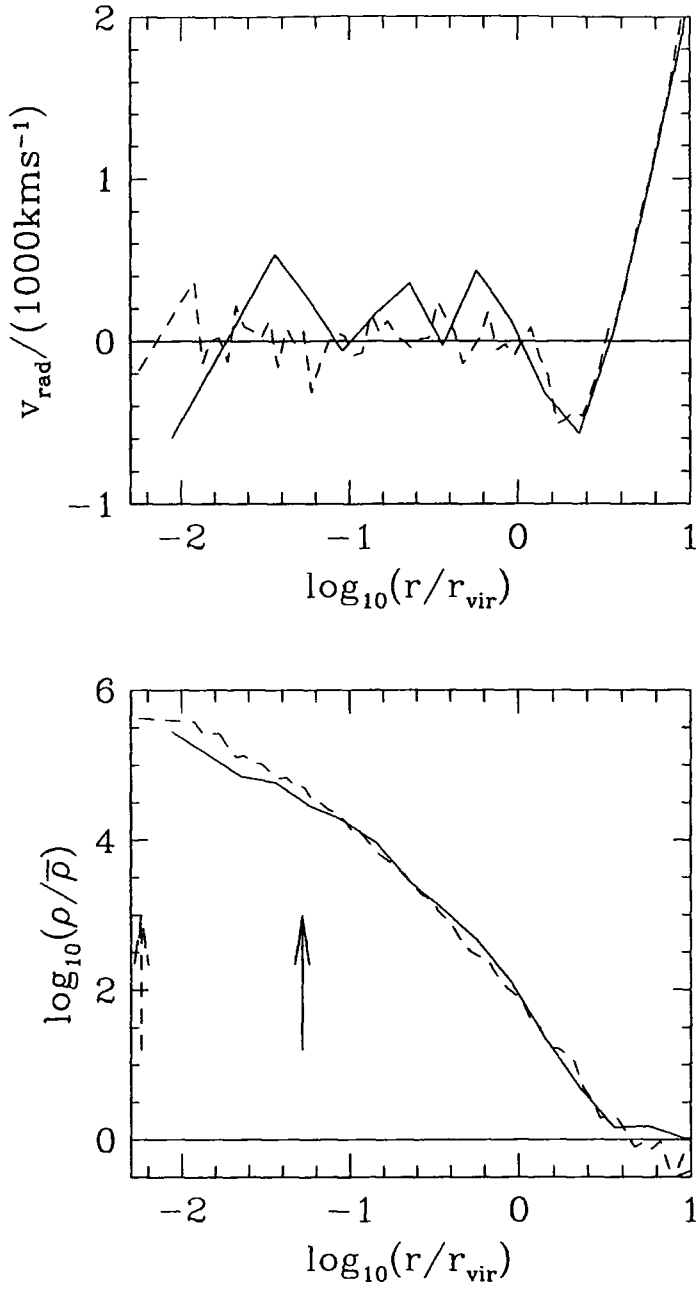

Figure 5.5: The radial velocity (top) and density (bottom) profiles for the most massive cluster in the AP^3M simulation (solid) and the high-resolution simulation (dashed lines) of the same cluster (cl01a in the next Chapter). Arrows denote the gravitational softenings in the two separate runs.

5.6 Conclusions

The conversion of TreeSPH to *GRAPE*-SPH has been outlined as has the flexibility which is provided by such a combination. With the present cost of a *GRAPE*-3Af being at least one order of magnitude less than a CRAY YMP, whilst at the same time producing very similar speeds for the type of cosmological simulation being considered here (Steinmetz 1996), the attractiveness of *GRAPE*-SPH is clear.

Details have been presented of a procedure for extracting a region of interest from a dark matter only simulation in order to resimulate it at higher resolution including additional short-wavelength power (as used by Navarro et al. 1995). This can increase the mass resolution of a cluster simulation by a factor of at least 10. Some simple tests have been performed to illustrate that the parameters used in the extraction are not significantly affecting the properties of the resimulated clusters.

Given that the matter collapsing to form the eventual cluster is more likely to have originated from an irregular rather than a cubic volume, additional pruning of the high-resolution region could, in future, be included in order to increase the resolution by an extra factor of a few (Tormen, private communication).

5.7 References

Aarseth S. J., 1963, MNRAS, 126, 223
Anninos P., Norman M. L., 1996, ApJ, 459, 12
Bardeen J. M., Bond J. R., Kaiser N., Szalay A. S., 1986, ApJ, 304, 15
Barnes J., Hut P., 1986, Nat, 324, 446
Bertschinger E., 1985, ApJS, 58, 39
Benz W., 1990a, ed de Loore C., Proceedings of the Second European Predoctoral Astrophysics School on Theory and Observation of Late Stages of Stellar Evolution and Computational Methods in Astrophysical Fluid Dynamics, Springer, Berlin
Benz W., 1990b, ed Buchler J. R., The Numerical Modeling of Stellar Pulsation, Kluwer, Dordrecht
Benz W., Bowers R. L., Cameron A. G. W., Press W. H., 1990, ApJ, 348, 647
Carlberg R. G., 1988, ApJ, 324, 664.
Cen R., 1992, ApJS, 78, 341
Cen R., Jameson A., Liu F., Ostriker J. P., 1990, ApJ, 362, L41.
Couchman H. M. P., 1991, ApJ, 368, L23
Couchman H. M. P., 1995, in Numerical Methods in Astrophysics, Vol. II, Springer-Verlag, New York, in press
Couchman H. M. P., Thomas P. A., Pearce F. R., 1995, ApJ, 452, 797
Efstathiou G., Davis M., Frenk C. S., White S. D. M., 1985, ApJS, 57, 241
Evrard A. E., 1988, MNRAS, 235, 911
Gelb J. M., Bertschinger E., 1994, ApJ, 436, 467
Gingold R. A., Monaghan J. J., 1977, MNRAS, 181, 375

Gramann M., Bahcall N. A., Cen R., Gott J. R., 1995, ApJ, 441, 449
Hernquist L., Katz N., 1989, ApJS, 70, 419
Hockney R. W., Eastwood J. W., 1981, Computer Simulation using Particles, New York, McGraw-Hill
Jernigan J. G., Porter D. H., 1989, ApJS, 71, 871
Katz N., 1992, ApJ, 391, 502
Katz N., Gunn J., 1991, ApJ, 377, 365
Katz N., White S. D. M., 1993, ApJ, 412, 455
Katz N., Weinberg D. H., Hernquist L., 1996, ApJS, 105, 19
Klypin A. A., Shandarin S. F., 1983, MNRAS, 204, 891
Lacey C., Cole S., 1994, MNRAS, 271, 676
Metzler C. M., Evrard A. E., 1994, ApJ, 437, 564
Miller R. H., 1983, ApJ, 270, 390
Monaghan J. J., 1992, ARA&A, 30, 543
Monaghan J. J., Gingold R. A., 1983, J Comput Phys, 52, 374
Monaghan J. J., Lattanzio J. C., 1985, A&A, 149, 135
Navarro J. F., White S. D. M., 1993, MNRAS, 265, 271
Navarro J. F., Frenk C. S., White S. D. M., 1995, MNRAS, 275, 720
Okumura S. K., Makino J., Ebisuzaki T., Ito T., Fukushige T., Sugimoto D., 1993, PASJ, 45, 329
Peebles P. J. E., 1980, The Large Scale Structure of the Universe. Princeton Univ. Press, Princeton, NJ
Steinmetz M., 1996, MNRAS, 278, 1005
Steinmetz M., Müller E., 1993, A&A, 268, 391
Steinmetz M., Müller E., 1994, A&A, 281, L97
Sugimoto D., Chikada Y., Makino J., Ito T., Ebisuzaki T., Umemura M., 1990, Nat, 345, 33
Umemura M., 1993, ApJ, 406, 361
White S. D. M., Frenk C. S., Davis M., 1983, ApJ, 274, L1
Zel'dovich Ya. B., 1970, A&A, 5, 84

Chapter 6

High-resolution simulations of galaxy clusters in an $\Omega_0 = 0.3$, $\Lambda_0 = 0.7$ universe

6.1 Introduction

Clusters of galaxies are sufficiently large that they are, on a cosmological scale, dynamically youthful objects. As such, they should provide more useful probes of the material from which they formed than smaller entities such as galaxies which have had time to grow and evolve in more complicated ways. For instance, the material within the turnaround radius of a large cluster is expected to have a baryonic to dark matter ratio very similar to the primordial one. Depending on how far the gas falls into the cluster before being shocked, and thus behaving differently from the collisionless component, this equality might be expected to hold at significantly smaller radii.

Predictions for the behaviour of collisional as well as collisionless material within the cluster environment in a variety of cosmologies are therefore valuable. This knowledge can be acquired using either analytical approximations or numerical simulations. The former route was taken by Kaiser (1986) who used the following scaling relations for cluster temperatures and luminosities as a function of cluster mass and redshift to predict the evolution of cluster properties:

$$T(M,z) \propto M^{2/3}(1+z) \tag{6.1}$$

and

$$L(M,z) \propto M^{4/3}(1+z)^{7/2}. \tag{6.2}$$

These formulae assume that the universe has $\Omega = 1$ and that the mass fluctuation spectrum is a power law. Also, radiative cooling and other physics that introduces a preferred scale, such as star formation and energy released by supernovae, has been ignored. For a CDM-dominated universe, the power spectrum is approximately

a power law on cluster scales, with an index of ~ -1. Most of the numerical simulations which have attempted to create and trace a population of clusters have assumed an Einstein-de-Sitter cosmology (Evrard 1990; Thomas & Couchman 1992; Katz & White 1993; Kang et al. 1994; Bryan et al. 1994; Metzler & Evrard 1994; Couchman, Thomas & Pearce 1995; Navarro, Frenk & White 1995 (NFW) for example), so it has been possible to compare the results with the above relations. In universes with $\Omega_0 < 1$ (e.g. Cen & Ostriker 1994; Evrard, Metzler & Navarro 1996) the cosmology itself imposes a length scale associated with the 'freezing' in the growth of perturbations. The validity of scaling relations thus becomes questionable.

Most of the hydrodynamical simulations carried out to investigate the properties of galaxy clusters have not allowed gas to cool radiatively and form stars, merely treating it as an ideal gas. Whilst this is clearly an attempt to solve a simplified problem, it should be viewed as a stepping-stone towards future simulations where additional physics can be included. If different methods cannot agree on the simple task, then it is not clear what benefits could be gained by exposing them to a more complicated situation. The cooling radius for a large cluster, defined as the radius inside which gas will radiate away all of its energy within a Hubble time, is expected to be typically $\sim 100h^{-1}$kpc (Fabian, Canizares & Nulsen 1984; Gunn & Thomas 1996) so this gives some idea of the extent to which this will affect the results. However, the cooling might be expected to be more important in the progenitor objects. Feedback will have the opposite effect and heat the gas. Enrichment of intracluster gas with heavy elements (David, Forman & Jones 1991; Loewenstein & Mushotzky 1996) formed during supernovae confirms that such processes are important in the gas evolution. However, the work of Metzler & Evrard (1994) suggests that even simulations incorporating extreme forms of feedback do not increase the average temperature of intracluster gas by more than $\sim 15\%$, so this provides some reassurance that the neglect of this additional physics should not grossly affect the properties of the galaxy clusters being simulated.

In most respects the different numerical experiments have produced similar results. However, on the matter of the X-ray luminosity, some discrepancies have been found. The Eulerian codes appear to find less emission from their clusters than the particle-based methods, particularly when low-mass clusters are considered. NFW ascribe this difference to a lack of spatial resolution in the grid based codes. Anninos & Norman (1996) confirm that, on decreasing the fundamental cell size to $100h^{-1}$kpc, the luminosities calculated in their nested-grid simulations do not converge. Unfortunately for the Eulerian approach, this lack of spatial resolution prevents the detailed study of the intracluster gas density and temperature profiles. Recent results from the *ASCA* satellite (e.g. Markevitch et al. 1996) have yielded well-resolved gas temperature profiles, so, in addition to considering the evolution of the bulk properties, testing the assumption of hydrostatic equilibrium in clusters is also a useful exercise in order to provide an estimate of the uncertainty in the inferred cluster masses. Bertschinger (1985) derived a self-similar solution for the spherically symmetric shocked accretion of gas onto an overdensity represented by a point mass. Whilst these results are of great importance for testing hydrodynamical methods, haloes form in the more popular cosmological models by mergers

of smaller self-gravitating bodies so numerical simulations are required for realistic calculations.

Modern cosmological research contains a large number of different strands providing various, and often mutually exclusive within the 'standard framework', constraints on the fundamental cosmological parameters such as Ω_0, Ω_b, Λ_0 and H_0. Before using a large amount of computer time investigating any particular model, some justification is deserved for the choice of parameters to be tested. A significant weight in this decision is often placed on the requirement of the inflationary paradigm, put forward by Guth (1981) and developed by Linde (1982) and Albrecht & Steinhardt (1982) to explain the apparent homogeneity of the universe on very large scales, that the universe should be spatially flat, i.e. $\Omega + \Lambda = 1$. Assuming that both Ω and Λ are positive, the energy associated with a non-zero Λ_0 scenario is a few meV (e.g. Kolb & Turner 1990), so much lower than the energies typical of particle physics and at a value of no obvious significance that it is often taken to imply that $\Lambda = 0$. Energies corresponding to various symmetry-breakings or phase transitions that might be candidates for providing a vacuum energy density term therefore give rise to Λ contributions many orders of magnitude greater than unity, i.e. intolerably large. This would appear to argue in favour of an $\Omega = 1$, $\Lambda = 0$ model. However in recent years, certain observational difficulties have appeared for this Einstein-de Sitter scenario.

From observations of galaxies, stars and hot gas in the Coma cluster, White et al. (1993) find that, assuming that any segregation effects are small and that the cluster density profiles are independent of cosmology, the ratio of baryonic to total matter contributions to the closure density within a radius of $1.5\,h^{-1}$Mpc satisfies

$$\frac{\Omega_b}{\Omega_0} \geq 0.029 + 0.051 h^{-3/2}. \tag{6.3}$$

The terms on the right-hand side correspond to stellar and gas contributions respectively and the inequality arises because some of the dark matter could be baryonic. Similar results have been found for a variety of other clusters (for example see Elbaz, Arnaud & Böhringer 1995; Buote & Canizares 1996). Walker et al. (1991) and Copi, Schramm & Turner (1995) use estimates of the primordial abundances of the light elements to provide the following 'nucleosynthesis' constraint on the fraction of the critical density in the form of baryonic material:

$$0.01 < \Omega_b h^2 < 0.015. \tag{6.4}$$

Of the many methods used to try and measure Hubble's constant, values from $50-100\mathrm{km\,s^{-1}Mpc^{-1}}$ appear with most frequency. For example, recent observations from *HST* of Cepheid variables in Leo I (Tanvir et al. 1995) lead to

$$h \approx 0.7, \tag{6.5}$$

a value which lies comfortably in this range. Measurements of the shape of the power spectrum using the *APM* galaxy survey (Peacock & Dodds 1994) suggest that it can be well described by a CDM-dominated universe with

$$\Gamma = \Omega_0 h \approx 0.25. \tag{6.6}$$

Each of the last four equations is capable of making many cosmologists squirm in discomfort, but anybody not too closely connected with the subject could quite happily recognise that the set of equations are approximately satisfied by $\Omega_0 = 0.3$, $\Omega_b = 0.03$ and $h = 0.7$. With the inclusion of a vacuum energy density term $\Lambda_0 = 0.7$ (well it cannot all be good news!) in order to keep the universe spatially flat, this cosmology predicts a universe $\sim$ 13 Gyrs old, a value which is not too uncomfortably low compared with age estimates of globular clusters (Chaboyer 1995). Adopting a pragmatic approach, however unpalatable, it is this scenario which is increasingly attracting the attention of researchers.

In the rest of this Chapter, a series of cluster simulations in an $\Omega_0 = 0.3$, $\Lambda_0 = 0.7$, $h = 0.7$ cosmology will be described. The procedure used will be that detailed in Chapter 5. More specific information concerning the method is given in Section 6.2, whilst the results and comparisons with previous authors are contained in Section 6.3. Concluding remarks are made in Section 6.4.

6.2 Method

6.2.1 Initial conditions

Using the 'spherical overdensity' algorithm referred to in Chapter 4 and described more fully by Lacey & Cole (1994), the ten most massive groups were identified in a large dark matter simulation of the $\Omega_0 = 0.3, \Lambda_0 = 0.7$ cosmology carried out using the AP^{3}M code (Frenk, private communication). The side of the simulation cube measured $180\,h^{-1}$Mpc and the region was filled with 64^3 particles. These were evolved, using an effective Plummer softening fixed in comoving coordinates at $140\mathrm{h}^{-1}$kpc, from an initial redshift of 25 until redshift zero which was chosen to be at $\sigma_8 = 1.05$, consistent with the results of White, Efstathiou & Frenk (1993). For this particular cosmology, the spherical collapse model defines the virial region as having a mean enclosed density contrast of $\sim$ 324 and this was the value used by the groupfinder to select the clusters. Fig. 6.1 depicts the projected positions of the ten most massive groups found by this procedure. Circles with radii 1.5 times the virial radius r_{vir} are shown and the labels give the rank, by mass, of the clusters with 1 corresponding to the most massive object. The number of particles in these groups varied between 1171 and 499.

For each cluster, all the particles within a sphere of radius at least $1.85r_{\mathrm{vir}}$ and no greater than the turnaround radius (see Chapter 5) were traced back to the initial conditions in the dark matter simulation and a cube encompassing all of these particles was extracted. Each cube was then filled with equal numbers of dark matter and gas particles and additional waves (from scales beneath the Nyquist wavelength in the original particle distribution) were added. The number of 'high-resolution particles' was chosen in order to resimulate all clusters with approximately the same resolution. All remaining material in the large simulation was coarse-sampled and

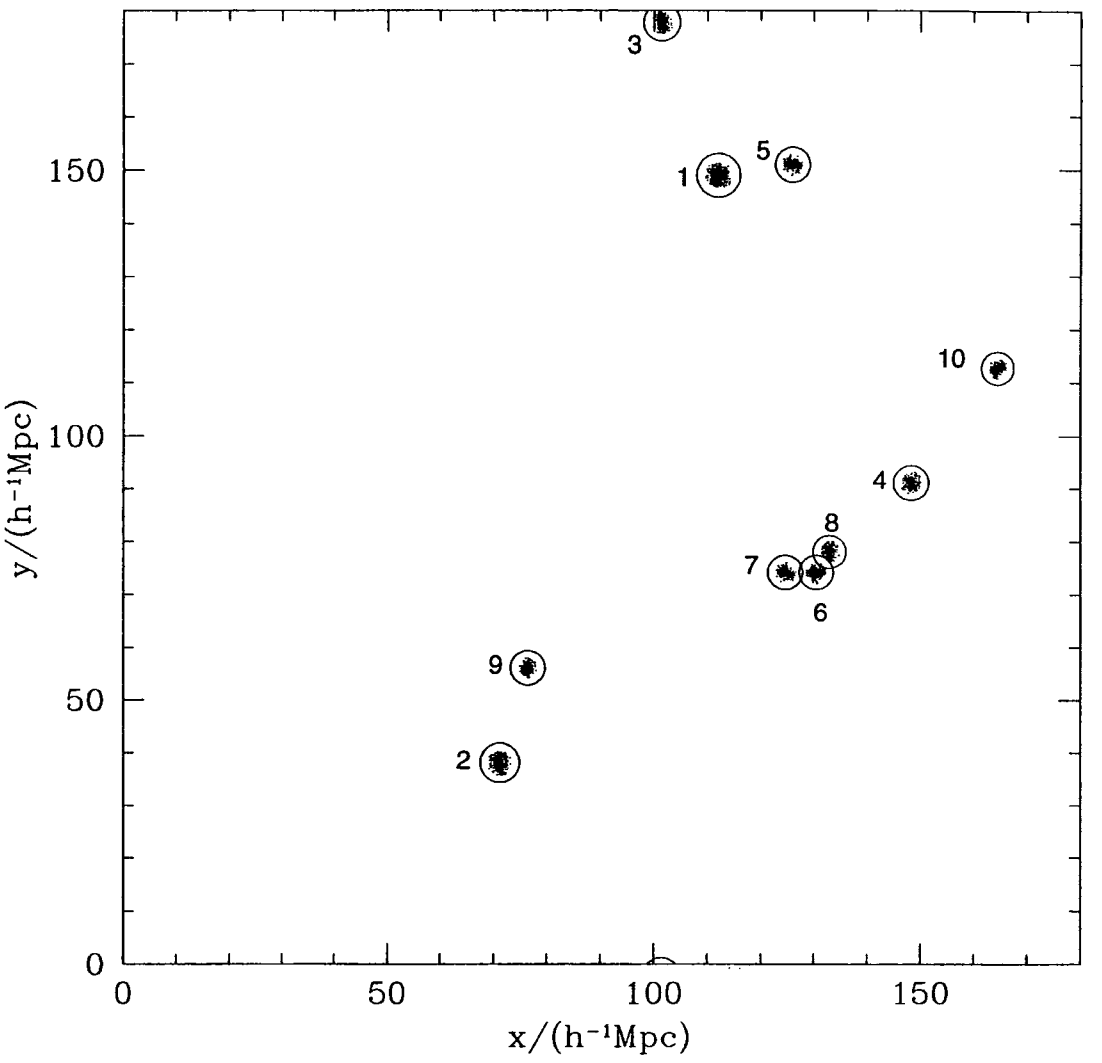

Figure 6.1: The projected positions of the ten resimulated clusters in the original AP^3M simulation. Each dot represents one dark matter particle associated with a cluster, and the circles around each halo have radii 1.5 times the virial radius. Clusters 6, 7 and 8 are physically close to each other, not just close together in this projection. Even for these clusters, none of the actual separations are less than $9\,h^{-1}$Mpc.

represented by approximately 10000 dark matter particles. The first four columns of Table 6.1 list the name of the cluster run, the size of the extracted cube in comoving units, the number of gas particles loaded into this region (equal to the number of high-resolution dark matter particles) and the mass of each gas particle. For all of the runs it was assumed that the fraction of mass in baryons was equal to 0.1 (i.e. the mass of a high-resolution dark matter particle is nine times the listed gas particle mass). In order to ensure that hydrodynamical forces did not play a significant part in the gas evolution at very early epochs, each gas particle was given an internal energy corresponding to a temperature of only ~ 15 K.

6.2.2 Resimulation details

A version of the SPH code described by Navarro & White (1993), adapted to work for a non-zero Λ_0 cosmology using the *GRAPE* hardware as detailed in Chapter 5, was employed to carry out the high-resolution gas simulations. No radiative cooling, photoionization or star formation was included, so, in addition to the gravity felt by all particles, the gas was subjected only to forces arising from pressure gradients and the artificial viscosity. The gas was assumed to have a ratio of specific heat capacities given by $\gamma = 5/3$. Hubble's constant was set to be 70 kms^{-1} Mpc^{-1}, although distances, masses and luminosities will be quoted in terms of h ($H_0 = 100h$ kms^{-1} Mpc^{-1}) to make explicit the dependence of these variables on this parameter. A gravitational softening equal to $14\mathrm{h}^{-1}$kpc fixed in physical coordinates was used. All of the clusters were evolved starting at a redshift of 25 as in the original dark matter simulation. The hierarchy of timesteps for the particles had twelve levels ranging from $\sim 0.64 - 1300$ Myr and each simulation took approximately one week of CPU time on the *GRAPE-3AF* at Edinburgh.

The centres of the resimulated clusters were found by locating the densest clump of ~ 100 dark matter particles. Virial properties were then computed assuming that the edge of the cluster was defined by the overdensity given by the spherical collapse model. The entropy per particle was defined as $s_\mathrm{i} = \ln(T_\mathrm{i}/\rho_\mathrm{i}^{2/3})$ and absolute X-ray luminosities were calculated using the same estimator as NFW, namely

$$\frac{L_\mathrm{bol}}{10^{30}\ h^{-2}\mathrm{Js}^{-1}} = 1.69\ h^3 \left(\frac{m_\mathrm{gas}}{10^{10}h^{-1}\mathrm{M}_\odot}\right) \sum_\mathrm{i} \left(\frac{\rho_\mathrm{i}}{10^{10}\ h^2\ \mathrm{M}_\odot\ \mathrm{Mpc}^{-3}}\right) \left(\frac{kT_\mathrm{i}}{\mathrm{keV}}\right)^{\frac{1}{2}}, \quad (6.7)$$

where the sum is performed over all the gas particles within the virial radius of the cluster.

6.3 Results

The bulk properties of all of the resimulated clusters and the number of particles within the virial radius in each case are listed in Table 6.1. Clusters 7 and 8 are less well resolved than the others. This is a result of their proximity to each other and

Table 6.1: Table of parameters for the resimulated clusters. The columns give the cluster name (1) (increasing numerical order with decreasing mass in the original simulation); the size of the resimulated high-resolution cube (2); the number of gas particles in the high-resolution region (3); the mass of each gas particle (4); the number of gas particles in the resimulated virialised cluster (5); the number of dark matter particles in the resimulated virialised cluster (6); the resimulated cluster virial mass (7); its virial radius (8); the dark matter velocity dispersion of the resimulated cluster (9); the luminosity-weighted gas temperature within the cluster (10) and the estimated X-ray cluster luminosity (11).

(1) Name of run	(2) $l_{\rm hr}$ h^{-1}Mpc	(3) $n_{\rm gas}^{1/3}$	(4) $m_{\rm gas}$ $10^9 h^{-1}{\rm M}_\odot$	(5) $N_{\rm gas}$	(6) $N_{\rm DM}$	(7) $M_{\rm vir}$ $10^{14} h^{-1}{\rm M}_\odot$	(8) $r_{\rm vir}$ h^{-1}Mpc	(9) σ_{1D} kms^{-1}	(10) $kT_{\rm gas}$ keV	(11) $L_{\rm bol}$ 10^{37} h^{-2} Js^{-1}
cl01a	42.2	35	14.6	9387	11146	16.0	2.42	1139	9.9	8.01
cl02a	42.2	40	9.77	13634	16008	15.4	2.39	1075	8.5	7.96
cl03a	39.4	38	9.26	13876	16242	14.8	2.36	1077	7.8	6.59
cl04a	33.8	34	8.14	10688	11977	9.65	2.04	952	5.0	3.55
cl05a	36.6	38	7.42	11760	13065	9.59	2.04	1153	9.7	10.8
cl06a	39.4	40	7.94	11015	12937	10.1	2.08	942	6.9	4.98
cl07a	42.2	40	9.77	7367	8798	8.45	1.96	926	5.9	2.43
cl08a	42.2	40	9.77	7176	8484	8.16	1.93	960	6.9	2.36
cl09a	36.6	40	6.36	8087	10149	6.32	1.78	775	3.1	0.483
cl10a	33.8	37	6.32	11414	12513	7.84	1.91	952	6.2	3.18

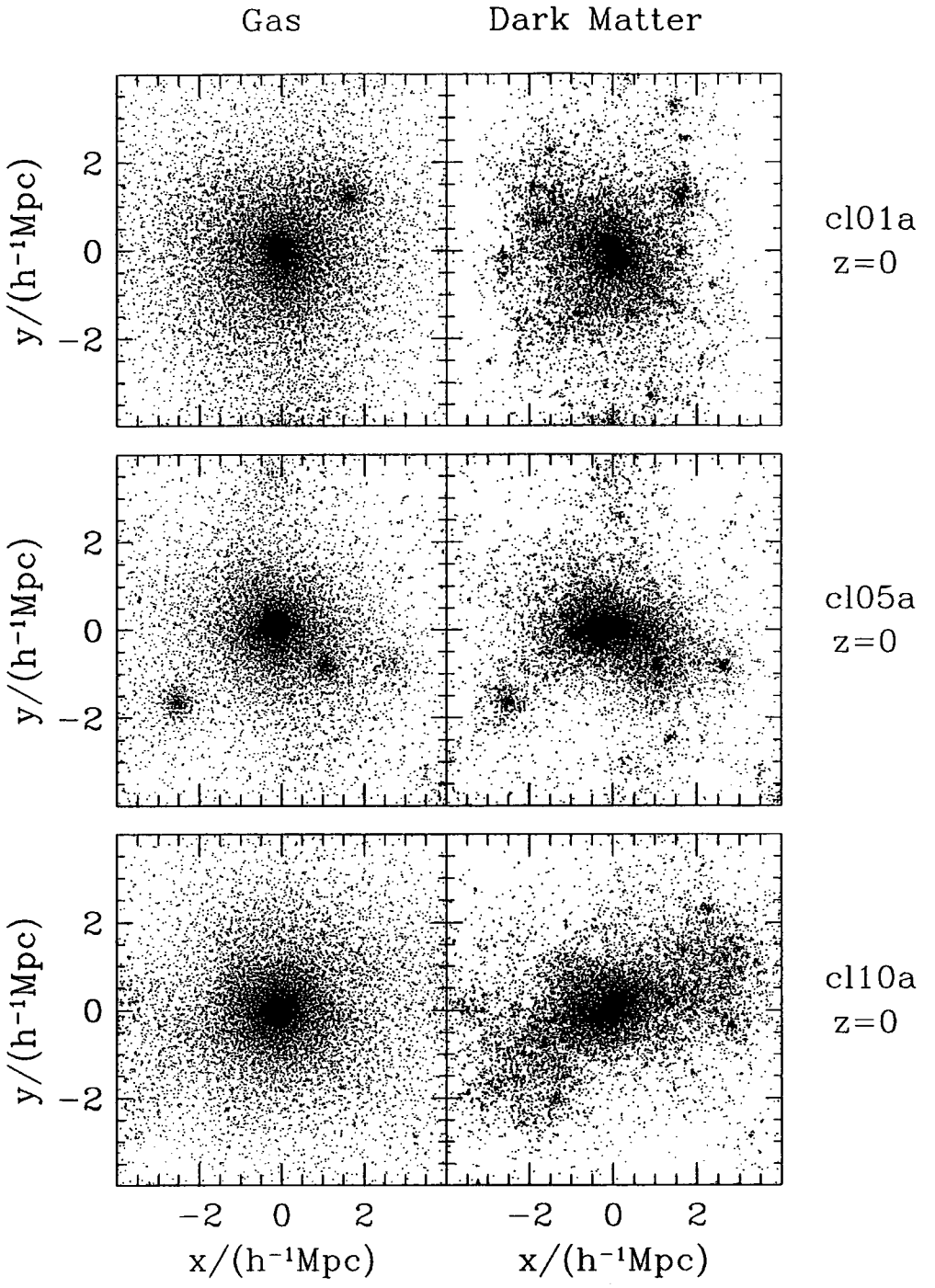

Figure 6.2: Dot plots showing the projected final particle positions in cubes of side $8\,h^{-1}$Mpc centred on three of the resimulated clusters. From top to bottom the rows correspond to clusters cl01a, cl05a and cl10a. The gas distribution is plotted in the left-hand panel and the dark matter in the right-hand panel.

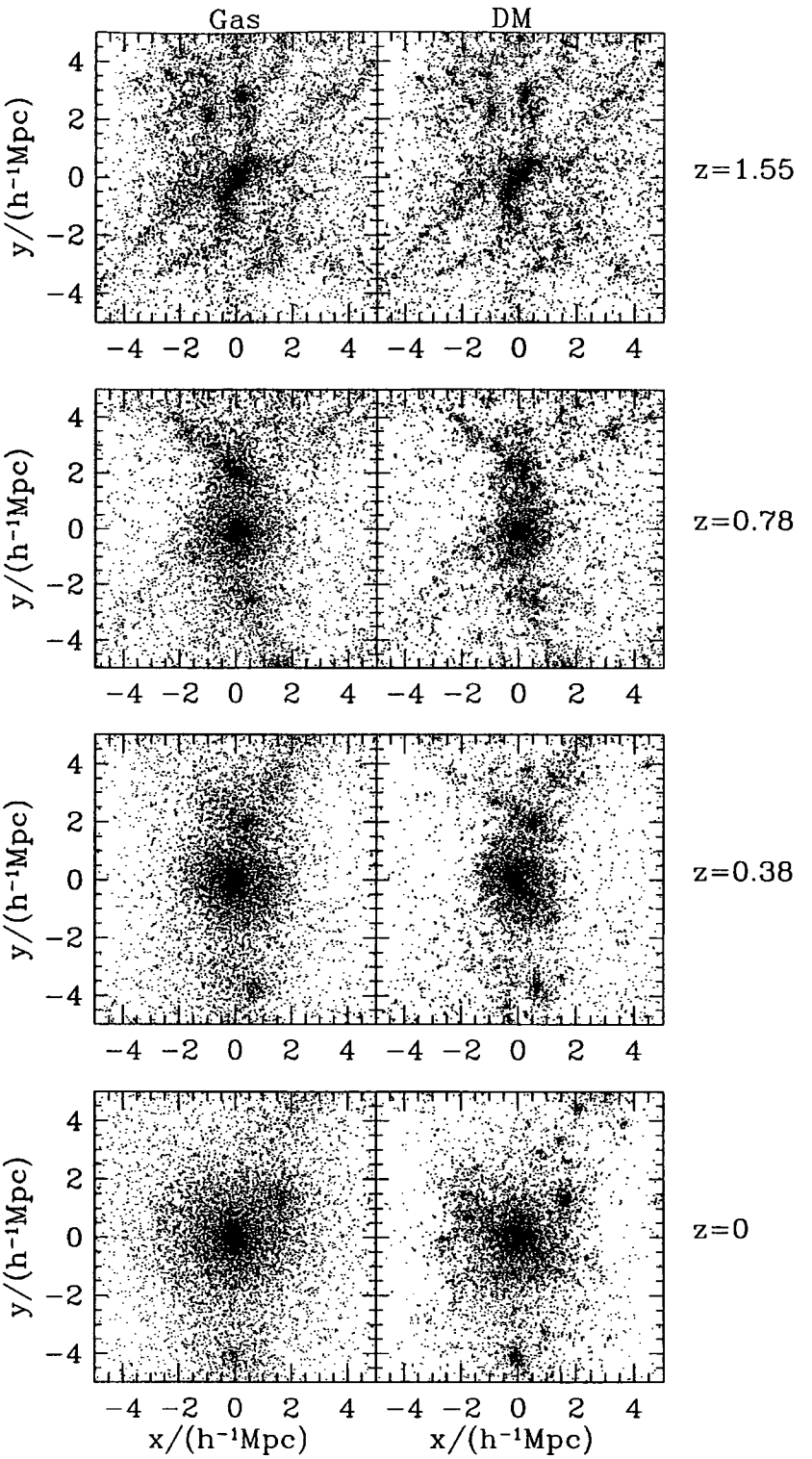

Figure 6.3: Dot plots showing the projected particle positions in cubes of physical size $10\,h^{-1}$Mpc centred on cluster cl01a. In each case, a random sample of half the particles is shown. From top to bottom the rows correspond to $z = 1.55$, 0.78, 0.38 and 0. The gas distribution is plotted in the left-hand panels and the dark matter in the right-hand panels.

to cluster 6 which requires a large initial high-resolution cube in order to enclose all the material ending up within twice the virial radius of the centre.

Fig. 6.2 shows the gas and dark matter distributions at redshift zero for three of the simulations. All particles within a cube with side $8\,h^{-1}$Mpc centred on the cluster are plotted. It is apparent that for each cluster the dark matter has more small-scale structure than the gas. The gas, which it should be remembered has not been allowed to cool, adopts a smoother, more spherically symmetric distribution. In the lower two rows corresponding to clusters 5 and 10, the main dark matter haloes are markedly non-spherical. Fig. 6.3 shows the gas and dark matter distributions at four diferent epochs for cluster cl01a. A random sample of half the particles within the $10\,h^{-1}$Mpc cube (fixed in physical coordinates and centred on the most massive progenitor object) is used. The relative clumpiness of the dark matter is again visible.

6.3.1 Applicability of the spherical collapse model

In the $\Omega_0 = 1$ cosmology the spherical collapse model predicts that the virialised region should extend outwards until the mean enclosed density contrast is 178, independent of redshift. For low-Ω_0 this factor becomes a function of redshift, only tending to 178 at large redshifts when $\Omega \rightarrow 1$. To check that the spherical collapse model is providing a useful description of where the 'edge' of the cluster is, the infall patterns have been considered. The three left-hand panels in Fig. 6.4 show the radial velocity profile as a function of $r/r_{\rm vir}$, averaged over all ten cluster simulations at three different redshifts (c.f. fig 11 of Cole & Lacey 1996). Solid and dashed lines represent dark matter and gas respectively.

For each of the redshifts, the spherically averaged profiles show a central virialised volume with essentially no net radial velocity, a zone where the material has stopped expanding away and is falling in towards the central mass and, at large distances, the cosmological expansion. If the crossover between the first two of these regions occurs at the 'edge' of the cluster then it can be seen that, for both gas and dark matter, this is reasonably well described by the spherical collapse model. At $z = 0$ the agreement is particularly good whereas at the higher redshifts the model appears to predict a value for the virial radius which encloses a region with small negative velocities. This is similar to the results of Crone, Evrard & Richstone (1994) who found that just interior to a radius encompassing an overdensity of 300 the material was settling inwards slowly. If the virial overdensity had been fixed at 178 then the disagreement would have been worse. The $z = 0$ clusters have masses of between 25 and $65M_*$, where M_* represents the mass satisfying $\sigma(M_*) = \delta_c$. These are therefore rarer objects than those produced from an $n = -1$ power spectrum by Cole & Lacey (1996). This could well explain the relative lack of infall interior to the virial radius in their clusters. In what follows all cluster properties are calculated within the virial radius as determined from the spherical collapse model.

It should be noted that the individual cluster infall patterns do have considerable

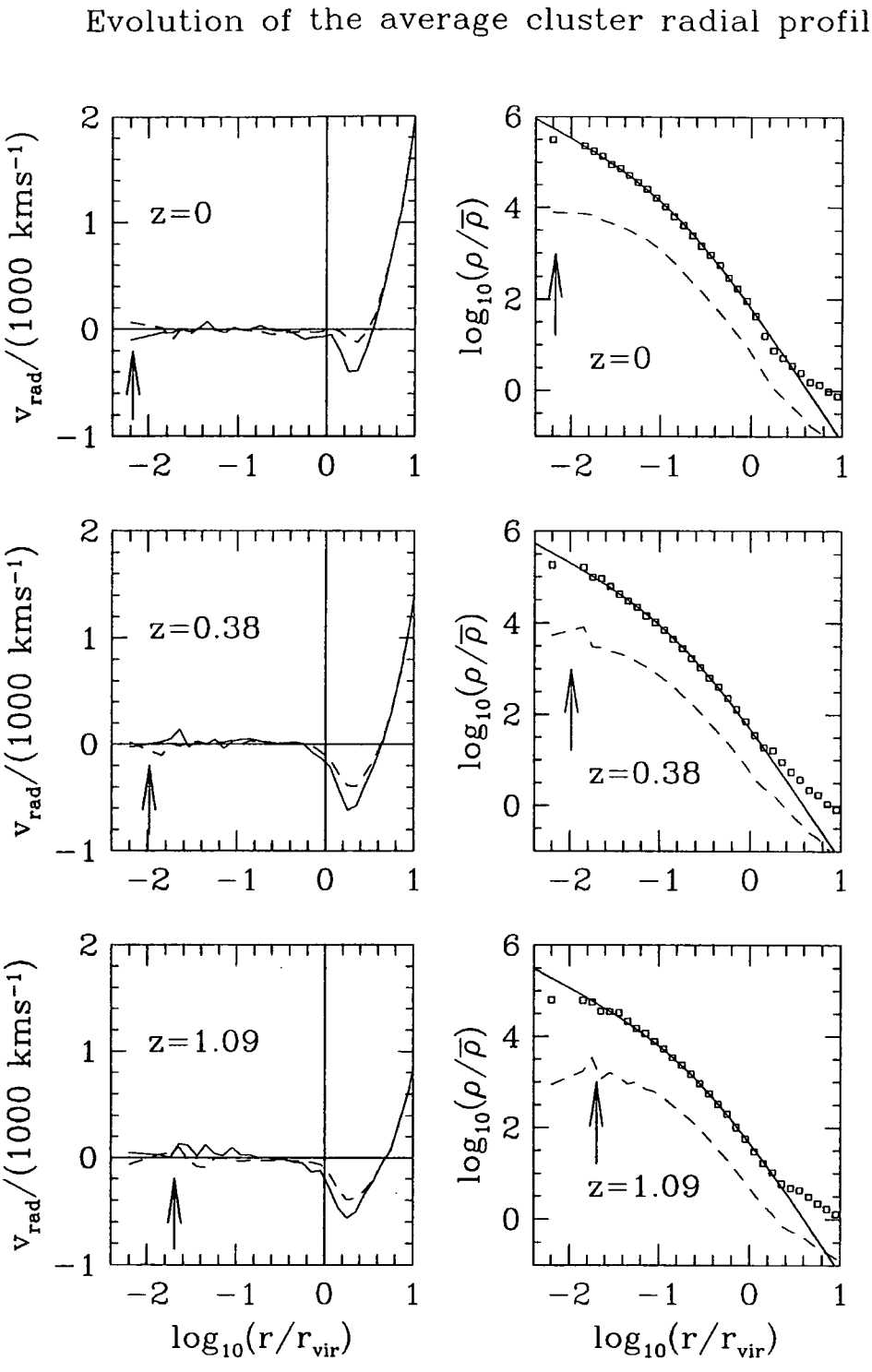

Figure 6.4: The radial velocity profiles, averaged over all ten clusters, of both gas (dashed lines) and dark matter (solid lines) as a function of redshift (three left-hand panels). On the right, the evolution of the average radial overdensity profiles of the clusters are shown. Gas is again represented with a dashed line, whilst the dark matter is plotted with squares. The solid lines show an NFW fit to the average dark matter profile. In each panel the average softening scale is illustrated by an arrow.

scatter about the mean profile (see Fig. 6.5 and Figs. E.1-E.9). This results from merger events. As mentioned by Cole & Lacey (1996) for their $\Omega_0 = 1$ simulations, the non-uniformities in the individual cluster profiles are sufficient to prevent a useful cluster 'edge' being defined for any particular object.

6.3.2 Density profiles

A useful formula for fitting the radial density profiles of the dark matter haloes in their $\Omega_0 = 1$ simulations was given by NFW. Modifying this slightly to take into account the variable overdensity used to define the cluster boundaries in the low-density cosmology gives the following expression:

$$\frac{\rho(x)}{\bar{\rho}} = \frac{A}{x(x + x_c)^2}. \tag{6.8}$$

Here $\bar{\rho}$ represents the mean background density, x is the radius in units of the virial radius and x_c and A are parameters to be fitted. The concentration parameter used by NFW is analogous to the reciprocal of x_c in the case where the lengths are scaled in units of r_{200} rather than $r_{\rm vir}$. This formula describes a density profile with $\rho \propto r^{-1}$ near the centre, $\rho \propto r^{-3}$ at large radii; the transition between these two regimes occurs at around a dimensionless scale-length of x_c. The fitting procedure involves a one-parameter χ^2 minimisation over all points with $x < 0.9$ to find the best x_c. The fact that equation (6.8) provides a good fit to the density profiles implies that there is only really one free parameter. Once a best-fitting scale-length is found, the normalisation A is determined by the constraint that the mass within the virial radius should correspond to the correct overdensity. This being the case, only the scale-length will be referred to.

The redshift-zero density profiles for each of the ten clusters are illustrated in Fig. 6.5 and Figs. E.1-E.9, with the softening length marked by an arrow. Solid and dashed lines show the dark matter and gas distributions respectively. In the three panels on the right of Fig. 6.4, the average over all ten clusters is shown for three different redshifts together with the best-fitting NFW profile for the average dark matter density profile. The x_c values for the three different redshifts, in order of increasing z, are 0.15, 0.17 and 0.24. As the density is averaged over spherical shells, any merging clumps at radii larger than about half the virial radius cause only small distortions to the profiles, even for most of the individual clusters.

The effect of the gravitational softening can be seen in the $z = 1.09$ panel of Fig. 6.4, where the core of the dark matter has nearly constant density. Also the deviation from the NFW profile at radii greater than $2r_{\rm vir}$ is slightly more marked at the higher redshifts indicating the greater importance of accreting material at high redshifts.

Fig. 6.6 shows the best-fitting scale-lengths for each of the ten clusters at redshifts 0 (squares), 0.55 (crosses) and 1.09 (stars) as a function of the virial mass. Large scale-lengths can be seen in a few particular cases, notably the star representing

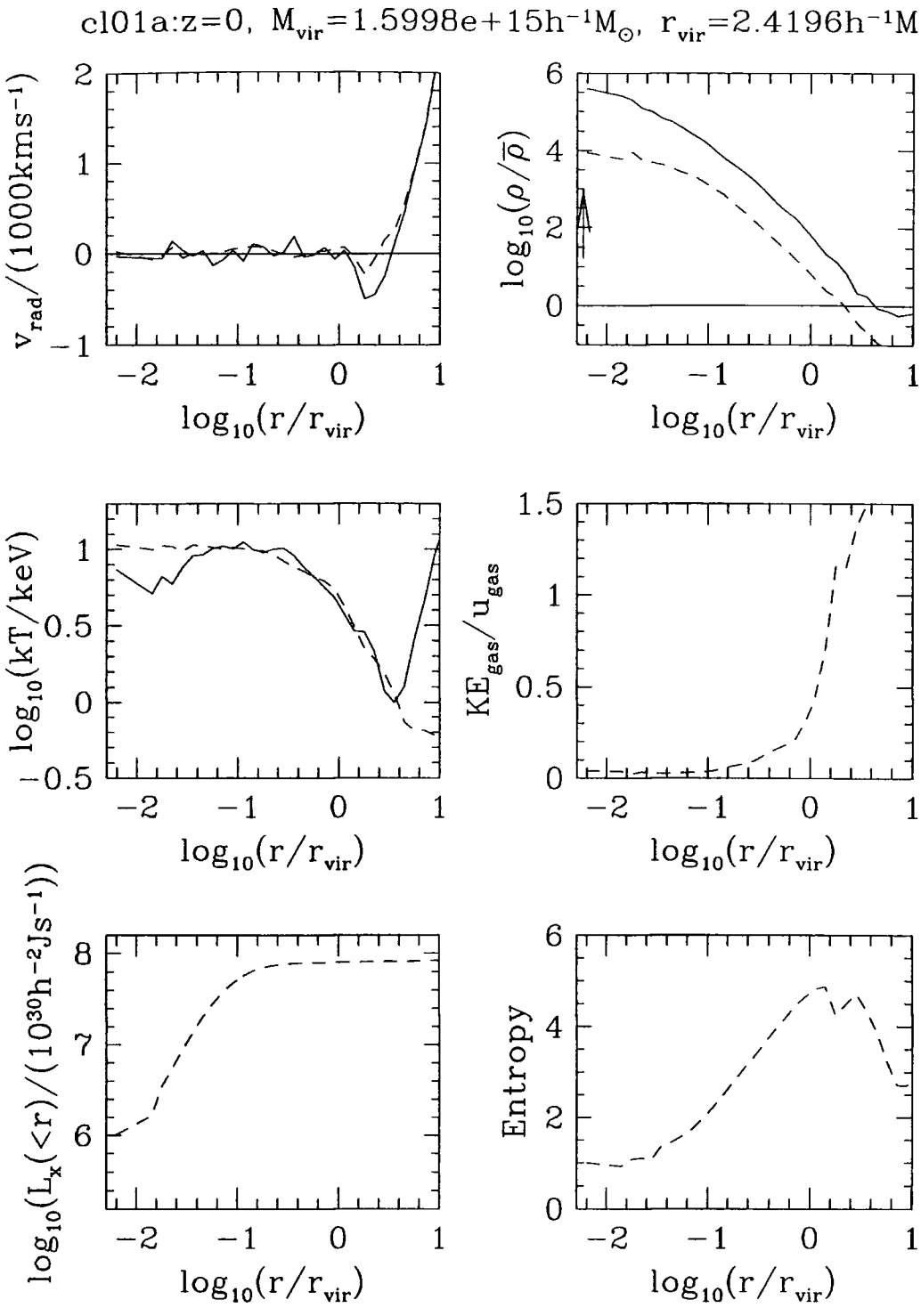

Figure 6.5: Radial profiles of various properties for cluster cl01a at a redshift of zero. Where two lines are shown, the solid one refers to the dark matter and the dashed one represents the gas. The cluster virial mass and radius are given at the top of the figure. Infall velocity and overdensity are shown in the top two panels. The middle row illustrates the cluster temperature (velocity dispersion in the case of the dark matter), and the radial dependence of the ratio between gas kinetic and internal energies. Cumulative luminosity and average particle entropy (in arbitrary units) profiles are shown in the bottom row.

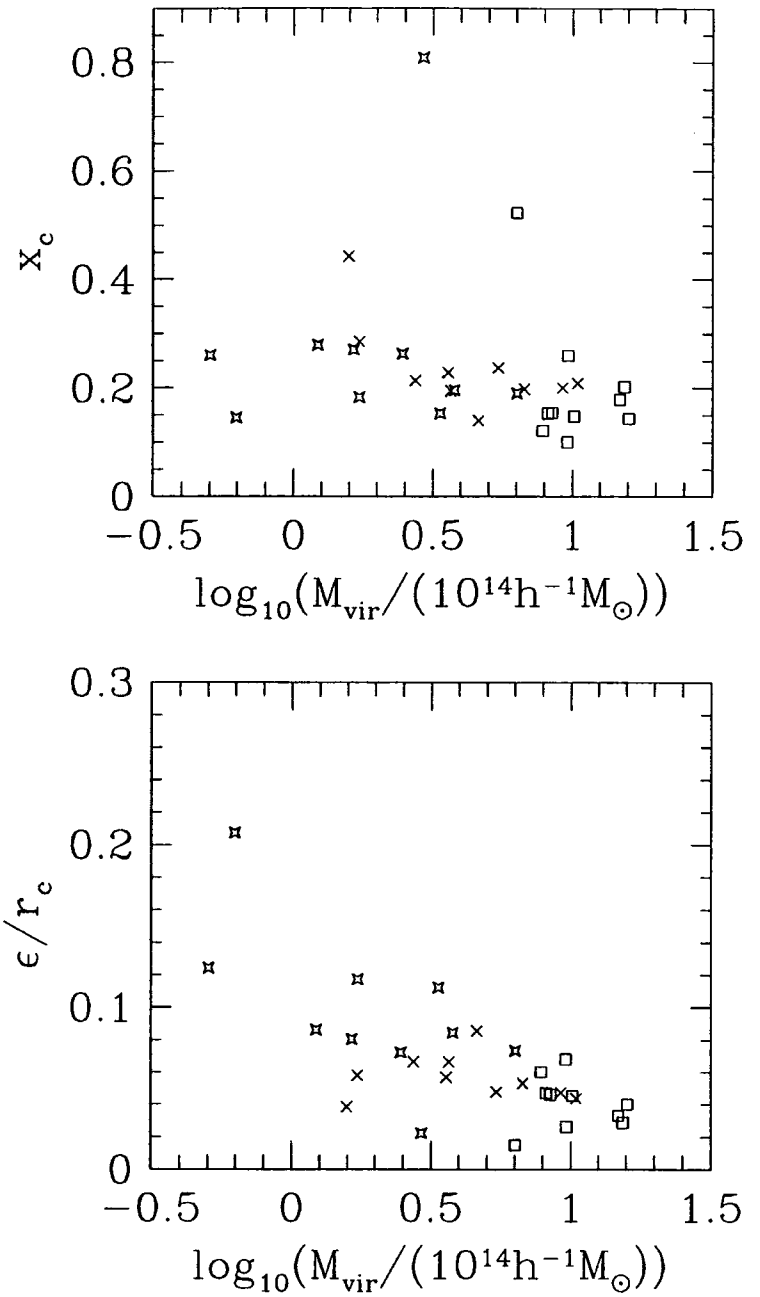

Figure 6.6: The mass and redshift dependence of the best-fitting x_c values for the ten individual clusters is given in the top panel. Squares, crosses and stars correspond to $z = 0$, 0.55 and 1.09 respectively. The ratio of the softening length to the physical scale-length for each case is given in the lower panel, with symbols as for the upper panel.

cluster 6 with $x_c \approx 0.8$ at $z = 1.09$. These points correspond to large merger events where a significant second mass concentration exists within 0.9 $r_{\rm vir}$ of the main cluster. This creates only a minor bump in the density profile, but because there are large numbers of particles in these outer bins the error bars are relatively small. Consequently the best-fitting density profile becomes more extended. There is no strong dependence of x_c on redshift or mass, although the high-redshift points do have a slightly greater mean value than those at redshift zero. A likely cause of this is the fact that at the higher redshift the clusters are accreting a larger fraction of their mass than at the present-day. The lower panel shows the ratio of the gravitational softening (ϵ) to the physical size of the scale-length, denoted by r_c ($= x_c r_{\rm vir}$). In all cases, even at $z = 1.09$, the softening is no more than a quarter of the size of the best-fitting scale-length and for most points it is less than a tenth of this, so it is unlikely that these results are strongly affected by this numerical limitation.

These findings can be compared with the results given by Navarro, Frenk & White (1996, NFW2) for their $\Omega_0 = 1$ massive clusters at redshift zero. They quote halo concentration parameters, defined as $1/x_c$ where r_{200} not $r_{\rm vir}$ is used to normalise the radius. Taking the reciprocals of the reported concentration parameters gives values in the range $0.15 - 0.20$, similar to the best-fitting values of x_c found here. The conversion factor from r_{200} to $r_{\rm vir}$ is approximately 0.8 at the final time when the virial radius encloses a density contrast of 324. For the $\Omega_0 = 0.3$, $\Lambda_0 = 0.7$ haloes simulated here, the physical size of the fitted scale-length at $z = 0$ is therefore $\sim 20\%$ smaller than the NFW $\Omega_0 = 1$ cases. At earlier times, when the low-density model resembles the $\Omega_0 = 1$ case, x_c takes values closer to those found by NFW and NFW2. It should be stressed that the overall differences between the different profiles are small.

As found by NFW, the gas distribution appears to trace the dark matter well at radii larger than $\sim r_{\rm vir}/10$, but nearer to the centre, the density profile flattens more rapidly. At redshift zero there are typically 1000 gas particles within this central region, so the gas smoothing length and the gravitational softening length are both significantly lower than $\sim r_{\rm vir}/10$. Thus it seems likely that at least some of this difference is real. Of course, in real clusters other physical processes might be expected to affect the gas distribution on these relatively small scales.

6.3.3 The cluster baryon fraction

The cluster baryonic mass fraction is a quantity of much current interest (e.g. Gunn & Thomas 1996 and references therein). Fig. 6.7 shows how the cumulative baryon fraction interior to a particular radius varies as a fraction of the universal value, assumed to be 0.1 in these simulations. The upper panel shows the cluster-to-cluster variation of this ratio for the 10 clusters at $z = 0$. Values at $r_{\rm vir}$ (open squares and crosses) and $3r_{\rm vir}$ (filled squares and stars) are shown in the lower panel as a function of mass for the clusters at $z = 0.38$ and $z = 0$ respectively. Within the virial radius, the baryon fraction is found to be about 90% of the global value, and there is no significant trend with redshift or mass. At $3r_{\rm vir}$, the calculated

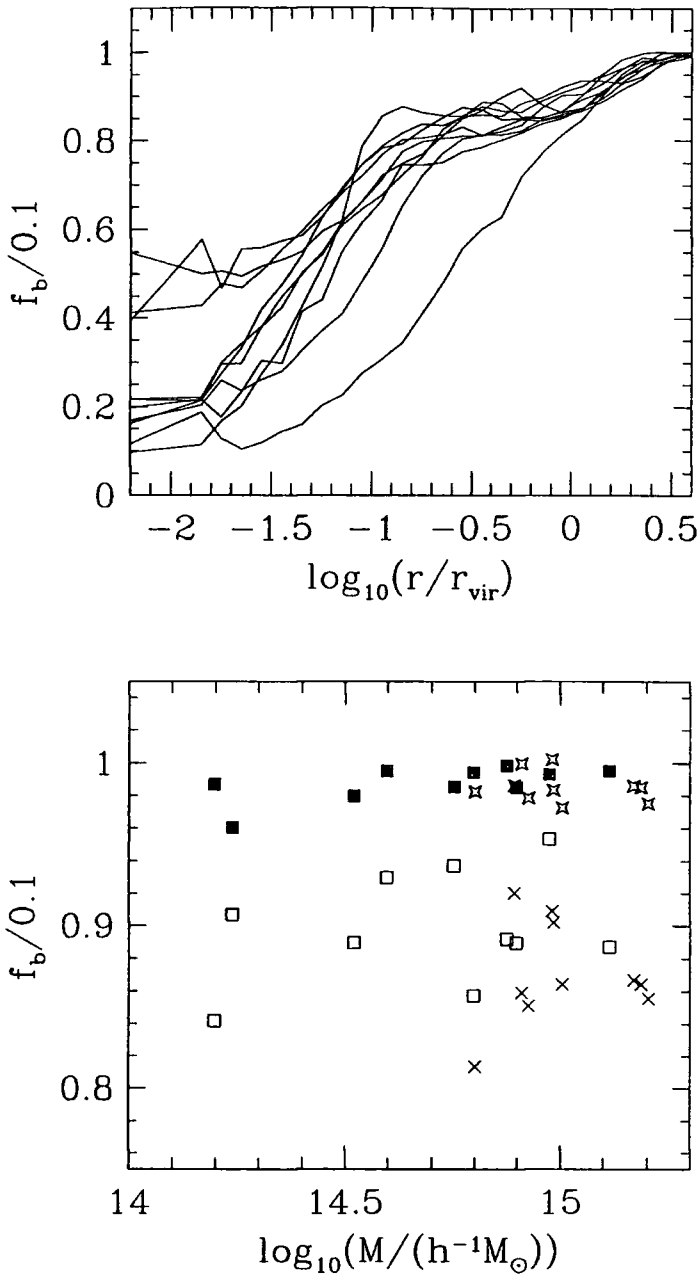

Figure 6.7: The top panel shows the radial variation of the ratio of the cumulative mass fraction in baryons to the universal value of 0.1. Each of the 10 clusters is represented by one solid line. The lower panel shows the value of this ratio at the virial radius and at $3r_{vir}$ for each cluster at $z = 0$ and $z = 0.38$. Open and filled squares represent $z = 0.38$ clusters with the ratio evaluated at r_{vir} and $3r_{vir}$. Crosses and stars show the corresponding quantities at $z = 0$.

baryonic mass fraction is within 4% of the universal value. The turnaround radius is typically only slightly greater than $3r_{\rm vir}$ for the clusters resimulated here. It should be remembered that the supply of gas particles could run out at such a large distance from the cluster centre because of the finite size of the high-resolution region. The fact that the baryonic mass fractions are so close to the underlying value confirms that the high-resolution regions were not chosen to be too small.

In the central regions, the baryon fraction is significantly lower than the true background mass fraction of 0.1. For one particular cluster, the mass in baryons within $0.1r_{\rm vir}$ is only 30% of the global value. However, the uncertain effect on this ratio, measured at such a small scale, of neglected physical processes, such as radiative cooling and energy ejected during supernovae, make the cumulative fraction at the virial radius a more meaningful prediction from the simulations.

6.3.4 Temperature profiles and hydrostatic equilibrium

Having studied the distribution of the gravitationally dominant component of the cluster, the radial dependence of the dark matter velocity dispersion and the gas temperature will now be investigated. Fig. 6.5 and Figs. E.1-E.9 illustrate these two quantities. As for the density profiles, solid and dashed lines correspond to dark matter and gas respectively. The dark matter velocity has been converted to a temperature and plotted in keV along with the gas. This is accomplished for the dark matter using the following equation:

$$kT_{\rm DM} = \mu m_{\rm p} \frac{|\mathbf{v}|^2}{3}, \tag{6.9}$$

where $\mu m_{\rm p}$ is the the mean molecular mass, taken to be $0.588 m_{\rm p}$. Note that at large radii, the dark matter velocity becomes dominated by the Hubble expansion, so it does not reflect a 'temperature' at these scales. Across each cluster, the dark matter and gas temperatures are approximately constant. At radii larger than $\sim 0.5\ r_{\rm vir}$, the temperatures tend to decrease outwards, but not by very much. On average the gas temperature decreases by a factor of two going from the centre to the virial radius. These findings are similar to those of Evrard (1990), Couchman et al. (1994), NFW and Evrard et al. (1996).

In the central few percent of the virial radius, the dark matter velocity dispersion declines whereas the gas temperature remains reasonably constant. This effect is quite small but it can be seen in a few of the individual clusters as well as the average profiles given in Fig. 6.8. In this figure, the solid and long-dashed lines represent the dark matter and gas at redshift zero whereas the short-dashed and dotted lines correspond to the same quantities at redshift 0.38. The dark matter 'temperature' is calculated using a velocity dispersion in this figure, so that the Hubble expansion does not affect the results well outside the virial radius. As can be seen from the gas temperature profiles, there are more significant bumps outside the virial radius for the higher-redshift case. This can be interpreted as the shocks associated with accreting material being more important in the past when the rate of accretion was

larger. Knowing both the density and temperature profiles of both gas and dark matter components, it is now possible to check whether or not the individual clusters are in equilibrium.

The equation of hydrostatic equilibrium for a spherically symmetric gas distribution can be written as

$$M_{\rm est}(< r) = -\frac{kT(r)r}{G\mu m_{\rm p}}\left[\frac{{\rm dln}T}{{\rm dln}r} + \frac{{\rm dln}\rho_g}{{\rm dln}r}\right]. \tag{6.10}$$

$M_{\rm est}$ represents the total enclosed mass estimated under the assumption that the gas is in hydrostatic equilibrium, and ρ_g is the gas density. To estimate the total mass using the dark matter requires Jeans' equation:

$$M_{\rm est}(< r) = -\frac{\overline{v_r^2}r}{G}\left[\frac{{\rm dln}\overline{v_r^2}}{{\rm dln}r} + \frac{{\rm dln}\rho_{DM}}{{\rm dln}r} + 2\beta\right], \tag{6.11}$$

where $\overline{v_r^2}$ is the mean square radial velocity and the velocity anisotropy is expressed through

$$\beta = 1 - \frac{\overline{v_t^2}}{2\overline{v_r^2}}. \tag{6.12}$$

$\overline{v_t^2}$ is the two-dimensional mean square tangential velocity. Equation (6.11) assumes that the mean dark matter radial and tangential velocities are both zero and that the mass distribution is spherically symmetric.

The lower panel of Fig. 6.9 shows the mean dark matter velocity anisotropy averaged over all ten clusters. With the definition provided by equation (6.12), $\beta = 0$ implies isotropic orbits and radial orbits have $\beta = 1$. A slight radial bias to the dark matter velocities is therefore shown. The upper panel of this figure shows the radial variation of the ratio of estimated to true cluster mass averaged over all clusters. Equations (6.10) and (6.11) have been used to produce the solid and dashed lines respectively. The radial derivatives are calculated by differencing the values found averaging the relevant quantities in radial shells. For the gas case, the average estimated total mass is about 10% too low. As noted by Evrard (1990) and NFW, this discrepancy comes from motions in the gas providing some pressure support, and 10% is approximately the ratio of gas kinetic to thermal energies. Of the individual clusters only cl09a would cause a significantly worse mass estimate. This object has large amounts of kinetic energy still in the gas because of a recent merger event (see Figs. E.8 and E.17). Consequently, the estimated binding mass is too low by about 30%. For the dark matter mass estimator, the average $M_{\rm est}$ over all ten clusters is distorted to a value greater than $M_{\rm true}$ by three clusters which are very far from being in equilibrium. The cluster mass evolution in Figs. E.13, E.16 and E.17 shows the large recent merger events that make clusters cl05a, cl08a and cl09a so discrepant. The remaining clusters underestimate the true mass by approximately 10%.

Ignoring the terms in square brackets in equations (6.10) and (6.11), because their radial dependence will be very slight, it can be seen that a binding mass profile with

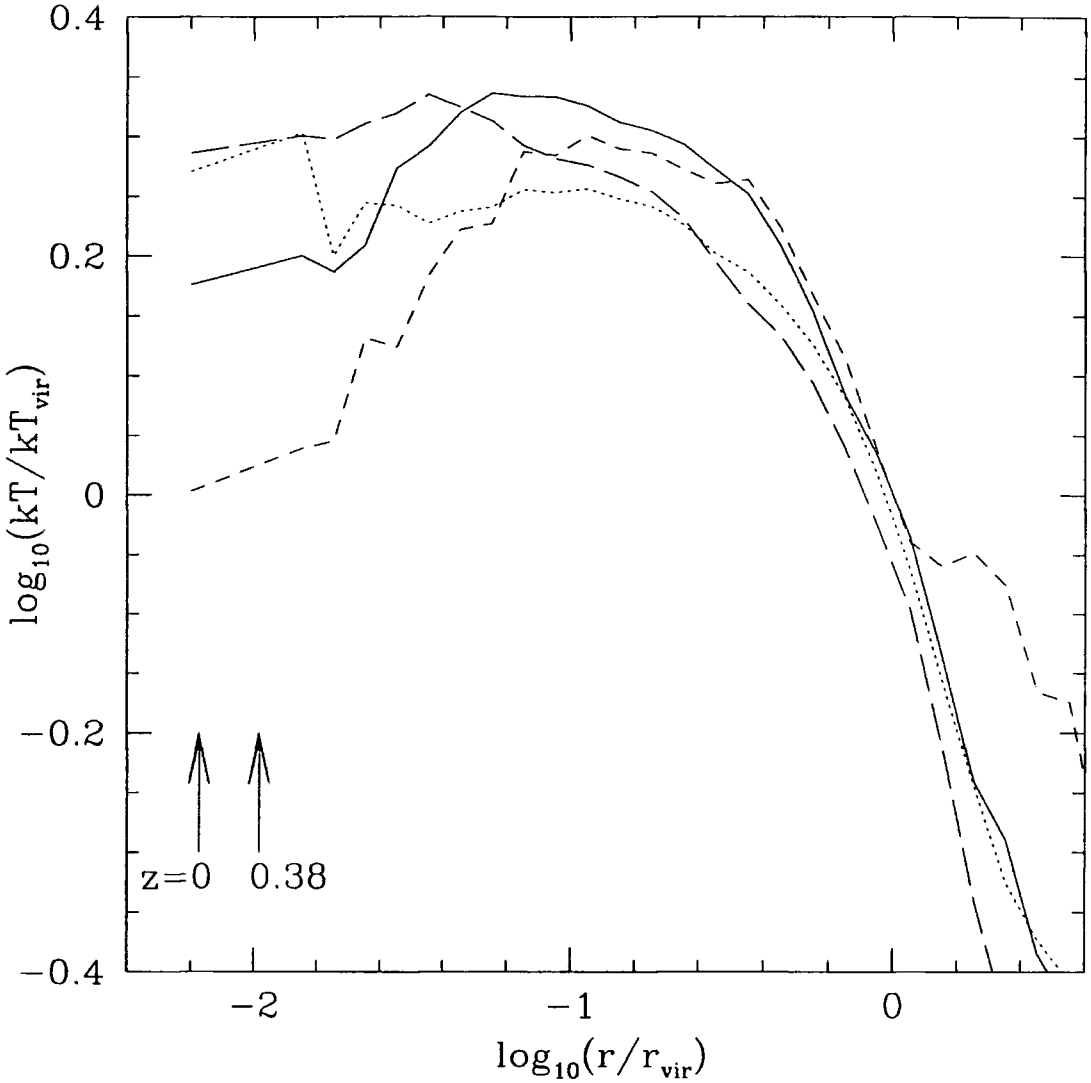

Figure 6.8: Gas temperature and dark matter velocity dispersion curves, averaged over all ten clusters at two different redshifts. The solid and long-dashed lines represent dark matter and gas respectively at a redshift of zero, whilst the corresponding quantities at $z = 0.38$ are shown by the short-dashed and dotted lines. Average softenings at the two redshifts are given by the arrows.

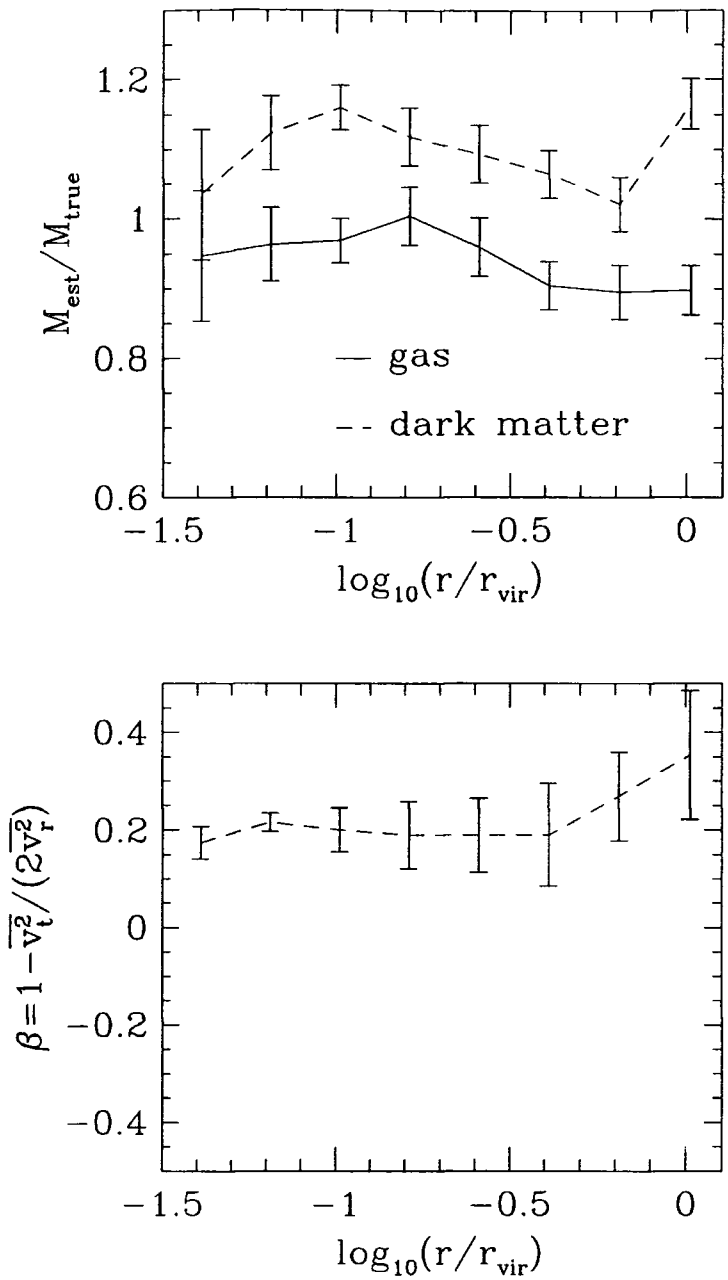

Figure 6.9: In the upper panel, the ratio of estimated to true total cluster mass, averaged over all 10 clusters, is shown as a function of radius. Equations (6.10) and (6.11) have been used to produce the gas (solid line) and dark matter (dashed line) estimates respectively. Error bars refer to the uncertainty in the mean over all clusters. The lower panel shows the radial variation of the mean velocity anisotropy β and the error in this mean.

$\rho \propto r^{-2}$ will require an isothermal (constant velocity dispersion) gas (dark matter) distribution in order to maintain equilibrium. This is what is happening across most of each cluster. In the centre of some of the individual clusters, and also clear in the average temperature profile, the gas temperature remains constant whereas the dark matter velocity dispersion drops slightly. Why this happens is addressed in the next subsection.

6.3.5 Other gas properties

The other gas properties that have been calculated are the entropy and luminosity (Fig. 6.5 and Figs. E.1-E.9). For each cluster at $z = 0$, the average entropy per particle is a minimum in the centre but only cluster *cl*05*a* has a large central region of constant entropy. This particular object has a large constant density gas core and the gas kinetic energy is at least 30% of its internal energy in this region, suggesting that the cluster is experiencing turbulence caused by a recent merger. Confirmation of this explanation is provided by Fig. 6.10. The four left-hand panels show the positions of the gas and dark matter particles that make up the central 10% of the final cluster mass as a function of redshift. (See the caption for the redshifts of each panel.) On the right are shown the corresponding positions of particles, again comprising 10% of the cluster mass, ending in another dense knot at a position $(0.24, -0.07, 0.21)\, h^{-1}\mathrm{Mpc}$ away from the main cluster centre. Dark matter is shown in black for both cases and gas is green (for the main cluster centre) or magenta (for the subsidiary peak in the density field). In the sense that the gas and dark matter are in a variety of different haloes at $z = 1.09$, this is representative of all the clusters that have been resimulated. However, the magnitude of the collision occurring between $z = 0.11$ and $z = 0.01$ is unusually large for the ten clusters as a whole. Particularly interesting in this example is the way that the final core dark matter and gas particles appear to originate predominantly in different haloes. This is an illustration of the halo-swapping found in the simulations of Pearce, Thomas & Couchman (1992). In a head-on collision between two haloes, both consisting of gas as well as a gravitationally-dominant dark matter component, the dark matter emerges on the other side while the gas is shocked and falls back into the 'wrong' halo. The sharp shock front can be seen particularly well in the $z = 0.01$ panel showing the particles ending up in the larger halo. It is apparent at $z = 0$ that both dark matter haloes are further from the shock than the gas that has become associated with them, and the radial velocities plotted in Fig. E.4 show the secondary dark matter peak moving away from the cluster centre, closely followed by some gas at $\log_{10}(r/r_{\mathrm{vir}}) \approx -1$ which corresponds to $0.2\, h^{-1}\mathrm{Mpc}$.

By tracing back the central cluster particles at $z = 0$, only the clusters experiencing a large merger in the recent past will exhibit this kind of behaviour because the two dark matter haloes mix together quite rapidly as a result of dynamical friction. However, for sufficiently head-on collisions, there is no reason to expect that this type of process is uncommon. As was noted by Pearce et al. (1992) and also NFW, one consequence of this behaviour is that a transfer of energy occurs from the dark

matter to the gas, leading to a central gas distribution that is more extended than the dark matter. Another cause of such heating of the gas in the centre would be the numerical two-body heating described by Steinmetz & White (1996). However, the radius at which the heating time is equal to the dynamical time is only slightly greater than the softening length. This is about a factor of three less than the radius interior to which the gas is significantly hotter than the dark matter. Also the fact that NFW also conclude that energy is transferred from dark matter to gas, from simulations with a different resolution, suggests that this is not just a numerical artefact.

The cumulative luminosities shown in Fig. 6.5 and Figs. E.1-E.9 illustrate well how the emission is concentrated in the cores of the clusters. In all examples, at least half of the total calculated luminosity comes from within a sphere of radius $0.1r_{\rm vir}$. It should be reiterated that no radiative cooling has been included in the simulations. If a cluster has 10000 gas particles within the virial radius then about one tenth of these will be in this central region providing over half of the total luminosity. The fraction of the total calculated luminosity emitted from within a sphere of radius equal to the typical gas smoothing length in the centre of the cluster at $z = 0$, $(30 - 40\,h^{-1}{\rm Mpc})$ is $< 10\%$ in all of the clusters. For the $z = 1.09$ clusters, the typical gas softening in the cluster centre corresponds to $3 - 4\%$ of the virial radius. The redshift zero results suggest that a central sphere with this radius would enclose $\sim 25\%$ of the total luminosity. This gives a rough indication of the extent to which the SPH kernel and lack of resolution will affect the total cluster luminosity calculated from the simulations. NFW concluded that, at least $2000 - 3000$ particles are needed in order to provide reliable estimates of the luminosity. Given that the central gas density and temperature profiles in this study are very similar to theirs, a similar rule-of-thumb is expected to apply here. With no large central cusp in the gas density, the SPH technique will not be smoothing over any significant region of X-ray emission. Thus, any discrepancies between the simulation results and real clusters (particularly at $z = 0$) are more likely to result from the lack of additional physics in the simulations rather than numerical limitations.

6.3.6 Bulk properties: evolution and correlations

Fig. 6.11 and Figs. E.10-E.18 show how the bulk properties of the individual clusters evolve with time. The top left panels illustrate the growth of the virial mass (dotted line), the mass within a density contrast of 200 (dashed line) and the mass within a comoving sphere with size equal to the $z = 0$ virial radius (solid line). Although there is a considerable variation between the individual cases, the averaged evolution shown in Fig. 6.12 implies that after a slow start, clusters accrete approximately the same amount of material in any interval of time, independent of redshift. The fraction of mass being accreted is therefore decreasing with time and mergers have less and less effect on the cluster as a whole. For redshifts much above 1, the clusters have generally acquired less than 20% of their final virial mass. Thus, they are likely to contain less than 2000 gas particles and a similar number of dark matter particles,

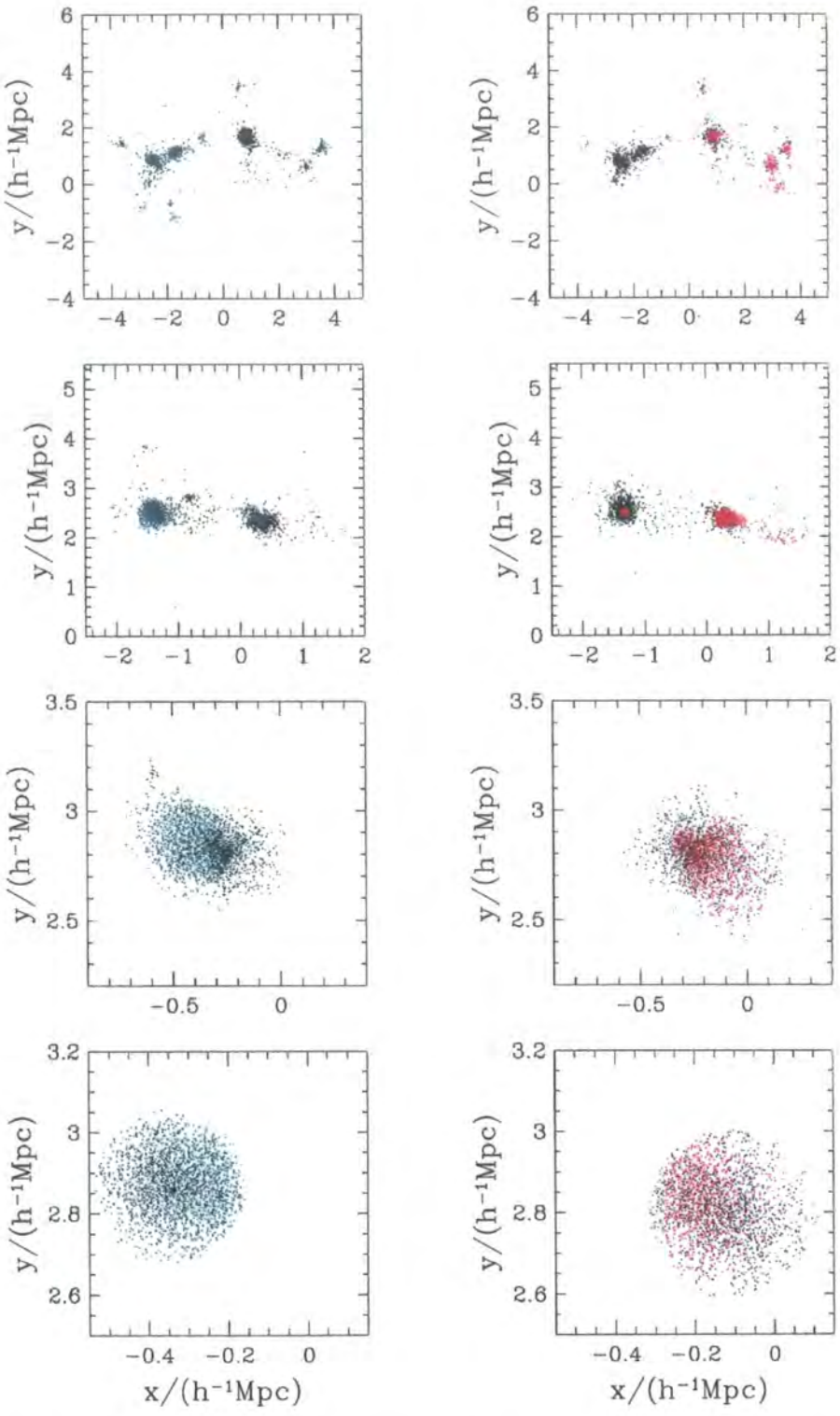

Figure 6.10: Projected positions at 4 different epochs of the particles which comprise the central 10% of the mass of cluster cl05a at $z = 0$ are shown in the left-hand panels. On the right, the same amount of mass but from a region displaced by $(0.24, -0.07, 0.21)\, h^{-1}$Mpc (corresponding to a secondary dark matter density peak within the cluster) at the final time is plotted. From top to bottom the panels refer to redshifts of 1.09, 0.11, 0.01 and 0. Black points represent dark matter and this is overplotted with green or magenta points for the gas. The units are in physical h^{-1}Mpc. Note that the scales change for each row of two panels.

and the results become compromised by lack of numerical resolution.

The velocity dispersion and temperature panels of Fig.6.12 show similar results, with the rate of change of these properties decreasing with time. Both mass- and luminosity-weighted temperatures are given in units of the final mass-weighted cluster temperature. The extent to which these two measures are different reflects the non-isothermality of the gas, and at $z = 0$ the luminosity-weighted temperature is 1.3 times larger.

The average entropy per particle is shown for the central tenth of the cluster gas (dotted line) and the outermost tenth of the gas (solid line). Whilst the entropy is increasing with time in both cases, the effect is more pronounced in the outer regions. This results from the recently accreted material, which has suffered the largest shock because it has fallen into a bigger cluster than previously accreted material, gaining large amounts of entropy and remaining predominantly towards the edge of the cluster.

In the β panel, four different curves are shown. These relate the gas temperature, either mass- or luminosity-weighted, to the virial mass (using equation (2.2)) or the dark matter velocity dispersion through

$$\beta k T_{\rm gas} = \mu m_{\rm p} \sigma_{1D}^2. \tag{6.13}$$

$\mu m_{\rm p}$ is the the mean molecular mass. The nomenclature used for the β parameters is that the first letter in the subscript refers to the type of temperature weighting and the second one is M if equation (2.2) has been used to relate temperature to mass, or σ if equation (6.13), with velocity dispersion not mass, was utilised. All of the four cases show negligible evolution out to a redshift of about 1. However the short- and long-dashed curves, relating the virial mass to the mass- and luminosity-weighted temperatures respectively, do increase by $10 - 15\%$ going back to $z \approx 1.5$. With β defined by equation (2.2), this could be interpreted as the virial mass being overestimated at early times, but it is a relatively small effect. The β parameters will be discussed in more detail in the next subsection.

Correlations between cluster properties are given in Fig. 6.13. All temperatures shown are luminosity-weighted. Each square represents a cluster at redshift zero, whereas the crosses and stars correspond to $z = 0.55$ and $z = 1.09$. It should be noted that there are more orders of magnitude shown in the panels containing luminosity, so despite the similar appearance to the other relationships there is a larger scatter when luminosity is involved. Presumably, the inclusion of more gas physics in the simulations would exaggerate this difference.

The solid lines shown in the panels not involving luminosity are the predictions for $z = 0$ (or all redshifts in the case of the velocity dispersion against temperature plot) of the spherical collapse model assuming that the gas is isothermal and that $\beta = 1$, and the dashed lines represent the results at $z = 1.09$. Equations (2.2) and (6.13) are used to relate gas temperature to virial mass and velocity dispersion respectively. As a result of the fact that only the most massive clusters were chosen for resimulation, there is a lack of range in the virial masses of the redshift zero

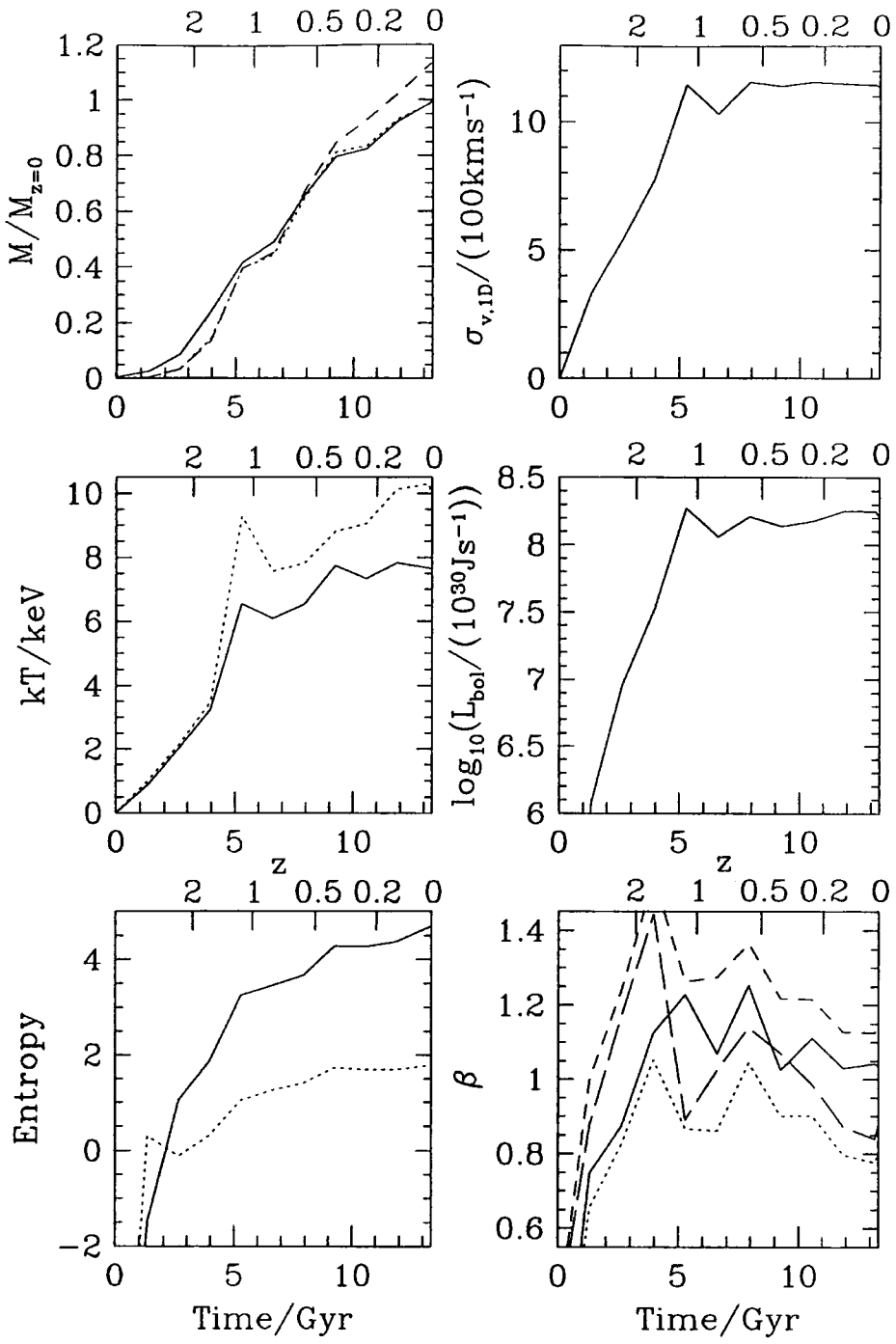

Figure 6.11: The evolution of the bulk properties of cluster cl01a. The top-left panel shows the virial mass (dotted line), the mass within a density contrast of 200 (dashed line), and the mass within a comoving radius equal to the final cluster virial radius (solid lines). The middle-left panel shows mass- and luminosity-weighted temperatures by solid and dotted lines respectively. In the bottom-left panel, the average entropy per gas particle (in the same units as Fig. 6.5) for the central 10% (dotted line) and outermost 10% (solid line) of the cluster gas is shown. The one-dimensional velocity dispersion for the dark matter is given in the top-right box. The middle-right panel shows the luminosity, calculated using equation (6.7) and summing over all gas within the virial radius. The final panel contains information about the four different β parameters. $\beta_{M\sigma}$ (solid), $\beta_{L\sigma}$ (dotted), β_{MM} (short-dashed) and β_{LM} (long-dashed) are shown.

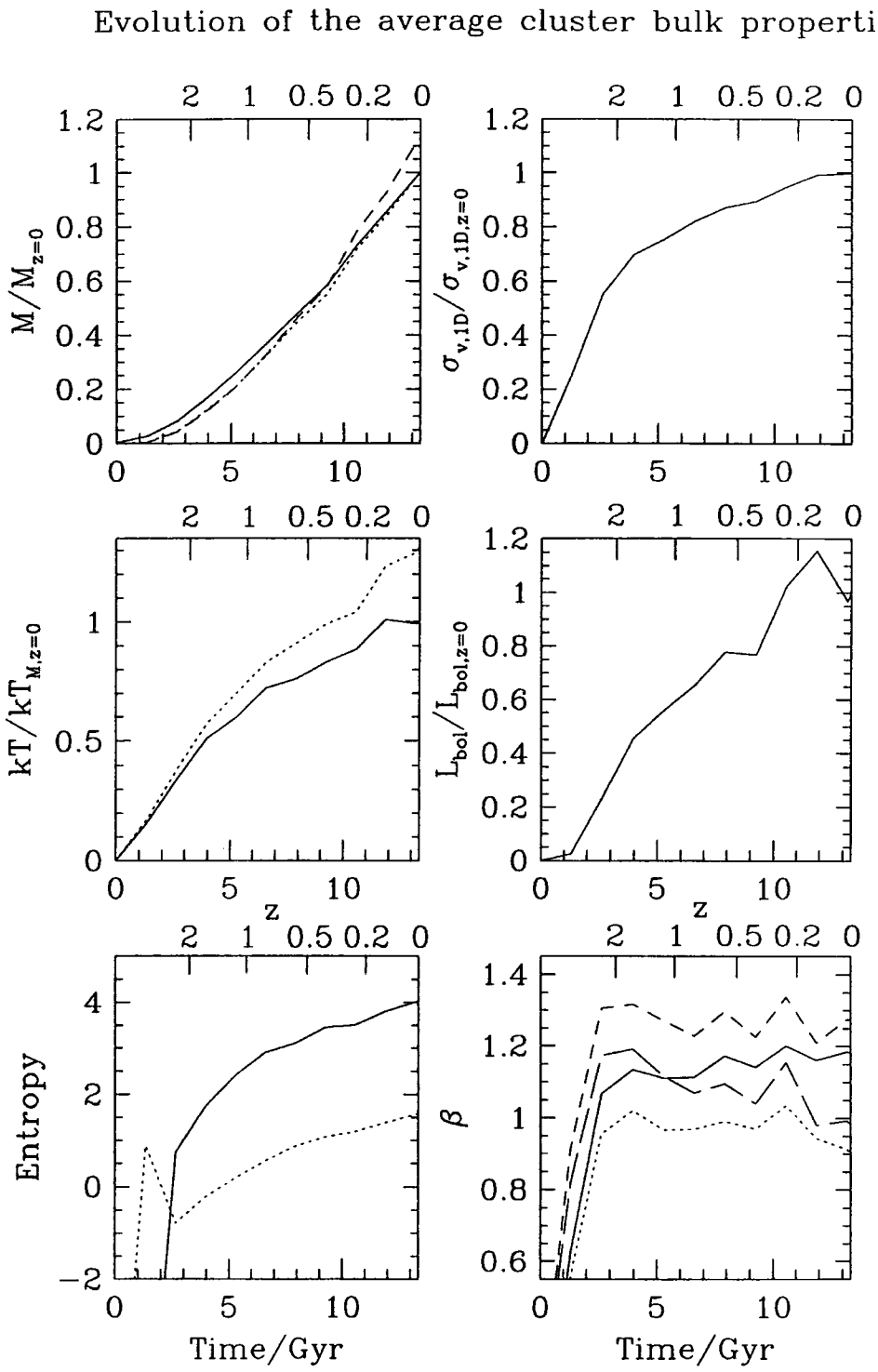

Figure 6.12: Evolution of the bulk cluster properties, averaged over all ten clusters. The quantities shown in each panel are the same as those in Fig. 6.11. Velocity dispersions, temperatures and luminosities are shown as a fraction of the final value.

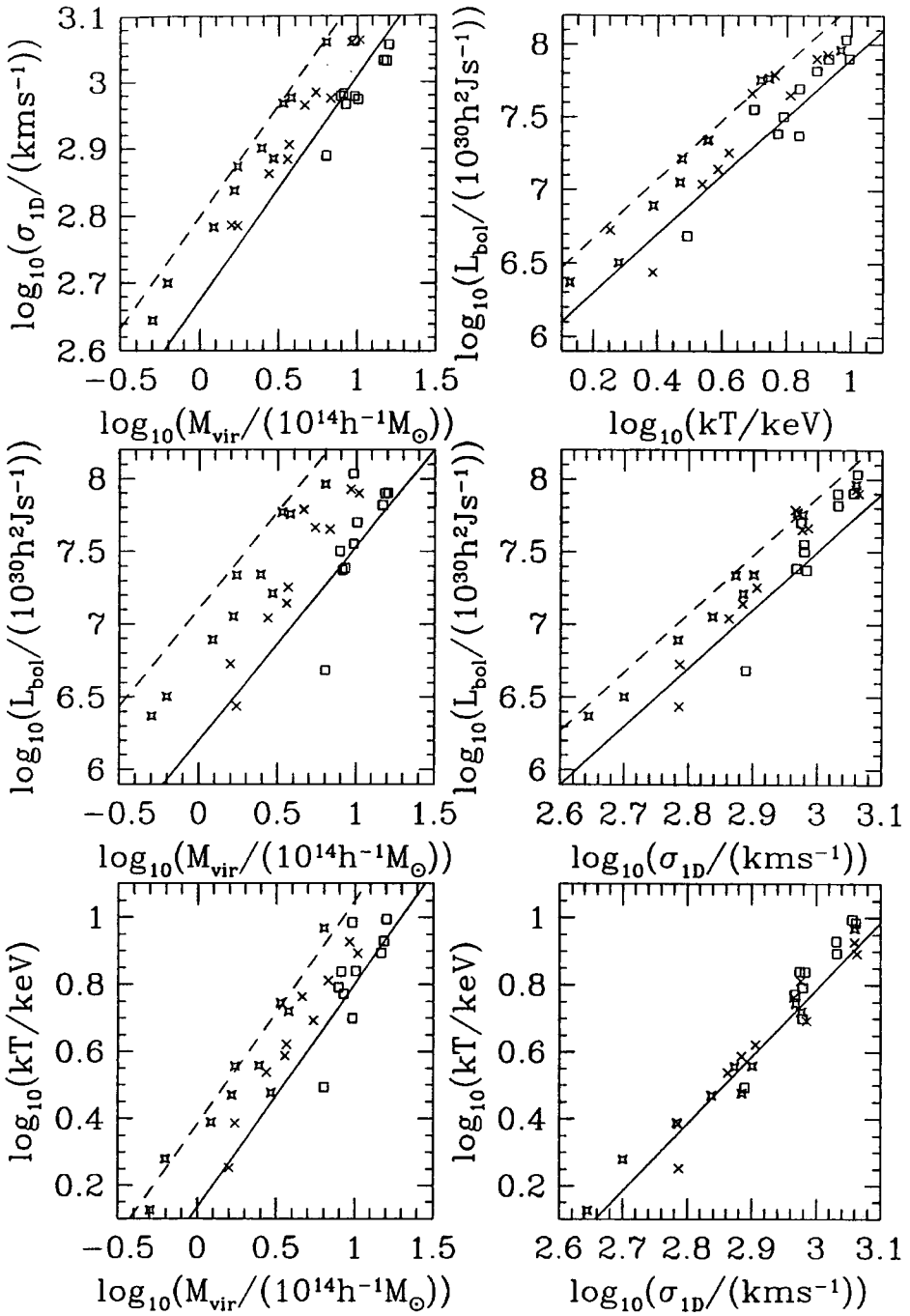

Figure 6.13: Correlations between the cluster properties. Virial mass is defined within an overdensity given by the spherical collapse model, velocity dispersion is for all of the dark matter particles within the virial radius, luminosity-weighted temperatures are shown and the luminosity is estimated using equation (6.7). Each square represents a cluster at redshift 0, and the crosses and stars correspond to $z = 0.55$ and $z = 1.09$ respectively. In the top left panel and the two bottom panels, the lines show predictions made assuming the cluster is isothermal and that the relevant β parameter is equal to 1. Solid lines show the model at $z = 0$ and the dashed lines at $z = 1.09$. The lines in the plots that include luminosity have arbitrary normalisation, and the evolution between $z = 0$ and $z = 1.09$ is given by equation (6.15).

objects. Nevertheless, the diversity of accretion histories for different clusters allows a better comparison to be made at the earliest redshift, where it can be seen that the predicted power laws provide a good fit to the simulation results. If anything, the simulation velocity dispersions are slightly on the low side, but the scale is so expanded that this is only a very minor discrepancy.

It is more difficult to make predictions for the evolution of the cluster luminosities. As was noted by Kaiser (1986), the scaling relations which NFW used with their $\Omega_0 = 1$ simulations are not applicable for the $\Omega_0 = 0.3, \Lambda_0 = 0.7$ cosmology because of the extra scale-length introduced in this model. This additional physical scale removes the temporal self-similarity that exists in the $\Omega = 1$ universe. However the scaling relations can be modified to take into account the evolution of the density contrast predicted by the spherical collapse model, leading to

$$T(M,z) \propto M^{2/3}(1+z)\left(\frac{\Omega_0\Delta_c(z)}{\Omega(z)\Delta_c(0)}\right)^{1/3} \tag{6.14}$$

and

$$L(M,z) \propto M^{4/3}(1+z)^{7/2}\left(\frac{\Omega_0\Delta_c(z)}{\Omega(z)\Delta_c(0)}\right)^{7/6} \tag{6.15}$$

The solid lines in the panels involving cluster luminosities in Fig. 6.13 have slopes consistent with these scaling relations, and normalisations that have been chosen arbitrarily. Equation (6.15) is then used to produce the $z = 1.09$ predictions (dashed lines). The evolution in the luminosities of the simulated clusters is lower than that predicted by equation (6.15). However, slightly more evolution is seen in these $\Omega_0 = 0.3, \Lambda_0 = 0.7$ clusters than was seen in the NFW $\Omega_0 = 1$ runs over approximately the same redshift interval, despite the fact that the low density cosmology would be expected to show less evolution. The most likely explanation for this is the extra resolution in the simulations run here with the GRAPE.

One final point worth making about the correlations in Fig. 6.13 is that the gradient of the luminosity-temperature relation is approximately 2, whereas the observational data favour a steeper $L \propto T^3$ power law. Exactly the same result was produced by NFW, but they showed that by including some pre-heating of the gas (along the lines suggested by Evrard & Henry 1991), the central density of the gas in low-mass clusters would be suppressed sufficiently to reduce the luminosities of these low-temperature clusters and hence recover a logarithmic slope of 3. The fact that the clusters simulated here also produce an incorrect $L_x - T_x$ relation could merely result from a lack of physical processes in the simulations.

6.3.7 The β parameters

Assuming that the cluster gas is isothermal and that the spherical collapse model estimate of the mean virial overdensity is reasonable, then the cluster gas temperature can be related to the virial mass through equation (2.2) or to the dark matter velocity dispersion with equation (6.13). In both cases the temperature referred to

Table 6.2: Table of mean β parameters for different redshifts. The first letter in the subscript refers to whether a Mass- or Luminosity-weighted temperature is relevant and the second letter represents a comparison with either the dark matter velocity dispersion or the virial mass.

Redshift	$\bar{\beta}_{M\sigma}$	$\bar{\beta}_{L\sigma}$	$\bar{\beta}_{MM}$	$\bar{\beta}_{LM}$
0	1.18 ± 0.03	0.90 ± 0.04	1.27 ± 0.06	0.98 ± 0.07
0.55	1.17 ± 0.03	0.99 ± 0.04	1.30 ± 0.03	1.10 ± 0.04
1.09	1.11 ± 0.03	0.97 ± 0.03	1.27 ± 0.04	1.12 ± 0.07

can be either mass- or luminosity-weighted giving rise to four different β parameters. Fig. 6.14 shows the values of all of these quantities as a function of mass for all ten clusters at three different redshifts. Squares depict redshift zero clusters and crosses and stars represent $z = 0.55$ and 1.09.

In general there appears to be no strong redshift dependence, although β_{LM} does show a $\sim 10\%$ increase between $z = 0$ and $z = 1.09$. At the two higher redshifts, where there is a larger range in cluster masses a slight increase of the β values with increasing mass is seen, but more clusters would be required to make this statistically significant. A list of mean βs with the scatter about these values is given in Table 6.2 for each of these redshifts.

The mean $\beta_{M\sigma}$ is 1.18 ± 0.03. A value of 1 would be expected if the specific energies in the cluster gas and dark matter were the same and the gas had zero kinetic energy. For individual clusters, the ratio of the cluster gas kinetic energy to its internal energy is usually in the range $5 - 20\%$, with a few significantly larger results coming from recent merger events.

β_{MM}, which is the parameter relevant for converting a mass-weighted temperature, of the sort measured by the Sunyaev-Zel'dovich effect, to a virial mass, has a mean value of 1.27 ± 0.06 averaged over all clusters at $z = 0$. If a luminosity-weighted temperature is measured, from X-ray data, then to convert to a virial mass the β_{LM} parameter with average value 0.98 ± 0.07 should be used. This is the parameter relevant to the normalisation of the temperature function performed in Chapter 2, so this result suggests that the choice of $\beta = 1.00 \pm 0.10$, was appropriate.

6.4 Conclusions

It has been demonstrated in this Chapter that the method for coarse-sampling the large scale mass distribution and concentrating the particles into a high-resolution region where the cluster of interest is forming can be used, in conjunction with the *GRAPE*, to produce high-resolution cluster simulations. This has provided over at

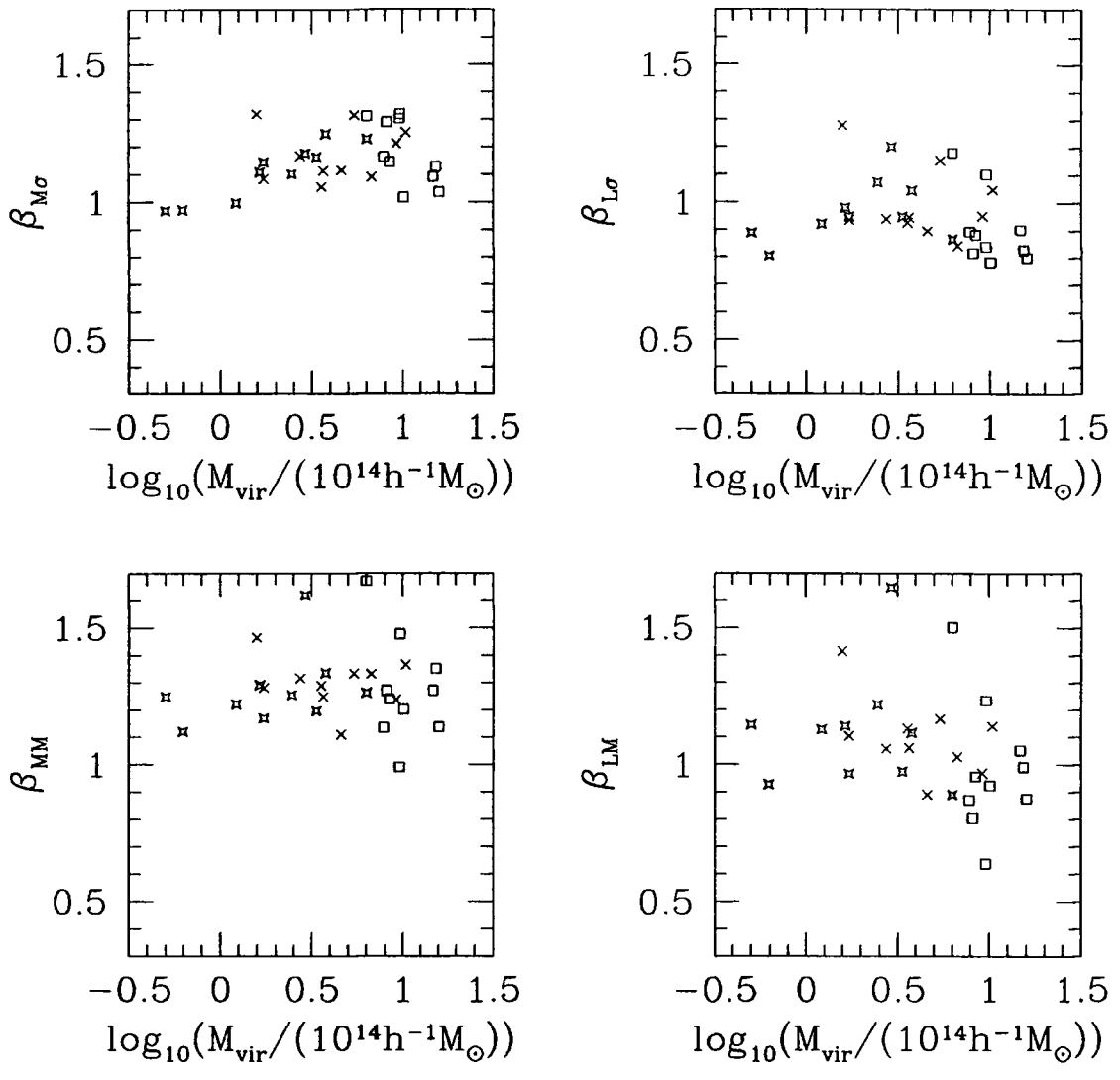

Figure 6.14: Mass and redshift dependence of the four different β parameters (see main text for details), relating mass- and luminosity-weighted gas temperatures to the virial mass or dark matter velocity dispersion. As in the previous figure, squares, crosses and stars correspond to $z = 0$, 0.55 and 1.09 respectively.

least a factor of 20 increase in the number of particles in the cluster compared with the original AP^{3}M run, allowing the final cluster structure to be resolved significantly better.

The mean virial overdensity predicted by the spherical collapse model provides a good description of the transition between the material falling into the cluster and the region with zero net radial velocity. There is, however, a significant variation from cluster to cluster.

The spherically-averaged dark matter density profiles are all reasonably well described by an NFW-type expression with the density proportional to r^{-1} in the centre and r^{-3} at large radii. Whilst the gradient of the gas density profile is similar at large radii, it flattens more rapidly than the dark matter within the central regions of the cluster. This leads to an underdensity of gas by a factor of about three in the central few tens of h^{-1}kpc compared with the assumption that gas traces mass.

The baryonic mass fraction is measured to be lower than the global value within each of the clusters. At the virial radius, it is typically 0.09 compared with the chosen $f_b = 0.1$. By $3r_{vir}$, which is approximately the turnaround radius, the baryon fraction converges to the background value.

The average dark matter velocity dispersion profile has a peak at about one tenth of the virial radius and it decreases by approximately 40% into the centre of the cluster and a factor of 2 out to the virial radius. By contrast, the average gas temperature profile stays reasonably constant all the way to the centre of the cluster. This higher temperature for the gas is required in order to maintain sufficient pressure support given that the gas density flattens more than an NFW model in the central regions. Estimating the total cluster mass assuming that the gas is in hydrostatic equilibrium leads to a value typically 10% too small. This discrepancy is produced because the kinetic pressure support provided by the gas is not taken into account.

The evolution of the bulk properties and the correlations between them shows that, on average, the virial mass triples from $z = 1$ to $z = 0$, but the dark matter velocity dispersion, gas temperature and luminosity evolve by significantly less than this. Assuming that the cluster is isothermal out to the virial radius (given by the spherical collapse model), in the vast majority of cases the cluster mass can be inferred to within $\sim 25\%$ from the gas temperature. The evolution of this correlation to a redshift of one is also well described by equation (2.2). Cluster luminosities are found to evolve less than would be predicted by the simple scaling laws. However these are not applicable because of the non-self-similar evolution in the $\Omega_0 = 0.3$, $\Lambda_0 = 0.7$ model. Of greater interest is the fact that slightly more evolution is seen in the mass-luminosity relation than was found by NFW for some clusters formed in $\Omega_0 = 1$ simulations. This is a demonstration of the superior spatial resolution of these simulations run on the *GRAPE*. The luminosity-temperature relation is $L \propto T^2$, shallower than that constructed from observational data, suggesting that important physics is missing from the simulations.

Four different β parameters, relating gas temperature to the dark matter halo properties, have been measured from the simulations. These quantities do not evolve significantly over the redshift range considered here. At the present epoch the average $\beta_{M\sigma}$, $\beta_{L\sigma}$, β_{MM} and β_{LM} values all lie between 0.90 and 1.27. β_{LM} which is relevant for the normalisation of the power spectrum attempted in Chapter 2 has an average of 0.98 ± 0.07 and the scatter in the individual cluster values is just $\sqrt{9}$ times this uncertainty. However, the individual clusters have β values which are not really distributed in a Gaussian fashion about the mean value. A few extreme values resulting from recent merger events give rise to significant tails in the distributions.

An increase in resolution in the code by a factor of a few could be made by optimising the shape of the high-resolution region filled with low-mass particles. However, for the type of simulations detailed here, a more useful route for progress in the understanding of galaxy clusters via numerical simulations is to include additional physics into the experiments. Primary among these processes should be radiative cooling of gas, star formation and energy feedback from supernovae.

6.5 References

Albrecht A., Steinhardt P. J., 1982, Phys Rev Lett, 48, 1220
Anninos P., Norman M. L., 1996, ApJ, 459, 12
Bertschinger E., 1985, ApJ, 58, 39
Bryan G. L., Cen R., Norman M. L., Ostriker J. P., Stone J. M., 1994, ApJ, 428, 405
Buote D. A., Canizares C. R., 1996, ApJ, 457, 565
Cen R., Ostriker J. P., 1994, ApJ, 429, 4
Chaboyer B., 1995, ApJ, 444, L9
Cole S., Lacey C., 1996, MNRAS, 281, 716
Copi C. J., Schramm D. N., Turner M. S., 1995, Science, 267, 192
Couchman H. M. P., Thomas P. A., Pearce F. R., 1995, ApJ, 452, 797
Crone M. M., Evrard A. E., Richstone D. O., 1994, ApJ, 434, 402
Elbaz D., Arnaud M., Böhringer H., 1995, A&A, 293, 337
Evrard A. E., 1990, ApJ, 363, 349
Evrard A. E., Henry J. P., 1991, ApJ, 383, 95
Evrard A. E., Metzler C. A., Navarro J. F., 1996, ApJ, submitted
Fabian A. C., Canizares C. R., Nulsen P. E. J., 1984, Nat, 310, 733
Gunn K. F., Thomas P. A., 1996, MNRAS, 281, 1133
Guth A., 1981, Phys Rev D, 23, 347
Kaiser N., 1986, MNRAS, 222, 323
Kang H., Cen R., Ostriker J. P., Ryu D., 1994, ApJ, 428, 1
Katz N., White S. D. M., 1993, ApJ, 412, 455
Kolb E. W., Turner M. S., 1990, The Early Universe, Addison Wesley
Lacey C., Cole S., 1994, 271, 676
Linde A. D., 1982, Phys Lett, 108B, 389
Loewenstein M., Mushotzky R. F., 1996, ApJ, 466, 695

Markevitch M., Mushotzky R. , Inoue H., Yamashita K., Furuzawa A., Tawara Y., 1996, ApJ, 456, 437
Metzler C. M., Evrard A. E., 1994, ApJ, 437, 564
Navarro J. F., White S. D. M., 1993, MNRAS, 265, 271
Navarro J. F., Frenk C. S., White S. D. M., 1995, MNRAS, 275, 720 (NFW)
Navarro J. F., Frenk C. S., White S. D. M., 1996, ApJ, 462, 563 (NFW2)
Peacock J. A., Dodds S. J., 1994, MNRAS, 267, 1020
Pearce F., Thomas P. A., Couchman H. M. P., 1994, MNRAS, 268, 953
Steinmetz M., White S. D. M., 1996, MNRAS, submitted (astro-ph 9609021)
Tanvir N. R., Shanks T., Ferguson H. C., Robinson D. R. T., 1995, Nat, 377, 27
Thomas P. A., Couchman H. M. P., 1992, MNRAS, 257, 11
Walker T. P., Steigman G., Schramm D. M., Olive K. A., Kang H.-S., 1991, ApJ, 376, 51
White S. D. M., Efstathiou G., Frenk C. S., 1993, MNRAS, 262, 1023
White S. D. M., Navarro J. F., Evrard A. E., Frenk C. S., 1993, Nat, 366, 429

Chapter 7

Conclusions

In this thesis, some of the different ways in which clusters of galaxies can be used to measure fundamental cosmological quantities have been considered.

Chapter 2 extensively used the formalism introduced by Press & Schechter (1974) and developed by Bond et al. (1991) and Lacey & Cole (1993). It was shown that the Press-Schechter expression provides a good fit to the mass function of dark matter haloes found in large numerical simulations of cosmologies with $\Omega_0 = 1$, $\Omega_0 = 0.3$ $\Lambda_0 = 0$ and $\Omega_0 = 0.3$ $\Lambda_0 = 0.7$. This conclusion holds for haloes satisfying $10^{14} \lesssim M_{\rm vir}/h^{-1}{\rm M}_\odot \lesssim 1.5 \times 10^{15}$ at $z = 0$. The formula was applied to the problem of normalising the power spectrum of mass fluctuations using the redshift-zero cluster temperature function. The main uncertainty in this procedure is the conversion between a measured cluster temperature and the virial mass inferred from this. Using the mean β parameter from the simulations of Navarro, Frenk & White (1995) with a 1σ Gaussian dispersion of 0.1 about the mean value of 1.0, the rms fluctuations in the mass in spheres of radius $8\,h^{-1}$Mpc (σ_8) was found to be $\sigma_8 = (0.52 \pm 0.04)\Omega_0^{-0.46+0.10\Omega_0}$ for the case with no vacuum energy density, and $\sigma_8 = (0.52 \pm 0.04)\Omega_0^{-0.52+0.13\Omega_0}$ when $\Lambda = 1 - \Omega$. These results are in reasonable agreement with the *COBE* 4-year data extrapolated to a scale of $8\,h^{-1}$Mpc assuming that $\Gamma = \Omega_0 h \approx 0.2$.

In the remainder of the chapter detailed predictions for the redshift distributions of clusters were presented. The cluster size was quantified using the virial mass, luminosity-weighted temperature or Sunyaev-Zel'dovich decrement. This illustrated the strong dependence on cosmology of the evolution of the cluster population, with high-redshift clusters in the high-density model being significantly rarer than those in the low-density cases. X-ray data from the *ASCA* satellite will soon yield a measurement of the cluster temperature function at $z \approx 0.3$, and this will be of considerable interest.

The presently available data on clusters at high-redshifts are not readily compared with the predictions of Chapter 2. However, in Chapter 3 different techniques were employed to study the *EMSS* catalogue of X-ray luminous clusters and the

pointed observations of individual high-redshift objects observed either with *ASCA* or through their weak gravitational lensing of faint background galaxies.

Using the Press-Schechter formula and assuming that the cluster luminosity-temperature relation does not evolve and can thus be adequately described by that inferred from $z = 0$ data, the number of $0.4 < z < 0.6$ clusters expected in the *EMSS* was predicted for $\Omega_0 = 1$, $\Omega_0 = 0.3$ $\Lambda_0 = 0$ and $\Omega_0 = 0.3$ $\Lambda_0 = 0.7$ models. It was found that the low-density cosmologies, in particular, overpredict the number of high-redshift clusters by factors of ~ 8 and 10 for the $\Lambda_0 = 0.7$ and $\Lambda_0 = 0$ cases respectively. These results are very sensitive to the normalisation, σ_8, and the amplitude of the scatter about the $L_x - T_x$ mean relation. Nevertheless, allowing σ_8 to vary according to the Gaussian error estimated in Chapter 2 and altering, within apparently reasonable bounds, the uncertainty with which a luminosity can be inferred from a temperature, the predicted number of clusters for the $\Omega_0 = 0.3$, $\Lambda_0 = 0$ model remains difficult to reconcile with the mere 7 high-redshift *EMSS* identifications. The statistical rejection of this model was found to be at a level of approximately 95%.

Some methods were presented to quantify the probability of finding particular rare objects at high-redshifts. These were again based on the formalism of Press & Schechter, and they employed order statistics as well as marginalisation techniques in order to take into account the uncertainties on both σ_8 and measured (or inferred) cluster masses. With the presently available data, insufficient large clusters at high redshifts have been detected to be able to exclude the $\Omega_0 = 1$ model to any interesting extent. With the addition of future observations, the methods described here will become increasingly powerful.

Chapter 4 investigated the topic of the spatial distribution of clusters found in large dark matter simulations. Previous studies by Bahcall & Cen (1992) and Croft & Efstathiou (1994) had reached different conclusions concerning the strength of the correlation of rich galaxy clusters. Here, it was shown that a significantly large variation in the measured correlation length could be produced by changing the way in which clusters are defined. The groupfinder used to detect overdensities and the statistic with which the clusters were then ranked in order to create a volume limited catalogue with a particular mean intercluster separation both contribute significantly to the uncertainty in the correlation length for the cluster population. In addition, the number density of the clusters, whether or not their redshift-space separations are used to calculate the correlation function and the assumed value of σ_8 also produce systematic differences. The magnitude of these uncertainties suggests that the discrepancy between the studies of Bahcall & Cen (1992) and Croft & Efstathiou (1994) is not particularly surprising. Comparing the $\Omega_0 = 1$ model predictions with observational results from both the *APM* survey (Dalton et al. 1994) and *ROSAT* measurements (Romer et al. 1994), it was found that a satisfactory agreement exists on scales less than $\approx 20\,h^{-1}$Mpc. Above this, where the observed signal is small, the model produces less correlation than is seen in the data, even when the best case model is used.

Chapter 5 contained a description of some of the main numerical simulation techniques, before going on to show how the *GRAPE* supercomputer may be used for cosmological simulations. The multi-mass technique for improving the mass and spatial resolution of simulations was then detailed and sensible values for the parameters used in the particular implementation adopted here were found using a few simple tests.

In Chapter 6, the numerical procedure outlined in Chapter 5 was employed to study the formation and adiabatic evolution of 10 different clusters in a universe with $\Omega_0 = 0.3$ and $\Lambda_0 = 0.7$. The spherical collapse model was shown to provide a good estimate of the overdensity within which the material had no net radial infall, although there is quite a large variation in the infall patterns of the individual clusters so this only gives a statistical description. The density profiles of the dark matter haloes were well fitted by the formula proposed by Navarro et al. (1995), with the gas having a slightly more extended central distribution. Radial temperature profiles for the gas showed an isothermal region extending out to $\sim 10-20\%$ of the virial radius, before falling by a factor of 2 out to $r_{\rm vir}$. The majority of the calculated cluster X-ray luminosity originates from within $0.1r_{\rm vir}$. This illustrates the requirement for sufficient spatial resolution in order to measure this quantity from simulations. The β parameter relating the luminosity-weighted gas temperature to the virial mass of the cluster was found to have an average value of 0.98 ± 0.07, confirming the assumption made in Chapter 2 when estimating the power spectrum normalisation σ_8. Correlations between the virial mass, dark matter velocity dispersion and gas temperature of the clusters were found to follow the expectations for an isothermal sphere with its boundary defined by the spherical collapse model. The evolution of these correlations is also reasonably well obeyed by the simulations. For the mass-luminosity relation, slightly more evolution was found than Navarro et al. (1995) saw in their $\Omega_0 = 1$ simulations despite the fact that this low-density cosmology would be expected to produce less evolution at low redshifts. This is in line with the suggestion by Navarro et al. that the luminosity is underestimated at $z \approx 1$ in their simulations as a result of poor numerical resolution.

Future work to include additional gas physics into simulations of large-scale structure formation will play an important part in reducing the uncertainties associated with some of the conclusions drawn from the experiments reported in this thesis. Recent advances in observational techniques should also yield data in the next few years that will allow some of the tests descibed here to provide compelling rather than merely suggestive results.

7.1 References

Bahcall N. A., Cen R., 1992, ApJ, 398, L81
Bond J. R., Cole S., Efstathiou G., Kaiser N., 1991, ApJ, 379, 440
Croft R. A. C., Efstathiou G., 1994, MNRAS, 267, 390
Dalton G. B., Croft R. A. C., Efstathiou G., Sutherland W. J., Maddox S. J., Davis

M., 1994, MNRAS, 271, L47
Lacey C., Cole S., 1993, MNRAS, 262, 627
Navarro J. F., Frenk C. S., White S. D. M., 1995, MNRAS, 275, 720
Press W. H., Schechter P., 1974, ApJ, 187, 425
Romer A. K., Collins C. A., Cruddace R. G., MacGillivray H., Ebeling H., Böhringer H., 1994, Nature, 372, 75

Appendix A

The linear theory overdensity for a collapsed spherical perturbation in flat, $\Omega_0 < 1$ models

The redshift of collapse, $z_{\rm coll}$, is calculated for a spherical 'top-hat' overdensity in an $\Omega_0 + \Lambda_0 = 1$, $\Omega_0 < 1$ universe.

It can be shown (see Peebles P. J. E., 1984, ApJ, 284, 439) that the variation of the radius of a spherical overdensity r with scale factor a is described by:

$$\left(\frac{\mathrm{d}r}{\mathrm{d}a}\right)^2 = \frac{r^{-1} + \omega r^2 - \kappa}{a^{-1} + \omega a^2}, \tag{A.1}$$

where $a = (1+z)^{-1}$, $\omega = (\Omega_0^{-1} - 1) > 0$ and κ is a constant which, for overdensities, takes positive values. At fixed ω, a larger κ will produce a perturbation that collapses earlier than one with a smaller κ.

The following argument is split into two main parts. Firstly, equation (A.1) is solved to give the condition for an overdensity to collapse to a point and the expansion factor corresponding to this event is also found. Then the constant κ is related to some quantities more commonly used to define the amplitude of a mass fluctuation.

A.0.1 Does the fluctuation collapse, and if so then at what redshift?

The turnaround time is defined as the instant when the edge of the overdense sphere stops expanding, that is $\left(\frac{\mathrm{d}r}{\mathrm{d}a}\right) = 0$. From equation (A.1) this occurs when the radius of the overdensity satisfies

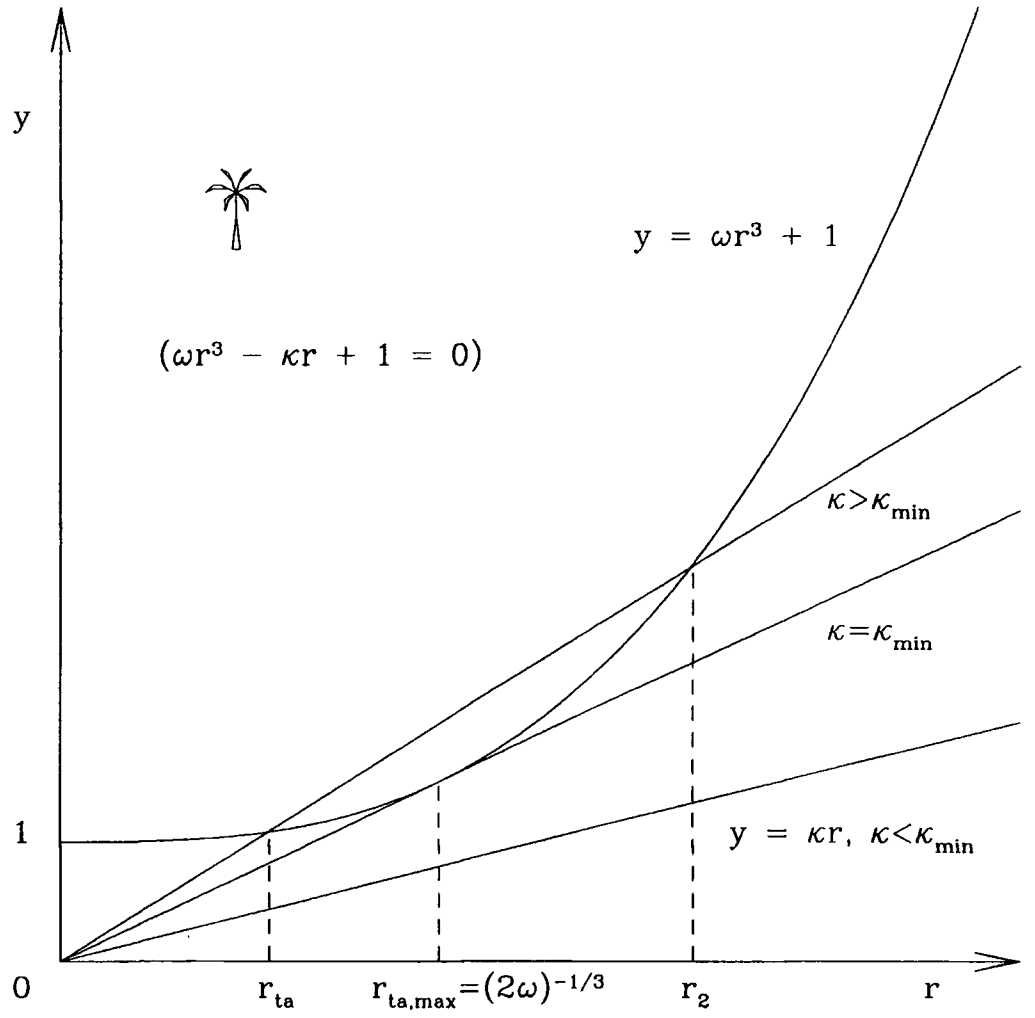

Figure A.1: The variation of the turnaround radius with κ for a particular value of ω.

$$\omega r^3 - \kappa r + 1 = 0. \tag{A.2}$$

The nature of the three solutions to this equation will depend upon the values of ω and κ. Consider the effect of varying κ at a fixed ω. Fig. A.1 shows the curves

$$y(r) = \omega r^3 + 1 \tag{A.3}$$

and

$$y(r) = \kappa r, \tag{A.4}$$

the intersections of which give the roots of equation (A.2). For κ less than a particular value, $\kappa_{\rm min}$, there are no real positive solutions. At $\kappa = \kappa_{\rm min}$ there are two degenerate positive roots in addition to the negative root, and for larger values of κ two distinct positive solutions exist ($r_{\rm ta}$ and r_2), the lower one of which, $r_{\rm ta}$, will correspond to the turnaround radius. To calculate $\kappa_{\rm min}$ in terms of ω, consider

equation (A.2) for the case $\kappa = \kappa_{\min}$, and rewrite the left-hand side in terms of the positive and negative roots $r_{\mathrm{ta,max}}$ and r_3 respectively. This gives

$$\omega r^3 - \kappa_{\min} r + 1 = \omega(r - r_{\mathrm{ta,max}})^2(r - r_3). \tag{A.5}$$

At $r = r_{\mathrm{ta,max}}$, both the left-hand side of equation (A.5) and its derivative with respect to r equal zero. Thus two simultaneous equations are produced, which can be solved to give

$$\kappa_{\min} = \frac{3\omega^{\frac{1}{3}}}{2^{\frac{2}{3}}} \tag{A.6}$$

and

$$r_{\mathrm{ta,max}} = (2\omega)^{-\frac{1}{3}}. \tag{A.7}$$

In order to calculate the scale factor at the turnaround time, a_{ta}, it is necessary to find the roots of a cubic equation. The details of this procedure are in Appendix B. Quoting the results obtained by solving equation (A.2), it is found that for $\kappa > \kappa_{min}$ the root corresponding to the perturbation radius at turnaround is given by

$$r_{\mathrm{ta}} = -2s^{\frac{1}{3}} \cos\left(\frac{\theta}{3} - \frac{2\pi}{3}\right) \tag{A.8}$$

where

$$s = \left(\frac{3}{2}\right)^3 \left(\frac{\kappa}{\kappa_{\min}^3}\right)^{\frac{3}{2}} \tag{A.9}$$

and θ satisfies

$$\cos\theta = \left(\frac{\kappa_{\min}}{\kappa}\right)^{\frac{3}{2}} \qquad 0 < \theta < \frac{\pi}{2}. \tag{A.10}$$

Thus the turnaround radius is known as a function of ω and κ.

To proceed one needs to separate the variables in equation (A.1) and integrate, giving

$$\int_0^{r_{\mathrm{ta}}} \frac{r^{\frac{1}{2}}}{(\omega r^3 - \kappa r + 1)^{\frac{1}{2}}} \mathrm{d}r = \int_0^{a_{\mathrm{ta}}} \frac{a^{\frac{1}{2}}}{(\omega a^3 + 1)^{\frac{1}{2}}} \mathrm{d}a. \tag{A.11}$$

The positive root for $\left(\frac{\mathrm{d}r}{\mathrm{d}a}\right)$ has been taken because the sphere is expanding. For the period when the perturbation is collapsing the negative gradient is relevant. Thus defining

$$I(\omega, \kappa) = \int_0^{r_{\mathrm{ta}}} \frac{r^{\frac{1}{2}}}{(\omega r^3 - \kappa r + 1)^{\frac{1}{2}}} \mathrm{d}r \tag{A.12}$$

which must be evaluated numerically, the expansion factors at turnaround, a_{ta}, and at collapse, a_{coll}, satisfy the implicit equations

$$I(\omega, \kappa) = \int_0^{a_{\mathrm{ta}}} \frac{a^{\frac{1}{2}}}{(\omega a^3 + 1)^{\frac{1}{2}}} \mathrm{d}a \tag{A.13}$$

and

$$2\, I(\omega, \kappa) = \int_0^{a_{\mathrm{coll}}} \frac{a^{\frac{1}{2}}}{(\omega a^3 + 1)^{\frac{1}{2}}} \mathrm{d}a. \tag{A.14}$$

Using the substitution $u = \omega^{\frac{1}{2}} a^{\frac{3}{2}}$, these equations can be integrated analytically to give

$$a_{\rm ta} = \left[\frac{e^{3\sqrt{\omega}I(\omega,\kappa)} - 1}{2\sqrt{\omega}e^{\frac{3}{2}\sqrt{\omega}I(\omega,\kappa)}}\right]^{\frac{2}{3}} \tag{A.15}$$

and

$$a_{\rm coll} = \left[\frac{e^{6\sqrt{\omega}I(\omega,\kappa)} - 1}{2\sqrt{\omega}e^{3\sqrt{\omega}I(\omega,\kappa)}}\right]^{\frac{2}{3}}. \tag{A.16}$$

Therefore $a_{\rm coll}$, or equivalently $z_{\rm coll}$, the redshift of collapse of a spherical overdensity, is given as a function of ω and κ.

A.0.2 The relation between κ and the linear theory overdensity of a perturbation.

If the overdensity of a spherical perturbation is defined as

$$\delta = \frac{\Delta\rho}{\bar{\rho}} = \frac{\rho - \bar{\rho}}{\bar{\rho}} \tag{A.17}$$

where ρ and $\bar{\rho}$ are the density and mean density respectively, then this can be related to the radius of the region and the scale factor by

$$1 + \delta = \left(\frac{a}{r}\right)^3. \tag{A.18}$$

Expressing the radius of the perturbation as

$$r = a(1 - \epsilon) \tag{A.19}$$

it is found that

$$\delta = 3\epsilon + \mathrm{O}(\epsilon^2) \quad \text{as} \quad \epsilon \to 0. \tag{A.20}$$

Substituting for r and $\left(\frac{\mathrm{dr}}{\mathrm{da}}\right)$ in equation (A.1) using equation (A.19) and its derivative with respect to a and then letting a and $\epsilon \to 0$ gives the relationship between κ and ϵ

$$\epsilon = \frac{\kappa}{5}a + \mathrm{O(a^2)}. \tag{A.21}$$

Therefore, for $a \ll 1$,

$$\delta = \frac{3\kappa}{5}a + \mathrm{O(a^2)} \ll 1. \tag{A.22}$$

In the linear regime one can also express the overdensity by

$$\delta = \frac{\delta_0 D(a)}{D(a_0)} \tag{A.23}$$

where $D(a)$ represents the linear growth factor and the subscript zero denotes a quantity measured at redshift zero. For the $\Omega_0 + \Lambda_0 = 1, \Omega_0 < 1$ case

$$D(a) = \frac{A(x)}{A(x_0)} \tag{A.24}$$

with

$$x = ax_0 \tag{A.25}$$

$$x_0 = (2(\Omega_0^{-1} - 1))^{\frac{1}{3}} \tag{A.26}$$

and

$$A(x) = \frac{(x^3+2)^{\frac{1}{2}}}{x^{\frac{3}{2}}} \int_0^x \left(\frac{u}{u^3+2}\right)^{\frac{3}{2}} \mathrm{d}u. \tag{A.27}$$

(Peebles P. J. E., 1980, The Large Scale Structure of the Universe. Princeton Univ. Press, Princeton, NJ.) Looking again at the situation where $a \ll 1$ and hence $x \ll 1$, these formulae combine to give

$$\delta = \frac{\delta_0 x_0}{5A(x_0)} a + \mathrm{O(a^2)}. \tag{A.28}$$

Comparing this with equation (A.22) allows the following expression for κ as a function of Ω_0 and δ_0, the linear theory prediction for the overdensity of the sphere at a redshift of 0, to be calculated:

$$\kappa = \frac{x_0}{3A(x_0)} \delta_0. \tag{A.29}$$

Appendix B

Solution of a cubic equation

Consider the equation

$$x^3 + px + q = 0. \tag{B.1}$$

Let

$$\alpha = e^{\frac{2\pi i}{3}} \tag{B.2}$$

and note that

$$x^3 - 3GHx + (G^3 + H^3) = (x + G + H)(x + \alpha G + \alpha^2 H)(x + \alpha^2 G + \alpha H). \tag{B.3}$$

With p and q defined by $p = -3GH$ and $q = G^3 + H^3$, then G^3 and H^3 are the roots of the quadratic

$$t^2 - qt - \left(\frac{p}{3}\right)^3 = 0. \tag{B.4}$$

These solutions are given by

$$t = \frac{q \pm \sqrt{q^2 + \frac{4}{27}p^3}}{2}. \tag{B.5}$$

In order to produce three distinct real solutions to equation (B.1) (the case under consideration here) it is required that G and H have non-zero imaginary components, that is

$$q^2 + \frac{4p^3}{27} < 0. \tag{B.6}$$

(H is the complex conjugate of G.) Then, writing $t = se^{i\theta}$ with

$$s = \left(\frac{|p|}{3}\right)^{\frac{3}{2}} \tag{B.7}$$

and

$$\cos\theta = \frac{q}{2s}, \tag{B.8}$$

the three solutions are therefore given by

$$x = -G - H = -s^{\frac{1}{3}}(e^{\frac{i\theta}{3}} + e^{-\frac{i\theta}{3}}) = -2s^{\frac{1}{3}}\cos\left(\frac{\theta}{3}\right), \tag{B.9}$$

$$x = -\alpha G - \alpha^2 H = -2s^{\frac{1}{3}} \cos\left(\frac{\theta}{3} + \frac{2\pi}{3}\right) \tag{B.10}$$

and

$$x = -\alpha^2 G - \alpha H = -2s^{\frac{1}{3}} \cos\left(\frac{\theta}{3} - \frac{2\pi}{3}\right). \tag{B.11}$$

For equation (A.2), $p = -\frac{\kappa}{\omega}$ and $q = \frac{1}{\omega}$. Equation (B.6) is equivalent to the statement $\kappa > \kappa_{min}$ and it is the third of the above roots, with θ satisfying $0 < \theta < \frac{\pi}{2}$ that corresponds to the turnaround radius.

Appendix C

The Sunyaev-Zeldovich Y for clusters

Inverse Compton scattering of microwave background photons by hot electrons in an intracluster plasma will heat the photons and decrease the low-energy flux. The size of this decrease in flux can be used to probe the cluster properties. Y is the integral of the usual y-parameter over the entire cluster volume and is given by

$$Y = \frac{\sigma_{\mathrm{T}} k T_{\mathrm{e}}}{m_{\mathrm{e}} c^2} \frac{M f_{\mathrm{b}}}{m_{\mathrm{p}}} \frac{(1+X)}{2} \frac{1}{r_{\mathrm{d}}^2} \tag{C.1}$$

where

M is the halo mass,
σ_{T} is the Thomson scattering cross-section,
f_{b} is the baryon fraction ($= 0.1$),
X is the mass fraction in hydrogen, taken to be ($= 0.76$) and
r_{d} is the angular diameter distance.

Y can be considered as a solid angle of sky over which the microwave background is blocked out by the cluster.

Using the following relation between T_{e} and M

$$k T_{\mathrm{e}} = \frac{\mu m_{\mathrm{p}} G}{\beta} \left(\frac{\pi \rho_{\mathrm{c},0} \Delta_{\mathrm{c}}}{6} \right)^{\frac{1}{3}} \left(\frac{MH}{H_0} \right)^{\frac{2}{3}} \tag{C.2}$$

where

$\mu = 4/(5X + 3)$ is the mean particle mass,
$\beta = 1$ and

$\rho_{c,0}$ is the present day critical density, T_e can be eliminated to give

$$Y = \frac{\sigma_T f_b G}{2 m_e c^2 \beta}(1+X)\frac{4}{5X+3}\left(\frac{\pi \rho_{c,0}\Delta_c}{6}\right)^{\frac{1}{3}} M^{\frac{5}{3}}\left(\frac{H}{H_0}\right)^{\frac{2}{3}}\frac{1}{r_d^2} \tag{C.3}$$

which leads to

$$\frac{Y}{10^{40}} = 1.89 h^{-1}\Delta_c^{\frac{1}{3}}\left(\frac{M}{10^{15}h^{-1}M_\odot}\right)^{\frac{5}{3}}\left(\frac{H}{H_0}\right)^{\frac{2}{3}}\frac{1}{r_d^2}, \tag{C.4}$$

where the angular diameter distance r_d is measured in metres.

Now the angular diameter distance satisfies

$$r_d^2 = \frac{1}{4\pi}\frac{dV_{com}}{dz}(1+z)^{-2}\left(\frac{dr_{com}}{dz}\right)^{-1} \tag{C.5}$$

and

$$\frac{dr_{com}}{dz} = \frac{c}{H(z)} \tag{C.6}$$

where r_{com} and dV_{com}/dz represent the comoving radial distance and the differential comoving volume respectively, so

$$r_d^2 = 2.527.10^{40} h^{-2}\frac{H}{H_0}(1+z)^{-2}\frac{dV_{com}}{dz}\frac{1}{(h^{-1}\mathrm{Mpc})^3}\ \mathrm{m}^2. \tag{C.7}$$

Combining this with equation (C.4) produces the following expression for Y:

$$\begin{aligned} Y \;=\; & 497.8 h f_b\left(\frac{\Delta_c}{178}\right)^{\frac{1}{3}}\left(\frac{M}{10^{15}h^{-1}M_\odot}\right)^{\frac{5}{3}}\left(\frac{H}{H_0}\right)^{-\frac{1}{3}} \\ & \left(\frac{dV_{com}}{dz}\frac{1}{(100\,h^{-1}\mathrm{Mpc})^3}\right)^{-1}(1+z)^2\ \mathrm{arcmin}^2. \end{aligned} \tag{C.8}$$

Appendix D

Calculation of the lensing mass from a projected mean mass surface density

For a singular isothermal sphere, the mass density can be written as

$$\rho(r) = \frac{\rho_c \Delta_c}{3} \left(\frac{r}{r_{vir}}\right)^{-2} \tag{D.1}$$

where ρ_c is the critical density, Δ_c is the ratio of the mean halo density interior to the virial radius to the critical density and r_{vir} is the virial radius. The projected mass surface density interior to a radius r is given by

$$\Sigma(r) = 2\int_0^\infty \rho(\sqrt{r^2 + y^2}\ )\ \mathrm{d}y. \tag{D.2}$$

Using the fact that

$$\frac{\mathrm{d}}{\mathrm{d}y}\left(\frac{1}{r}\tan^{-1}\left(\frac{y}{r}\right)\right) = \frac{1}{r^2 + y^2}, \tag{D.3}$$

this integral yields

$$\Sigma(r) = \frac{\pi \rho_c \Delta_c r_{vir}^2}{3r}. \tag{D.4}$$

The mean projected mass surface density interior to a radius r is related to $\Sigma(r)$ through

$$\bar{\Sigma}(r) = \frac{\int_0^r 2\pi x \Sigma(x)\mathrm{d}x}{\pi r^2} = 2\Sigma(r), \tag{D.5}$$

and by definition, the virial mass of an isothermal halo is given by

$$M_{vir} = \frac{4\pi}{3}\rho_c \Delta_c r_{vir}^3. \tag{D.6}$$

Combining these two equations to eliminate the virial radius and expressing ρ_c in terms of Hubble's constant and the gravitational constant gives

$$M_{vir} = \frac{4}{H}\left(\frac{G r^3 \bar{\Sigma}(r)^3}{\Delta_c}\right)^{1/2}. \tag{D.7}$$

Appendix E

Individual profiles and evolution of the bulk properties for the $\Omega_0 = 0.3$, $\Lambda_0 = 0.7$ clusters

The first nine figures in this Appendix show the radial profiles for a variety of properties in clusters $2 - 10$ (see also Fig. 6.5). Where two lines are shown, the solid one refers to the dark matter and the dashed one represents the gas. The cluster virial mass and radius are given at the top of the figures. Infall velocity and overdensity are shown in the top two panels. The middle rows illustrate the cluster temperature (velocity dispersion in the case of the dark matter), and the radial dependence of the ratio between gas kinetic and internal energies. Cumulative luminosity and average particle entropy (in arbitrary units) profiles are shown in the bottom rows.

Figs. E.10-E.18 illustrate the evolution of a number of the bulk properties for clusters $2 - 10$ (see also Fig. 6.11). In the top-left panels the virial mass (dotted), mass within a density contrast of 200 (dashed) and mass within a comoving radius equal to the final cluster virial radius (solid) are illustrated. Mass- and luminosity-weighted temperatures are given by solid and dotted lines in the panels in the middle of the left-hand columns. The average entropy per gas particle (in the same units as Fig. 6.5) for the central 10% (dotted line) and outermost 10% (solid line) of the cluster gas is shown in the lowest panels in the left-hand columns. One-dimensional velocity dispersions for the dark matter only are given at the top right. Beneath these are the luminosities calculated using equation (6.7) and summing over all gas within the virial radii. The final panels contain information about the four different β parameters. $\beta_{M\sigma}$ (solid), $\beta_{L\sigma}$ (dotted), β_{MM} (short-dashed) and β_{LM} (long-dashed) are shown.

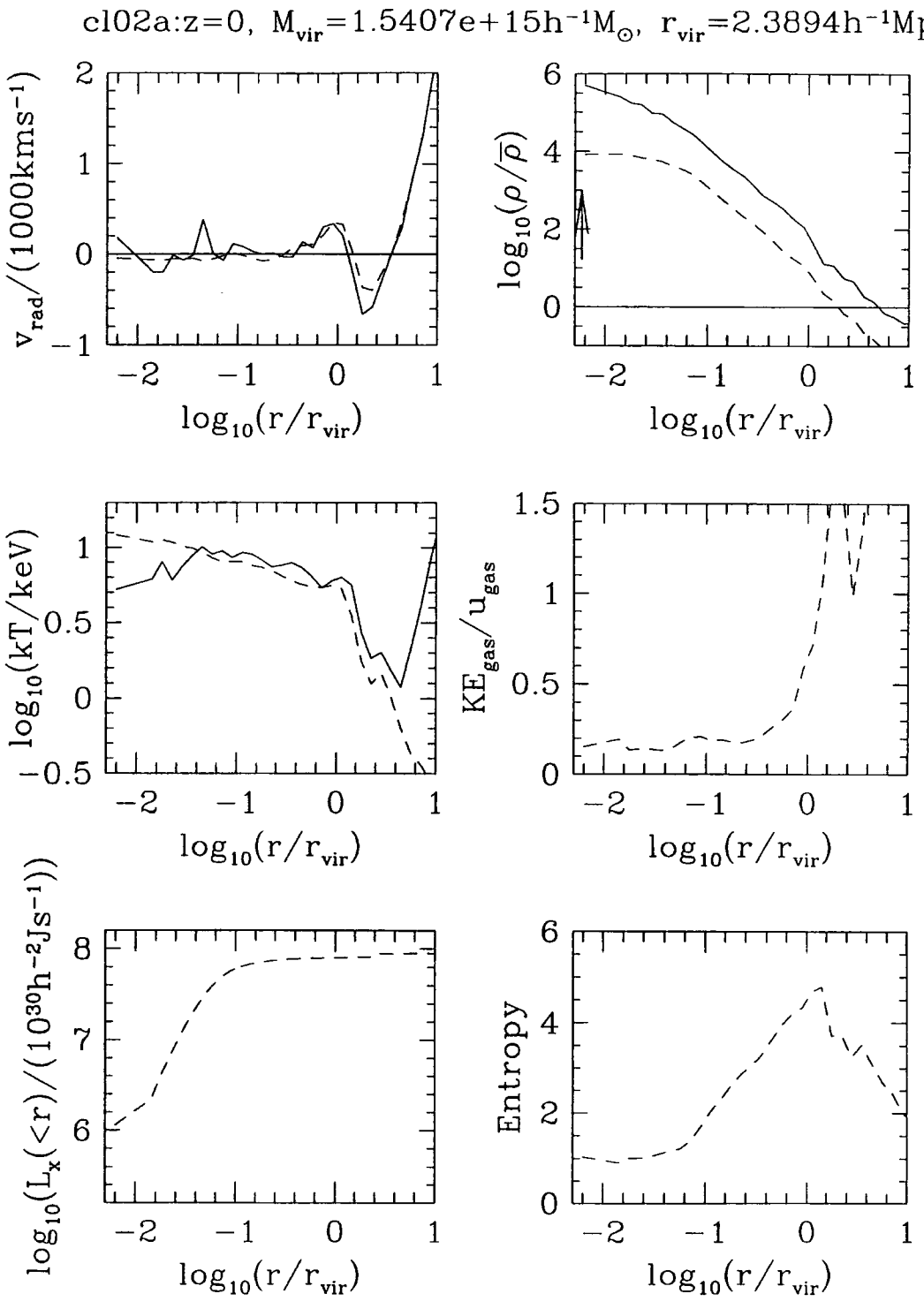
cl02a:z=0, M_{vir}=1.5407e+15$h^{-1}M_\odot$, r_{vir}=2.3894h^{-1}Mpc
$v_{rad}/(1000kms^{-1})$
$\log_{10}(\rho/\bar{\rho})$
$\log_{10}(kT/keV)$
KE_{gas}/u_{gas}
$\log_{10}(L_x(<r)/(10^{30}h^{-2}Js^{-1}))$
Entropy
$\log_{10}(r/r_{vir})$

Figure E.1:

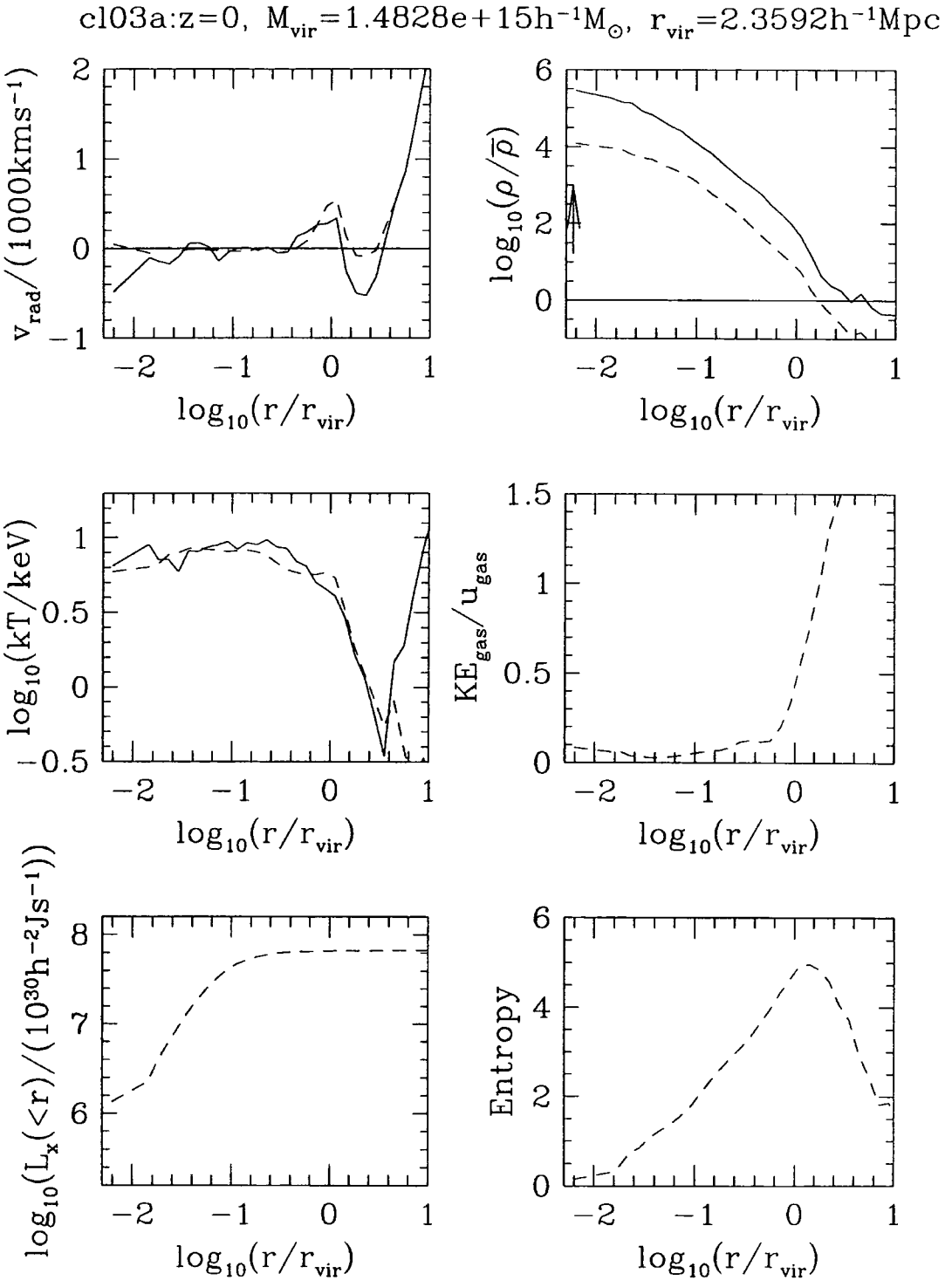
cl03a:z=0, M_{vir}=1.4828e+15$h^{-1}M_\odot$, r_{vir}=2.3592h^{-1}Mpc
$v_{rad}/(1000kms^{-1})$
$\log_{10}(\rho/\bar{\rho})$
$\log_{10}(kT/keV)$
KE_{gas}/u_{gas}
$\log_{10}(L_x(<r)/(10^{30}h^{-2}Js^{-1}))$
Entropy
$\log_{10}(r/r_{vir})$

Figure E.2:

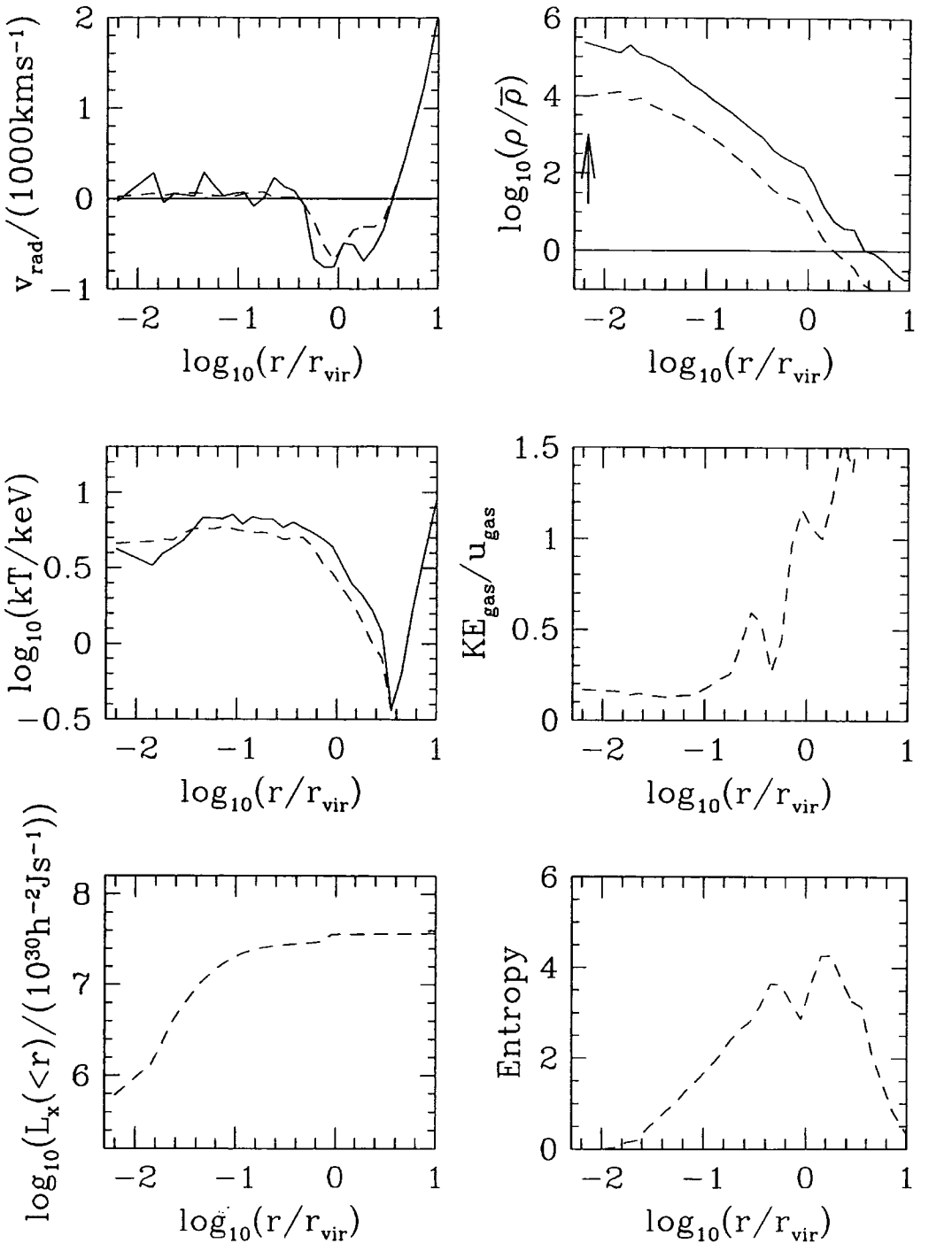
cl04a:z=0, M_{vir}=9.6468e+14$h^{-1}M_\odot$, r_{vir}=2.0442h^{-1}Mpc
$v_{rad}/(1000kms^{-1})$
$\log_{10}(\rho/\bar{\rho})$
$\log_{10}(kT/keV)$
KE_{gas}/u_{gas}
$\log_{10}(L_x(<r)/(10^{30}h^{-2}Js^{-1}))$
Entropy
$\log_{10}(r/r_{vir})$

Figure E.3:

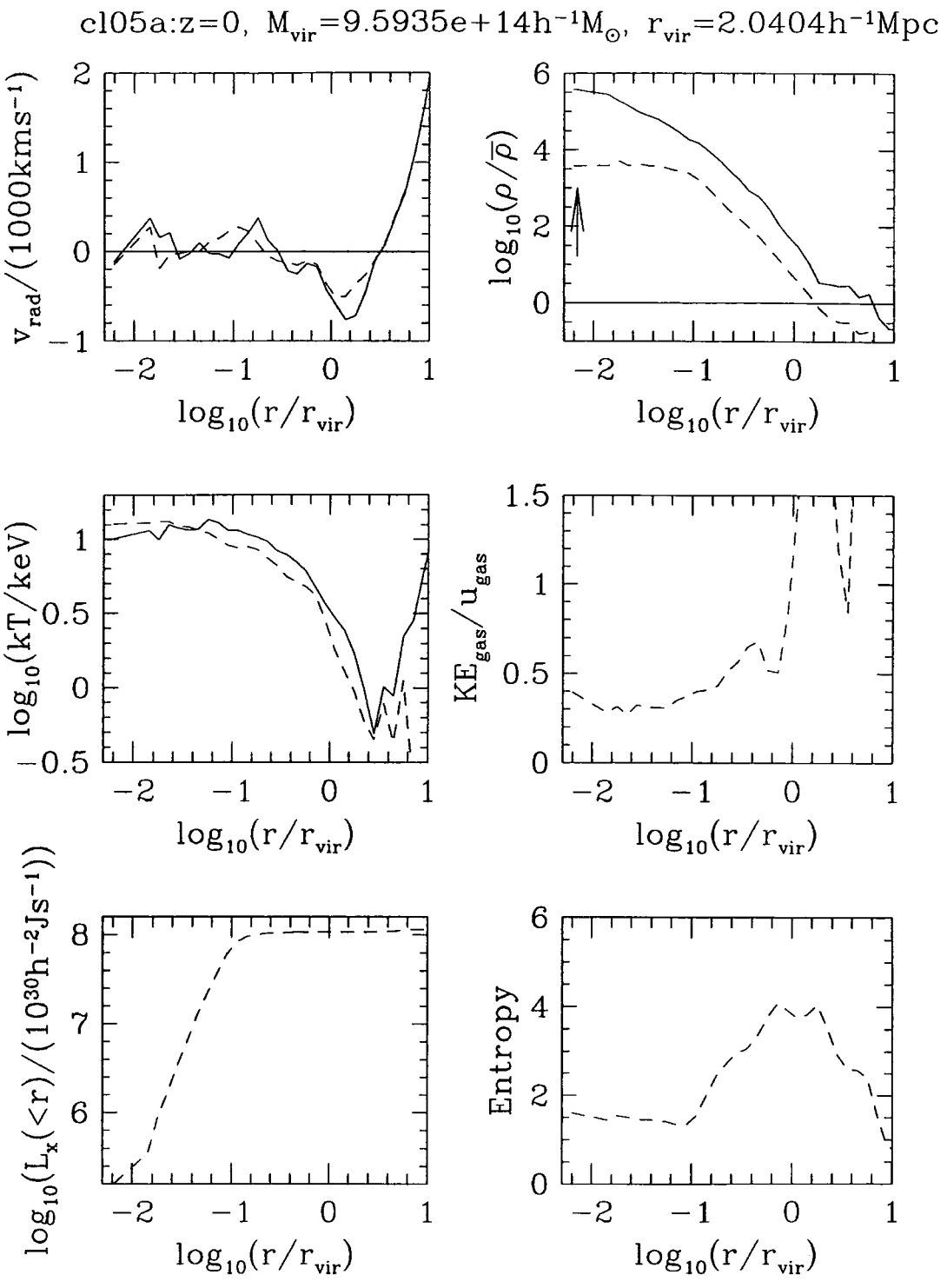
cl05a:z=0, M_{vir}=9.5935e+14$h^{-1}M_{\odot}$, r_{vir}=2.0404h^{-1}Mpc
$v_{rad}/(1000kms^{-1})$
$\log_{10}(\rho/\bar{\rho})$
$\log_{10}(kT/keV)$
KE_{gas}/u_{gas}
$\log_{10}(L_x(<r)/(10^{30}h^{-2}Js^{-1}))$
Entropy
$\log_{10}(r/r_{vir})$

Figure E.4:

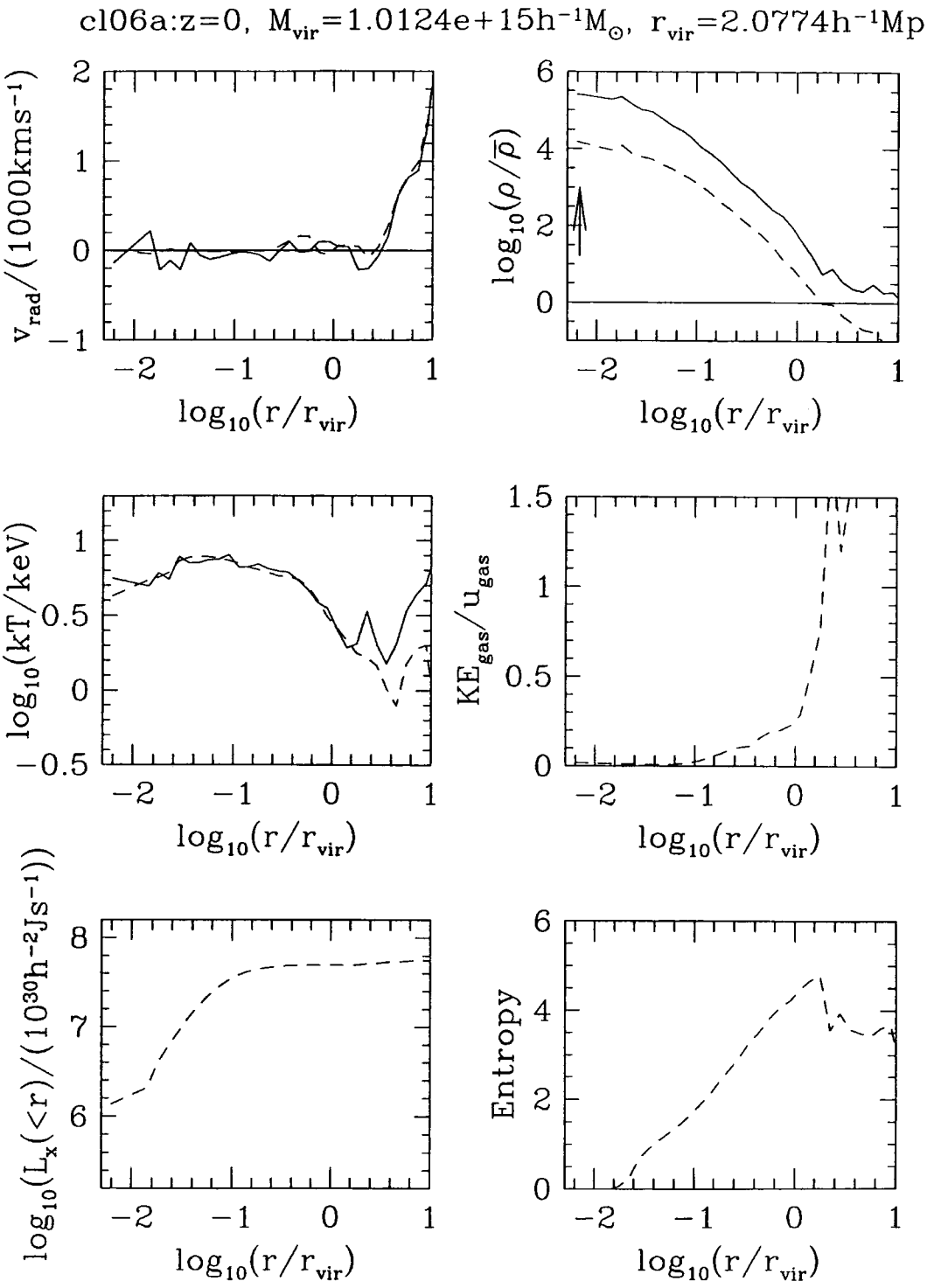
cl06a:z=0, M_{vir}=1.0124e+15h$^{-1}M_{\odot}$, r_{vir}=2.0774h^{-1}Mpc
$v_{rad}/(1000kms^{-1})$
$\log_{10}(\rho/\bar{\rho})$
$\log_{10}(kT/keV)$
KE_{gas}/u_{gas}
$\log_{10}(L_x(<r)/(10^{30}h^{-2}Js^{-1}))$
Entropy
$\log_{10}(r/r_{vir})$

Figure E.5:

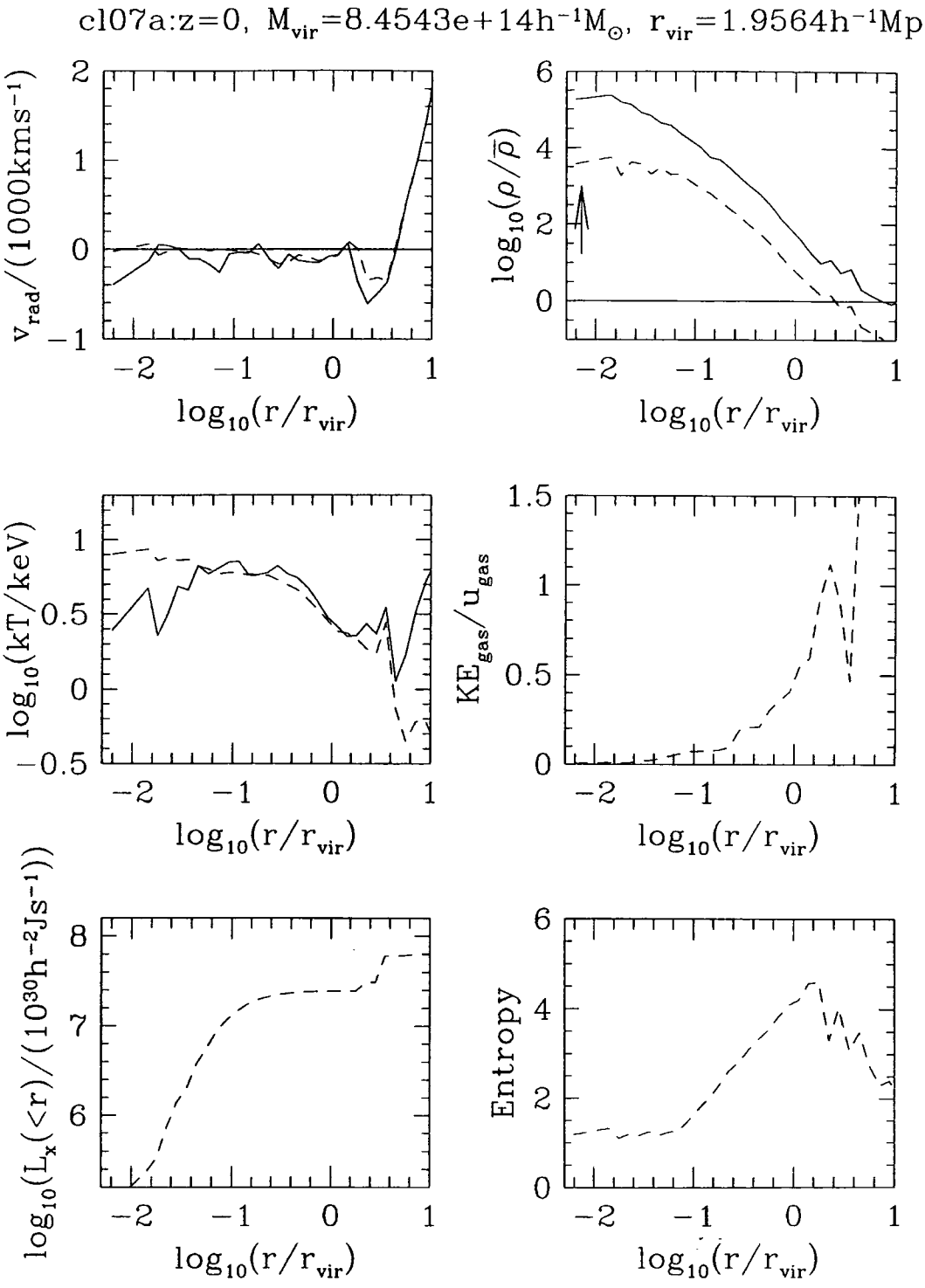
cl07a:z=0, M_{vir}=8.4543e+14$h^{-1}M_\odot$, r_{vir}=1.9564h^{-1}Mpc
$v_{rad}/(1000kms^{-1})$
$\log_{10}(\rho/\bar{\rho})$
$\log_{10}(kT/keV)$
KE_{gas}/u_{gas}
$\log_{10}(L_x(<r)/(10^{30}h^{-2}Js^{-1}))$
Entropy
$\log_{10}(r/r_{vir})$

Figure E.6:

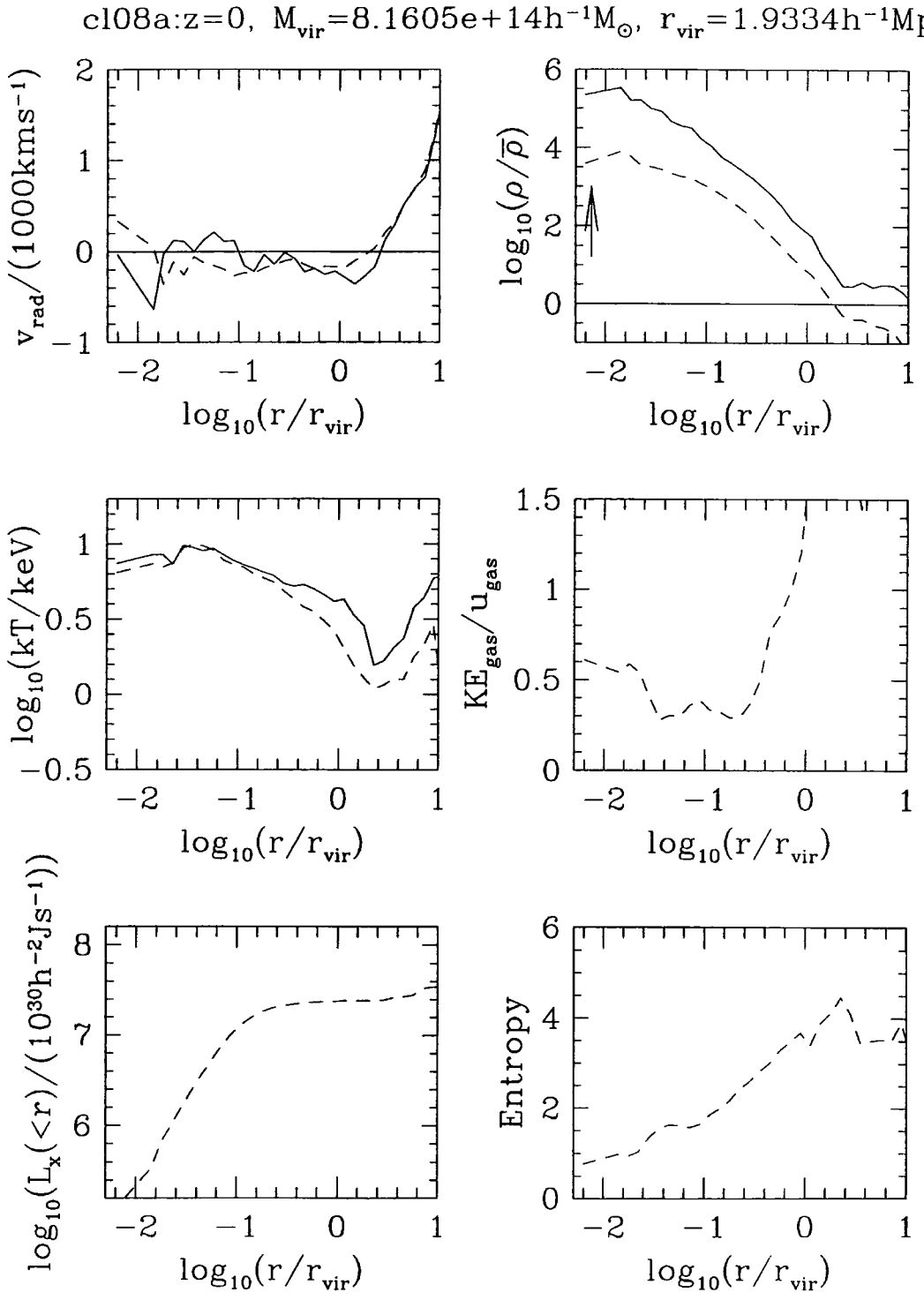
cl08a:z=0, M_{vir}=8.1605e+14$h^{-1}M_\odot$, r_{vir}=1.9334h^{-1}Mpc
$v_{rad}/(1000kms^{-1})$
$\log_{10}(\rho/\bar{\rho})$
$\log_{10}(kT/keV)$
KE_{gas}/u_{gas}
$\log_{10}(L_x(<r)/(10^{30}h^{-2}Js^{-1}))$
Entropy
$\log_{10}(r/r_{vir})$

Figure E.7:

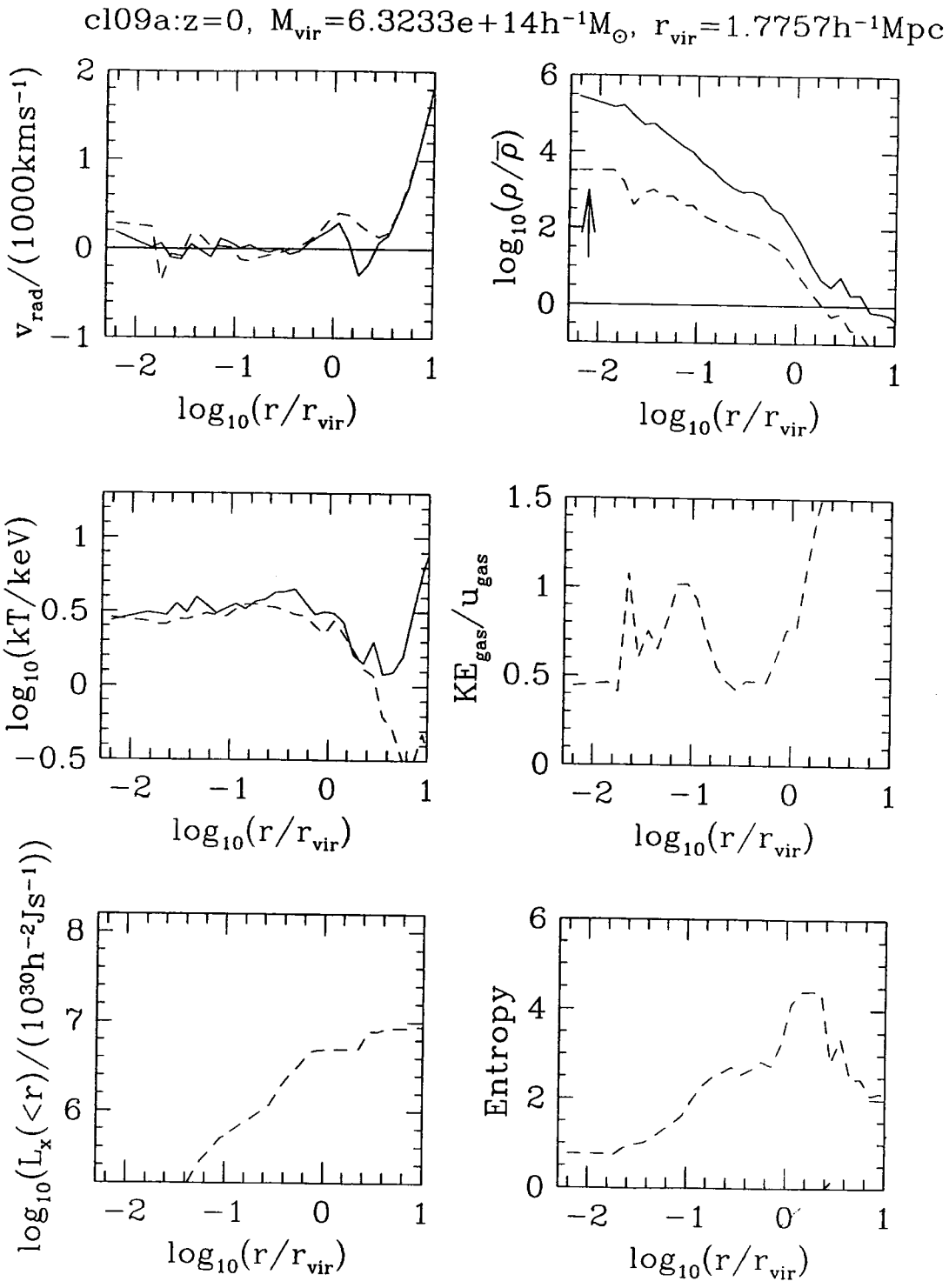
cl09a:z=0, M_{vir}=6.3233e+14$h^{-1}M_{\odot}$, r_{vir}=1.7757h^{-1}Mpc
$v_{rad}/(1000kms^{-1})$
$\log_{10}(\rho/\bar{\rho})$
$\log_{10}(kT/keV)$
KE_{gas}/u_{gas}
$\log_{10}(L_x(<r)/(10^{30}h^{-2}Js^{-1}))$
Entropy
$\log_{10}(r/r_{vir})$

Figure E.8:

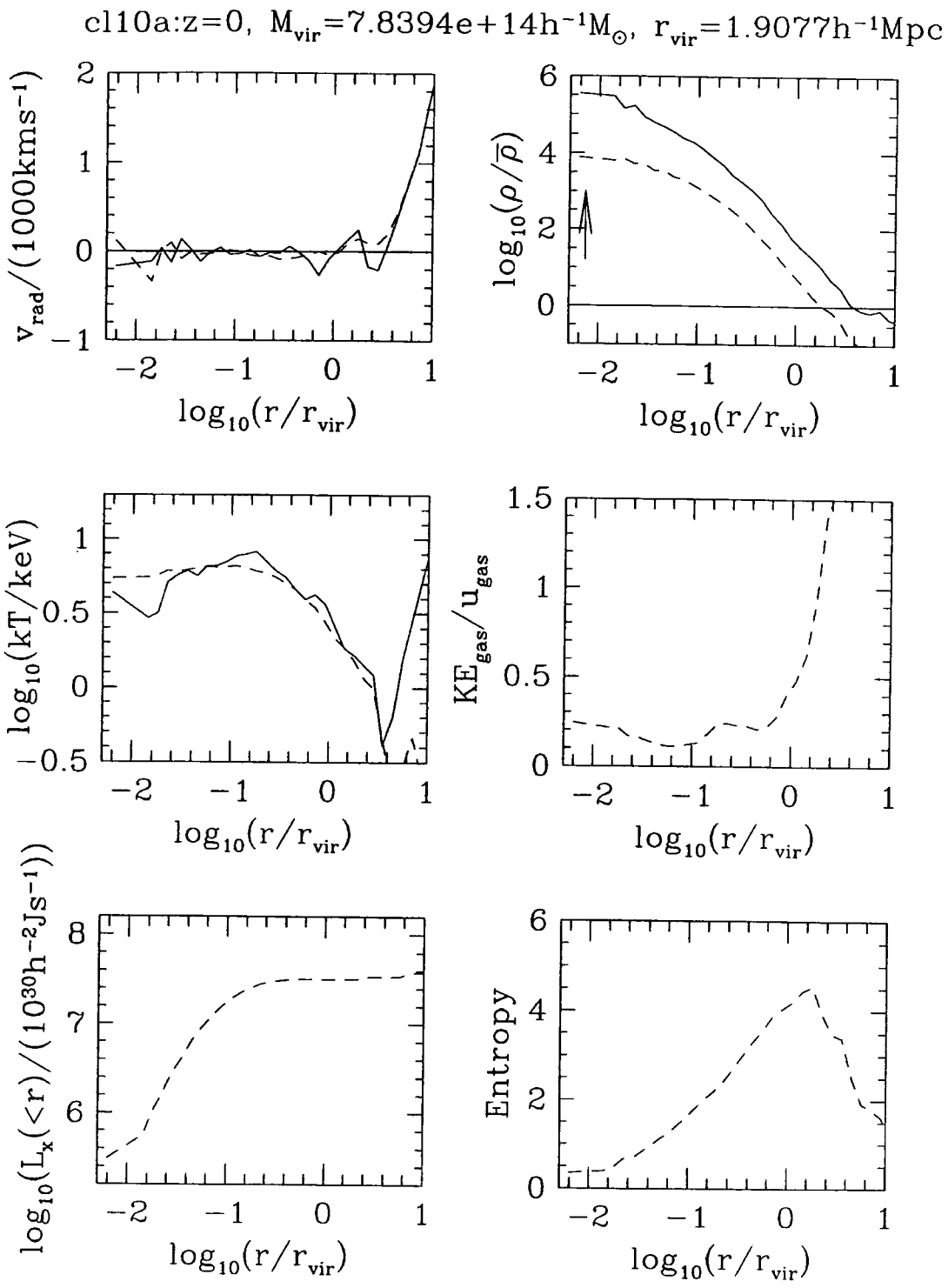
cl10a:z=0, M_{vir}=7.8394e+14$h^{-1}M_\odot$, r_{vir}=1.9077h^{-1}Mpc
$v_{rad}/(1000kms^{-1})$
$\log_{10}(\rho/\bar{\rho})$
$\log_{10}(kT/keV)$
KE_{gas}/u_{gas}
$\log_{10}(L_x(<r)/(10^{30}h^{-2}Js^{-1}))$
Entropy
$\log_{10}(r/r_{vir})$

Figure E.9:

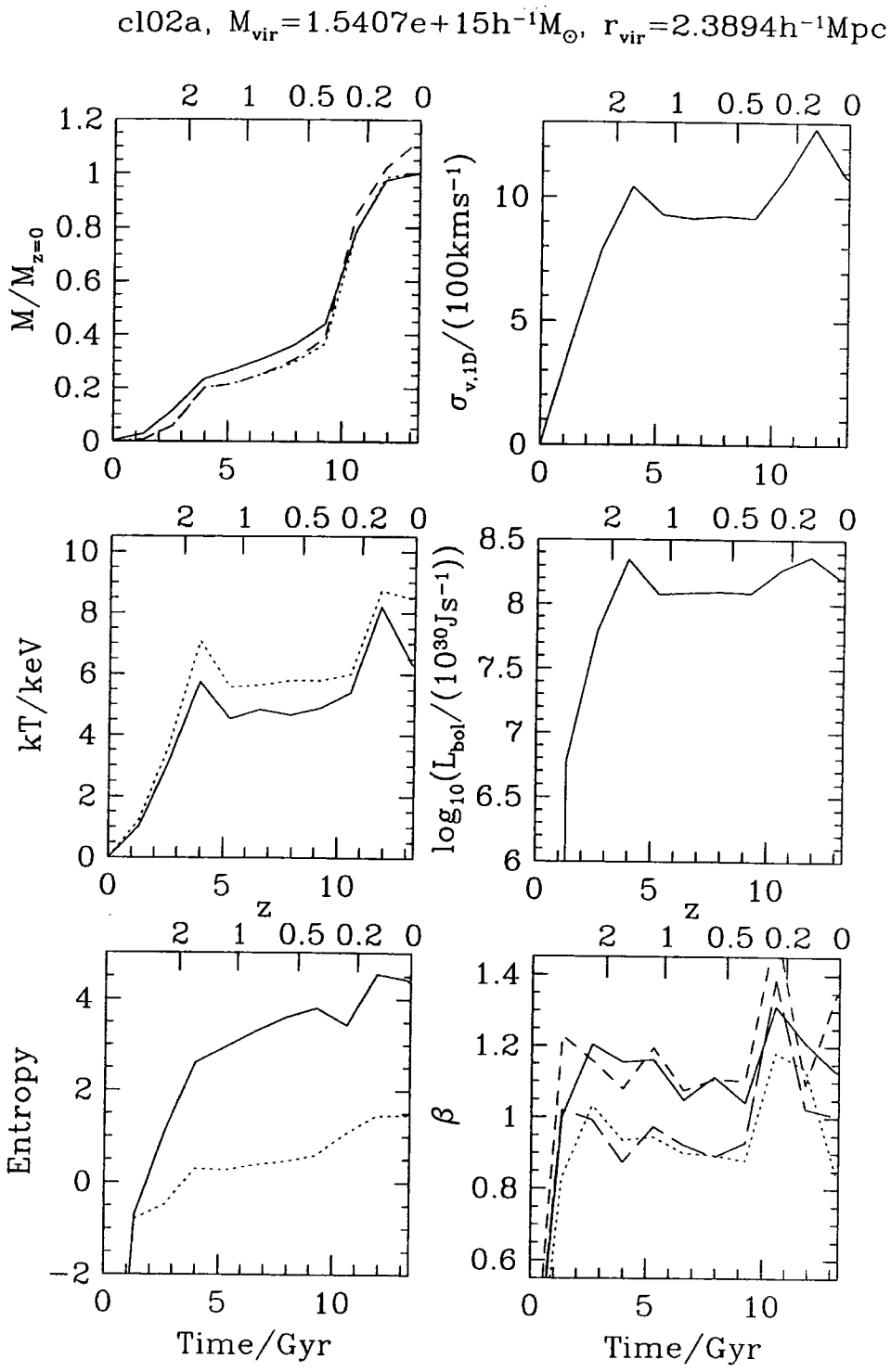
cl02a, M_{vir}=1.5407e+15$h^{-1}M_{\odot}$, r_{vir}=2.3894h^{-1}Mpc
2 1 0.5 0.2 0
M/$M_{z=0}$
$\sigma_{v,1D}$/(100kms^{-1})
kT/keV
$\log_{10}(L_{bol}/(10^{30}Js^{-1}))$
z
Entropy
β
Time/Gyr

Figure E.10:

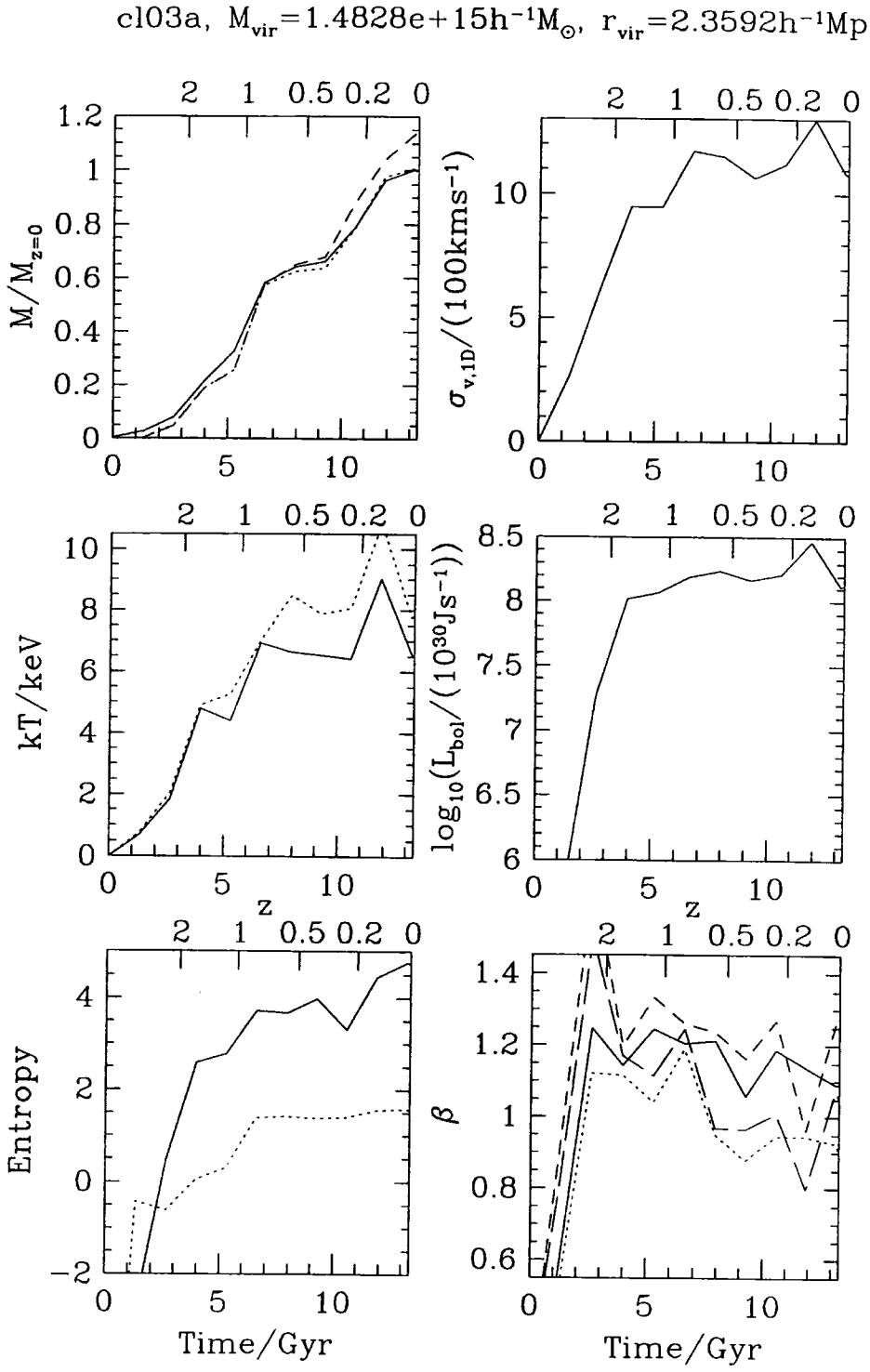
cl03a, M_{vir}=1.4828e+15$h^{-1}M_{\odot}$, r_{vir}=2.3592h^{-1}Mpc
$M/M_{z=0}$
$\sigma_{v,1D}/(100kms^{-1})$
kT/keV
$\log_{10}(L_{bol}/(10^{30}Js^{-1}))$
Entropy
β
z
Time/Gyr

Figure E.11:

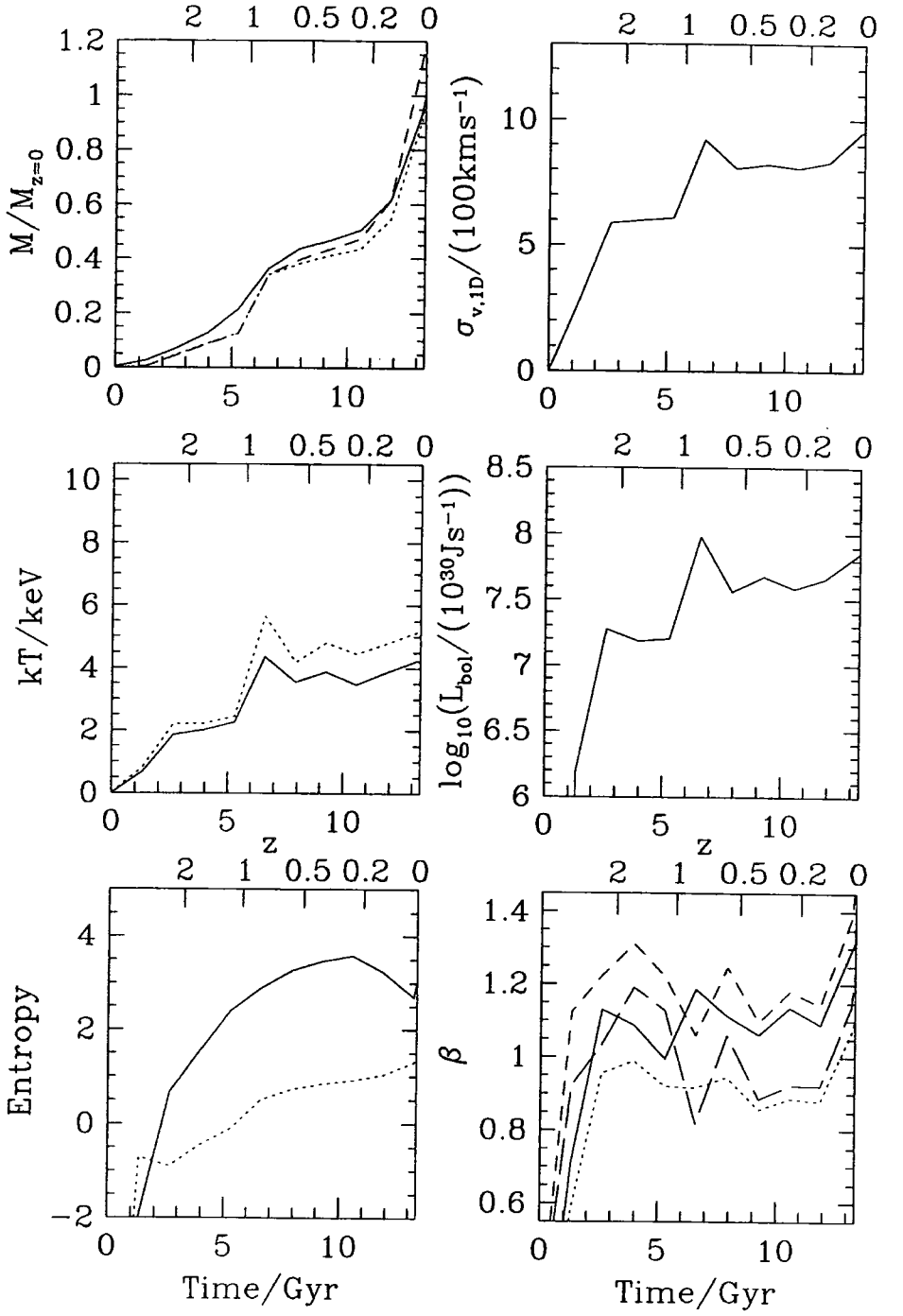
cl04a, M_{vir}=9.6468e+14$h^{-1}M_{\odot}$, r_{vir}=2.0442h^{-1}Mpc
2 1 0.5 0.2 0
$M/M_{z=0}$
$\sigma_{v,1D}/(100kms^{-1})$
kT/keV
$\log_{10}(L_{bol}/(10^{30}Js^{-1}))$
z
Entropy
β
Time/Gyr

Figure E.12:

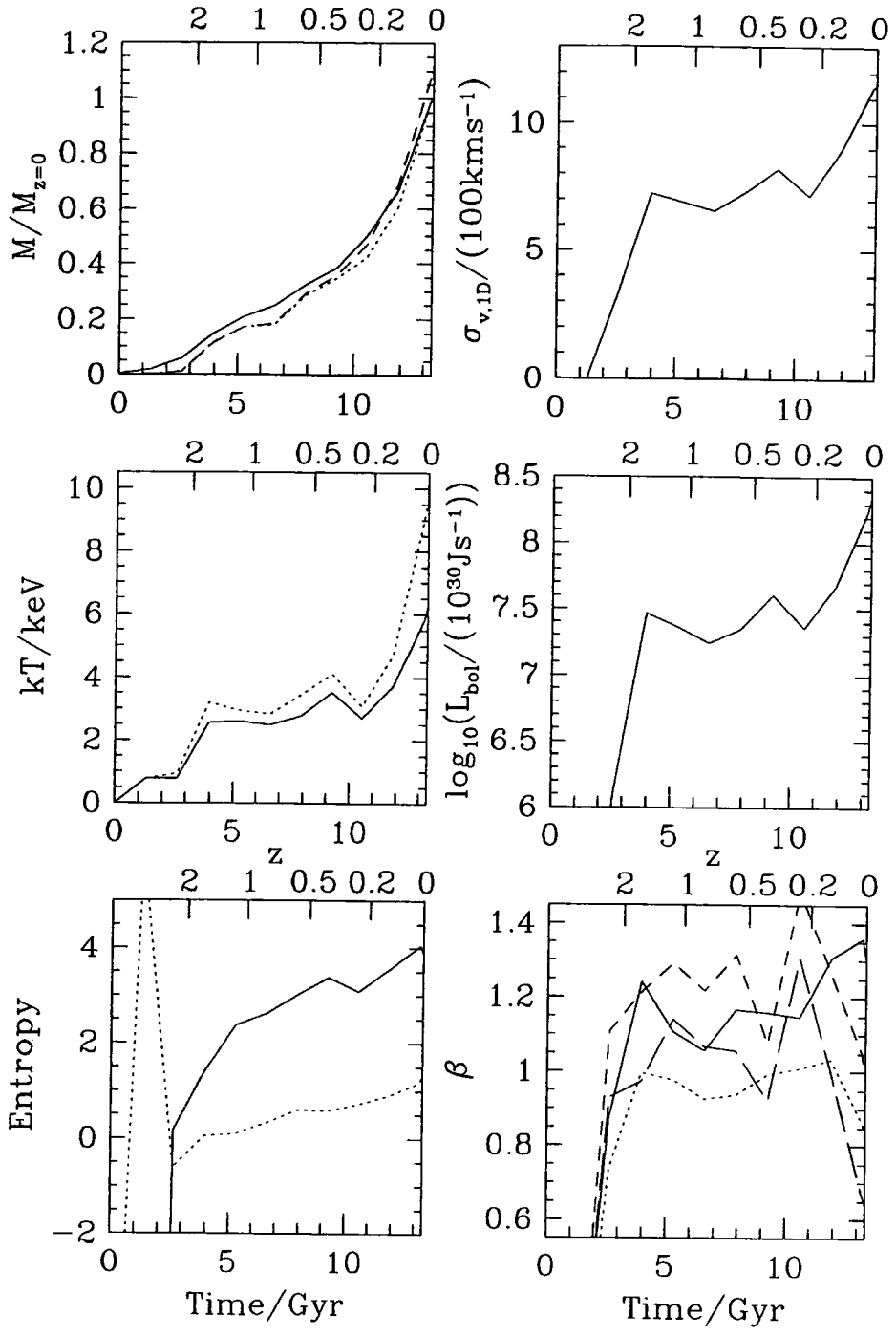
cl05a, M_{vir}=9.5935e+14h^{-1}M$_\odot$, r_{vir}=2.0404h^{-1}Mpc
M/M$_{z=0}$
$\sigma_{v,1D}$/(100kms^{-1})
kT/keV
log$_{10}$(L$_{bol}$/(10^{30}Js^{-1}))
Entropy
β
z
Time/Gyr

Figure E.13:

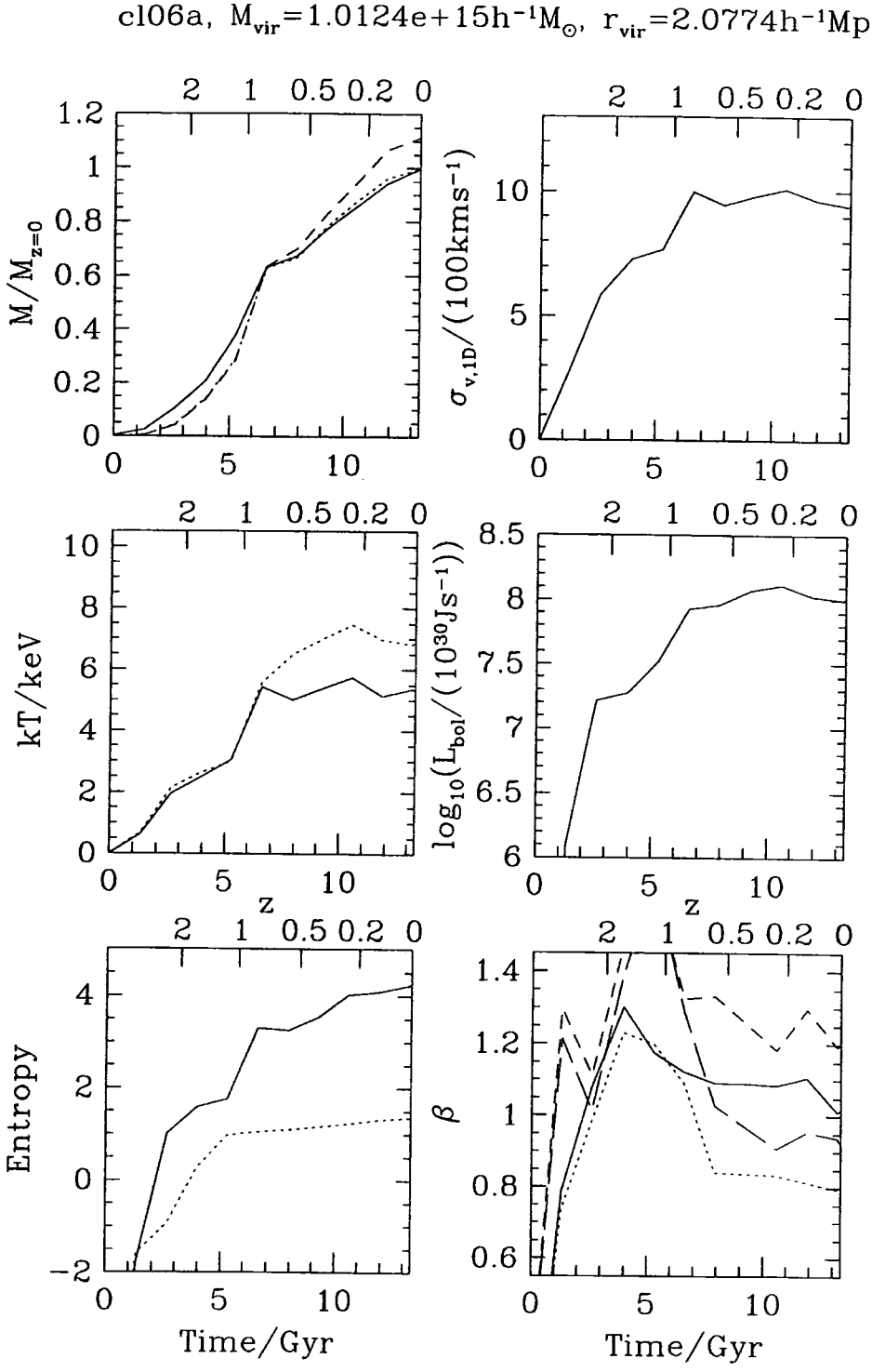
cl06a, M_{vir}=1.0124e+15h^{-1}M$_\odot$, r_{vir}=2.0774h^{-1}Mpc
M/M$_{z=0}$
$\sigma_{v,1D}$/(100kms^{-1})
kT/keV
log$_{10}$(L$_{bol}$/(10^{30}Js^{-1}))
Entropy
β
z
Time/Gyr

Figure E.14:

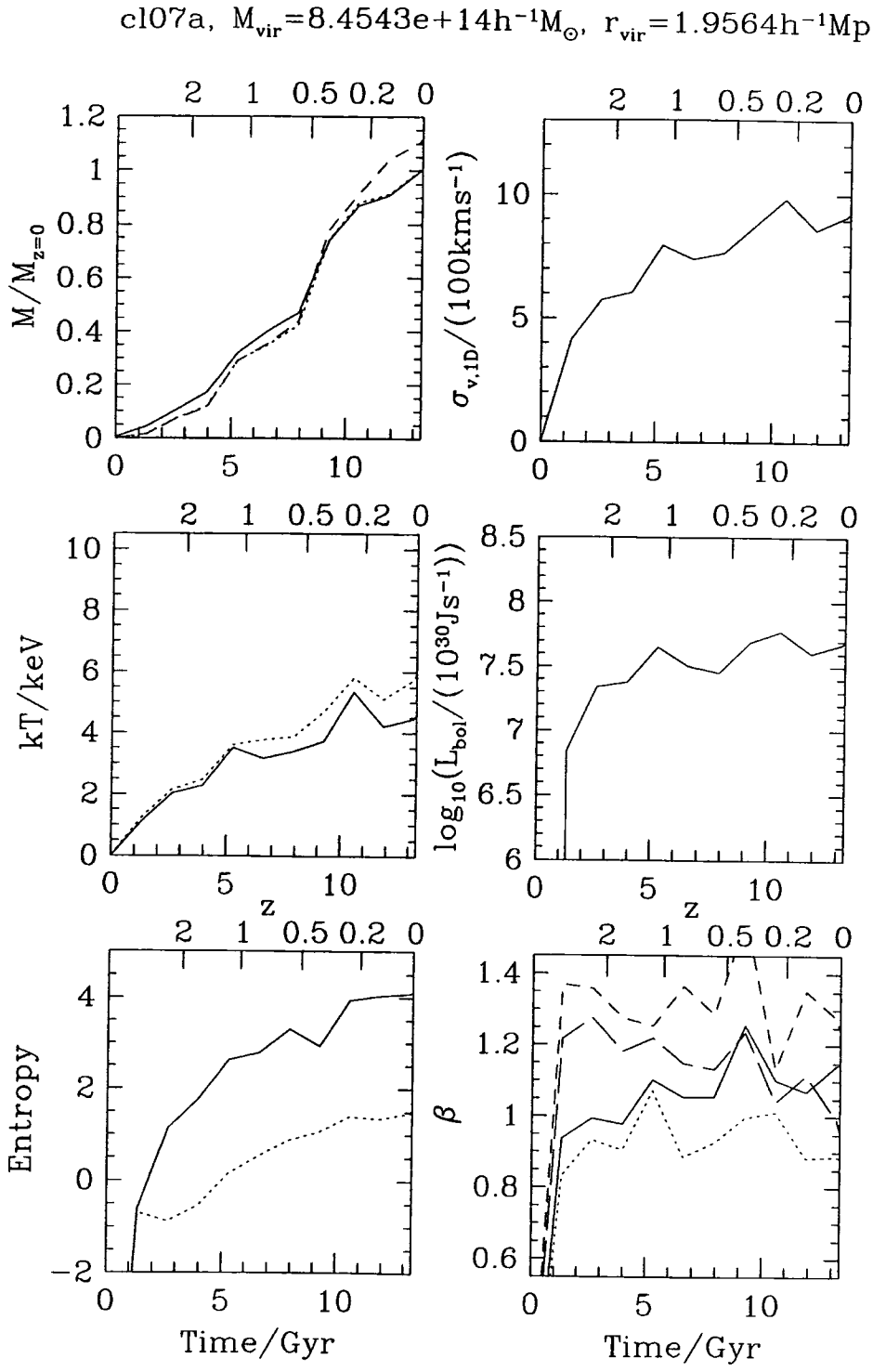
cl07a, M_{vir}=8.4543e+14$h^{-1}M_{\odot}$, r_{vir}=1.9564h^{-1}Mpc
2 1 0.5 0.2 0
$M/M_{z=0}$
$\sigma_{v,1D}/(100kms^{-1})$
kT/keV
$\log_{10}(L_{bol}/(10^{30}Js^{-1}))$
z
Entropy
β
Time/Gyr

Figure E.15:

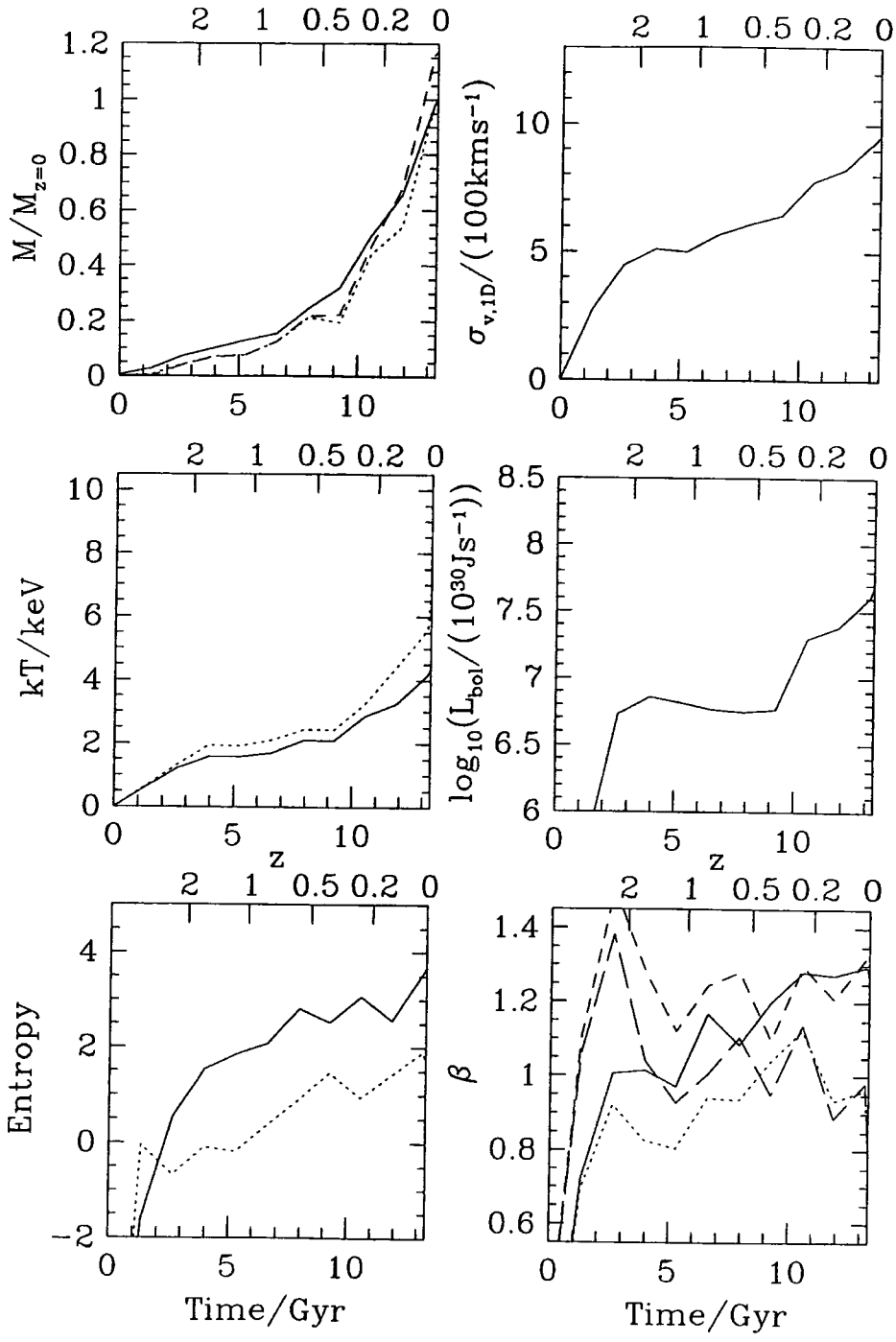
cl08a, M_{vir}=8.1605e+14$h^{-1}M_{\odot}$, r_{vir}=1.9334h^{-1}Mpc
2 1 0.5 0.2 0
$M/M_{z=0}$
$\sigma_{v,1D}/(100kms^{-1})$
kT/keV
$\log_{10}(L_{bol}/(10^{30}Js^{-1}))$
z
Entropy
β
Time/Gyr

Figure E.16:

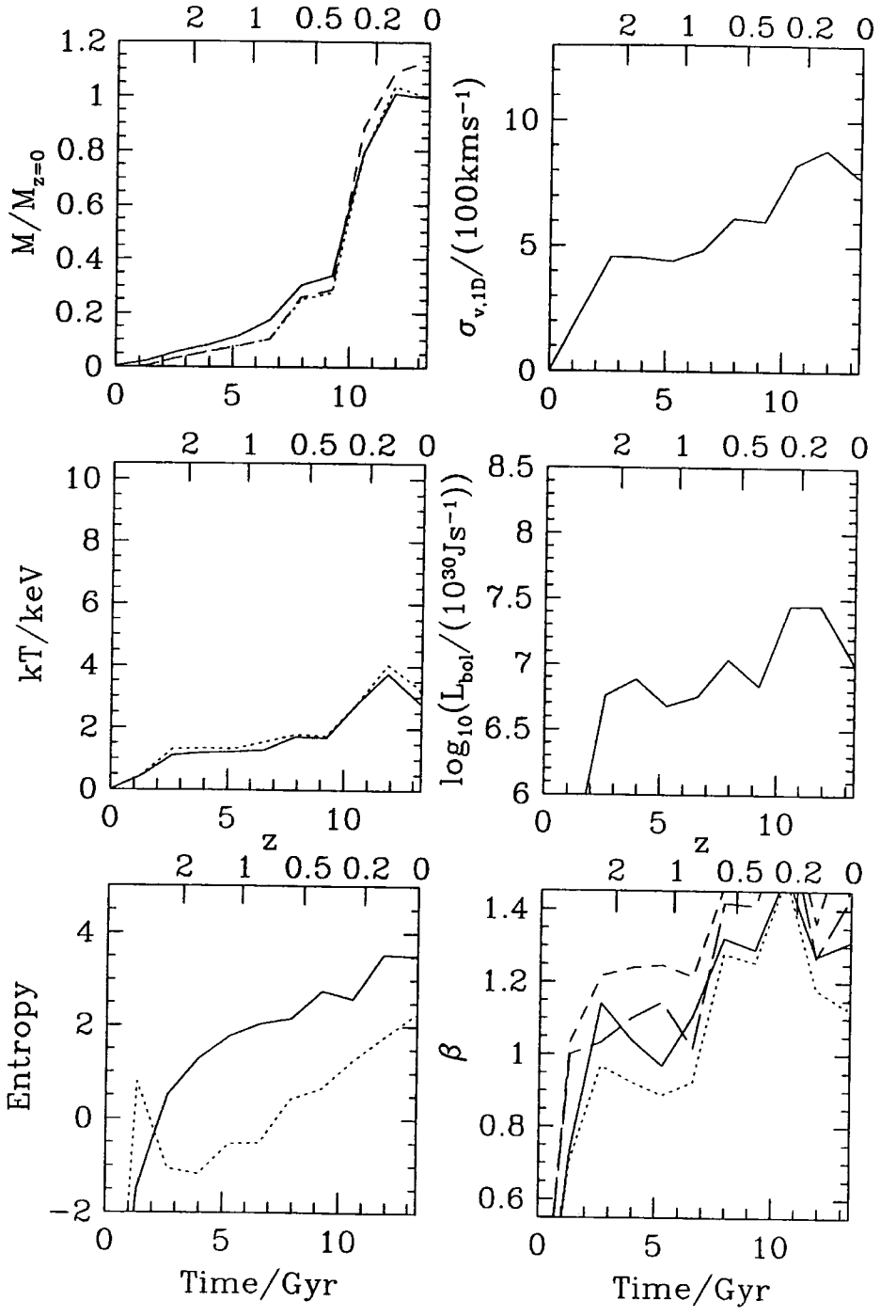
cl09a, M_{vir}=6.3233e+14$h^{-1}M_\odot$, r_{vir}=1.7757h^{-1}Mpc
M/M$_{z=0}$
$\sigma_{v,1D}$/(100kms^{-1})
kT/keV
log$_{10}$(L$_{bol}$/(10^{30}Js^{-1}))
Entropy
β
z
Time/Gyr
2 1 0.5 0.2 0

Figure E.17:

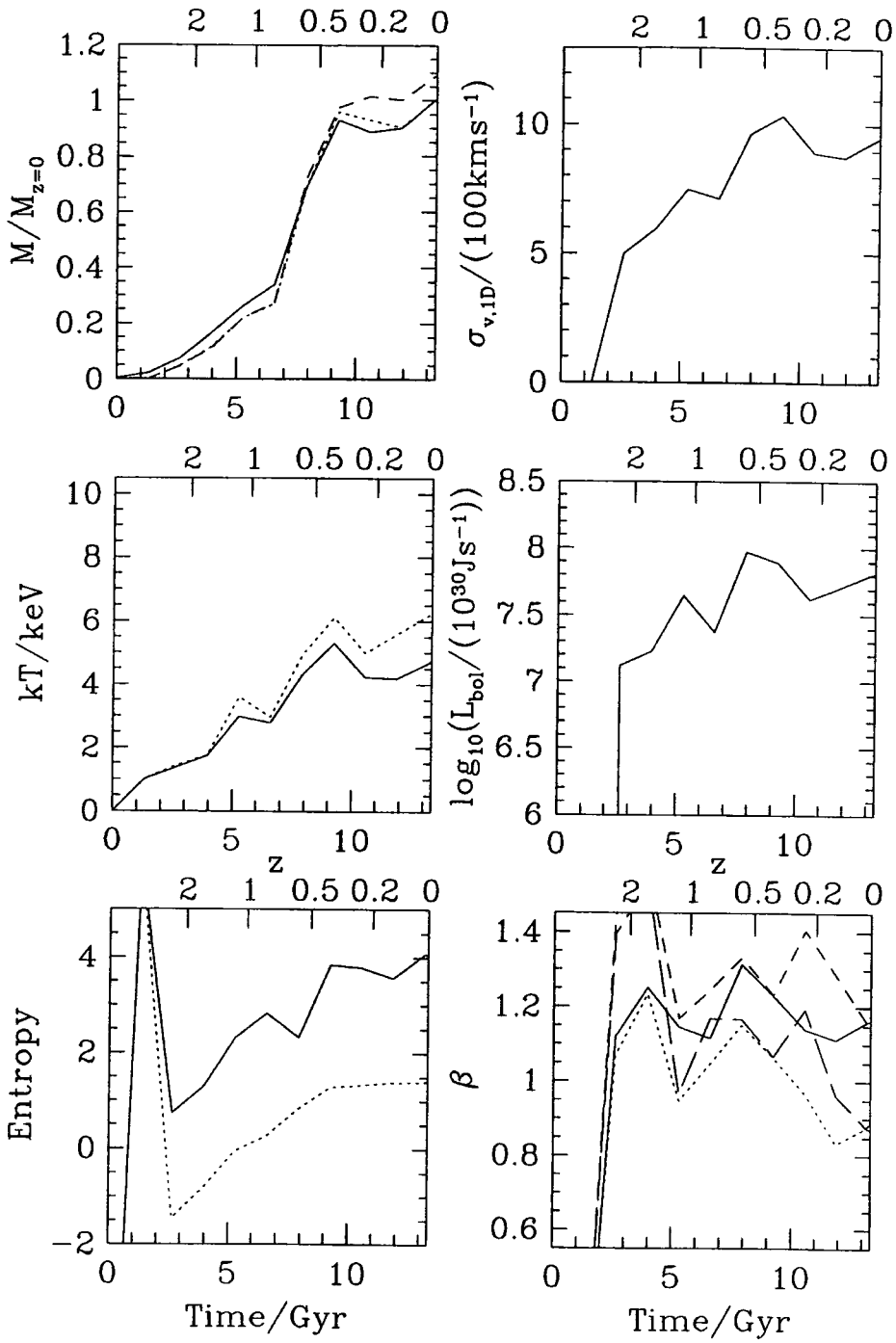
cl10a, M_{vir}=7.8394e+14$h^{-1}M_{\odot}$, r_{vir}=1.9077h^{-1}Mpc
2 1 0.5 0.2 0
M/M$_{z=0}$
$\sigma_{v,1D}/(100kms^{-1})$
kT/keV
$\log_{10}(L_{bol}/(10^{30}Js^{-1}))$
z
Entropy
β
Time/Gyr

Figure E.18: